University of Illinois at Urbana-Champaign

ACRC

Air Conditioning and Refrigeration Center A National Science Foundation/University Cooperative Research Center

Air-Side Heat Transfer Enhancement for Offset-Strip Fin Arrays Using Delta Wing Vortex Generators

H. Ge, A. M. Jacobi, and J. C. Dutton

ACRC TR-205 October 2002

For additional information:

Air Conditioning and Refrigeration Center
University of Illinois
Mechanical & Industrial Engineering Dept.
1206 West Green Street
Urbana, IL 61801

(217) 333-3115

Prepared as part of ACRC Project #104
Combined Transverse and Streamwise Vorticity
to Enhance Air-Side Heat Transfer
A. M. Jacobi and J. C. Dutton, Principal Investigators

The Air Conditioning and Refrigeration Center was founded in 1988 with a grant from the estate of Richard W. Kritzer, the founder of Peerless of America Inc. A State of Illinois Technology Challenge Grant helped build the laboratory facilities. The ACRC receives continuing support from the Richard W. Kritzer Endowment and the National Science Foundation. The following organizations have also become sponsors of the Center.

Alcan Aluminum Corporation
Amana Refrigeration, Inc.
Arçelik A. S.
Brazeway, Inc.
Carrier Corporation
Copeland Corporation
Dacor
Daikin Industries, Ltd.
Delphi Harrison Thermal Systems
Embraco S. A.
General Motors Corporation
Hill PHOENIX
Honeywell, Inc.
Hydro Aluminum Adrian, Inc.
Ingersoll-Rand Company
Kelon Electrical Holdings Co., Ltd.
Lennox International, Inc.
LG Electronics, Inc.
Modine Manufacturing Co.
Parker Hannifin Corporation
Peerless of America, Inc.
Samsung Electronics Co., Ltd.
Tecumseh Products Company
The Trane Company
Valeo, Inc.
Visteon Automotive Systems
Wolverine Tube, Inc.

For additional information:

Air Conditioning & Refrigeration Center
Mechanical & Industrial Engineering Dept.
University of Illinois
1206 West Green Street
Urbana, IL 61801

217 333 3115

Abstract

Offset-strip fins are used in many compact heat exchanger applications because of excellent thermal-hydraulic performance. Enhancing the air-side heat transfer performance for offset-strip fins can lead to smaller, more efficient heat exchangers. In this research, an innovative concept of generating streamwise vortices in offset-strip fin arrays has been investigated experimentally to seek further air-side heat transfer enhancement. Flow visualization, PIV, naphthalene sublimation, and pressure drop measurements were performed for a baseline offset-strip fin array and six arrays enhanced with delta wing vortex generators (VGs) over a Reynolds number range (based on hydraulic diameter) from 400 to 3700, to obtain comprehensive heat transfer enhancement and pressure drop results and to develop a clear understanding of associated flow field mechanisms.

Array-averaged heat transfer enhancement is present for all VG-enhanced arrays even at very low Reynolds numbers, and it increases with increasing Reynolds number. The heat transfer enhancement reaches a maximum at $Re \cong 1000$, with the largest enhancement being 32% for the 8VG at Rows 1 and 5 - enhanced array. The overall enhancement in this low Re range is caused by streamwise vortices only. As Re is increased beyond 1000, the array-averaged enhancement starts to decrease and reaches a minimum at $Re \cong 1630$ for all enhanced arrays. Streamwise vortices suppress spanwise vortex shedding along the paths of their travel, and shedding is either delayed to higher Reynolds numbers or weakened in the regions adjacent to the streamwise vortices. This behavior causes the decreasing trend of heat transfer enhancement in this Reynolds number range. For $Re = 2040$, the enhancement returns and increases as Re increases. The flow in the downstream part of the array becomes chaotic and exhibits turbulent-like features for both the baseline array and the VG-enhanced arrays at these high Reynolds numbers. However, the heat transfer enhancement for the first three rows increases with increasing Re, due to the stronger streamwise vortices at higher Reynolds numbers, which contributes to the overall enhancement return and the increasing trend with Re.

The largest array-averaged heat transfer enhancement for the 2VG-enhanced array, 4VG-enhanced array, and 4VG at Rows 1 and 5 - enhanced array is 7.6%, 16%, and 22%, respectively, which is accompanied by a pressure drop penalty of 0.4%, 25%, and 57%, respectively.

The re-generated streamwise vortices in the middle of the array are found to be weaker and decay more quickly in the flow direction than the streamwise vortices generated at the inlet of the array.

Table of Contents

List of Figures

Page

List of Tables

Page

Nomenclature

English Symbols

A_{core}	minimum free-flow area of the test array
A_{Total}	total surface area of the test array
A_f	naphthalene surface area
A_{VG}	vortex generator surface area
b	vortex generator base dimension or plate spacing
c	vortex generator chord length
d_τ	particle image diameter
d_p	true particle diameter
D_h	hydraulic diameter
D_{na}	mass diffusion coefficient of naphthalene in air
f	friction factor
f_0	baseline friction factor
$f^{\#}$	lens f-number
H	channel height
h_m	mass transfer coefficient
$\overline{h_m}$	fin-averaged mass transfer coefficient
j	Colburn factor
j_0	baseline Colburn factor
L	fin length
L_{core}	length of the test array
M	magnification
m	mass
N	number of data points
Nu	Nusselt number
$\overline{Nu}$	fin-averaged Nusselt number
Nu_o	baseline Nusselt number
P	pressure
Pr	Prandtl number
Re	Reynolds number, based on hydraulic diameter unless otherwise noted
Re_t	Reynolds number, based on plate or fin thickness
S	fin spacing
Sc	Schmidt number
Sh	Sherwood number
$\overline{Sh}$	fin-averaged Sherwood number
$\overline{Sh}_{int}$	local Sherwood number integral
St	Strouhal number
t	time or fin thickness
T	temperature
U	streamwise velocity
U_c	core (maximum) velocity
V	transverse velocity normal to fin surface
$\|V\|$	velocity magnitude

W	spanwise velocity
X	streamwise coordinate or horizontal coordinate for image evaluation
X_o	X dimension of spot window
X^*	dimensionless fin location, $X^* = X/L$
Y	transverse coordinate normal to fin surface or vertical coordinate for image evaluation
Y_o	Y dimension of spot window
Z	spanwise coordinate

Greek Symbols

α	attack angle of vortex generator
$\delta_{nat, avg}$	naphthalene natural sublimation depth
δ_{sb}	local naphthalene sublimation depth
ν	kinematic viscosity
μ	dynamic viscosity
Δ	variable change
λ	wavelength of light
Λ	vortex generator aspect ratio, $\Lambda = 2b/c$
ω	vorticity
ρ	density
$\rho_{n, s}$	density of solid naphthalene
$\rho_{n, v}$	density of naphthalene vapor

Abbreviations

CCD	charge coupled device
CHC	choice code
FFT	fast fourier transform
Nd:YAG	neodymium-yttrium-aluminum-garnet
PIV	particle image velocimetry
RMS	root mean square
SNR	signal-to-noise ratio
VEIF	vortex-enhanced interrupted fin
VG	vortex generator

Chapter 1. Introduction

1.1 Introduction

Liquid-to-air and two-phase-to-air heat exchangers have been used in a wide variety of applications, such as power generation, air conditioning, refrigeration, petrochemical processing, food processing, among others. Improving the performance of these heat exchangers can lead directly to material and energy savings. A heat exchanger with higher performance requires smaller heat transfer area, and thus the mass and volume of the heat exchanger are reduced, making it cost and space efficient. A thermal system with high-performance heat exchangers uses less energy, so it reduces the operational cost. In the air conditioning and refrigeration industries, compact heat exchangers require less refrigerant charge in the system, which mitigates the potential environmental impact in case of system leakage.

For air heating and cooling applications, the thermal resistance of a heat exchanger consists of three components: the liquid or two-phase tube-side convective resistance, the wall or tube conductive resistance, and the air-side convective resistance. The air-side convective resistance has been found to be the largest resistance for most air-conditioning and refrigeration applications. According to Admiraal and Bullard (1995), the air-side resistance is 76% of the total evaporator thermal resistance and 95% of the condenser thermal resistance for residential refrigerators, when the evaporator and condenser are operated in the two-phase region. Thus, efforts to improve the heat exchanger performance to the maximum extent should focus on reducing the dominant air-side thermal resistance and enhancing air-side convective heat transfer.

Interrupted-fin surfaces have been widely investigated due to their high efficiency for air-side convective heat transfer. The boundary layer restarts on the leading edge of each new interrupted fin. Boundary-layer restarting makes each fin perform like a short plate which has a much smaller average boundary-layer thickness than a long plate; therefore, an interrupted surface usually has a much higher average heat transfer coefficient than a continuous surface. Another heat transfer enhancement mechanism relevant to interrupted surfaces is spanwise vortex shedding. The fins will shed vortices when the Reynolds number is above some critical value. Spanwise vortex shedding greatly improves fluid mixing and thus enhances the air-side heat transfer dramatically.

For continuous fins, streamwise vortex generation has been investigated as a promising heat transfer enhancement method, with application in fin-tube heat exchangers. Streamwise vortices can be passively generated by wing-type structures. Figure 1.1 (a) shows four wing-type vortex generators that have been widely investigated in the past. When the approaching flow encounters a delta wing, the delta wing generates a tip vortex system that is carried downstream, as shown in Figure 1.1 (b). These streamwise vortices interchange fluid near the plate surface with the free stream fluid, improve bulk mixing and thus enhance the surface heat transfer.

Both streamwise and spanwise vortices can increase fluid mixing and thus enhance heat transfer. It is, therefore, promising to evaluate flow and heat transfer with simultaneous spanwise and streamwise vortices. In the research presented in this thesis, simultaneous spanwise and streamwise vortices are created by implementing an offset strip fin array with delta-wing vortex generators. Specifically, this research will explore the impact of the vortex generators on the heat transfer and pressure drop of the offset strip fin array, the flow field characteristics of this complex flow, and the mechanisms responsible for heat transfer enhancement with this new technique.

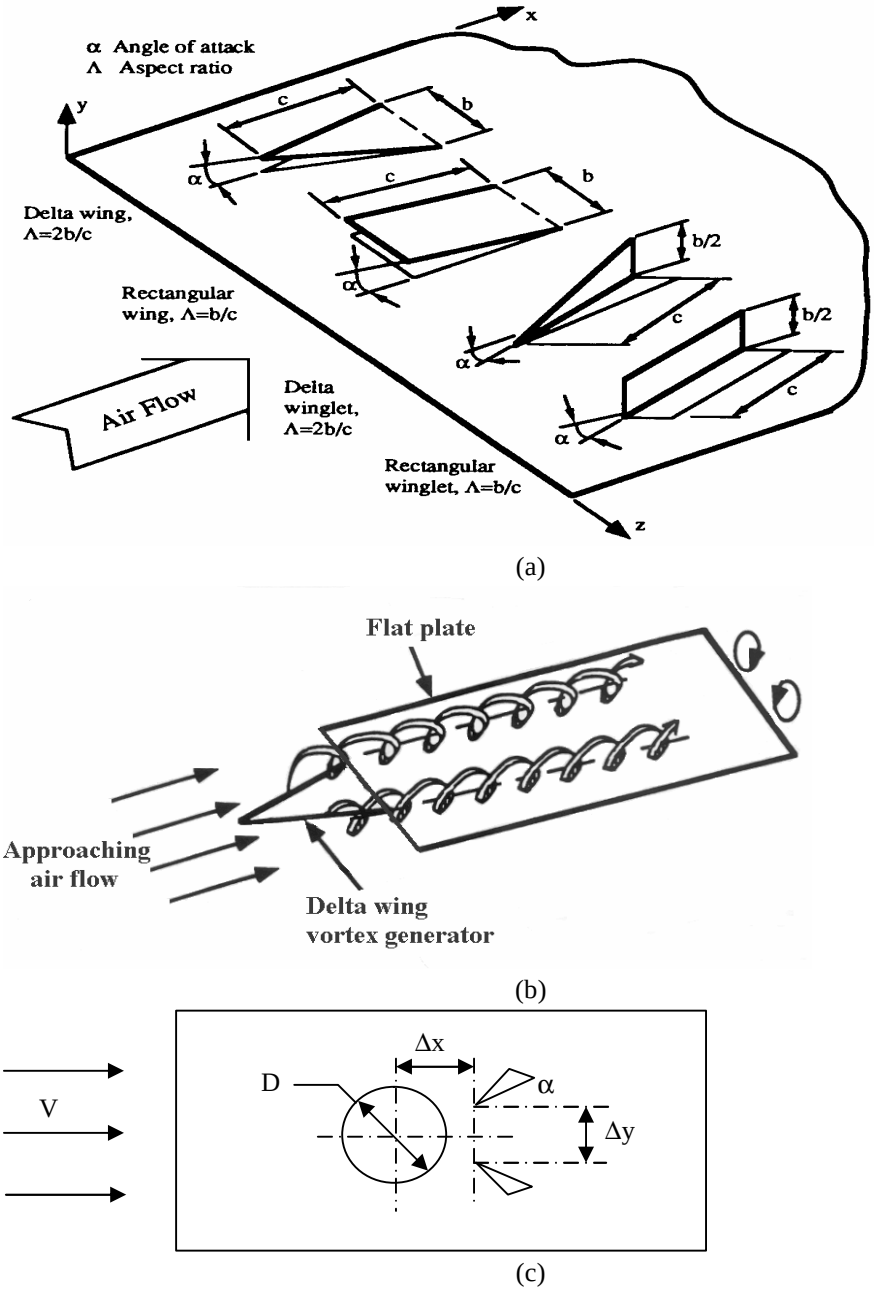

Figure 1.1 – Schematic of: (a) four wing-type vortex generators and their geometric definitions (Jacobi and Shah, 1995); (b) streamwise vortices generated by a delta wing on the leading edge of a flat plate; (c) winglet pair location in a fin-tube element by Fiebig *et al.* (1990)

1.2 Literature Review

1.2.1 Longitudinal Vortex Generation

Extensive research has been performed on heat transfer enhancement using longitudinal vortex generators. Thorough reviews of recent progress were completed by Jacobi and Shah (1995) and Fiebig (1995a, b, 1996). The literature review presented here will focus on the work most directly related to the research reported herein. It will

be organized in three sections: flat-plate flow enhancement, channel flow enhancement, and heat exchanger enhancement.

1.2.1.1 Vortex Generation in Flat Plate Flow

Most work on the heat transfer impact of longitudinal vortices on a flat-plate flow has been experimental. Several experimental methods have been used to obtain the local heat transfer coefficient, velocity components, and flow visualization images. Edwards & Alker (1974) measured the local surface temperature using a luminescent phosphor technique and then obtained the local heat transfer coefficient. Turk and Junkhan (1986) measured air and surface temperatures using thermocouples in order to determine local heat transfer coefficients. Yanagihara and Torii (1990) used an array of 130 thermocouples to measure the surface temperature distribution and a hot-wire anemometer to measure the streamwise velocity and turbulence intensity. Later, Torii *et al.* (1991) performed naphthalene sublimation experiments and smoke-wire flow visualization. Torii *et al.* (1994) also employed a probe rotation technique with a slanted miniature probe to measure all the mean velocity components behind a vortex generator. Gentry and Jacobi (1997) visualized the flow by smoke illuminated by a laser sheet, and obtained the plate average heat transfer coefficient by conducting naphthalene sublimation experiments. Eibeck and Eaton (1987) measured air and surface temperatures with thermocouples to get the local heat transfer coefficient. A four-hole pressure probe was also used in their work to obtain all three components of the mean velocity.

Other researchers investigated the impact of vortex generators on heat transfer and pressure drop for a laminar flat-plate flow. Edwards & Alker (1974) used a row of delta winglets (with attack angles of 12.5° and 25°) to generate co-rotating vortices, and a row of rectangular winglets (with an attack angle of 15°) to generate counter-rotating vortices. Counter-rotating vortices were found to be much more effective than co-rotating vortices in enhancing heat transfer. Vortex generators with larger attack angles were noted to produce greater heat transfer enhancement. A local heat transfer enhancement of up to 42 % was reported. No pressure drop measurements were mentioned in their work.

Turk and Junkhan (1986) evaluated the impact of counter-rotating longitudinal vortices on heat transfer for a flat plate laminar flow. Vortices were generated by a row of rectangular winglet pairs, with the aspect ratio varying from 0.12 to 0.47 but the attack angle fixed at 20°. It was found that imposing a favorable pressure gradient over the plate could create a larger heat transfer enhancement. Smaller spacing between the winglet pairs also created larger heat transfer enhancement. The authors reported a maximum enhancement of 300% for the spanwise-averaged heat transfer coefficient at a distance of more than 30 wing lengths downstream from the winglets. A correlation of the overall heat transfer enhancement was given based on the winglet geometry and entrance boundary layer thickness. The authors did not mention any pressure drop measurements.

Yanagihara and Torii (1990) investigated the effects of a single and a pair of delta winglet vortex generators on an otherwise laminar flat-plate boundary layer. The maximum enhancement they reported was 80% for the single vortex generator and 110% for the pair.

Gentry and Jacobi (1997) studied the impact of a single delta-wing vortex generator on the flow and heat transfer in a laminar boundary layer. Their test matrix included variation of Reynolds number (Re = 600, 800, and 1000), aspect ratio (Λ = 0.5, 1, 1.5, and 2) and angle of attack (α = 10°, 25°, 40°, and 55°) of the delta wings.

Optimized delta-wing geometries for maximum heat transfer enhancement for all three Reynolds numbers were presented. A 50% to 60% enhancement of average heat transfer was reported for these optimal geometries, with an estimated pressure drop penalty of 50% to 100%.

Inspired by the significant heat transfer enhancement obtained with longitudinal vortex generators, some researchers also studied the influence of longitudinal vortices on the flow field, trying to clarify the mechanisms responsible for the heat transfer enhancement.

Yanagihara and Torii (1990) investigated the flat-plate flow field with delta-winglet vortex generators embedded in the laminar boundary layer. For a single vortex generator, greater heat transfer enhancement was observed in the downwash region due to the thinning of the boundary layer while the heat transfer enhancement was less in the upwash region. When the attack angle of the vortex generator increased, the local heat transfer enhancement increased, and the longitudinal vortices affected a larger surface area. For a pair of delta winglets, higher heat transfer enhancement was observed when the common flow between the two main vortices was downwash (toward the surface) rather than upwash (away from the surface). A smaller distance between the winglets produced a higher heat transfer coefficient along the centerline. Further work by Torii *et al.* (1991) revealed that the main vortices, the corner vortices and the induced secondary vortices behind a delta winglet played a major role in distorting the flow and enhancing the heat transfer. The main reason for heat transfer enhancement in the region near the generator was found to be boundary layer thinning by the main and corner vortices. The authors recommended a smaller distance between the generators with the common flow downwash and a larger attack angle for optimal heat transfer enhancement.

Torii *et al.* (1994) experimentally investigated the three-dimensional highly skewed flow field downstream of a single delta-winglet vortex generator in an otherwise laminar boundary layer on a flat plate. Their measurements showed that an axial mean velocity defect occurred locally in the vortex core. The positions of the local peak heat transfer were found to correspond well to the downwash side of the main vortex and the second corner vortex. The local heat transfer coefficient was less in the upwash region than in the downwash region, although the onset of local turbulent transition in the upwash region resulted in strong velocity fluctuations. The turbulence characteristics in these localized turbulent regions were similar to those reported for a turbulent boundary layer.

Gentry and Jacobi (1997) investigated the interaction of longitudinal vortices with a laminar boundary layer. A delta wing was used to generate the longitudinal vortices. Flow visualization showed that the two vortices generated by the delta wing spread apart and lifted away from the surface as they traveled downstream. Based on the flow visualization images, the plate-to-core and core-to-core distances were obtained for the tip vortices. These distances were used to determine the vortex circulation and then were incorporated into a “goodness” factor. Mass transfer data were found to be in reasonable agreement with the goodness factor predictions. The optimized delta-wing geometries with maximum heat transfer enhancement for Reynolds numbers of 600, 800, and 1000 suggested that the streamwise vortices should be strong and located near the edge of the boundary layer for best performance. In further research, Gentry and Jacobi (1998) observed a periodic waviness in the longitudinal vortices when the plate-to-vortex distance was less than the viscous boundary layer thickness. Vortex breakdown, a condition for

which the longitudinal vortices become poorly defined and incoherent, was also noted for tip vortices with high strength. The local mass transfer results indicated that the vortex strength contributed more to the heat transfer enhancement than the vortex location relative to the boundary layer.

Others have conducted research on the impact of longitudinal vortices on flow and heat transfer in a turbulent boundary layer. Eibeck and Eaton (1987) experimentally studied the flow and heat transfer in a turbulent flow above a flat plate with a built-in single delta winglet. The measured velocity was compared to a Rankine vortex model. The results showed that the boundary layer on the downwash side of the vortex was thinner, and the local Stanton number was enhanced by as much as 24%. For the same conditions, the boundary layer on the upwash side was thicker and a reduction of 14% in the Stanton number was reported.

Pauley and Eaton (1988) investigated the vortical flow in a two-dimensional turbulent boundary layer above a flat plate with built-in delta winglet pairs in common-inflow, common-outflow, and co-rotating configurations. All three components of mean velocity were measured with a five-hole pressure probe. The vorticity field was calculated from the velocity gradients. Common-inflow vortex pairs were observed to spread and lift from the surface while common-outflow vortex pairs moved toward each other and lifted from the surface more rapidly. Co-rotating vortex pairs were observed to move toward each other and merge into a single vortex as they convected downstream.

1.2.1.2 Vortex Generation in Channel Flow

Some researchers have conducted experimental research to evaluate the impact of vortex generators in a channel flow.

Russell *et al.* (1982) studied the effect of delta and rectangular winglet pairs on heat transfer and pressure drop in a channel flow. A transient paint-melting technique was used to measure the local heat transfer coefficient. Heat transfer and pressure drop measurements were conducted for different Reynolds numbers, and the results were presented as Colburn j factor and friction factor f. Among all VG configurations they studied, the rectangular winglets with an attack angle of 20° in a staggered placement were found to give the best overall heat transfer enhancement. For Reynolds numbers between 500 and 2000, the j factor increased approximately 40% and the f factor increased about 20%, as compared to typical plain-fins. The results would have been more convincing if the j and f results had been compared to measurements in the same channel flow without vortex generators.

Fiebig *et al.* (1986, 1991) investigated the effect of a single vortex generator in a developing laminar channel flow. Vortex structures were visualized by smoke illuminated by a laser light sheet. The unsteady liquid crystal thermography technique was used to determine the local heat transfer coefficient. Instead of measuring the tiny pressure drop directly, they used a balance to measure the drag caused by a test fin. Vortex generators, in the form of delta wings, rectangular wings, delta winglets, and rectangular winglets (as shown in Figure 1.1(a)), were evaluated with the aspect ratio varying from 0.8 to 2.0 and the attack angles varying from 10° to 60°. The range of Reynolds number based on channel height was from 1360 to 2270. The critical attack angle for stable longitudinal vortices to exist in a channel flow was found to be much higher than those in a flat plate flow. It was found that the drag induced by the vortex generators was proportional to the VG area and increased with VG attack angle. Local heat transfer enhancement of more than 300% and total heat transfer enhancement (based on an area more than 50

times the VG area) of more than 50% were reported. The authors concluded that the delta wings were most effective per unit VG area for heat transfer enhancement, followed by delta winglets and rectangular winglets.

Tiggelbeck *et al.* (1992, 1993) studied the impact of single and double rows of vortex generators on the heat transfer and flow structure of a channel flow in the transition regime. The flow was visualized by smoke illuminated by a laser light sheet. The local heat transfer coefficient was measured by unsteady liquid-crystal thermography. Delta winglet pairs were punched out of the channel walls, with an aspect ratio of 2 and attack angles of 45° and 65°. Two configurations were investigated for double rows of vortex generators, with the second row either aligned or staggered with respect to the first row. The flow visualization results showed that the vortex structure behind the first row of winglets included counter-rotating primary vortices, as well as two secondary vortices in the regions between neighboring primary vortices. The vortex structure behind the second row of winglets was found to be almost the same as that behind the first row, with vortex unsteadiness slightly larger. The maximum local heat transfer enhancement was observed immediately behind the second row of winglets, where the longitudinal vortices were the strongest. A local heat transfer enhancement of up to 460% was observed for the aligned double-row configuration with a row-spacing of 7 times the channel height. The aligned double-row configuration showed slightly larger heat transfer enhancement and pressure drop than the staggered double-row configuration. A global heat transfer enhancement of 80% and pressure drop increase of 165% were reported for the aligned double-row configuration at Re=6000. The ratio of global heat transfer to pressure drop, each normalized with its plain-duct value, in the form of $(Nu/Nu_0)/(C_F/C_{F0})$, was reported to reach a maximum of 0.67 for the aligned double-row configuration at Re=6000 and Re=8000. The authors thus concluded that the double-row configuration of vortex generators generates more benefit at higher Reynolds numbers than at lower Reynolds numbers.

Biswas *et al.* (1996) measured the three-dimensional velocity field in a fully developed laminar channel flow with a single built-in delta winglet, by using a probe rotation technique. Vorticity contours from their measurements showed the complete vortex system behind the winglet, which included a main vortex, a corner horseshoe vortex, and an induced vortex. The experimental velocity results validated their numerical calculations, which will be discussed later in this literature review.

Gentry and Jacobi (1998) investigated the influence of a delta wing vortex generator on the flow structure, heat transfer, and pressure drop in a laminar developing channel flow. The flow was visualized by dye-in-water, and vortex strength was measured with a vane-type vortex meter. The local and average mass transfer coefficients were measured by means of naphthalene sublimation tests. The flow visualization showed that the tip vortices first spread and traveled away from the surface until they reached the channel centerline, and then they traveled in parallel paths along the centerline. The periodic waviness and vortex breakdown noted in the flat-plate flow were not observed in the channel, even for much stronger tip vortices than those in the flat-plate flow. Maximum local mass transfer enhancement of 150% was obtained. The total mass transfer coefficients averaged on both channel walls increased 20%, 40%, and 50%, while the pressure drop increased 50%, 70%, and 110%, for Reynolds numbers of 400, 1200, and 2000, respectively.

Liou *et al.* (2000) studied the effect of 12 different vortex generators of various shapes, including delta wings and winglet pairs, on the heat transfer and flow patterns in a square duct at a fixed Reynolds number of 12,000. Local Nusselt number distributions were measured using transient liquid crystal thermography. Flow patterns were measured using laser-Doppler velocimetry, and friction factors were obtained using a pressure transducer. The direction and strength of the secondary flow with respect to the channel wall were found to be the dominant factors contributing to the heat transfer enhancement. The delta wing configuration was found to be one of the best, creating an enhancement of 170% in heat transfer under a constant Reynolds number, while only introducing a 30% increase in friction factor.

Numerical studies have also been performed for channel flows with built-in longitudinal vortex generators. Biswas *et al.* (1989) computed the laminar flow and heat transfer in a rectangular channel. A single delta wing, with an aspect ratio of 1 and attack angles of 20° and 26°, was mounted on the channel wall without a punched hole underneath. The effect of Grashof number (i.e., natural convection) was considered. Higher spanwise-averaged Nusselt numbers were noted with larger Grashof numbers. At a Reynolds number of 500 (based on channel height), an average Nusselt number increase of 34% was reported while the friction factor increased 79%. In a further study, Biswas and Chattopadhyay (1992) included the effect of the punched hole under the delta wing and calculated the flow and heat transfer for an otherwise identical situation. They found that with the hole under the delta wing, the increase in Nusselt number was only 10%, while the friction factor increase was 48%.

Fiebig *et al.* (1989) calculated the laminar velocity and temperature fields in a rectangular channel with a row of built-in vortex generators in the form of slender delta wings and winglet pairs. Density variations due to temperature changes were considered in the calculation. Axial velocity defect occurring in the vortex cores was noted for both delta wings and winglet pairs. Vortex breakdown was observed for attack angles larger than 50°. The vortex cross-sectional structure downstream of the delta wings became highly elliptical. An average heat transfer enhancement of 300% was reported based on their calculations.

Biswas *et al.* (1994a) and Deb *et al.* (1995) calculated the laminar flow and heat transfer in a rectangular channel. A single vortex generator, in the form of a delta wing and winglet-pair, was included in the computational domain. The effect of the stamping hole under the vortex generator was taken into consideration. An irreversibility analysis was introduced to analyze the influence of the vortex generators. The overall Nusselt number and friction factor increased as the attack angle increased. The overall heat transfer and friction factor without the stamping hole were found to be higher than those with the stamping hole. They concluded that the delta wing was more effective than the winglet-pair in terms of heat transfer, but less effective than the delta winglet pair in terms of entropy generation.

Fiebig *et al.* (1995c) numerically investigated the impact of rectangular winglet vortex generators for the channel flow. At a Reynolds number of 1000, the influence of attack angle (from 15° to 45°) on the average heat transfer and pressure drop was analyzed for eight configurations of vortex generators mounted on the channel walls. A maximum average heat transfer enhancement of up to 500%, accompanied by a friction factor increase of 45%, was found with an attack angle of 15° for an in-line, symmetric configuration with the rectangular winglets attached

on both channel walls. However, these numerical results were not compared to any experimental results for an identical situation.

Biswas *et al.* (1996) calculated the flow and heat transfer for a fully developed laminar channel flow with a single built-in delta winglet. Their calculation was performed at a single Reynolds number of 1580 (based on channel height), with winglet attack angles between 15° and 45°. The calculated velocity field was corroborated by three-dimensional velocity measurements. The computed average heat transfer and pressure drop results were presented as the ratio of the Colburn *j* factor to the Fanning friction factor: *j/f*. A higher value of *j/f* was noted for the winglet with a smaller attack angle. By comparing with the *j/f* result obtained for a winglet pair (Biswas *et al.* 1994a), they concluded that the single winglet showed better performance than a winglet pair for the channel flow.

1.2.1.3 Vortex Generation in Heat Exchangers

Recent progress on vortex generation for heat exchangers has been mostly focused on fin-tube heat exchangers. Fin-tube heat exchangers with round, flat and oval tubes have been studied both experimentally and numerically. Fiebig and his research group have been very active in this area.

1.2.1.3.1 Vortex Generation in Fin-Tube Heat Exchangers with Round Tubes

Fiebig *et al.* (1990) evaluated the impact of a punched-out delta-winglet pair on the heat transfer and pressure drop in a single fin-tube element, as shown in Figure 1.1 (c). The aspect ratio of the winglet pair was 2, and the attack angle varied from 25° to 55°. The local heat transfer coefficient was found to increase by up to a factor of 2 compared to the heat transfer without the vortex generators. An optimal winglet pair configuration, with $\Delta x/D = 0.6$, $\Delta y/D = 0.8$ and the attack angle $\alpha = 45°$ (as shown in Figure 1.1 (c)), was observed to provide an average heat transfer increase of 20% while reducing the friction factor up to 10%. The authors explained the friction factor reduction by noting that the longitudinal vortices generated by the delta-winglet pair bring high momentum fluid into the region behind the tube and delay flow separation after the tube.

Fiebig *et al.* (1993) studied the influence of delta winglet vortex generators on a three-row fin-tube heat exchanger, focusing on the difference between the inline and staggered tube configurations. Delta winglets with an aspect ratio of 2 and an attack angle of 45° were punched out from the fins at locations of $\Delta x/D = 0.6$ and $\Delta y/D = 1.0$ (refer to Figure 1.1 (c)). The highest heat transfer enhancement due to the vortex generators was found with the inline tube arrangement, which showed a 55-65% increase in heat transfer and a 20-45% increase in the friction factor, for Reynolds numbers from 600 to 2700. The corresponding increases for the staggered tube arrangement were found to be lower.

Biswas *et al.* (1994b) numerically investigated the flow structure and heat transfer in a three-row fin-tube heat exchanger with built-in delta winglet pairs. The tube rows were arranged in a staggered way, and a punched-out delta winglet pair with an aspect ratio of 2 and attack angle of 45° was located behind each tube with $\Delta x/D = 0.5$ and $\Delta y/D = 1.0$ (refer to Figure 1.1 (c)). At a Reynolds number of 500, a local heat transfer increase of more than 240% was reported at a location about 12 times the channel height downstream of the inlet. The spanwise-average Nusselt number at Re = 646 compared favorably to experimental results from the same geometry for most streamwise locations, although large discrepancies existed at some streamwise locations. It must be noted that the constant

temperature boundary condition used in the numerical calculation was not satisfied in the experimental work to which the authors compared their computations.

Fiebig *et al.* (1995d) performed a three-dimensional numerical calculation of conjugate convective and conductive heat transfer in a fin-tube element (with a round tube) for different Reynolds numbers (in a range from 100 to 1000) and fin efficiency parameters. Flow patterns, pressure distributions, Nusselt number distributions, heat flux distributions, and fin efficiency were presented for thermally and hydrodynamically developing laminar flows. The Nusselt numbers were found to increase with increasing Re and decreasing fin efficiency. When the fin efficiency was small and Re was large, it was noted that there was a special region in the tube wake where the heat transfer reversed, degrading the heat exchanger performance. In a further study, Fiebig *et al.* (1995e) presented a solution to avoid the heat transfer reversal and augment the heat transfer by using a delta winglet pair vortex generator. Numerical calculations were carried out for Reynolds number of 250 and 300. The delta winglet pair, with an aspect ratio of 2 and an attack angle of 45°, was punched out of the fin surface right behind the tube with $\Delta x/D = 0.5$ and $\Delta y/D = 0.8$ (refer to Figure 1.1 (c)). The numerical results showed that the longitudinal vortices greatly reduced the separated region in the tube wake. Therefore, the heat transfer reversal was avoided, and heat transfer in the tube wake area was greatly enhanced. The authors reported a maximum global heat transfer enhancement of 31% due to the delta winglet pair.

1.2.1.3.2 Vortex Generation in Fin-Tube Heat Exchangers with Flat Tubes

Fiebig *et al.* (1994) measured the heat transfer enhancement and flow losses for a fin-tube heat exchanger with three rows of flat tubes in a staggered arrangement. Delta winglet pairs with an aspect ratio of 2 and attack angle of 45° were used to generate longitudinal vortices. The results were compared to similar experimental results for round tubes (Fiebig *et al.* 1993). The heat transfer was found to increase dramatically (100%) for flat tubes while only marginally (10%) for round tubes. The heat exchanger element with flat tubes and vortex generators was reported to give nearly twice as much heat transfer and only half as much pressure drop as the corresponding heat exchanger element with round tubes.

Valencia *et al.* (1996) measured the heat transfer and friction factor on a heat exchanger element with a flat tube and a pair of delta winglets. Three different locations of winglet pairs relative to the flat tube were studied at a Reynolds number of around 2400. The best location was found to increase heat transfer by 50% and pressure drop by 36%; the vortex generators were found to only affect the fin near the rear part of the tube.

1.2.1.3.3 Vortex Generation in Fin-Tube Heat Exchangers with Oval Tubes

Chen *et al.* (1998a-d, 2000) have performed extensive numerical studies of the heat transfer enhancement for finned oval tube heat exchangers.

Chen *et al.* (1998a, b) first carried out a conjugate numerical study on three-dimensional steady-state developing flow and heat transfer in a finned oval tube heat exchanger element without vortex generators. Then they (1998c) numerically calculated the vortex-enhanced flow and heat transfer in the same element. A single delta winglet pair was punched from the fin surface to generate the longitudinal vortices. Three different attack angles (20°, 30°, and 45°) and two different aspect ratios (1.5 and 2) were investigated at a Reynolds number of 300. Numerical results for the velocity and temperature fields, vortex formation, local heat transfer characteristics, and

global heat transfer characteristics were presented. Higher heat transfer and pressure drop were observed with larger attack angle and small aspect ratio. The winglet configuration with an attack angle of 30° and an aspect ratio of 2 was found to give the best ratio of heat transfer enhancement to pressure drop penalty with $(j/j_0)/(f/f_0)$ = 1.04. The authors also noted a corner vortex formed by the fluid from the lower part of the trailing edge and the fluid near the tip of the winglet.

Later, Chen *et al.* (1998d, 2000) numerically investigated the impact of multiple vortex generators on the finned oval tube heat exchanger element. Delta winglets with the optimal attack angle of 30° and aspect ratio of 2 discovered previously (Chen *et al.* 1998a) were adopted, with the Reynolds number fixed at 300. Chen *et al.* (1998d) first studied the inline configuration of delta winglets, with one to three winglet pairs placed inline on the fin surface. Stronger longitudinal vortices were found behind the second and third winglets than behind the first winglet due to the "booster effect" of the upstream vortex on the newly generated vortex. The authors reported a ratio $(j/j_0)/(f/f_0)$ of 1.04, 1.01 and 0.97 for a fin oval tube element with one, two, and three delta winglet pairs in-line. In a continuation of this work, Chen *et al.* (2000) investigated the staggered configuration of delta winglets, with two to four winglet pairs placed staggered along the tube. The results showed a ratio $(j/j_0)/(f/f_0)$ of 1.151 and 1.097 for a fin oval tube element with two and four staggered winglets. By comparing to the inline configuration (Chen *et al.* 1998d), the authors showed that the winglets in the staggered arrangement achieved larger heat transfer enhancement for oval fin-tube heat exchangers than winglets in the in-line arrangement. The authors explained that the interaction of longitudinal vortices generated by the staggered winglets influenced a larger area and intensified the fluid motion normal to the main flow direction.

1.2.2 Offset Strip Fin Array and Spanwise Vortex Shedding

Extensive research has been conducted on offset strip fin surfaces. Manglik and Bergles (1995) provided a complete review of the past literature. Here a survey related to the current research will be presented.

1.2.2.1 Flow Characteristics in Offset Strip Fin Array

Mochizuki and Yagi (1982) visualized flow through 13 scaled-up models of offset-strip fin arrays with the number of rows varied from one to twenty. Dye and hydrogen bubbles were used to visualize the flow in the water tunnel while a hot-wire anemometer was used to measure the vortex shedding frequency in the wind tunnel. For a single plate, the Strouhal number decreased stepwisely from 0.18 to 0.16 at Re_t=250 and then remained constant with further increases in Re_t. For arrays with two rows, two Strouhal numbers were found to be present due to the different wakes generated by the two rows. The vortex shedding frequency was found to be higher for the upstream row than for the downstream row. For arrays with three to eight rows, multiple Strouhal numbers were found to occur for high Re_t while only one Strouhal number existed for low Re_t. For arrays with nine to twenty rows, only one Strouhal number with a constant value of 0.13 was detected for $Re_t \leq 110$, while no clear frequency was found for higher Re_t. The onset location for vortex shedding was observed to move upstream in the array with increasing Re_t. The authors classified three regimes for the flow: steady laminar, oscillating, and turbulent flow. In a related study, Mochizuki *et al.* (1987) observed that high turbulence intensity prevailed in the middle and downstream regions at low Re. With an increase of Re, high turbulence intensity was observed to move to upstream regions while the

turbulence intensity gradually decreased in the middle and downstream regions. When Re exceeded a critical value, uniform turbulence intensity was found throughout the core.

Mullisen and Loehrke (1986) investigated the flow structure and heat transfer behavior in both the in-line and staggered interrupted-plate arrays for a Re range from 100 to 10,000. The schlieren technique was used to visualize the flow, and a transient heating technique was used to measure heat transfer. Three flow regimes, named as steady, generally unsteady, and periodic unsteady, were observed for both the in-line and staggered arrays. Strong acoustic emissions were noted in the periodic flow regime. Transition to turbulence in the staggered arrays was found to occur at a slightly larger Reynolds number and over a broader Reynolds number range than for in-line arrays. An array-averaged heat transfer enhancement of over 100%, as compared to flat plates, was reported for both arrays, which the authors explained as the result of increased mixing.

Joshi and Webb (1987) visualized the flow for three scaled-up geometries of offset-strip arrays and observed four flow patterns during the transition range. At low Reynolds number, a laminar flow with a smooth wake behind the first fin was observed. When the Reynolds number increased, oscillations were observed first upstream of the second fin. With a further increase in Re, these oscillations moved to the most upstream fin, until vortex shedding occurred at a high enough Re. The transition Reynolds numbers were reported for all three scaled-up arrays.

Xi *et al.* (1991) performed flow visualization for a five-row offset-strip fin array for $50 \leq Re_t \leq 200$ by injecting multiple dye streaks into a water tunnel. A probe composed of a hot-wire and a cold-wire was used to measure the velocity and temperature fluctuations simultaneously. They found that the wake of each fin became unsteady and showed a sinusoidal motion or street of discrete vortices as Re increased. The transition Reynolds number was found to be lower for a smaller ratio of fin pitch-to-length. They suggested that the wake flow instability and the motion of discrete vortices near the fin surface caused the heat transfer enhancement.

DeJong and Jacobi (1997) visualized the flow in an offset strip fin array by injecting dye into a water tunnel. Different flow patterns were observed as the Reynolds number increased. The flow was steady and laminar at low Reynolds numbers ($Re \leq 460$). As Re increased to 550, a feathery wake was observed. The wake exhibited a roughly sinusoidal appearance at $Re = 630$. Large-scale vortex shedding was observed first in the downstream rows of the array at $Re = 720$. The onset of vortex shedding moved upstream in the array for higher Reynolds numbers. The third row started to shed vortices at $Re = 850$. As Re increased to 1060, the vortex shedding was apparent in the whole array.

1.2.2.2 Heat Transfer and Pressure Drop Measurements

Sparrow and Hajiloo (1980) experimentally investigated the heat transfer and pressure drop for an offset-strip fin array for Reynolds numbers (based on hydraulic diameter) from 1200 to 9000. The effect of fin thickness was taken into account. The naphthalene sublimation method was used to obtain per-plate heat transfer results, and a Baratron capacitance-type pressure transducer was used to record the pressure drop. The per-plate heat transfer results were found to be constant for the second and all subsequent rows, which indicated the existence of a periodic fully developed flow with the velocity field repeating itself in each geometrically periodic module. Fin thickness was found to have almost no effect on the heat transfer result at the lowest Reynolds number of 1200, but it did

affect the heat transfer at higher Reynolds numbers. The Nusselt number was found to increase with Reynolds number at a faster rate for the thicker fins. The friction factor *f* was found to be independent of Reynolds number for the thickest fins, but decreased smoothly with an increase in Reynolds number for thin fins.

DeJong and Jacobi (1997) performed an experimental study of flow and heat transfer in three different offset strip fin arrays. Local and fin-averaged mass transfer data were obtained through the naphthalene sublimation and laser profilometry techniques. For laminar flow, the local Sherwood number distribution was the highest at the leading edge of the fin and decreased toward the trailing edge, suggesting the effect of the boundary layer restarting mechanism. For higher Reynolds numbers when vortex shedding occurred, the local Sherwood number increased to a maximum at 20% of the fin length from the leading edge and then decreased toward the trailing edge, which suggested that both boundary layer restarting and vortex shedding contributed to the enhancement. The row-by-row mass transfer data, as well as the flow visualization results, showed that shedding began first in the downstream rows and moved upstream as the Reynolds number increased. By comparing to theoretical solutions, the authors stated that for the vortex shedding regime, boundary-layer restarting accounted for 40% enhancement and vortex shedding accounted for another 40% enhancement over the continuous fin result.

1.2.2.3 Numerical Studies of Flow and Heat Transfer

Zhang *et al.* (1997) numerically investigated the flow field and heat transfer enhancement mechanisms for inline and staggered interrupted fin arrays. They were among the first to study the time-dependent flow regime due to vortex shedding by solving the two-dimensional unsteady Navier-Stokes and energy equations for these fin arrays. For comparison purposes, they also calculated the steady flow and heat transfer for otherwise identical conditions. Their results showed that the increased velocity and temperature gradients at the fin surface resulting from the significantly distorted unsteady flow field contributed to the increase of the *j* and *f* factors. The flow was steady at low Reynolds numbers. It became unsteady with a single dominant frequency when the Reynolds number exceeded a critical value. A strong secondary flow frequency, as well as the dominant frequency, appeared at even higher Reynolds numbers. The flow finally became chaotic when the Reynolds number was increased further.

DeJong *et al.* (1998) compared their experimental results for flow and heat transfer in offset strip fin arrays to numerical results in similar geometries. They also proposed a method to correct the data for mixed-mean naphthalene concentration gradients in their naphthalene sublimation experiments. The experimental results verified that the two-dimensional unsteady simulation captured the important features of the flow and heat transfer for Reynolds numbers less than 1300, while three-dimensionality became important at higher Reynolds numbers. The thermal boundary conditions were found to be important for Reynolds numbers below 1000.

1.2.2.4 Correlations for j and f Factors

Researchers have worked to develop correlations for the *j* and *f* factors to facilitate industrial applications. Wieting (1975) developed empirical correlations for *j* and *f* based on past experimental data for 22 offset strip fin geometries. Separate equations were provided for laminar flow with $Re_D \leq 1000$ and turbulent flow with $Re_D \geq 2000$, with a method provided to extend the correlations into the transitional Re_D range from 1000 to 2000.

Mochizuki *et al.* (1987) measured the heat transfer, pressure drop, and turbulence intensity behavior for 18 arrays, including one plain straight fin, five offset strip fins, and twelve slotted fins, over a Reynolds number range from 800 to 10,000. The results for the ratio of heat transfer to pressure drop showed that the offset strip fin array

was superior to both the slotted and plain straight fin arrays. Based on the measurements and Wieting's correlation, a modified correlation for the *j* and *f* factors was presented for laminar flow with Re_D<2000 and turbulent flow with $Re_D \geq 2000$.

Joshi and Webb (1987) investigated offset strip fin arrays using both analytical and experimental techniques. An equation predicting the transitional Reynolds number from laminar to turbulent flow was developed by visually estimating the slope change points of the *j* and *f* curves from 21 surfaces. Based on the transitional Reynolds number, Joshi and Webb developed correlations to predict *f* and *j* for both the laminar and turbulent regimes.

Manglik and Bergles (1995) reanalyzed the existing correlations and empirical *f* and *j* data for offset strip fins based on the latest understanding of the physical phenomena and enhancement mechanisms. They developed equations to describe the asymptotic behavior of the data in the deep laminar and fully turbulent flow regimes. A single correlation for *f* and *j* was provided, covering continuously the laminar, transitional, and turbulent flow regimes.

1.2.3 Summary

For offset strip fins, boundary layer restarting and vortex shedding are responsible for heat transfer enhancement (DeJong and Jacobi 1997). At low Reynolds numbers, when vortex shedding does not occur, the heat transfer is mostly dependent on the boundary-layer restarting effect, which contributes a 40% increase over the plain-fin baseline for typical interrupted-fin surfaces. Once vortex shedding begins, the vortices periodically sweep the fin surface and improve the local convective heat transfer. Another 40% increase in heat transfer is realized due to vortex shedding.

Streamwise vorticity has been investigated in flat-plate flow, channel flow, and fin-tube heat exchangers. A counter-rotating streamwise vortex pair is more effective for heat transfer enhancement than a co-rotating vortex pair (Edwards and Alker 1974). Vortex generator geometry is important in determining the vortex strength and its location relative to the boundary layer, which plays an important role in heat transfer enhancement (Gentry and Jacobi 1998). The delta wing is one of the most effective geometries for streamwise vortex generation (Fiebig *et al.* 1991, Biswas *et al.* 1994a).

The past research has revealed that increased mixing of the freestream fluid with the boundary layer fluid usually leads to greater heat transfer enhancement. Streamwise longitudinal vortices and spanwise vortex shedding can dramatically improve fluid mixing and thus enhance heat transfer. It is natural to expect that applying streamwise vortices to offset strip fin arrays could create vigorous fluid mixing and generate higher heat transfer enhancement. Unfortunately, to date there has been no research on applying longitudinal vortex generators in the offset strip fin array.

1.3 Objectives

As discussed in the literature review, there has been considerable research directed towards the offset strip fins and longitudinal vortex generators separately. However, to the author's knowledge, there has been no published research work addressing the implementation of longitudinal vortex generators on offset strip fins.

This research is conducted to study the concept of combining streamwise and spanwise vortices to enhance air-side heat transfer, to evaluate the benefits and penalties of this new technique, and to understand the flow field characteristics and the mechanisms responsible for the enhancement. The general approach is to create a flow with spanwise vortices using the offset-strip fin geometry and to introduce streamwise vortices by attaching delta wings at the leading edge of the fins.

The impact of delta wing vortex generators on the heat transfer and pressure drop for the offset-strip fin arrays has been evaluated experimentally in the current work. Using the naphthalene sublimation technique, the fin-local and fin-averaged mass transfer coefficients at different locations inside the offset-strip fin array have been measured, and quantitative results have been obtained. Heat transfer results have thus been obtained by using the heat and mass transfer analogy. Array pressure drop data have also been recorded. Delta wings with different aspect ratios and attack angles, as well as various placements of the delta wings in the array, have been investigated. Detailed heat transfer and pressure-drop data provide a useful guide for performance evaluation and future product design.

Secondly, an understanding of the flow field characteristics has been developed, with focus on the interaction of streamwise vortices with the offset-strip fin flow field. Qualitative flow visualization and quantitative full-field velocity results have been obtained for the baseline flow and the vortex-enhanced flow. The impact of streamwise vortices on the flow stability characteristics of offset-strip fin arrays has also been investigated. These results, as well as the detailed fin-local and fin-average heat transfer data, facilitate an understanding of how streamwise vortices interact with the interrupted fin flow and vortex shedding, and elucidate the flow mechanisms responsible for heat transfer enhancement and pressure drop penalty.

Chapter 2. Experimental Apparatus

Four experimental methods were employed in this research: flow visualization, particle image velocimetry (PIV), naphthalene sublimation, and differential pressure drop measurement. Dye-in-water flow visualization was conducted in a water tunnel to explore the qualitative flow behavior; the PIV experiments were conducted in the same water tunnel to obtain quantitative full-field velocity data. Naphthalene sublimation experiments were conducted in a wind tunnel to obtain the mass transfer behavior, which is analogous to the heat transfer behavior. The same wind tunnel was used for measuring the differential pressure drop across the test section.

2.1 Water Tunnel

The closed-loop water tunnel (Engineering Laboratory Design, Model 501), used for flow visualization and PIV measurements, is shown in Figure 2.1. The water tunnel is constructed of fiberglass-reinforced plastic, with the interior surface coated with smooth gel. The water tunnel was pumped by a 0.5 HP AC centrifugal pump, with the flow rate regulated with a variable-frequency controller. The water circulated from the pump, a plenum, a section of screens and honeycombs, a contraction with an area ratio of 6:1, a test section, a return plenum, a magnetic flow meter, and then returned to the pump. A clear acrylic plexiglass plate on the end wall of the return plenum provided optical access from the downstream direction, which was critical for the PIV measurements. During flow visualization, the dye was injected through a 1.3 mm diameter stainless steel micro-tube with its end bent into the flow direction. The dye was fed by gravity, with the volume flow rate regulated by a needle valve at the bottom of the dye reservoir. The dye was made by mixing red food coloring and water. The bottom of the test section was viewed horizontally by placing a mirror under the test section at a 45° inclination angle.

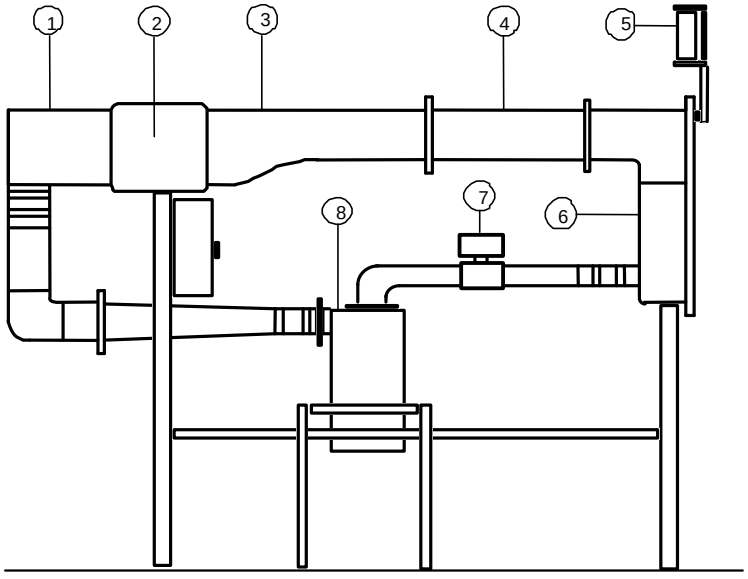

1. Plenum
2. Honeycomb
3. Contraction
4. Test Section
5. Dye Reservoir
6. Return Plenum
7. Magnetic Flow Meter
8. Pump

Figure 2.1 – Schematic of water tunnel

The freestream velocity of the water in the test section spanned from approximately 1.0 cm/s to 31 cm/s over the range of the current experiments. A nearly uniform freestream velocity profile (flat to within ±2.5% except very close to the walls) with low turbulence intensity (around 1%) for this water tunnel was determined with a 20-μm diameter hot-film anemometer (TSI 1212-20W) by Smotrys *et al.* (2001). The mean velocity profile of the water tunnel is shown in Figure 2.2, while the turbulence intensity distribution is given in Figure 2.3.

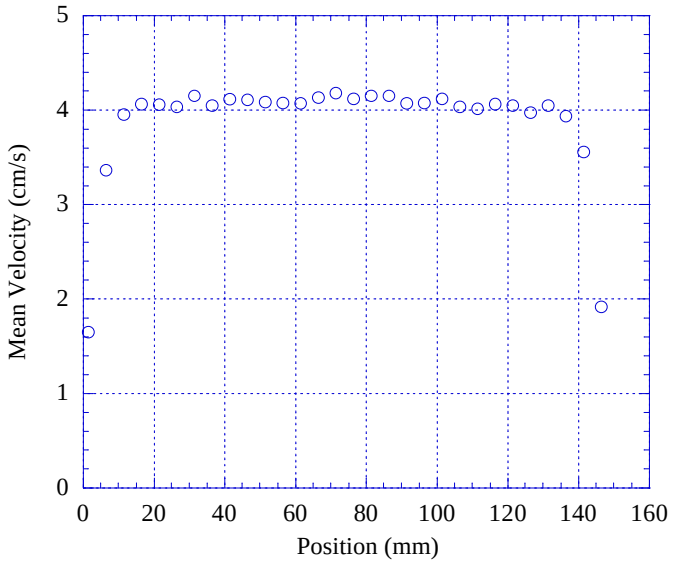

Figure 2.2 – Mean velocity profile for the water tunnel [taken from Smotrys *et al.* (2001)]

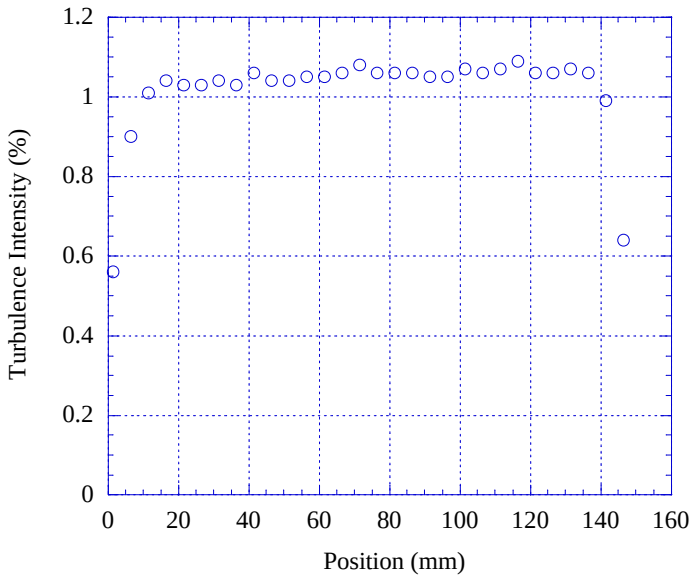

Figure 2.3 – Turbulence intensity distribution for the water tunnel [taken from Smotrys *et al.* (2001)]

2.2 Wind Tunnel

An open-loop induction wind tunnel was used to conduct the naphthalene sublimation experiments and pressure drop measurements. A schematic of the wind tunnel is shown in Figure 2.4. Hexagonal-cell honeycomb and screens were placed at the wind tunnel entrance to condition the airflow. The flow then passes through a contraction

with an area ratio of 9:1 and into the test section with a cross-sectional area of 15.24 cm × 15.24 cm. A honeycomb flow straightener was placed downstream of the test section to avoid possible downstream blower interference. The air was then exhausted outside of the room. The wind tunnel was driven by a blower connected to a variable speed motor, which was regulated through a variable-frequency controller. The freestream velocity in the test section can be varied from approximately 0.1 to 10 m/s.

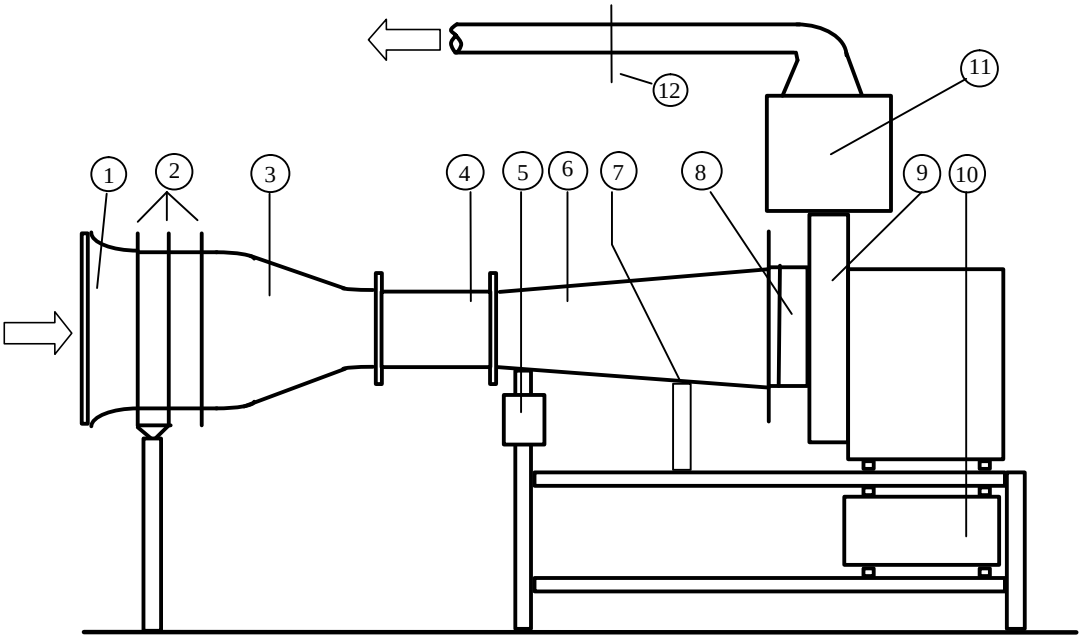

1. Elliptical Inlet
2. Flow Straighteners
3. 9:1 Contraction
4. Test Section
5. Control Key Pad
6. Diffuser
7. Isolation Mount
8. Flexible Coupling
9. Fan
10. Electrical Cabinet
11. Acoustic Plenum
12. Orifice Plate

Figure 2.4 – Schematic of wind tunnel

By using a 20-μm diameter hot-film anemometer (TSI 1212-T1.5), the freestream velocity profile for the wind tunnel was measured to be flat to within ±1.5% (except very close to the walls), and the turbulence intensity was measured to be around 1%. The mean velocity profile of the wind tunnel is shown in Figure 2.5, while the turbulence intensity distribution is presented in Figure 2.6.

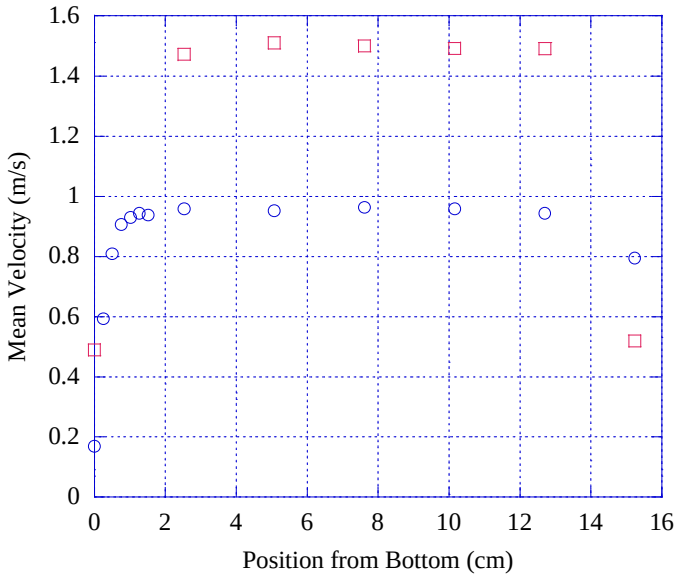

Figure 2.5 – Mean velocity profile for the wind tunnel

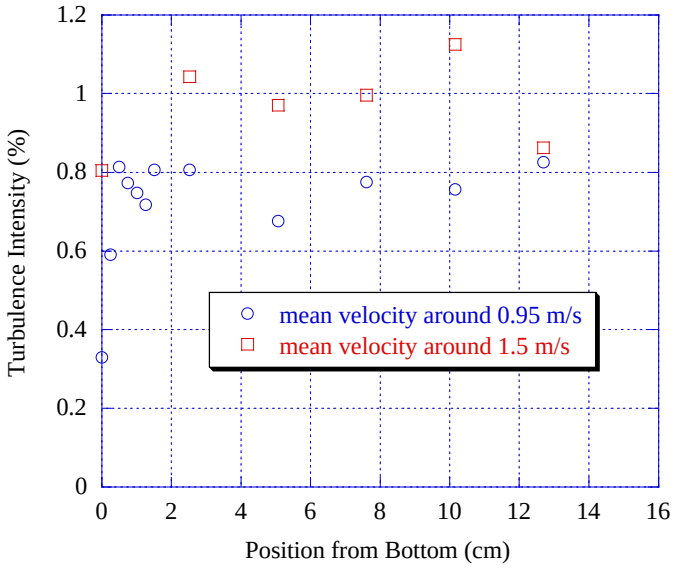

Figure 2.6 – Turbulence intensity distribution for the wind tunnel

2.3 Test Section

2.3.1 Baseline Offset-Strip Fin Array Geometry

A schematic of the model offset-strip fin array used for this research is shown in Figure 2.7. This array has a fin length of 25.4 mm, a fin spacing of 25.4 mm and a fin thickness of 3.175 mm. This is called the L×L array, meaning that the fin length is equal to the fin spacing. It consists of 48 fins in eight rows, and has a core length of 20.32 cm. The hydraulic diameter D_h for this array, as defined by Kays and London (1984), was calculated to be 39.5 mm. The numbering of the array rows and columns is also shown in Figure 2.7. The center columns (Columns 5 and 6) were the locations where all experiments, except for the pressure drop measurements, were conducted.

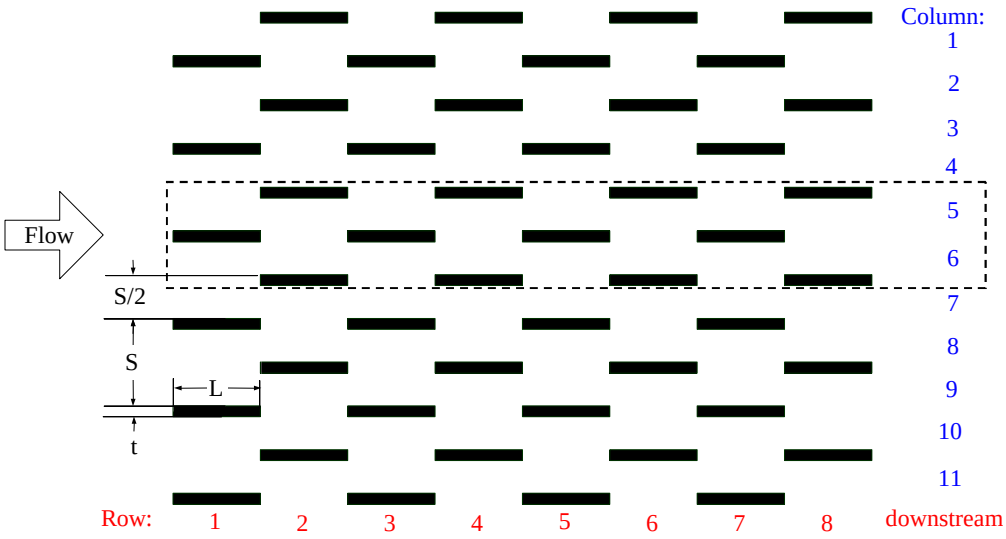

Figure 2.7 – Schematic of the baseline offset-strip fin array (L×L array) geometry and numbering of rows and columns: S = 25.4 mm, L = 25.4 mm, t = 3.175 mm (All experiments except pressure drop were conducted in Columns 5 and 6, which are surrounded by the dash lines)

2.3.2 Wind Tunnel Test Section

The wind tunnel test section was constructed using 1.27 cm thick, GM grade, clear acrylic plexiglass. A schematic of the test section is shown in Figure 2.8. The test section has an interior cross section of 15.24 cm square, and is 30.48 cm in length. Eight static-pressure taps were located one each on the center of all four sides of the test section, 2.54 cm upstream and downstream of the fin array. The four upstream taps were connected together using 3.175-mm diameter Tygon tubing to provide the average pressure, and the tubing was then connected to the pressure transducer. The downstream taps were connected in a similar way. Slots on the top and bottom plates were used to fix the location of the 48 fins in eight rows. There were eight easily removable center pieces located on the top plate, which enabled the fast insertion and removal of the naphthalene-cast fins. During the mass transfer experiments, eight naphthalene-cast fins were placed along both sides of the center column (Column 6 in Figure 2.7), and plain aluminum dummy fins made up the rest of the array. A schematic of the naphthalene-cast and dummy fins is shown in Figure 2.9. The naphthalene-cast fins were of the same geometry as the dummy fins, except that a cavity of 10.16 cm (length) × 2.46 cm (width) × 0.8 mm (depth) was machined out on one side of each fin. These fins were constructed using Grade C-1018 low-carbon steel to minimize the shape distortion during cavity machining.

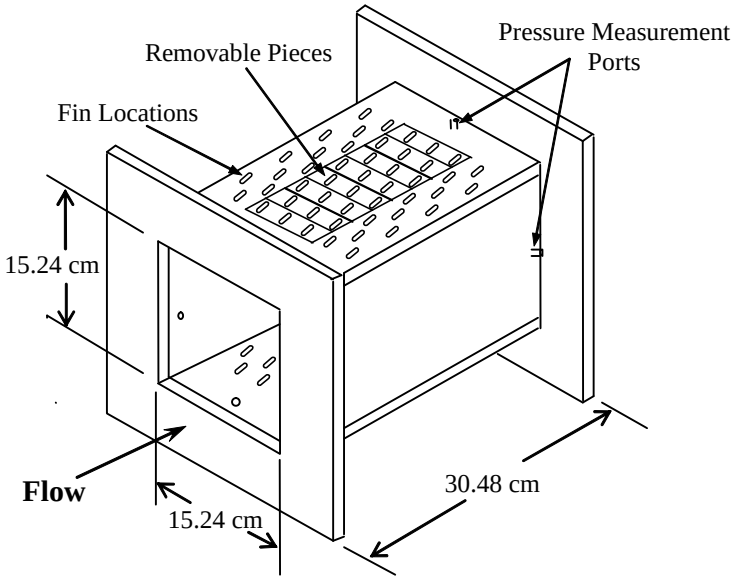

Figure 2.8 – Schematic of wind tunnel test section used for mass transfer and pressure drop experiments

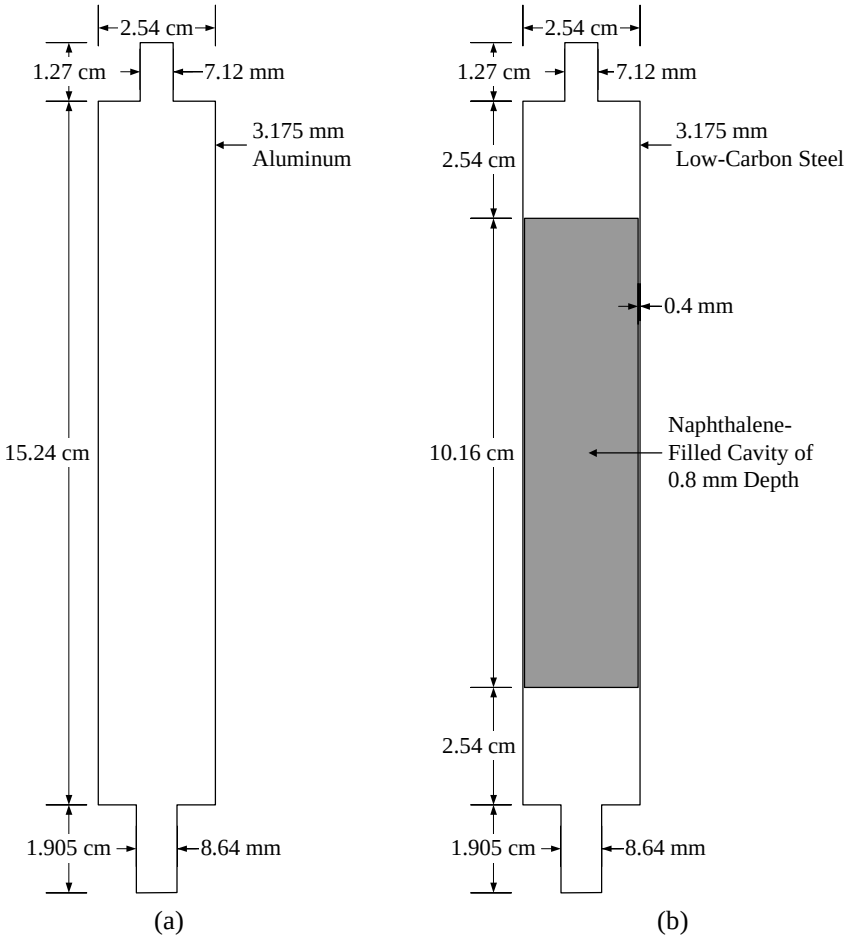

Figure 2.9 – Schematic of (a) dummy fin (b) naphthalene-cast fin used for wind tunnel experiments

2.3.3 Water Tunnel Test Section

The water tunnel test section had a cross-section area of 15.24 cm × 15.24 cm and was 45.72 cm long. The bottom and side surfaces of the test section were constructed of 1.27cm thick, GM-grade, clear acrylic plexiglass, while the top surface was open to the atmosphere. Two base plates, with forty-eight slots each, were constructed using 3.175 mm thick, GM-Grade acrylic plexiglass. These plates were used to secure forty-eight 14.6 cm long aluminum fins in the array as shown in Figure 2.7. For the PIV experiments, all aluminum fins were anodized black to reduce laser light reflection inside the array. To allow laser light to pass in an unobstructed manner through the center columns (Column 5 and Column 6) and avoid the "shadow" area behind the 1st, 3rd, and 5th row fins, three aluminum fins were replaced with highly-polished, transparent acrylic fins, as shown in Figure 2.10. Otherwise, shadow regions would be generated behind the 1st, 3rd, and 5th row fins, making it impossible to obtain flow field data in the wake regions immediately behind these rows.

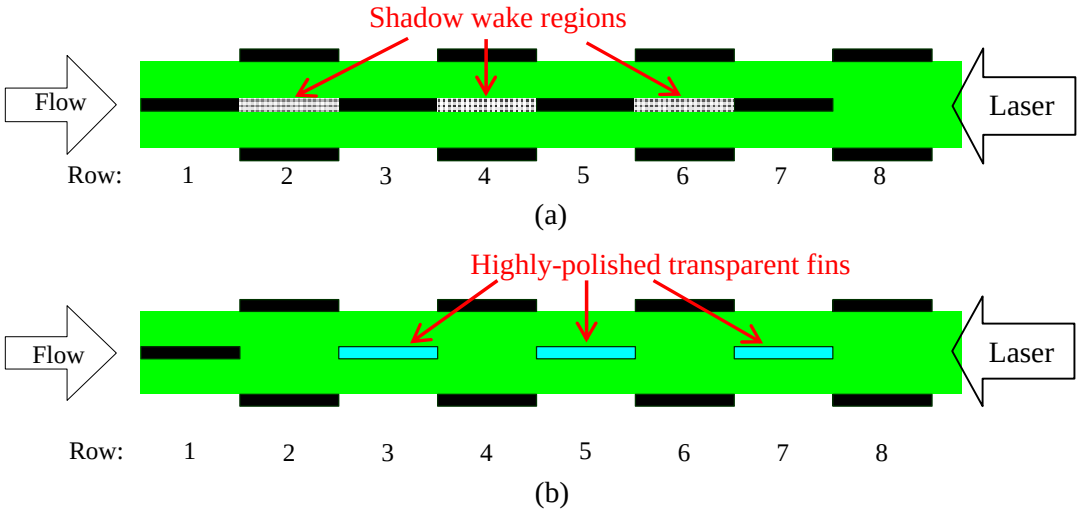

Figure 2.10 – Schematic of laser sheet illumination in the array: (a) all fins are aluminum; (b) three aluminum fins replaced with transparent fins

2.3.4 Vortex Generator Configuration

To investigate the impact of streamwise vortices on the offset-strip array performance, several new vortex generator (VG) configurations were fabricated for the L×L array, and series of experiments were conducted on the baseline and VG-enhanced arrays. The vortex generators used in this research are of the delta-wing type. The details of the VG configurations are given in the following subsections.

2.3.4.1 Inlet-Only Vorticity Generation - VGs Only at Array Inlet

Placing vortex generators on the leading edge of all first-row fins at the inlet of the array is a realistic design configuration that could be employed in practice. Streamwise vortices are generated at the inlet of the array and travel downstream in the flow direction. This configuration also makes manufacturing easy. Four inlet-only VG configurations were investigated in this research. A schematic of these VG configurations (top view and front view) is shown in Figure 2.11.

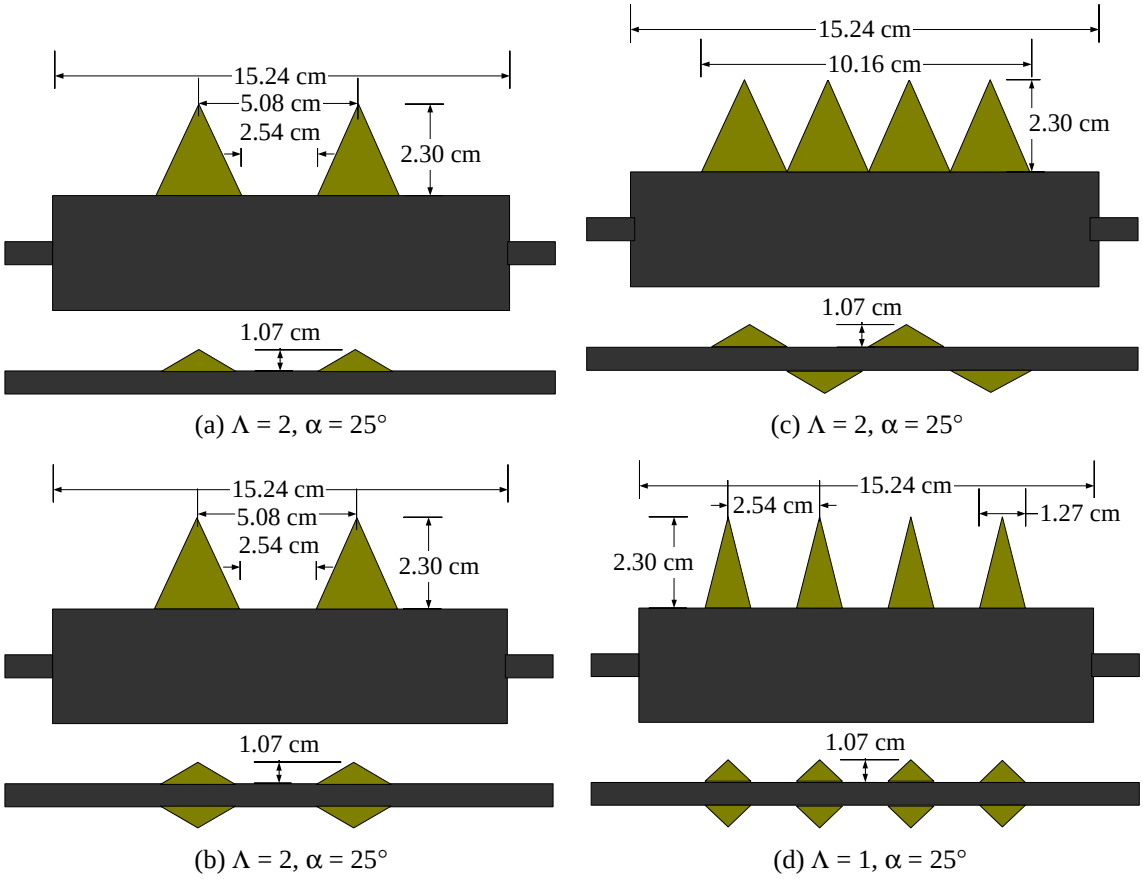

Figure 2.11 – Schematic of four inlet-only vortex generator configurations: (a) 2VG-enhanced leading fin; (b) 4VG-enhanced leading fin; (c) 4VG-staggered enhanced leading fin; (d) 8VG-enhanced leading fin

2.3.4.1.1 2VG-Enhanced Array

As shown in Figure 2.11 (a), this configuration has two delta wings on each of the leading fins of the array. The delta wings have a base length of 2.54 cm and a chord length of 2.54 cm, with aspect ratio Λ of 2 and attack angle α of 25°. The tip-to-tip spacing of the VGs is 5.08 cm.

2.3.4.1.2 4VG-Enhanced Array

As shown in Figure 2.11 (b), this configuration has four delta wings on each of the leading fins of the array, with two pointing upward and two downward. The VG geometry and distance between adjacent VGs are the same as that of the 2VG-enhanced array.

2.3.4.1.3 4VG-Staggered Enhanced Array

As shown in Figure 2.11 (c), this configuration differs from the 4VG-enhanced array only in the staggered placement of the VGs on the top and bottom surfaces of the leading fins. Due to the staggered arrangement, the interactions of vortex pairs on the upward VGs and those on the downward VGs are quite different from those of the 4VG-enhanced array.

2.3.4.1.4 8VG-Enhanced Array

As shown in Figure 2.11 (d), this configuration has eight slender delta wings on each of the leading fins of the array, with four pointing upward and four downward. The delta wings have a base length of 1.27 cm and a chord

length of 2.54 cm, with aspect ratio Λ of 1 and attack angle α of 25°. The tip-to-tip spacing of the VGs is 2.54 cm. The 8VG-enhanced array has the same total VG area as the 4VG-enhanced array.

2.3.4.2 Multiple Vorticity Generation – VGs at both Inlet and Inside the Array

Streamwise vortices will be damped when traveling downstream through the array. Therefore, for VGs to be effective in a large array, multiple generation of streamwise vortices inside the array might be necessary to obtain array-wise benefit from streamwise vortices. In this research, in addition to being attached at the leading edge of all first-row fins, delta wings are also attached at the leading edge of all 5th row fins to regenerate the streamwise vortices in the center of the array. A schematic of this approach is shown in Figure 2.12. Two configurations have been investigated.

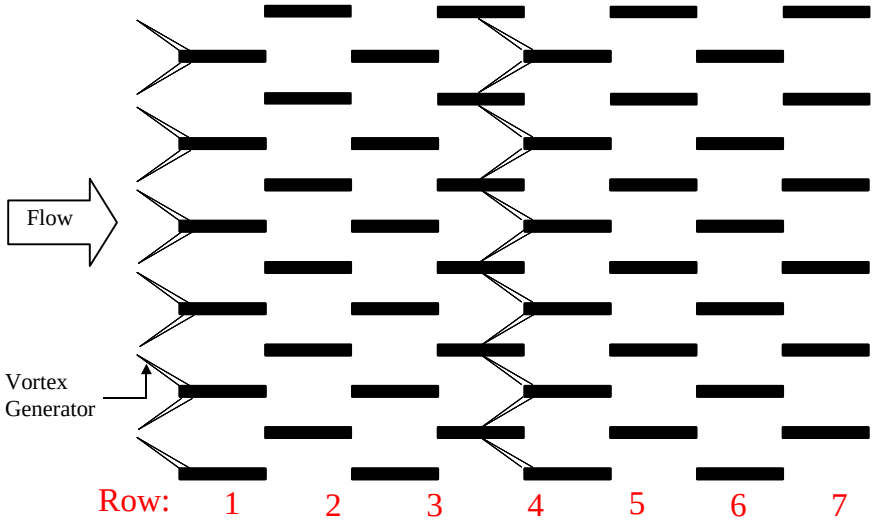

Figure 2.12 – Schematic of the L×L enhanced array with VGs on the leading edges of both first-row fins and fifth-row fins

2.3.4.2.1 4VG at Rows 1 and 5 - Enhanced Array

This configuration has the same VG attachment on the inlet leading fins as the 4VG-enhanced array (shown in Figure 2.11 (b)). In addition, it has four delta wings attached on the leading edge of The first all the 5th row fins. The VG geometry and placement are the same as the VGs on the inlet fins, except that the attack angle is 22°, due to the limited space available for them in the middle of the array.

2.3.4.2.2 8VG at Rows 1 and 5 - Enhanced Array

This array has the same VG attachment on the inlet leading fins as the 8VG-enhanced array (shown in Figure 2.11 (d)). In addition, it has eight delta wings attached on the leading edge of all 5th row fins. The VG geometry and placement are the same as the VGs on the inlet fins, except that the attack angle is 22°, due to the limited space available for them in the middle of the array.

2.3.5 Scaled-Down Array for Pressure Drop Measurements

The pressure drop across the original array at low Reynolds numbers was found to be comparable to the resolution of the differential pressure transducer (0.1 Pa), which generated a large uncertainty for the pressure drop results. To reduce the uncertainty, a scaled-down array with all length scales equal to half those of the original L×L array was built using GM-grade acrylic and was tested in the same wind tunnel described earlier. The scaled-down

array has a fin length of 1.27 cm, a fin spacing of 1.27 cm, and a fin thickness of 1.59 mm. Two base plates, constructed using 3.175 mm thick, GM-grade acrylic plexiglass, were used to secure ninety-two 14.6 cm long acrylic fins into the array. The delta wings for the scaled-down array are of the same aspect ratio and attack angle, and half the base length and chord length as those for the original L×L array.

2.4 PIV System

Quantitative flow velocity data were determined using a laser-based velocity measurement technique know as Particle Image Velocimetry (PIV). The principle of this technique is shown schematically in Figure 2.13. A CCD camera is used to acquire two consecutive images of small tracer particles in the flow region, which are illuminated by two consecutive, synchronized laser pulses. A correlation process is then applied to the two images to determine the distance of particle movement at each measurement volume in the plane of illumination. Knowing the time interval between the two images, the velocity at each measurement location can be calculated.

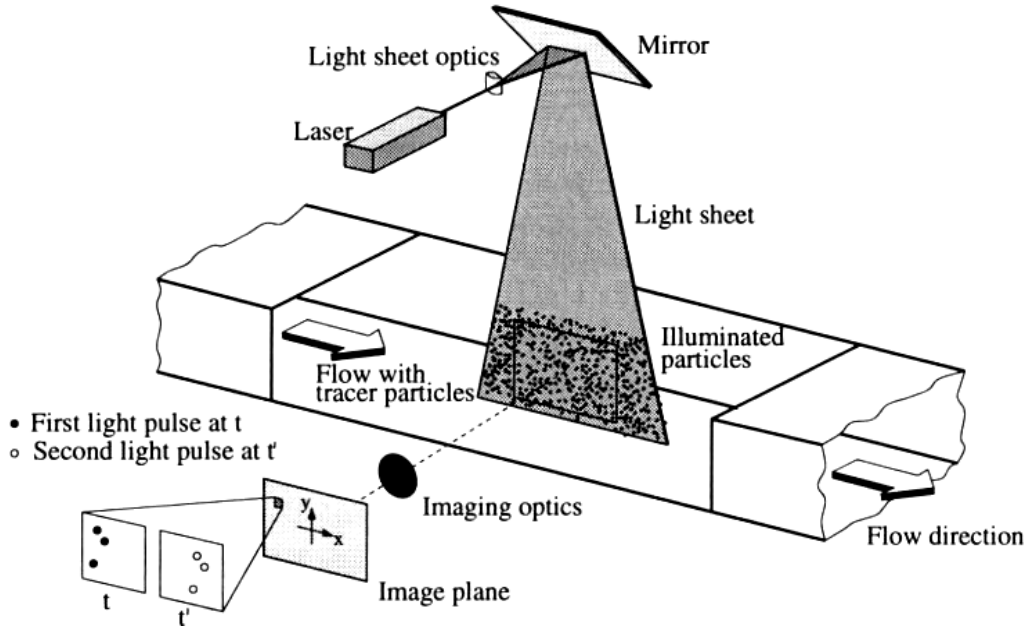

Figure 2.13 – Schematic of the principle of PIV measurements [taken from Raffel *et al*. (1998)]

A TSI PowerView Stereoscopic PIV system was used in this research. A schematic of this system is shown in Figure 2.14. A double-pulsed PIV Nd:YAG laser system with two laser heads (Continuum, Surelite III) is used to generate consecutive laser pulses in a specified time interval. The laser beams pass through a series of optics and into the water tunnel test section to form uniform laser sheets. A laser pulse synchronizer (TSI Model 610034) coordinates the laser pulses with the image acquisition of a cross-correlation camera (TSI Model 630147 PIVCAM 13-8). The synchronizer is connected to and controlled by a Dell Precision 410 workstation with two Pentium III 600 MHz processors, 512 MB RAM and TSI Insight Stereo PIV v3.3 software.

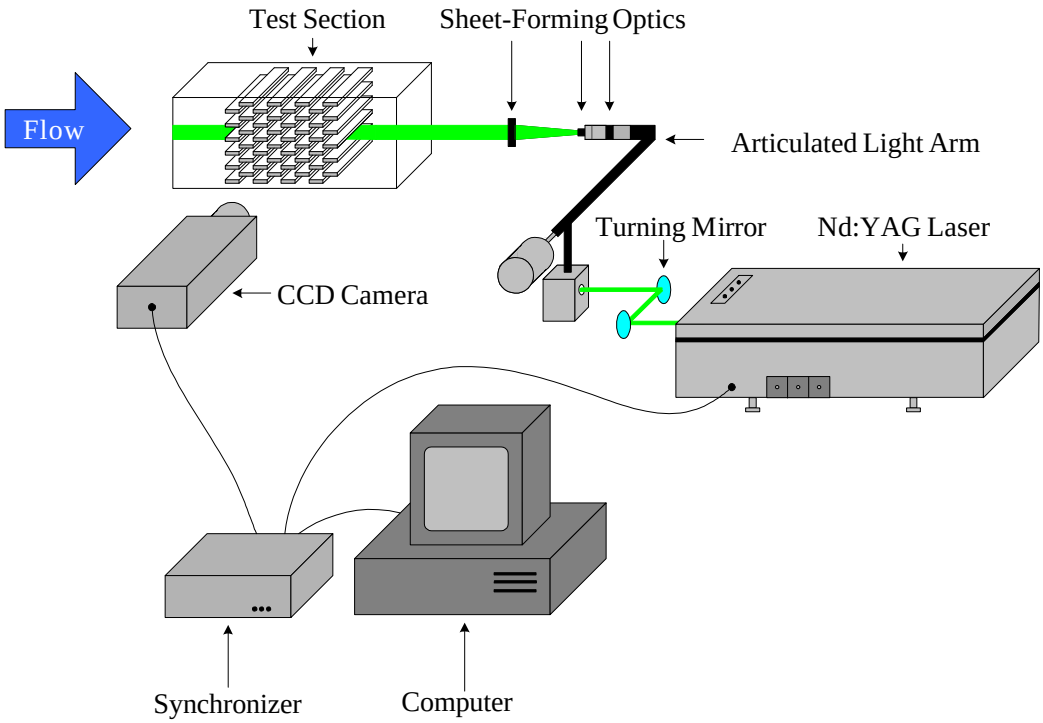

Figure 2.14 – Schematic of the PIV system and the experimental setup [taken from Smotrys *et al.* (2001)]

For a detailed discussion of PIV principles and the apparatus used in this research, the reader is directed to Smotrys *et al.* (2001).

2.5 Laser Profilometer

Local naphthalene sublimation depths on the fin surfaces were determined using an optical, non-contact surface-profiling technique known as laser triangulation. The principle of this technique is shown in Fig. 2.15. A laser beam directed onto a surface is reflected, and part of the reflected laser beam passes through a lens and into a photodetector. Surfaces of different heights reflect the laser beam to different positions on the photodetector. A laser profilometry system (Cyber Optics Corp., Cyber-Scan 206) based on this technique was employed in this research to obtain surface contours of the naphthalene fins. The system uses a 2.4 mW, 750 nm wavelength laser beam and a point range sensor which has a measuring range of 400 μm. The published accuracy for this profilometry system is ± 4 μm. However, repeated scans of a stainless steel surface showed a larger uncertainty of ± 6 μm. A detailed description of the principle and the system is given by Kearney and Jacobi (1995).

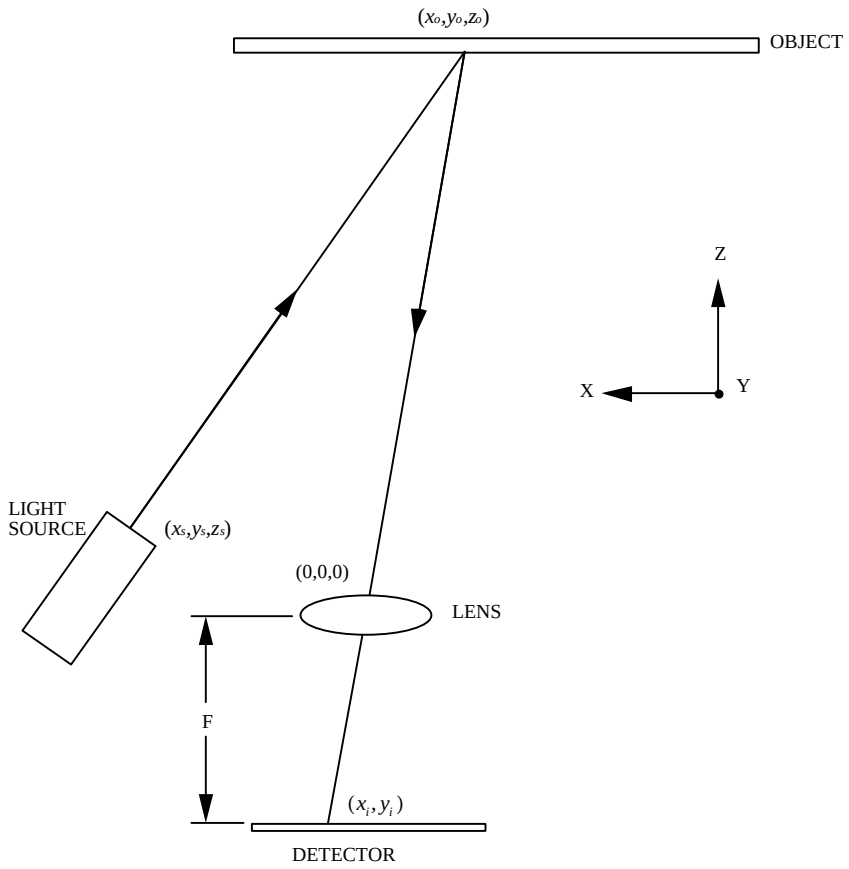

Figure 2.15 – Schematic of laser triangulation technique used to determine surface profiles [taken from Kearney and Jacobi (1995)]

2.6 Instrumentation and Data Acquisition

During the flow visualization and PIV experiments, which were performed in the water tunnel, the water temperature and volumetric flow rate were recorded. A NIST-traceable precision RTD thermometer (Omega Engineering DP251) with a factory-calibrated accuracy of 0.01 °C and a digital output display was used to determine the water temperature. A calibrated magnetic flowmeter (Omega Engineering FMG-730) with an uncertainty of ±3.34% was used to measure the volumetric flow rate. The flowmeter has a current output between 4 mA and 20 mA (linear with flow rate), which is digitally read using a digital ratemeter (Omega Engineering DPF64).

Upstream and downstream temperatures, freestream velocity, relative humidity, barometric pressure, exposure time, and fin mass were recorded each time the naphthalene sublimation experiment was performed in the wind tunnel. The upstream and downstream air temperatures were recorded using calibrated platinum RTDs located at the inlet of wind tunnel and downstream of the test section. Both RTDs were calibrated by using a NesLab isothermal bath and the NIST-traceable precision RTD thermometer (Omega Engineering DP251, accuracy within 0.01 °C); and the uncertainty of both RTDs is less than ±0.05° C. The freestream velocity was measured using a factory-calibrated portable air velocity meter (TSI VelociCalc® Model 8355). The uncertainty of the velocity meter is less than ±3%. The relative humidity was determined using a humidity indicator (Vaisala HMI 31) and the

barometric pressure using a mercury barometer (Princo NOVA™ 469). The mass of the test fins was determined by using a 200 g precision balance (Mettler AE200) with an accuracy of ±0.00005 g.

The pressure drop across the core was measured with a high-precision differential pressure transducer (Endress+Hauser, DELTABAR PMD235) powered by a 24V DC power supply. This transducer's freely adjustable span (100 ~ 1000 Pa) was set to 100 Pa during these experiments, with a factory-certified accuracy of 0.1 Pa.

The temperature and pressure drop data were recorded through a computerized data acquisition system. The RTDs were connected to one terminal block (National Instruments, SCXI-1321), and the pressure transducer was connected to the other terminal block (National Instruments, SCXI-1300). Both terminal blocks were securely placed in a chassis (National Instruments, SCXI-1000), which was connected through a cable to a 16-bit data acquisition board (National Instruments, AT-MIO-16E-2) in a personal computer (DELL Dimension P75t). A LABVIEW computer code was written to control the hardware and record the data.

Chapter 3. Experimental Procedure and Scope

This chapter will describe the experimental procedures for the dye-in-water flow visualization, PIV flow field velocity, naphthalene sublimation, and pressure drop measurements. A corresponding discussion of the experimental scope for each measurement method will also be included.

3.1 Dye-in-Water Flow Visualization

The flow visualization experiments were conducted in the water tunnel for the baseline offset strip fin array, 2VG-enhanced array, 4VG-enhanced array, and 4VG at Rows 1 and 5 - enhanced array. The dye was always injected in the freestream ahead of the first-row fin between Column 5 and Column 6 (as shown in Figure 2.7). The locations where the dye impinged on the fin are shown schematically in Figure 3.1. For the baseline array, the dye was directed to impinge at the spanwise center of the fin leading edge (location B as shown in Figure 3.1). For the 2VG-enhanced array, the dye was directed to impinge at the tip region of the delta wing (location A as shown in Figure 3.1). For the other two enhanced arrays, the dye was directed to impinge at the tip region of the delta wing and the spanwise center of the fin leading edge (locations A and B as shown in Figure 3.1).

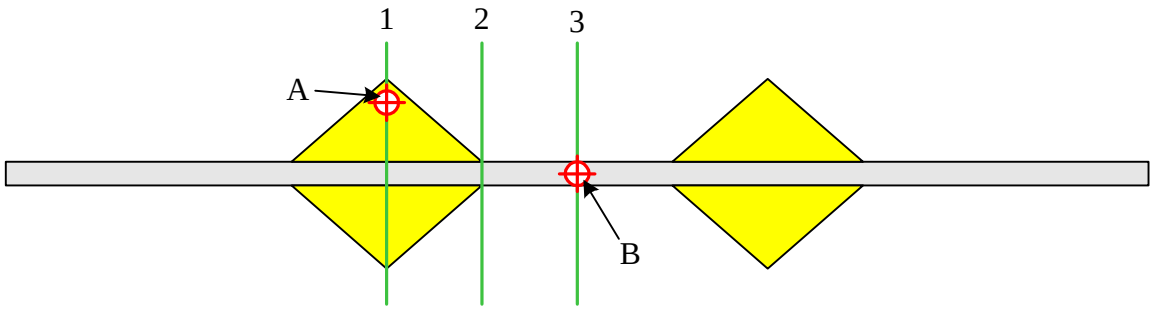

Figure 3.1 – Schematic of locations on a front-view first-row VG-enhanced fin for dye injection (A: VG tip; B: spanwise center) and the laser sheet (1, 2, and 3) for PIV side-view measurements

The volumetric flow rate of water in the tunnel was measured using a magnetic flow meter and a digital ratemeter, as described in Section 2.6. A precision RTD thermometer was used to measure the water temperature at the beginning and end of each experiment, and the average of these two was recorded as the mean water temperature to determine the water density and viscosity. Knowing the cross-sectional area of the test section, the freestream velocity was then determined, as well as the Reynolds number.

The test section lighting was provided using a photographic lamp (Smith-Victor, Model PL-8) with a photoflood-type GE ECA 3200K 250W bulb. The flow field was videotaped with a JVC GR-DVF31u MiniDV digital camcorder. Still images and video clips were edited from the videotape afterwards using Sony DVgate™ software with a Sony VAIO PCG-FX340 notebook computer.

3.2 PIV Flow Field Velocity Measurement

The procedure for obtaining PIV measurements in this research consisted of four stages: seeding preparation, image acquisition, image evaluation, and post processing.

3.2.1 Seeding Preparation

The flow seeding was accomplished using silver-coated hollow glass spheres (Potters Industries, SH400S33). The seeding particles have 33% silver content by weight, a true particle density of 1600 kg/m^3 and a size range of 10 ~ 30 μm (with mean size 15 μm). Kodak Photo-Flo 200 solution was added during the seeding preparation to reduce the tendency of the particles to agglomerate.

In order to prepare the particle solution, 8 g of particles were first mixed with 400 mL of water and 5 mL of Photo-Flo solution. The mixture was poured into a graduated cylinder and allowed to settle for more than three hours. Particle stratification developed in the cylinder based on buoyancy, with the heaviest particles at the bottom and the lightest particles at the top. The particle solution with neutrally buoyant particles in the middle of the cylinder was removed by use of a syringe, and then used as seeding for the PIV measurements.

3.2.2 Image Acquisition

The laser sheet and PIV camera were arranged in two ways in order to obtain the velocity and vorticity field results in both the plane perpendicular to the fin span (called side-view in the following) and the plane perpendicular to the flow direction (called end-view in the following). During the side-view measurements, the laser sheet was directed into the water tunnel through the plexiglass end wall of the return plenum (Figure 2.1), and the camera was placed to acquire images through the acrylic side wall of the test section, as shown in Figure 2.14. During the end-view measurements, the laser sheet was directed into the water tunnel through the acrylic side wall of the test section, and the camera was placed to acquire images through the plexiglass end wall of the return plenum.

The side-view measurements were conducted for the baseline array, 2VG-enhanced array, 4VG-enhanced array, and 4VG at Rows 1 and 5 - enhanced array. Three laser sheet locations, as shown in Figure 3.1, were considered in the side-view measurements. For the baseline array, the laser sheet was directed to pass location “3”, the center of the fin span. For the VG-enhanced arrays, location “2” at the root of the VGs is more representative of the flow field characteristics, according to Smotrys *et al.* (2001). Therefore, the laser sheet was directed to pass location “2” for all the three VG-enhanced arrays. The PIV images were captured two rows at a time, including the region downstream of the last fin of the array.

The end-view measurements were conducted only for the three VG-enhanced arrays mentioned earlier, since preliminary end-view measurements for the baseline array by Smotrys *et al.* (2001) showed that there was little interesting flow behavior for this case. The dimensionless position, X^*, specifies the location of image capture. X^* is defined as the ratio of the distance from the entrance of the array (X) to fin length (L), (*i.e.*, $X^* \equiv X/L$). The light sheet was placed at several X^* locations, as indicated in Figure 3.2.

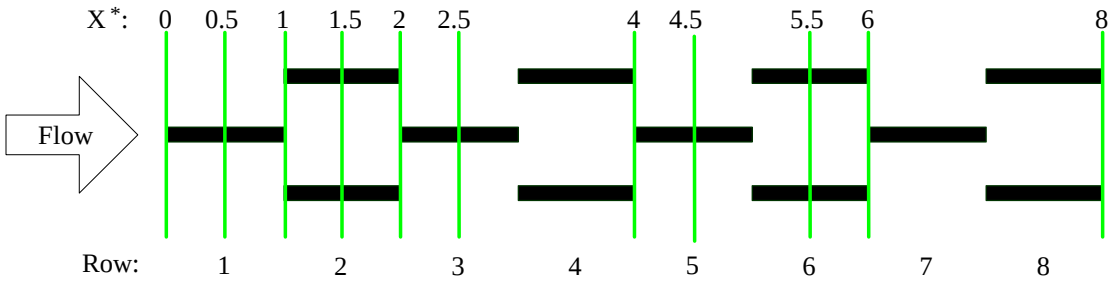

Figure 3.2 – Streamwise locations X^* for end-view images ($X^* = X/L$)

The Insight Stereo PIV v3.3 software was used to control the laser pulses and image acquisition through a connection to the Laser Pulse Synchronizer. Before data acquisition, the laser pulse separation value (Δt), the pulse repetition rate, the pulse delay, and the laser power level were set through Insight. The laser pulse separation value specifies the time between two laser pulses generated from the two laser heads. The pulse repetition rate refers to the repetition frequency of the laser pulse sequence. The pulse delay specifies the delay time from the trigger of the camera to the first laser pulse. In this research, the pulse repetition rate was set to 2 Hz, and the pulse delay was set to 0.25 ms. Details of the laser pulse timing (Δt) for the various configurations and the Reynolds numbers investigated will be presented in Section 3.2.5. PIV images were acquired by capturing 50 image pairs (frame "a" and frame "b") per Reynolds number and location, and saving the digital images to the computer hard disk. Each image pair represented the instantaneous flow field characteristics, and time-averaged characteristics were obtained by averaging the fifty instantaneous results.

3.2.3 Image Evaluation

PIV image pairs were evaluated by dividing the images into small interrogation spots, and then employing statistical methods (*i.e.*, cross-correlation,) to each interrogation spot to determine the local displacement vector, based on the illuminated particles in frame "a" and frame "b". Velocity vectors were then calculated by dividing the displacement vectors with the known time separation between pulses (Δt). Detailed review and analysis of PIV statistical evaluation methods have been provided by Adrian (1986), Keane and Adrian (1990, 1991a, 1991b, 1992), Raffel *et al*. (1998), and Westerweel (1993).

Two-frame cross-correlation analysis was employed as the evaluation method in this research. Two correlation algorithms for this analysis, Fast Fourier Transform (FFT) and Hart Correlation, are implemented in the Insight software. For a detailed discussion of these two methods and Insight image processing, the reader is directed to Smotrys *et al.* (2001).

In this research, the FFT algorithm with a Gaussian peak-finding routine was selected. Windows with 32 x 32 pixels and an overlap of 50% were used for all the processing, except that 64 x 64 pixels with an overlap of 75% were used for some end-view images for the 2VG-enhanced array (completed by Smotrys *et al.*, 2001).

During the image evaluation, images were first loaded into Insight, and the appropriate Δt was entered. Then the conversion factor from the number of pixels to a physical length was determined by measuring the number of pixels between two locations in the image that are separated by a known distance (*e.g.*, fin spacing). The

interrogation area was defined in the images, and fins inside the interrogation area were excluded from the correlation procedure with Insight's polygon editing tool.

A standard deviation filter with a tolerance of three and a local mean filter with a tolerance of two were applied to each velocity field to further validate the vectors. Blank points resulting from either failed signal-to-noise ratio or failure to pass the standard deviation filter were filled by interpolating over neighborhood sizes of 3 x 3 pixels. An average vector file and a statistics file were also generated from batch validation of 50 vector files.

3.2.4 Post-Processing

In the post-processing stage, the vorticity field was calculated, and both the velocity and vorticity field were formatted and output as Windows Metafile images. After image evaluation was performed, the velocity data were opened into Tecplot v8.0 using TSI's TecPIV macro. The vorticity was calculated with a central differencing scheme applied to the equations:

$$\omega_Z = \left(\frac{\partial V}{\partial X}\right) - \left(\frac{\partial U}{\partial Y}\right)$$
$$\omega_X = \left(\frac{\partial W}{\partial Y}\right) - \left(\frac{\partial V}{\partial Z}\right) \qquad (3.1)$$

where ω_Z is the spanwise vorticity and ω_X is the streamwise vorticity. The calculation of the vorticity field was also provided by TSI's TecPIV macro.

The velocity and vorticity fields were further formatted using self-written Tecplot macros. They were exported as Windows Metafiles, which can be opened in Microsoft Office.

3.2.5 PIV Experimental Scope and Measurement Uncertainty

The side-view measurements were performed for the baseline array, 2VG-enhanced array, 4VG-enhanced array, and 4VG at Rows 1 and 5 - enhanced array. The end-view measurements were performed for all three VG-enhanced arrays but not for the baseline array, since the baseline array contained no organized streamwise vorticity as compared to the VG-enhanced arrays (Smotrys *et al.*, 2001). For each array, the measurements were conducted at several Reynolds numbers. The Reynolds numbers and laser pulse timing parameters (Δt) for each array are shown in Table 3.1.

PIV errors are somewhat difficult to quantify and are not generalized for all applications. An extensive study on the effect of resolution on accuracy of PIV measurements has been provided by Prasad *et al*. (1992). The authors found that the measurement uncertainty for the PIV measurements can be approximated as one-tenth of the particle image diameter, d_τ, defined as:

$$d_\tau = \sqrt{\left(M \cdot d_p\right)^2 + \left(2.44 \cdot f^{\#} \cdot (M+1) \cdot \lambda\right)^2} \qquad (3.2)$$

for which M is the magnification, d_p is the true particle diameter, $f^{\#}$ is the f-number defined as the ratio between the focal length and the aperture diameter, and λ is the wavelength of the laser light. For the present study, d_τ = 12.3 μm for the side-view images (M = 0.16, $f^{\#}$ = 8), and d_τ = 11.5 μm for the end-view images (M = 0.11, $f^{\#}$ = 8).

Table 3.1 – Experimental scope for PIV measurements, including geometries, Reynolds numbers, and timing parameters (Δt: μs)

Δt / Re #	Baseline array, side-view	2VG-enhanced array, side-view	2VG-enhanced array, end-view		4VG-enhanced array, side-view	4VG-enhanced array, end-view		4VG at Rows 1 and 5 – enhanced array, side-view	4VG at Rows 1 and 5 – enhanced array, end-view
	All locations	All locations	X*=0,0.5,1, 1.5,2.5,5.5	X*=2,4, 6,8	All locations	X*=0.5,1,1.5, 2,2.5,4.5,6	X*=8	All locations	X*=4.5,6,8
540	N/A	N/A	N/A	N/A	5000	N/A	N/A	N/A	N/A
850	5000 **	5000 **	17000 **	20000 **	5000	10000	20000	5000	10000
1030	5000 **	5000 **	17000 **	20000 **	5000	8000	20000	5000	8000
1280	5000 **	4000 **	15000 **	15000 **	5000	N/A	N/A	N/A	N/A
1330	5000 **	4000 **	15000 **	15000 **	N/A	N/A	N/A	N/A	N/A
1470	4000 **	3000 **	10000 **	10000 **	N/A	N/A	N/A	N/A	N/A
1520	N/A	N/A	N/A	N/A	5000	6000	10000	5000	6000
1750	5000	N/A	N/A	N/A	5000	5000	8000	5000	5000
1980	N/A	N/A	N/A	N/A	4000	N/A	N/A	N/A	N/A
2140	2500 **	1500 **	6000 **	6000 **	N/A	N/A	N/A	N/A	N/A
2210	N/A	N/A	N/A	N/A	3500	N/A	N/A	N/A	N/A
2450	3000	N/A	N/A	N/A	3000	3500	5000	3000	3500
2680	N/A	N/A	N/A	N/A	2500	N/A	N/A	N/A	N/A
2910	N/A	N/A	N/A	N/A	2000	N/A	N/A	N/A	N/A
3120	1800	N/A	N/A	N/A	1800	2500	3000	1800	2500

** – measurements completed by Smotrys *et al.* (2001), with Reynolds numbers converted to be consistent with those in this research;
N/A – no measurements conducted.

For the PIV side-view experiments, the measurement uncertainty is determined to be ±1.23 μm in displacement. This displacement uncertainty corresponds to a velocity uncertainty of ±0.68 mm/s, considering that the minimum Δt for side-view experiments is 1800 μs (Table 3.1). Similarly, the end-view experiments have a displacement uncertainty of ±1.15 μm. Since the minimum Δt for the end-view experiments is 2500 μs (Table 3.1), the velocity uncertainty for the PIV end-view experiments is ±0.46 mm/s.

3.3 Naphthalene Sublimation Experiments

The naphthalene sublimation technique is a well-developed method for measuring convective mass transfer coefficients in complex flows with high accuracy. A review of recent progress on this technique has been provided by Goldstein and Cho (1995) and Mendes (1991). By using the heat and mass transfer analogy, mass average and local heat transfer coefficients can be obtained. In this research, the naphthalene sublimation experiments were conducted in the wind tunnel shown in Figure 2.4 using the test section shown in Figure 2.8.

3.3.1 Preparation of Naphthalene-Cast Fins

The low-carbon steel fin used for the naphthalene sublimation experiments is shown schematically in Figure 2.9 (b). In order to prepare the fins, scintillation grade naphthalene (99+% pure) was heated above its melting point of 80.2 °C in an 80 ml beaker. A small amount of iodide laser dye (Exciton, HITC) was added to the molten naphthalene only when local sublimation data were to be acquired using the laser Profilometer. The laser dye reduced the laser reflections from planes below the naphthalene surface. The molten naphthalene liquid was poured into the cavity until the entire cavity volume was filled and the liquid surface was slightly above the cavity edges.

After the naphthalene in the fin cavity solidified, the extra naphthalene was removed using a razor blade to scrape gently along two edges of the fin, until a smooth naphthalene surface level with the fin edges was obtained. Further smoothing of the naphthalene surface was accomplished with 150-grit sandpaper. After removing the naphthalene dust from the entire fin surface with a brush, the cast fins were inspected visually to make sure that the naphthalene surface was smooth and uniform with no contaminants embedded underneath. Finally, the cast fins were stored in a naphthalene-saturated sealed box for later use in the sublimation experiments.

3.3.2 Mass-Averaged Sublimation Experiments

Mass-averaged experiments were conducted by measuring the sublimed mass during exposure in the wind tunnel. Before each run, the barometric pressure, RTD temperatures upstream and downstream of the test section, and relative humidity were recorded. These parameters, as well as the Reynolds number, were used to calculate the required freestream air velocity in the wind tunnel. Eight naphthalene-cast fins were then weighed on a precision electronic scale, which was allowed to warm up for at least two hours. These fins were then placed one fin per row in the test section, with all naphthalene surfaces facing Column 6 shown in Figure 2.7. The tunnel was then started immediately. Meanwhile, a stop watch and the data acquisition system were started. The wind tunnel was maintained at the calculated freestream velocity throughout the run. The RTD temperatures upstream and downstream of the test section were collected every 5 seconds throughout each experiment, and their averaged value was used as the temperature in data reduction. Half way through and before the end of the run, the barometric pressure and relative humidity were recorded again. The averages of these three recordings were used in data reduction.

The naphthalene-cast fins were exposed to the wind tunnel flow for about 60 to 120 minutes, depending on the Reynolds number and lab temperature. At higher Reynolds numbers and warmer lab temperatures, the fins were exposed for a shorter period of time to avoid excessive sublimation which would distort the fin surface. At low Reynolds numbers and cooler lab temperatures, the fins were exposed for a longer period of time to ensure enough mass sublimation to keep the mass measurement uncertainty small. These fins were then removed from the test section and weighed again with the electronic scale.

The time taken to weigh the fins twice and insert and remove them was approximately three minutes. Repeated natural sublimation experiments at typical laboratory conditions showed that errors due to natural sublimation in three minutes fell within the uncertainty of the average Sherwood number calculation. Therefore, corrections for natural sublimation were neglected for the mass-averaged results.

The data were reduced using the following equations for the Reynolds number, average mass transfer coefficient, average Sherwood number, and modified Colburn j factor. For a detailed description of the data reduction, the reader is directed to DeJong and Jacobi (1995).

$$Re = \frac{U_c D_h}{n} \tag{3.3}$$

$$\overline{h_m} = \frac{\Delta m}{A_f \, r_{n,n} \Delta t} \tag{3.4}$$

$$\overline{Sh} = \frac{D_h \overline{h_m}}{D_{na}} \tag{3.5}$$

$$j = \frac{\overline{Sh}}{\mathrm{Re}\, Sc^{0.4}} \tag{3.6}$$

The uncertainties in the Reynolds number and the Sherwood number were determined to be 3.23% and 5% respectively, using the method provided by Kline and McClintock (1953).

3.3.3 Local Sublimation Experiments

The procedure for the local sublimation experiments was similar to that for the mass-averaged experiments except for two additional measurements of the naphthalene surface profile and the fin mass change during each surface profiling. The laser profilometer, as described in Section 2.5, was used to scan the naphthalene surfaces before and after wind tunnel exposure; therefore, the local sublimation depth data were determined. Prior to each local sublimation experiment, the test fin was weighed with the electronic scale. The first scan over the naphthalene surface was then performed. After the first scan, the fin was weighed again to obtain the natural sublimation mass during the scan, before it was placed into the wind tunnel. After exposure in the tunnel, the fin was weighed and scanned for the second time. The fin was weighed again after the second scan to obtain the fin mass change during the second scan.

Due to the symmetric behavior of the local mass transfer along the horizontal center line of the cavity, the scan covered a 5.08 cm $\times$ 2.54 cm area (exactly half of the naphthalene surface above the center line) in a grid of 80 $\times$ 40 equally spaced points, starting from the top-left corner of the cavity (Figure 2.9 (b)). For some local mass

transfer experiments, an additional 1.27 cm × 2.54 cm area below the center line was scanned to validate the symmetry characteristics. The scans also included the left and right metal edges of the cavity. A pre-written MATLAB script was used to adjust the surface profile data based on the height results of both metal edges, so that the edge heights from the second scan coincided with those from the first scan before the subtraction was performed to obtain the sublimation depth data.

A mounting fixture, as shown in Figure 3.3, was constructed to ensure that the same area was scanned each time and there was no distortion of the fins. Six spring plungers were used to secure the position of the test fin without applying any extra stress on the fin body. The base of the fixture was installed securely on the moving stage that was controlled by two stepper motors. The whole laser profilometry system, as well as the mounting fixture, was allowed to warm up for over four hours before any scan was performed. This long warm-up period was necessary to reduce errors due to thermal drift.

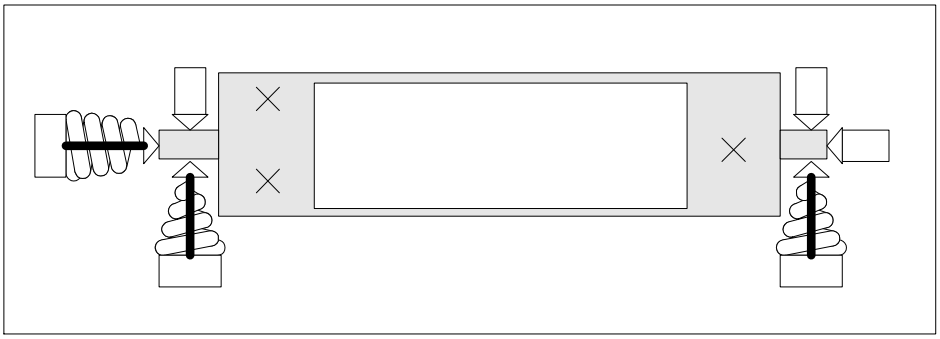

Top View

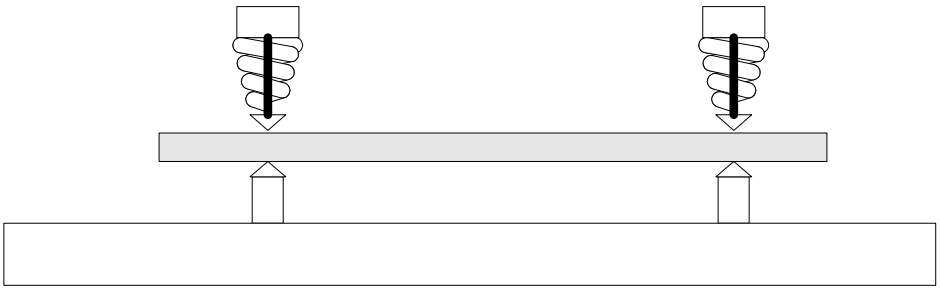

Front View

Figure 3.3 – Schematic of the mounting fixture for scanning the naphthalene surface

Each scan of the naphthalene surface took approximately 25 to 40 minutes. The natural sublimation during the scan was accounted for by measuring the mass change during two scans. An average local sublimation depth due to natural sublimation was calculated using Equation (3.7).

$$d_{nat,avg} = \frac{(\Delta m_{nat,1} + \Delta m_{nat,2})/2}{A_f \, r_{n,s}} \tag{3.7}$$

where A_f is the scan area, $r_{n,s}$ is the density of solid naphthalene, and $\Delta m_{nat,1}$ and $\Delta m_{nat,2}$ are the mass changes during the first and the second scans, respectively. The sublimation depth with the natural sublimation error corrected was then calculated using Equation (3.8).

$$d_{sb} = d_{scan} - d_{nat,avg} \tag{3.8}$$

The local mass transfer data were then reduced using Equations (3.9) and (3.10).

$$h_m = \frac{r_{n,s} d_{sb}}{r_{n,v} \Delta t} \tag{3.9}$$

$$Sh = \frac{h_m D_h}{D_{na}} \tag{3.10}$$

A redundant check was performed by integrating the local Sherwood numbers over the scanned area using Equation (3.11) and comparing to the mass-averaged Sherwood numbers.

$$\overline{Sh}_{\text{int}} = \frac{1}{N} \sum Sh \tag{3.11}$$

The local sublimation results were adopted only if $\overline{Sh}_{\text{int}}$ was within 10 % of the mass-averaged Sherwood number.

3.4 Pressure Drop Measurements

The pressure drop across the test section was measured using a high-precision differential pressure transducer. This transducer has a DC current output of 4-20 mA, which is linear with the differential pressure of 0-100 Pa with a manufacturer-certified accuracy of 0.1 Pa. A 250 Ω precision resistor was connected in the transducer output loop, and the voltage across the resistor was recorded every 0.1 second by the data acquisition system. The average of these voltages was converted to differential pressure, which was used for data reduction. In this research, the pressure drop results were reduced to the dimensionless friction factor *f* using Equation (3.12).

$$f = \frac{2\Delta P}{r U_c^{\,2}} \left(\frac{D_h}{4 L_{core}} \right) \tag{3.12}$$

Chapter 4. Flow Field Behavior

In this chapter, flow field behavior will be discussed for the baseline and VG-enhanced offset-strip fin arrays. Two experimental methods were employed to characterize the flow field. The flow visualization experiments offered qualitative flow characteristics, while the PIV experiments provided quantitative measurements of the instantaneous and time-averaged velocity and vorticity fields.

4.1 Flow Visualization

The flow visualization experiments were performed for the baseline array, 2VG-enhanced array, 4VG-enhanced array, and 4VG at Rows 1 and 5 - enhanced array, as described in Section 3.1. During all flow visualization experiments, the dye was introduced at the center columns: Columns 5 and 6 (Figure 2.7). For the flow visualization results and discussion of the 2VG-enhanced array, the reader is directed to Smotrys *et al.* (2001). The results for the other three arrays will be presented in the following.

4.1.1 Baseline Array

For the baseline array, the dye was directed to impinge at the spanwise center of the fin leading edge (location "B" as shown in Figure 3.1). The flow is found to be laminar throughout the array up to a Reynolds number of 1130, as shown in Figure 4.1. When Re is increased to 1200, wake instability starts to develop downstream of the array, which is demonstrated in Figure 4.2. When Re is increased further to 1260, spanwise vortex shedding occurs at the 7th row fins and downstream, as shown in Figure 4.3. The periodic shedding of vortices, which wash over the fin surfaces, strengthens the exchange of fluid in the fin boundary layers with the freestream, thus greatly enhancing the flow mixing effect and heat transfer performance (DeJong and Jacobi, 1995). The onset location of vortex shedding moves upstream as Re goes higher. At Re = 1440, spanwise vortex shedding occurs at the 3rd row and all following rows, as shown in Figure 4.4. At this Reynolds number, the spanwise vortices at the 7th row and downstream are stronger than those at Re = 1260 (Figure 4.3). When Re is increased to 1940, the onset of vortex shedding moves to the first row, as shown in Figure 4.5. Strong spanwise vortices are present in the first half of the array at this Reynolds number, while flow in the second half of the array is reasonably well-mixed, and the flow structure is hard to discern with the dye streak. The flow behavior at even higher Reynolds numbers is similar to that observed at Re = 1940, except that the mixing of fluid continues to increase.

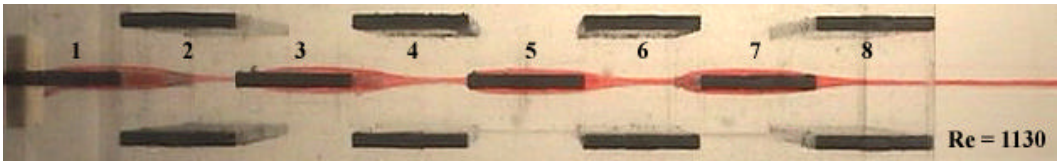

Figure 4.1 – Flow visualization for the baseline array at Re = 1130

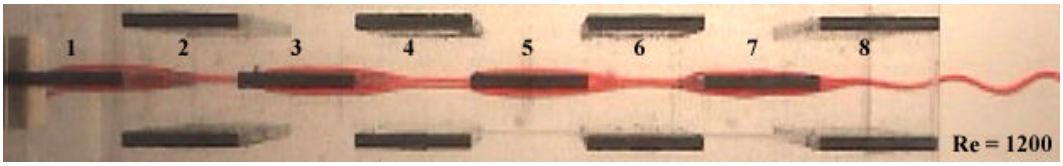

Figure 4.2 – Flow visualization for the baseline array at Re = 1200

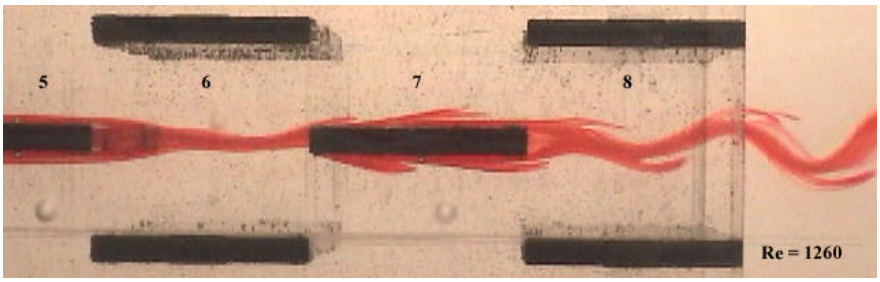

Figure 4.3 – Flow visualization for the baseline array: trailing fins at Re = 1260

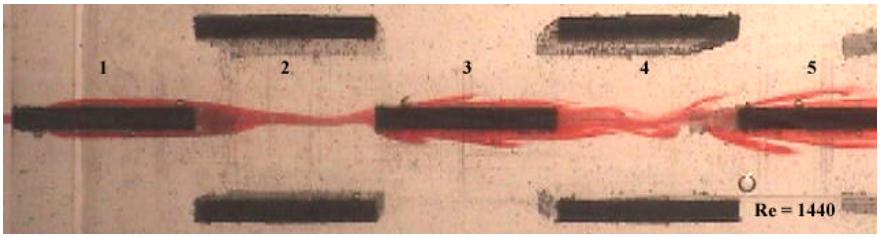

(a)

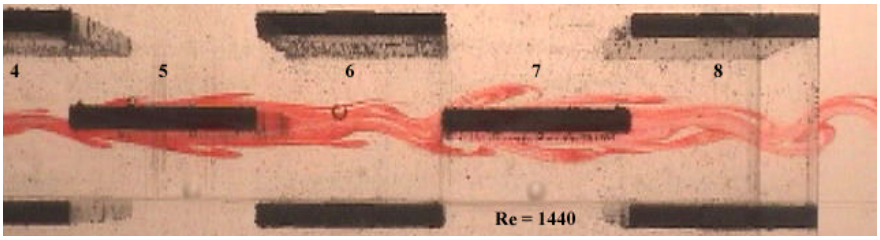

(b)

Figure 4.4 – Flow visualization for the baseline array at Re = 1440: (a) leading fins; (b) trailing fins

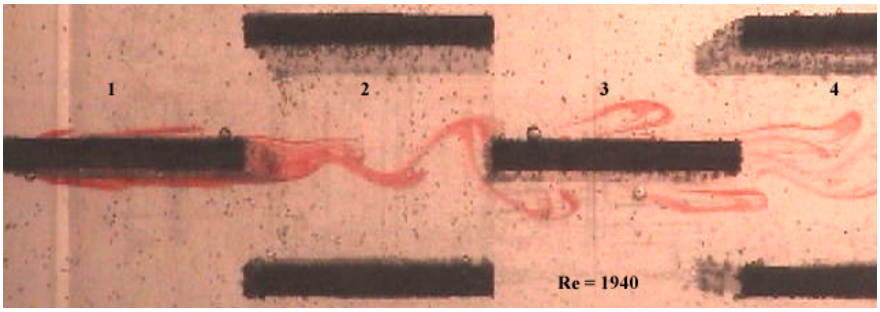

(a)

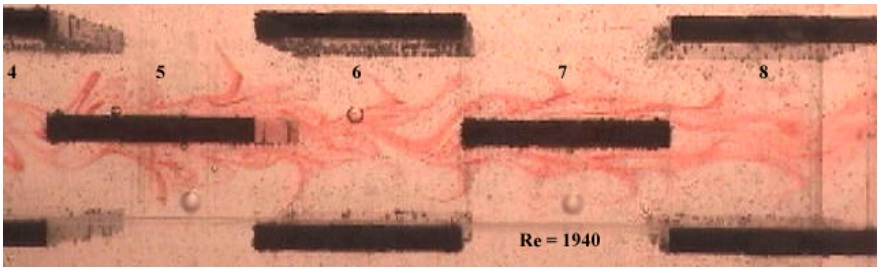

(b)

Figure 4.5 – Flow visualization for the baseline array at Re = 1940: (a) leading fins; (b) trailing fins

4.1.2 4VG-Enhanced Array

For the 4VG-enhanced array, the streamwise vortices were visualized by injecting the dye at the tip region of the delta wing (location A as shown in Figure 3.1). The dye was also directed to impinge at the spanwise center of the fin leading edge (location B as shown in Figure 3.1), to explore the spanwise vortex shedding behavior.

The flow visualization result at Re = 1030 is shown in Figure 4.6. The streamwise vortices are present in the form of long spiraling strands of fluid, and they remain coherent throughout the array (Figure 4.6 (a)). A closer look at the spiraling streamwise vortices in the front portion of the array is provided in Figure 4.6 (b). The flow throughout the array is laminar, as shown in Figure 4.6 (c). A portion of the dye streak originating from the spanwise center of the 1st row fin is entrained by the streamwise vortices from the 5th row and reveals the upwash movement of the streamwise vortices between VGs.

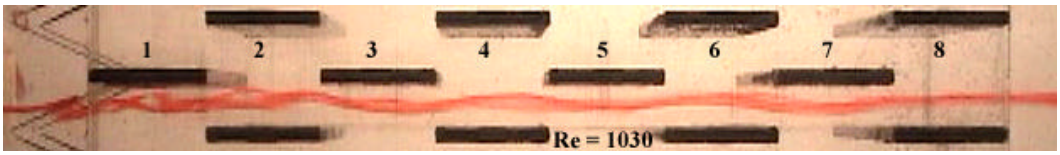

(a)

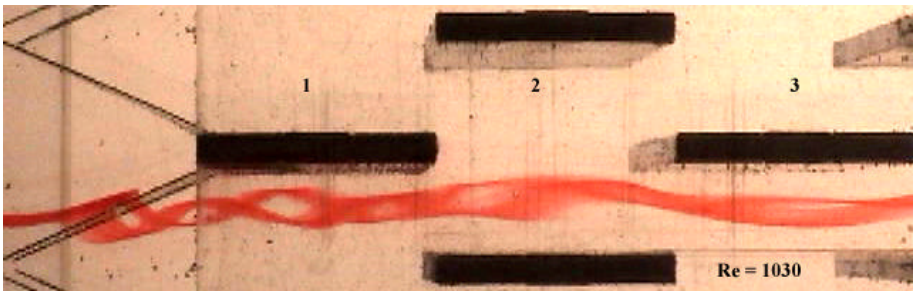

(b)

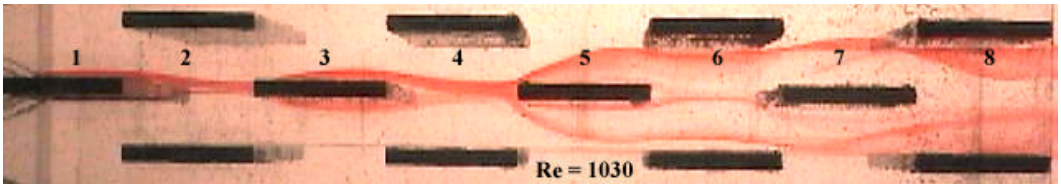

(c)

Figure 4.6 – Flow visualization for the 4VG-enhanced array at Re = 1030: (a) Dye location - VG tip; (b) Dye location - VG tip, front; (c) Dye location - spanwise center

Similar flow visualization behavior is observed at Re = 1280, as shown in Figure 4.7. The flow is still laminar, with the streamwise vortex strands remaining coherent throughout the array. In contrast with the baseline array, for which spanwise vortex shedding occurs at the seventh row at Re = 1260, the presence of delta wings delays the occurrence of spanwise vortex shedding to a higher Reynolds number.

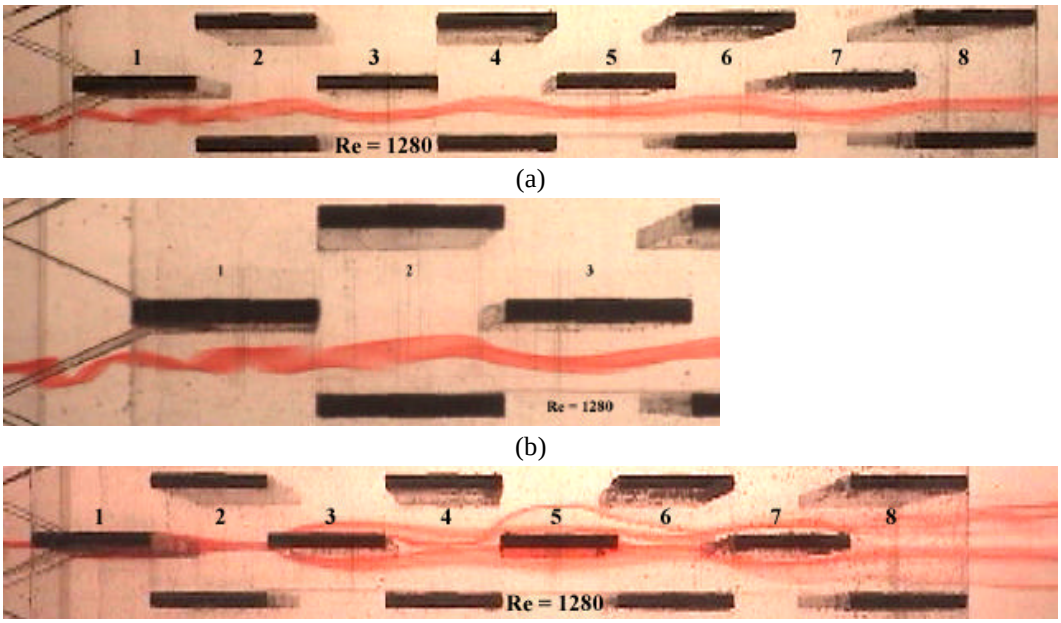

Figure 4.7 – Flow visualization for the 4VG-enhanced array at Re = 1280: (a) Dye location - VG tip; (b) Dye location - VG tip, front; (c) Dye location - spanwise center

When Re is increased to 1520, the tip vortices become much stronger and are located closer to the fin surfaces (Figure 4.8 (a)) as compared to those at Re = 1280. The long spiraling strands begin to thicken and diffuse away from their core after the 5th row (Figure 4.8 (b)). Meanwhile, spanwise vortex shedding is observed clearly at the third row in the spanwise center region between VGs (Figure 4.8 (c)). Weaker spanwise vortex shedding is observed at the fifth row, no spanwise vortex shedding at the seventh row, and no clear flow instability in the array wake region (Figure 4.8 (d)). This behavior is due to the interaction of streamwise vortices and spanwise vortex shedding. This interaction appears to weaken and suppress the spanwise vortex shedding at the downstream rows.

As the Reynolds number is increased further to 1750, the spiraling strands of the streamwise vortices begin to thicken and diffuse even before reaching the third row. The streamwise vortices are quite incoherent and become chaotic by about the third row (Figure 4.9 (a)). In the spanwise center region between VGs, spanwise vortex shedding is observed to start from the third row (Figure 4.9 (b)). The shedding becomes weaker by the fifth row, and even weaker at the seventh row, with no perceptible waviness in the array wake region (Figure 4.9 (c)), due to the destructive interaction of the streamwise vortices and spanwise vortex shedding.

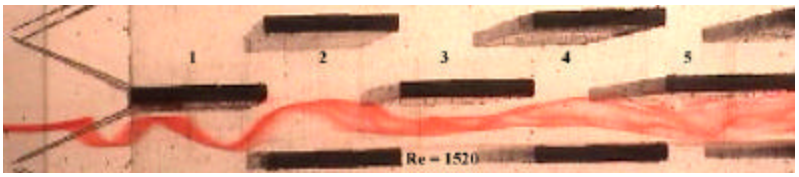

(a)

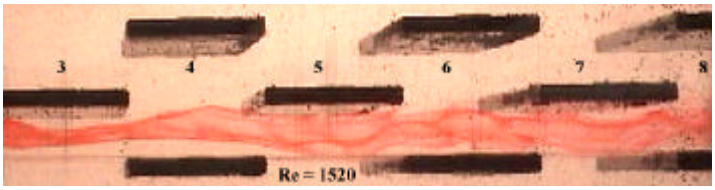

(b)

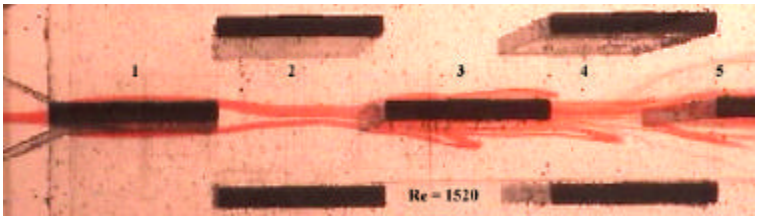

(c)

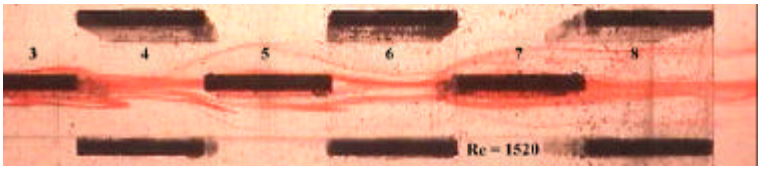

(d)

Figure 4.8 – Flow visualization for the 4VG-enhanced array at Re = 1520: (a) Dye location - VG tip, front; (b) Dye location - VG tip, back; (c) Dye location - spanwise center, front; (d) Dye location - spanwise center, back

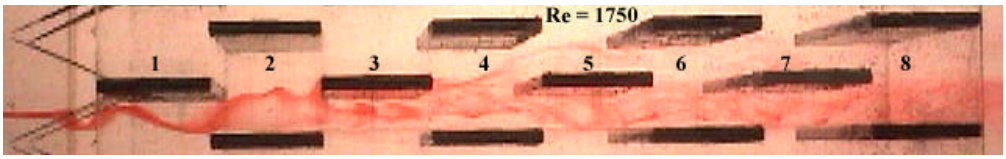

(a)

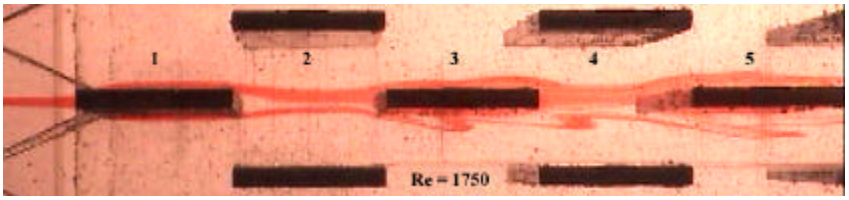

(b)

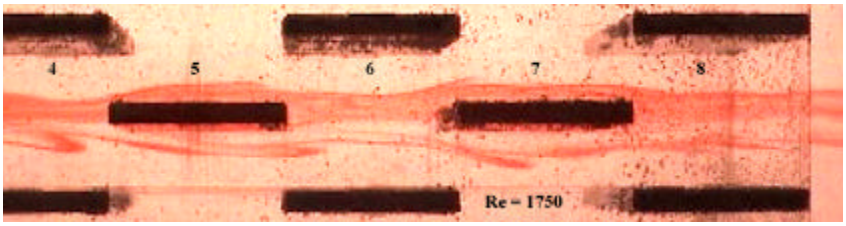

(c)

Figure 4.9 – Flow visualization for the 4VG-enhanced array at Re = 1750: (a) Dye location - VG tip; (b) Dye location - spanwise center, front; (c) Dye location - spanwise center, back

As the Reynolds number is increased to 1980, similar behavior of the streamwise vortices as that observed at Re = 1750 is found. In the spanwise center region, spanwise vortex shedding is observed even at the first row, and strong vortex shedding occurs at the third row (Figure 4.10 (a)). Although vortex shedding becomes weaker along the flow direction after the third row, it is present throughout the array and in the wake region (Figure 4.10 (b)).

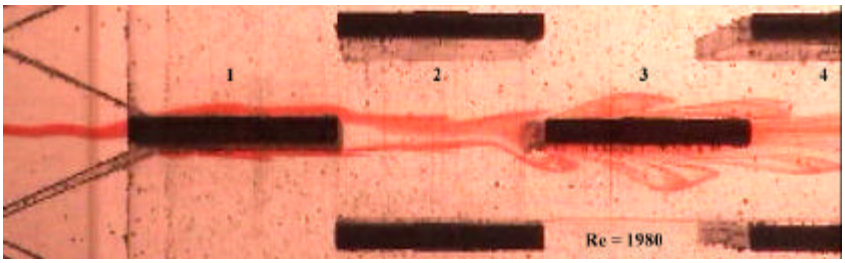

(a)

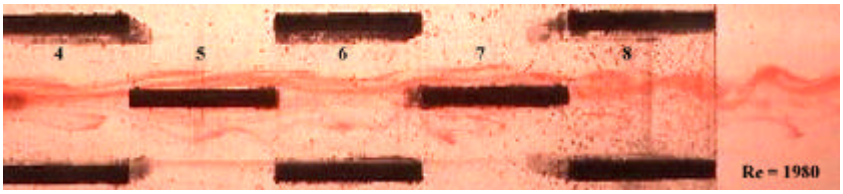

(b)

Figure 4.10 – Flow visualization for the 4VG-enhanced array at Re = 1980: (a) Dye location - spanwise center, front; (b) Dye location - spanwise center, back

4.1.3 4VG at Rows 1 and 5 - Enhanced Array

For this enhanced array, dye was injected at the same two locations as for the 4VG-enhanced array.

The flow visualization result at Re = 1030 is shown in Figure 4.11. The spiraling fluid strands of the streamwise vortices are present in the array, as shown in Figures 4.11 (a) and (b). The streamwise vortices become less coherent after passing the second row of delta wings at the 5th row. The flow is laminar throughout the array, until waviness develops at the 7th row (Figure 4.11 (c)). Clearly, the streamwise vortices generated by the second row of delta wings are more unstable due to the non-uniform incoming flow ahead of the second row of delta wings. The more complex interactions in this flow field introduce flow instability into an otherwise laminar flow.

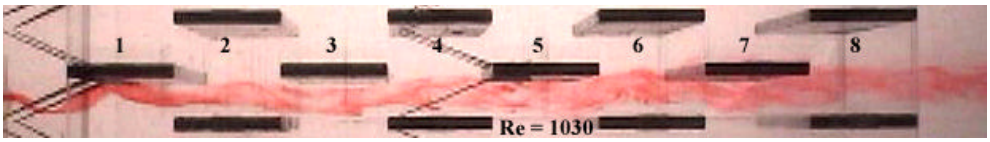

(a)

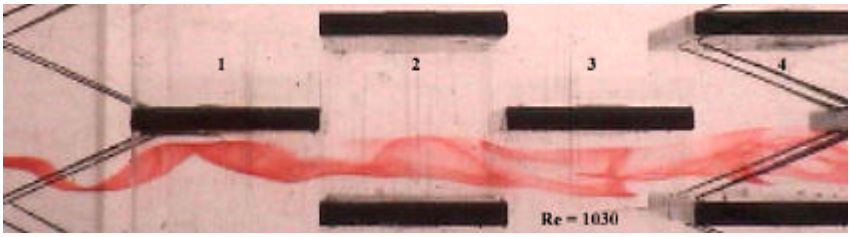

(b)

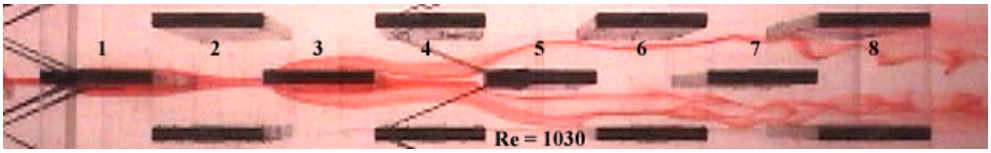

(c)

Figure 4.11 – Flow visualization for the 4VG at Rows 1 and 5 - enhanced array at Re = 1030: (a) Dye location - VG tip; (b) Dye location - VG tip, front; (c) Dye location - spanwise center

Similar flow visualization behavior is observed at Re = 1280, as shown in Figure 4.12. The streamwise vortices become poorly organized in the second half of the array (Figure 4.12 (a)), as compared to the situation at lower Reynolds numbers. The flow is laminar in the first half of the array and becomes chaotic and well mixed after passing the second row of delta wings (Figure 4.12 (c)).

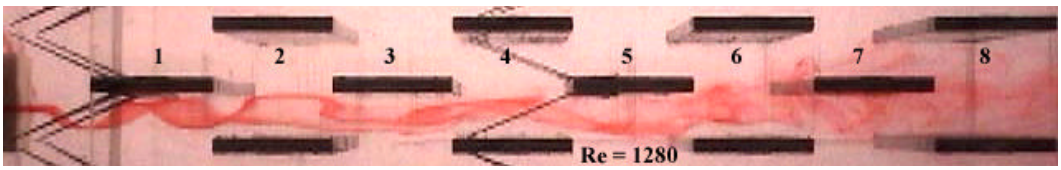

(a)

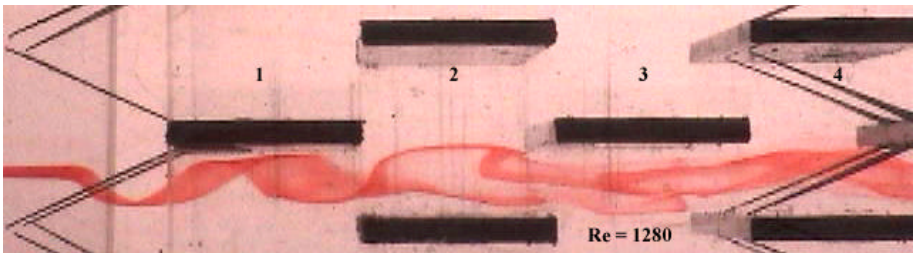

(b)

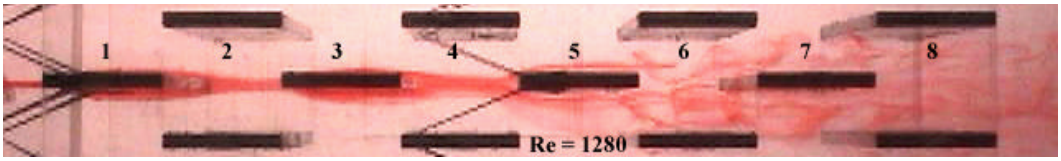

(c)

Figure 4.12 – Flow visualization for the 4VG at Rows 1 and 5 - enhanced array at Re = 1280: (a) Dye location - VG tip; (b) Dye location - VG tip, front; (c) Dye location - spanwise center

As the Reynolds number is increased to 1520, the streamwise vortices show the same behavior as that for Re = 1280, except that the flow is even more chaotic and well mixed in the second half of the array (Figure 4.13 (a)). Spanwise vortex shedding is observed at the third row in the spanwise center region (Figure 4.13 (c)), which is more obvious when observing the corresponding video clips of flow visualization.

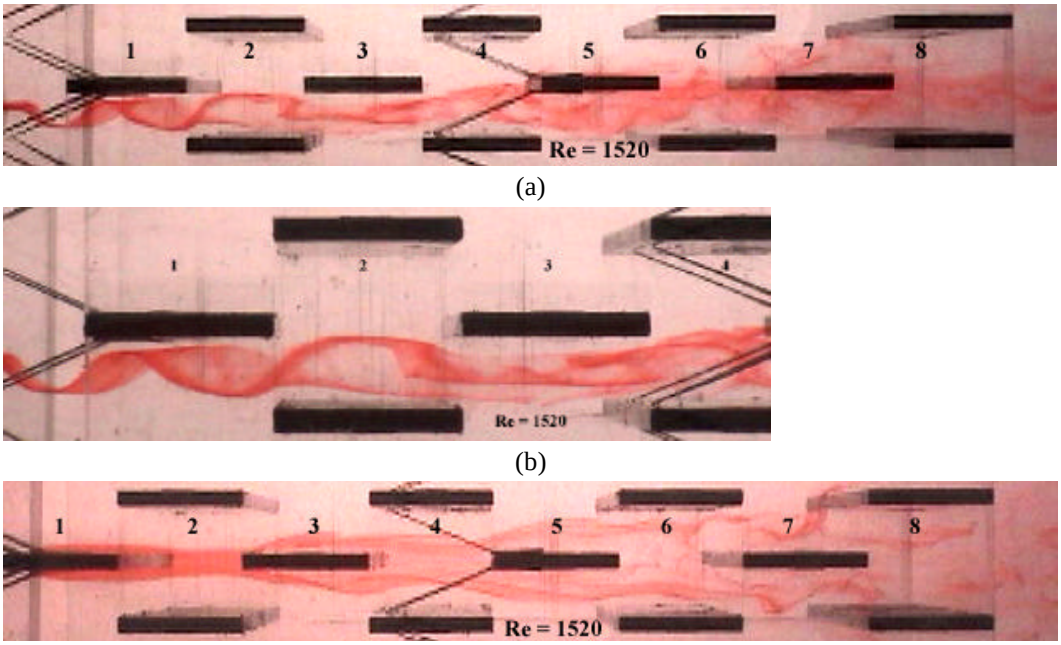

Figure 4.13 – Flow visualization for the 4VG at Rows 1 and 5 - enhanced array at Re = 1520: (a) Dye location - VG tip; (b) Dye location - VG tip, front; (c) Dye location - spanwise center

As the Reynolds number is increased further to 1750, the behavior of streamwise vortices is similar to that for the 4VG-enhanced array, with the flow even more chaotic due to the second row of delta wings (Figures 4.14 (a) & (b)). In the spanwise center region, spanwise vortex shedding is observed at the 3rd row and chaotic, well-mixed flow develops at all rows downstream from the 3rd row (Figures 4.14 (c) & (d)).

Spanwise vortex shedding is finally observed at the 1st row at Re = 1980 (Figure 4.15).

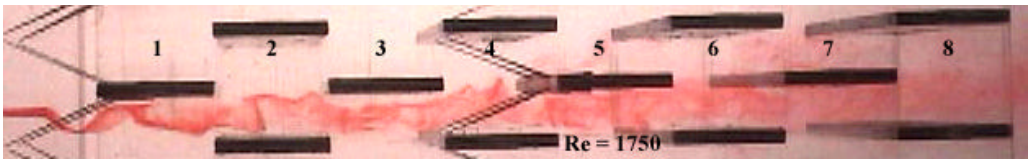

(a)

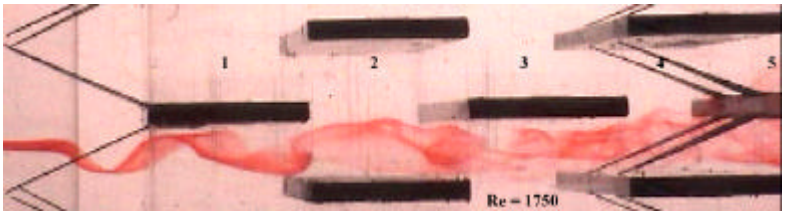

(b)

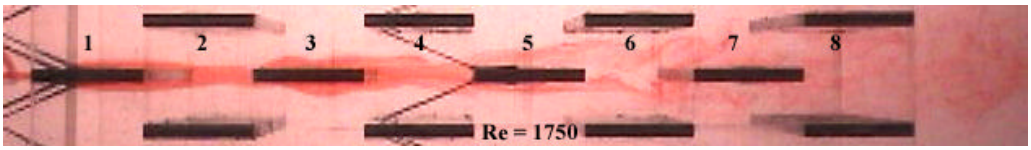

(c)

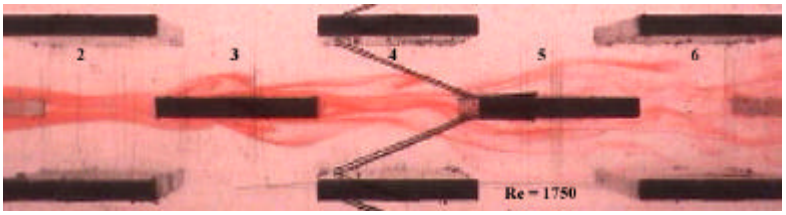

(d)

Figure 4.14 – Flow visualization for the 4VG at Rows 1 and 5 - enhanced array at Re = 1750: (a) Dye location - VG tip; (b) Dye location - VG tip, front; (c) Dye location - spanwise center; (d) Dye location - spanwise center, zoom-in

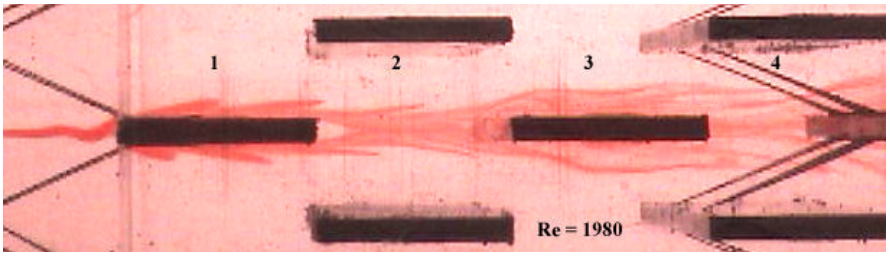

Figure 4.15 – Flow visualization for the 4VG at Rows 1 and 5 - enhanced array at Re = 1980: Dye location - spanwise center, front

4.2 PIV Results

The PIV experiments were performed for the baseline array, 2VG-enhanced array, 4VG-enhanced array and 4VG at Rows 1 and 5 - enhanced array, as described in Section 3.2. The scope of the entire set of PIV experiments is provided in Table 3.1. The side-view PIV data were obtained two rows of fins at a time, with the laser sheet passing the inner root of the VGs (location 2 as shown in Figure 3.1). The end-view PIV data were obtained at several streamwise locations as shown in Figure 3.2.

The accuracy and credibility of the PIV flow field results were mainly determined by the quality of the raw PIV images. In the TSI Insight software used in this research, the quality of the images is presented in the form of "choice codes" (CHC). The field distribution of the CHC reflects the quality of each PIV planar velocity field. A

CHC value of “one” indicates that the velocity vector is computed from a first-peak correlation - the highest correlation peak in the FFT calculation. A CHC value of “four” indicates that the velocity vector is interpolated by the validation scheme described in Section 3.2.3. Therefore, images that generate a velocity vector field with the fewest number of interpolated vectors (CHC value of “four”) are considered to be of the highest quality.

The ranges of choice-code distributions for both the side-view and end-view images are presented in Figures 4.16 - 4.19. For side-view images, the best case is that 1 out of 2170 measured vectors (0.046%) is interpolated (Figure 4.16), and the worst is that 46 out of 2100 measured vectors (2.19%) are interpolated (Figure 4.17). For end-view images, the best case is that 1 out of 1264 measured vectors (0.079%) is interpolated (Figure 4.18), and the worst is that 39 out of 1264 measured vectors (3.09%) are interpolated (Figure 4.19). It is noticed that most of the interpolated vectors are near the solid surfaces or at the edges of the measured domain, and are most likely due to light-sheet reflections. For most side-view and end-view results, the percentage of interpolated vectors is less than 1%, which is quite good. Even the worst case of 3.09% interpolated vectors is considered to be acceptable.

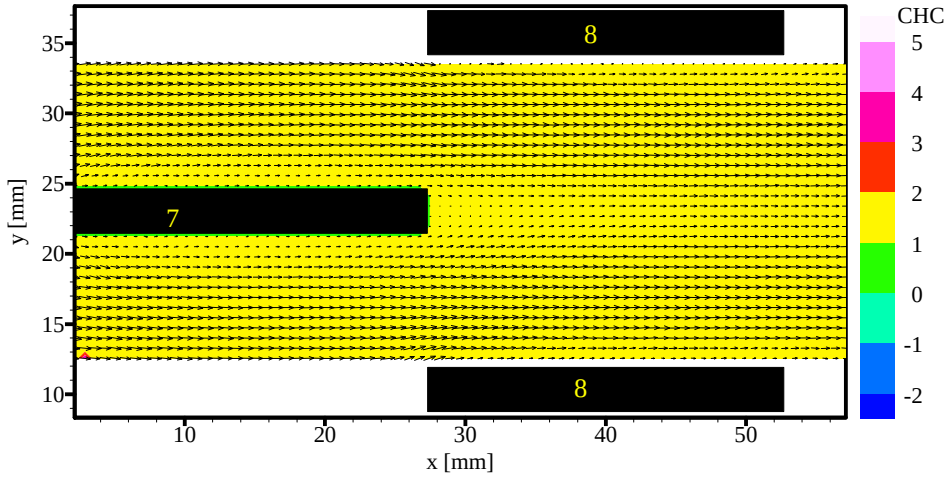

Figure 4.16 – Choice codes at Re = 1030, rows 7 and 8, side-view, for the 4VG-enhanced array

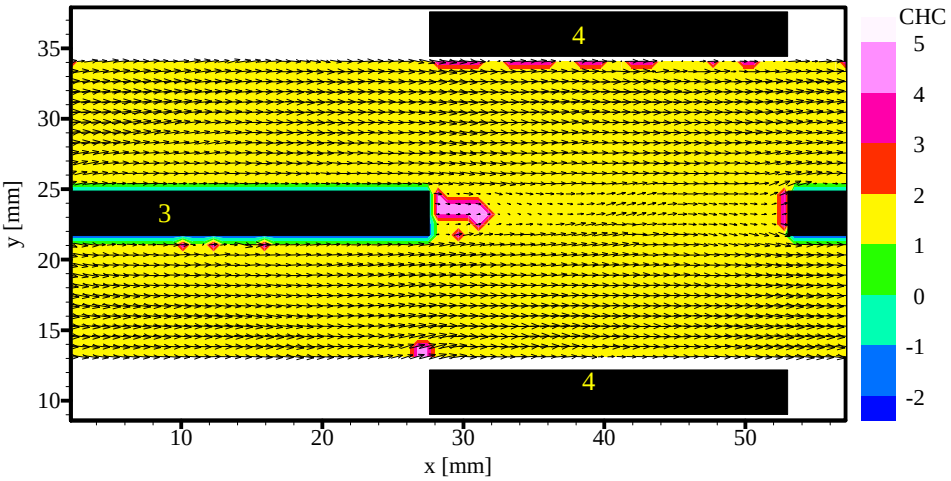

Figure 4.17 – Choice codes at Re = 2450, rows 3 and 4, side-view, for the 4VG-enhanced array

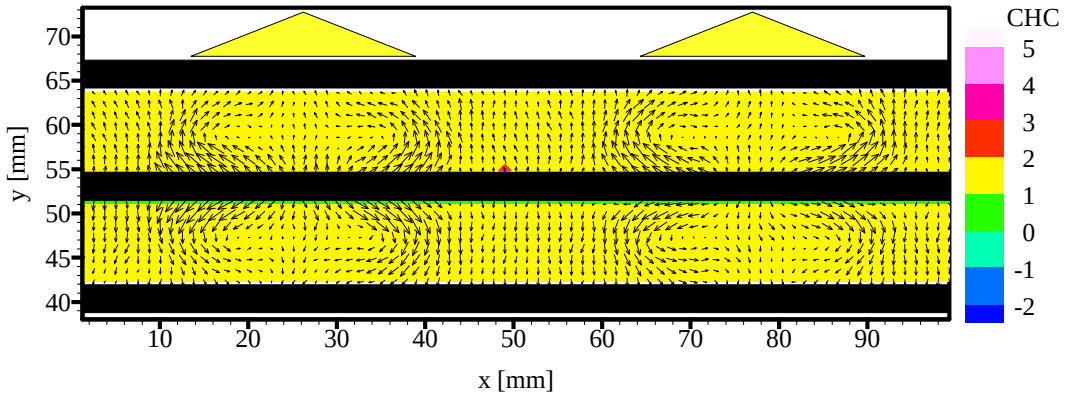

Figure 4.18 – Choice codes at Re = 850, X^* = 2.0, end-view, for the 4VG-enhanced array

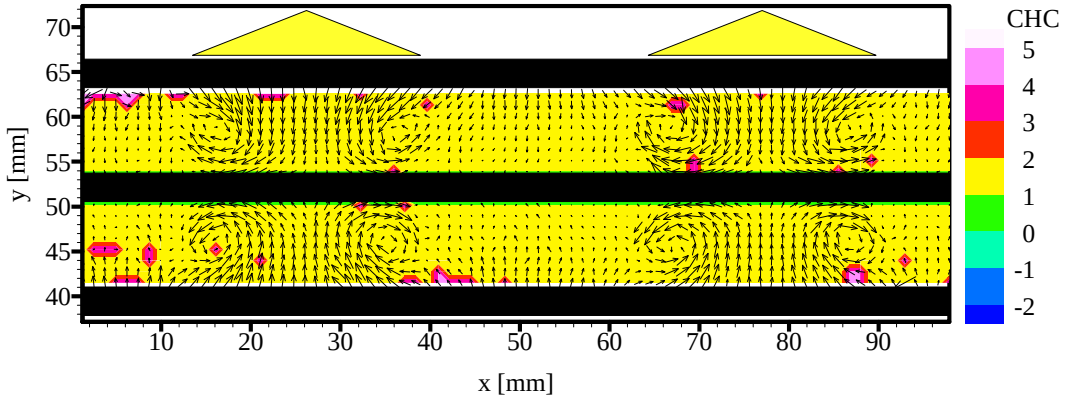

Figure 4.19 – Choice codes at Re = 1520, X^* = 1.0, end-view, for the 4VG-enhanced array

To illustrate the spanwise location of the delta wings, gold triangles are placed at the top of all end-view PIV plots, such as those in Figures 4.18 and 4.19. However, the actual delta wings are always attached on the middle column of fins at the 1st, and possibly 5th, rows in the end-view plots. In all end-view images, the main flow component (U) is directly out of the page.

Not all the PIV velocity and vorticity field results are presented here, due to the large volume of these results. The most significant results have been selected for presentation based on whether they reflect general flow field characteristics. Results that show flow field characteristics similar to those discussed earlier are not repeated.

4.2.1 Baseline Array

The PIV velocity field results for the baseline array are shown in Figures 4.20 – 4.26. The flow field for Re = 850 is shown in Figure 4.20; it is representative of the flow characteristics for Re ≤ 850. The flow is laminar throughout the array and no wake instability in the downstream region is observed. This laminar flow velocity field correlates well with the flow visualization results.

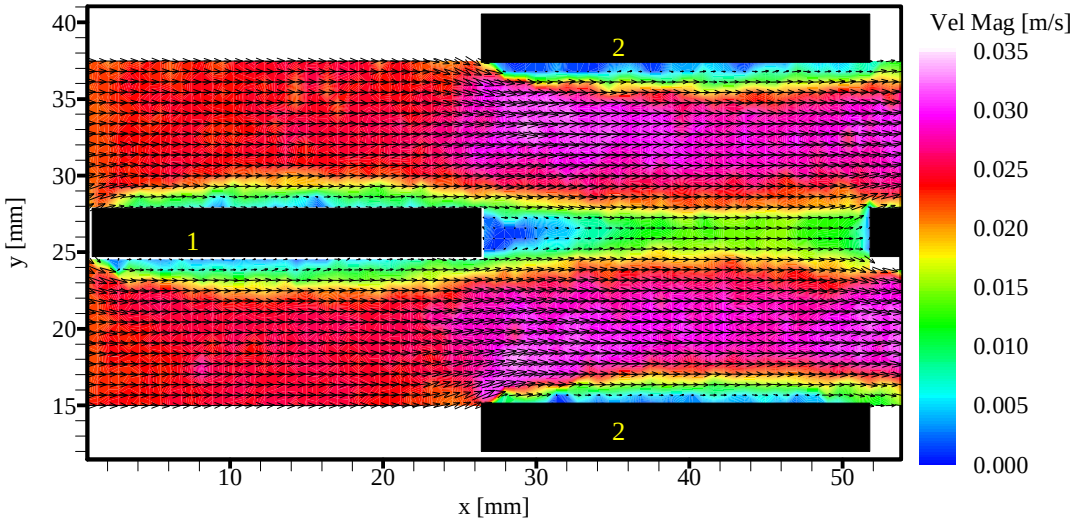
Vel Mag [m/s]
0.035
0.030
0.025
0.020
0.015
0.010
0.005
0.000
y [mm]
x [mm]
1
2
2

(a)

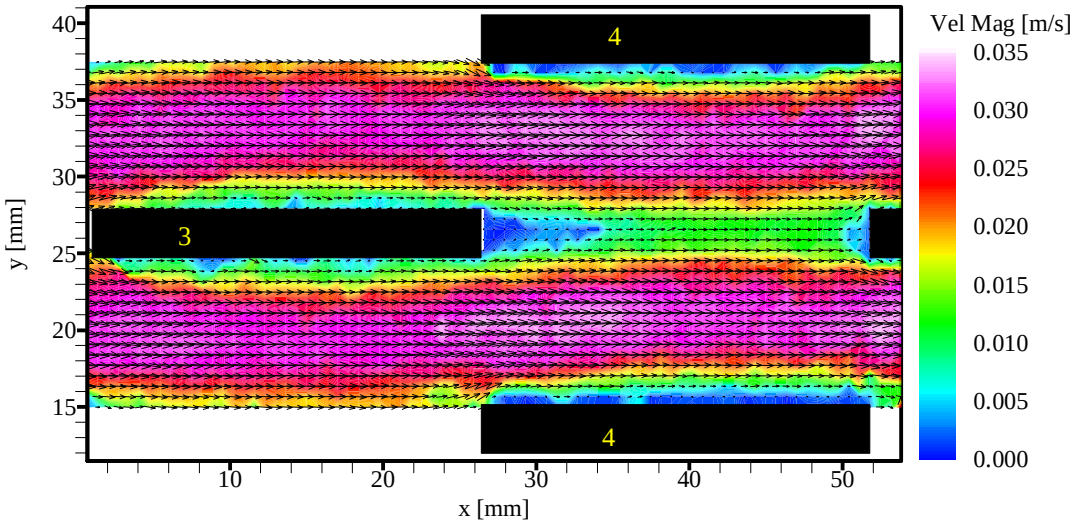
Vel Mag [m/s]
0.035
0.030
0.025
0.020
0.015
0.010
0.005
0.000
y [mm]
x [mm]
3
4
4

(b)

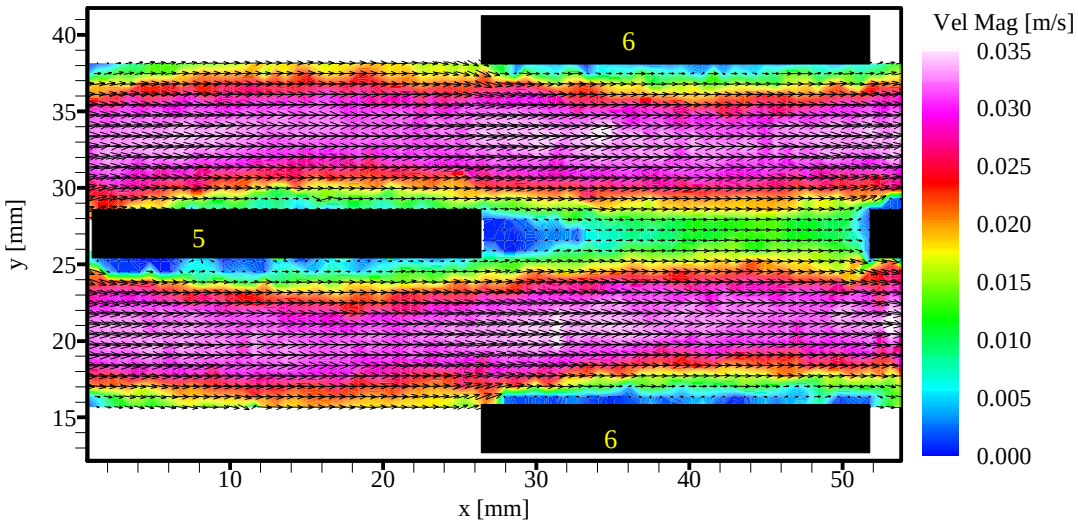
Vel Mag [m/s]
0.035
0.030
0.025
0.020
0.015
0.010
0.005
0.000
y [mm]
x [mm]
5
6
6

(c)

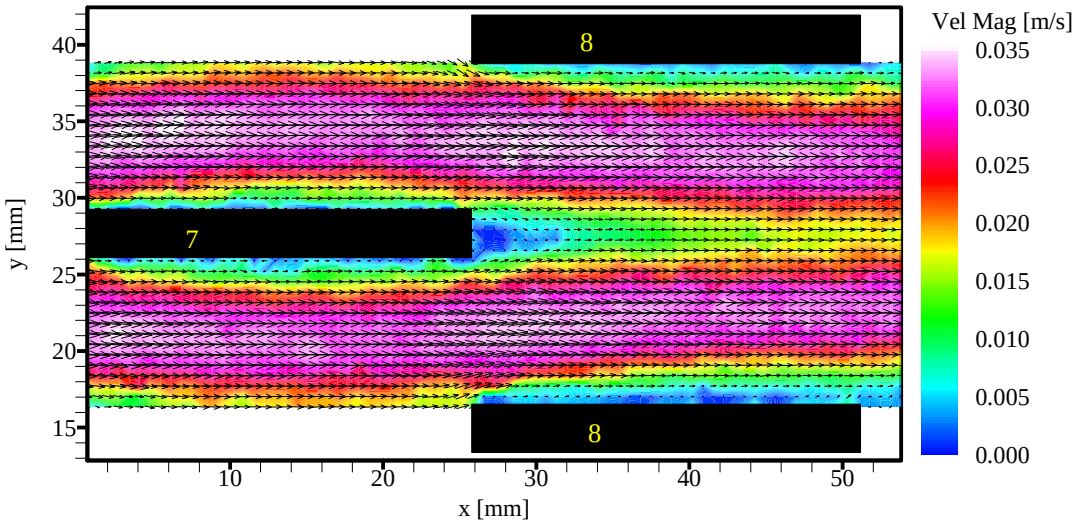

(d)

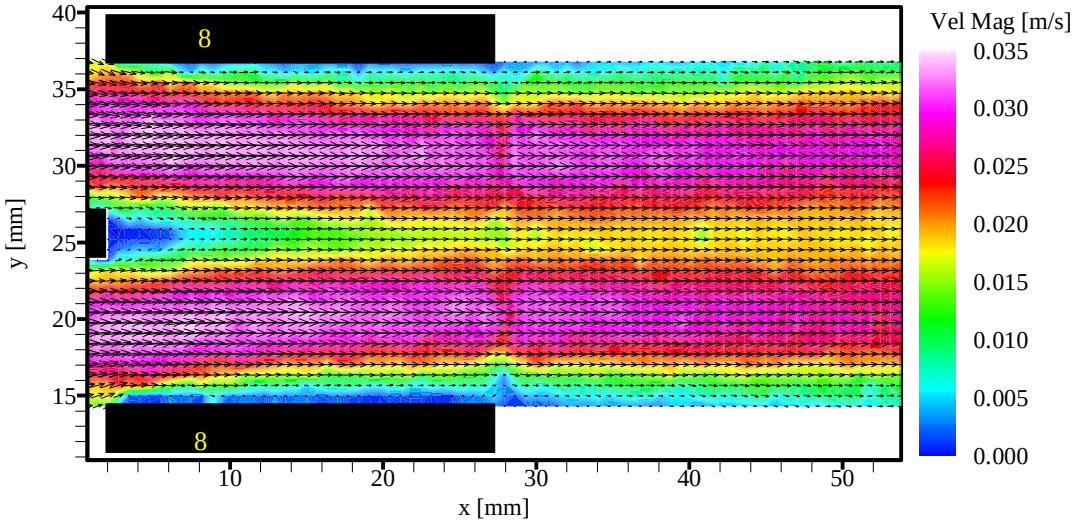

(e)

Figure 4.20 – Instantaneous velocity for baseline array at Re = 850: (a) Rows 1 and 2; (b) Rows 3 and 4; (c) Rows 5 and 6; (d) Rows 7 and 8; (e) Row 8 and downstream

The flow field characteristics inside the array for Re = 1030 are similar to those for Re = 850, except that the velocity and vorticity magnitudes increase as Re increases. However, some instability develops in the array wake region. As shown in Figure 4.21, the instantaneous PIV result for the 8th row and the downstream wake clearly reveals waviness, which means that shear layer instabilities have started to develop in this region. As is well known, these shear layer instabilities improve flow mixing and usually lead to heat transfer enhancement. Slightly different from the flow visualization results, for which wake instability is not observed until Re > 1130, the PIV results prove to be more sensitive and more accurate in revealing the instantaneous flow behavior than do the flow visualization results, and therefore reflect the flow field better.

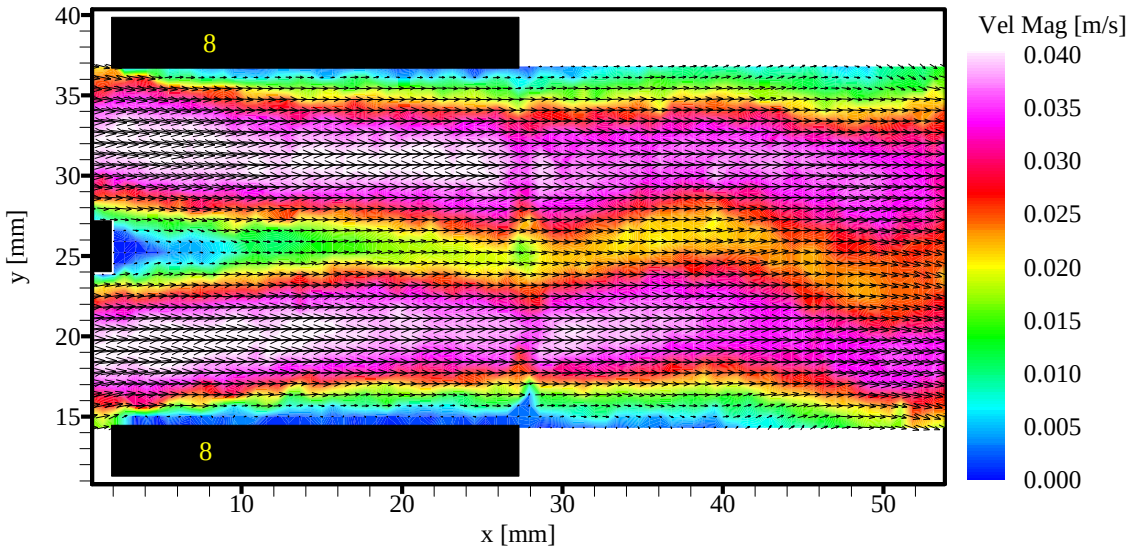

Figure 4.21 – Instantaneous velocity for baseline array at Re = 1030, Row 8 and downstream

As the Reynolds number is increased to 1280 (Figure 4.22), the onset of flow instability moves upstream to the wake of row 5, and separate high-velocity pockets (white color) are observed at row 6. Since the individual instantaneous PIV images show only a snapshot of the flow field, it is hard to identify the occurrence of periodic flow behavior such as spanwise vortex shedding using individual PIV images alone. However, 50 continuous instantaneous PIV results were obtained for all PIV experiments in this research. Continuous playback of the 50 velocity field results reveals the periodic behavior in the flow field. It is observed in the side-view PIV experiments that continuous playback of the PIV results always show spanwise vortex shedding behavior whenever flow instability and separate high-velocity pockets are present in the flow field. Therefore, for this case, spanwise vortex shedding starts to occur at row 6. Spanwise vortex shedding is more structured at row 7, row 8, and in the wake region for this Reynolds number. The array wake instability is much stronger than for Re = 1030. All these flow characteristics correspond closely with the flow visualization results at Re = 1260.

As the Reynolds number is increased further to 1330 (Figure 4.23), the onset of flow instability moves to the wake of row 3 fins, and spanwise vortex shedding is clearly observed at row 5 and downstream. Similar flow behavior is observed for a higher Reynolds number of 1470 (Figure 4.24), except that the instability in the wake of row 3 and spanwise vortex shedding at row 5 and downstream become stronger.

With the Reynolds number increasing further to 1750 (Figure 4.25), the onset of flow instability is observed in the wake of row 1 fins. Spanwise vortex shedding is clearly present throughout the array except at row 1. The spanwise vortices are stronger than those at lower Reynolds numbers. Although there are no large vortices at row 1, the irregular shape of the row 1 boundary layer does not look like a laminar flow either. This behavior indicates that shear layer instability occurs in the row 1 boundary layer at a much smaller scale than for downstream rows, which correlates well with the flow visualization at a slightly higher Re of 1940 (Figure 4.5). Once again, the PIV results demonstrate more accuracy and sensitivity in revealing the instantaneous flow characteristics than do the flow visualization results.

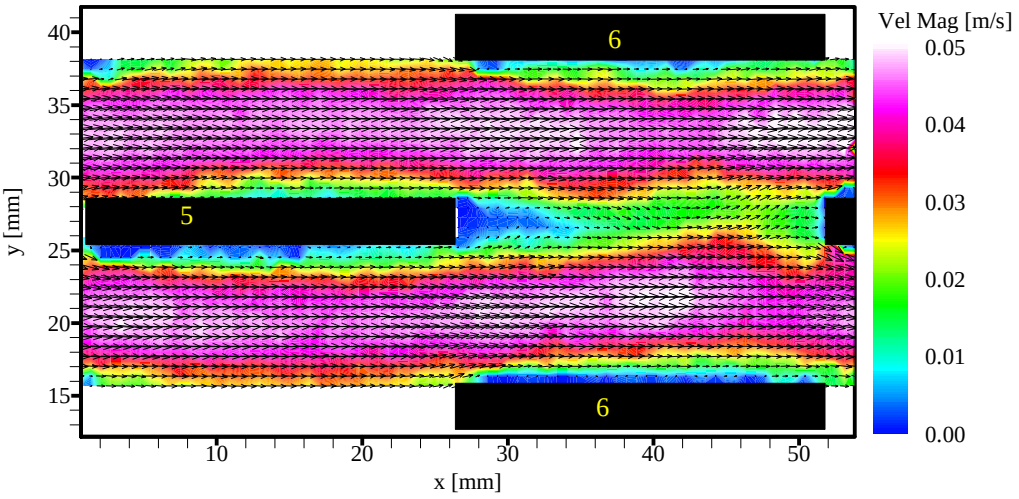

(a)

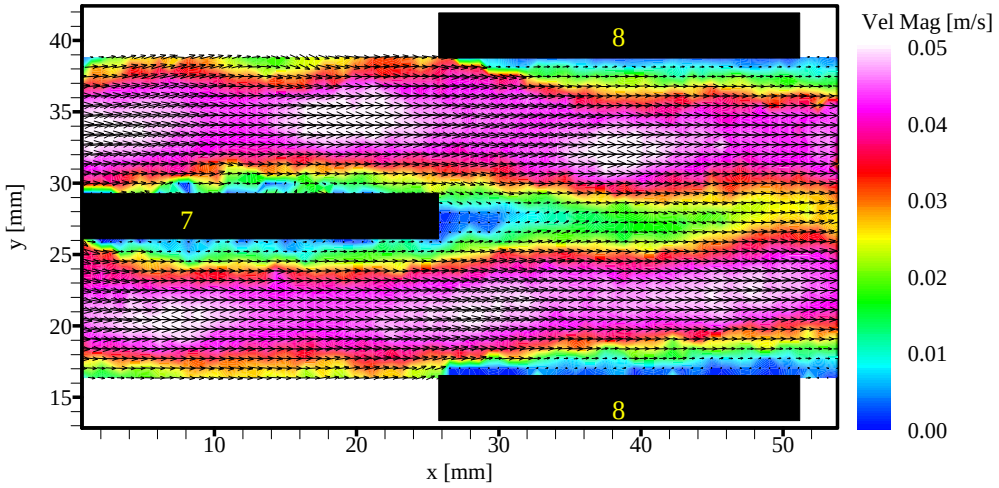

(b)

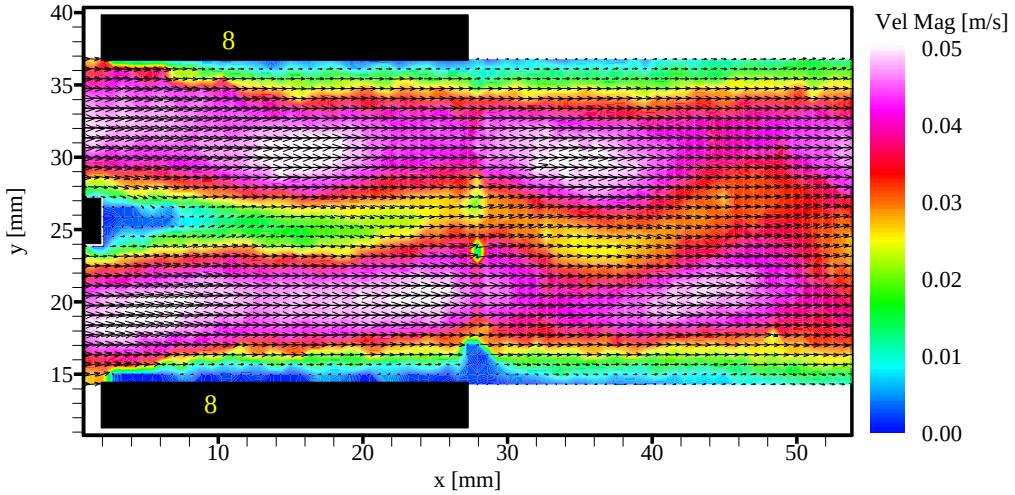

(c)

Figure 4.22 – Instantaneous velocity for baseline array at Re = 1280: (a) Rows 5 and 6; (b) Rows 7 and 8; (c) Row 8 and downstream

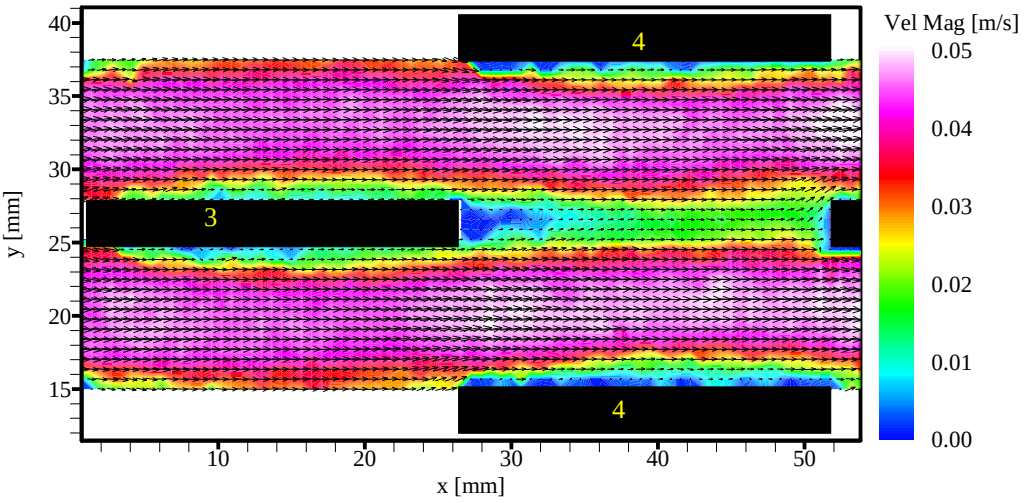

(a)

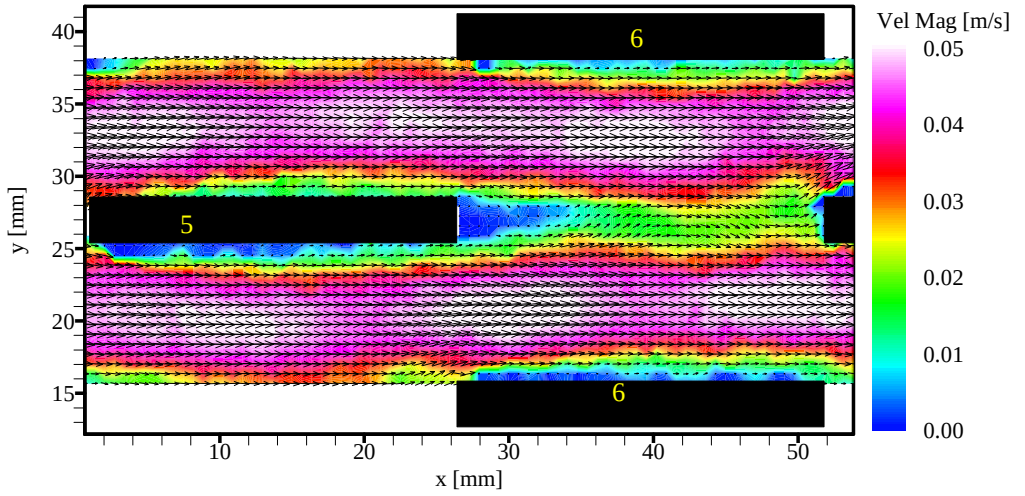

(b)

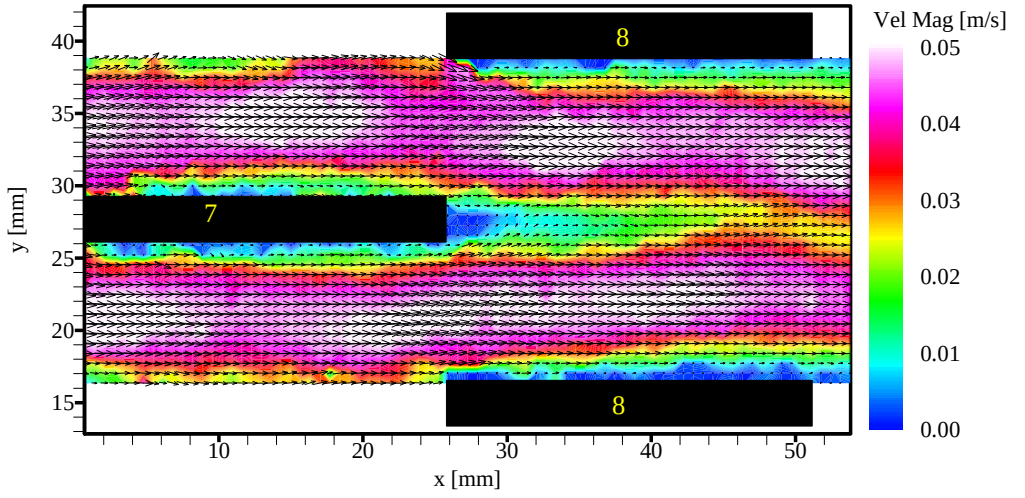

(c)

Figure 4.23 – Instantaneous velocity for baseline array at Re = 1330: (a) Rows 3 and 4; (b) Rows 5 and 6; (c) Rows 7 and 8

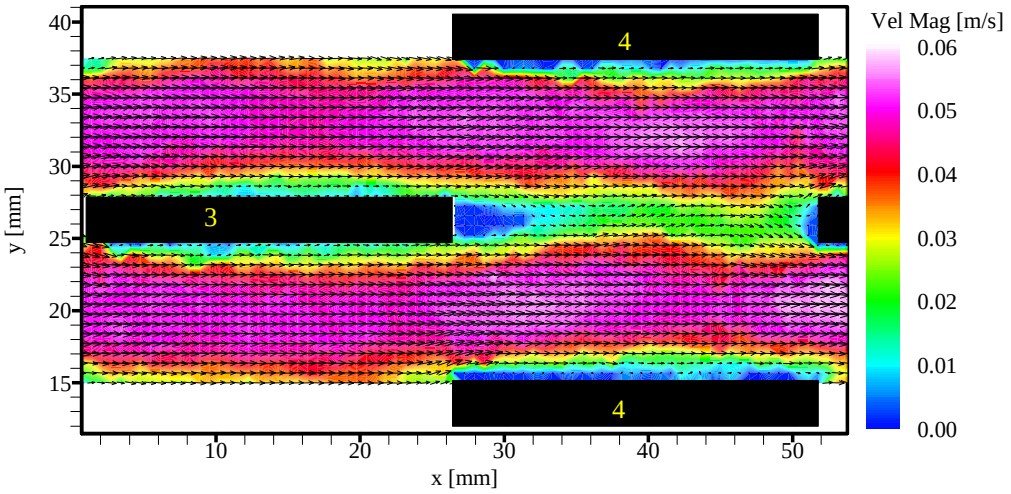

(a)

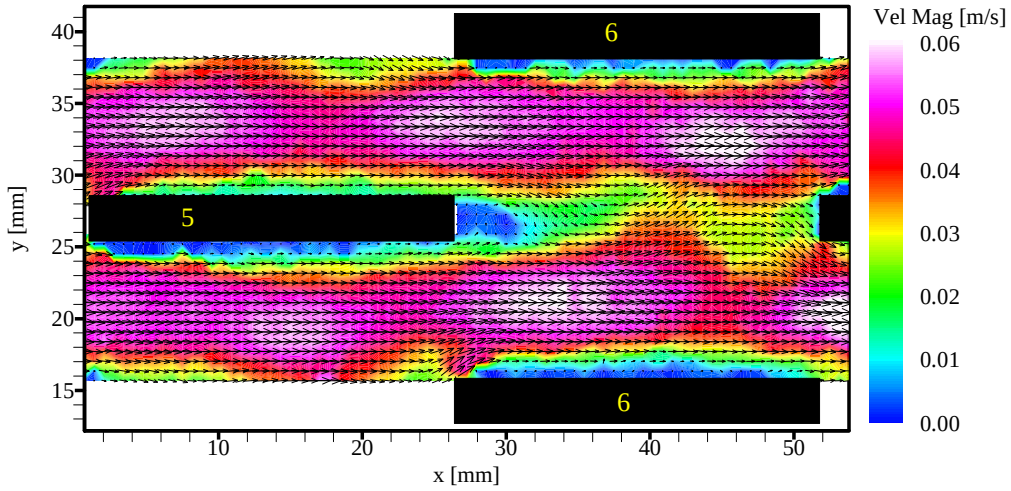

(b)

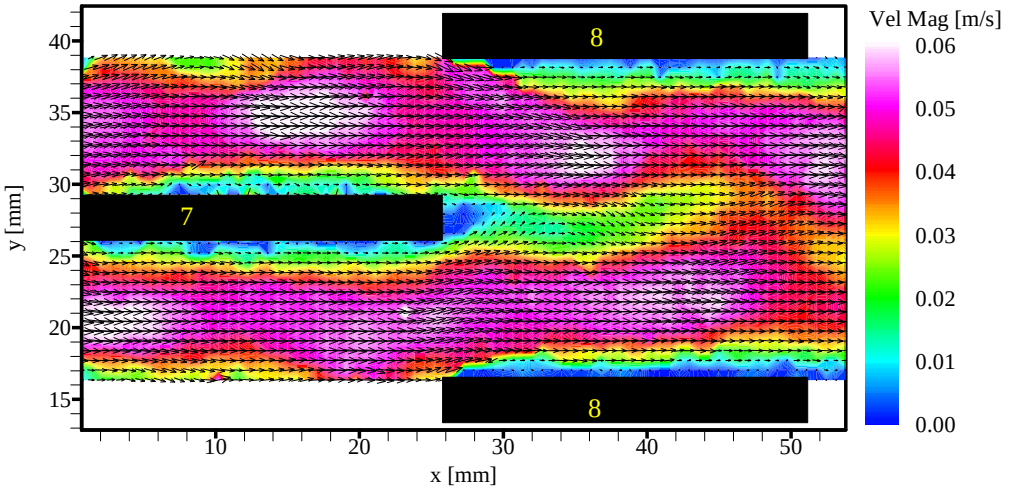

(c)

Figure 4.24 – Instantaneous velocity for baseline array at Re = 1470: (a) Rows 3 and 4; (b) Rows 5 and 6; (c) Rows 7 and 8

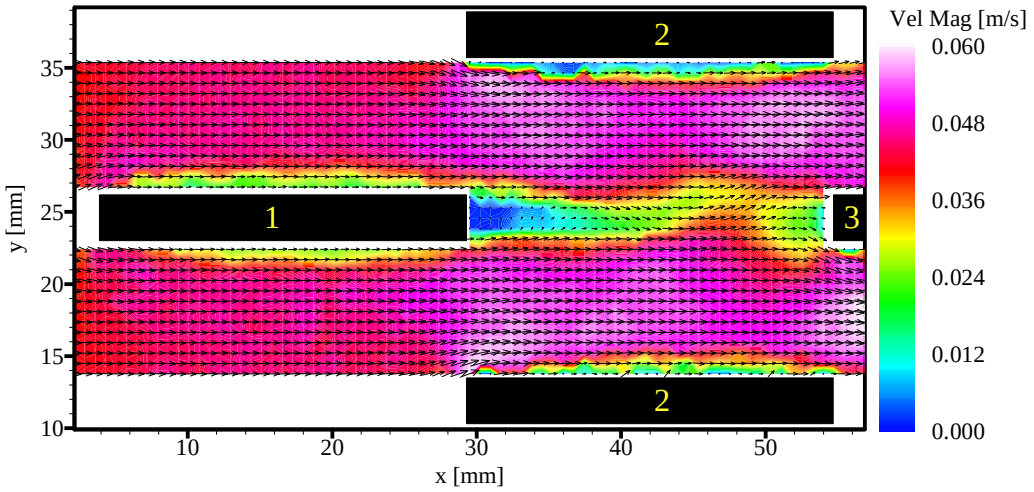

(a)

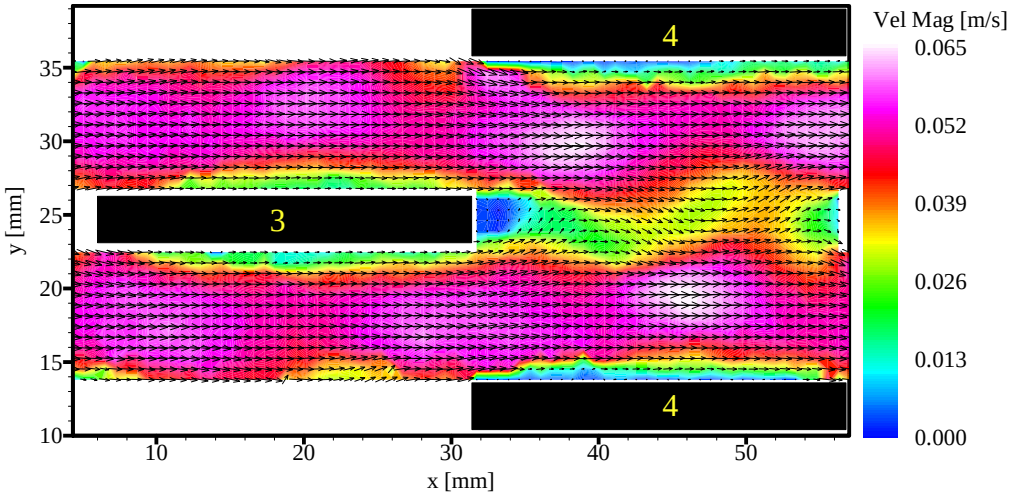

(b)

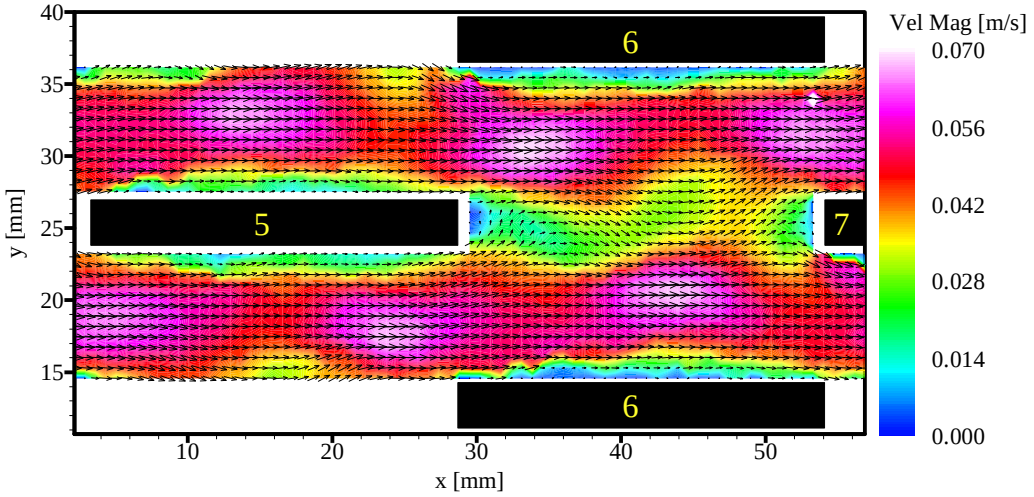

(c)

Figure 4.25 – Instantaneous velocity for baseline array at Re = 1750: (a) Rows 1 and 2; (b) Rows 3 and 4; (c) Rows 5 and 6

Similar flow behavior is obtained for Re = 2450 (Figure 4.26) and Re = 3120 (Figure 4.27), except that the instability in the wake of row 1 is much stronger, and high-velocity freestream fluid is entrained into the wake region right ahead of the leading edge of row 3. This enhanced flow mixing greatly improves the heat transfer performance for row 3 and all downstream rows, which will be validated by the naphthalene sublimation results in Chapter 5.

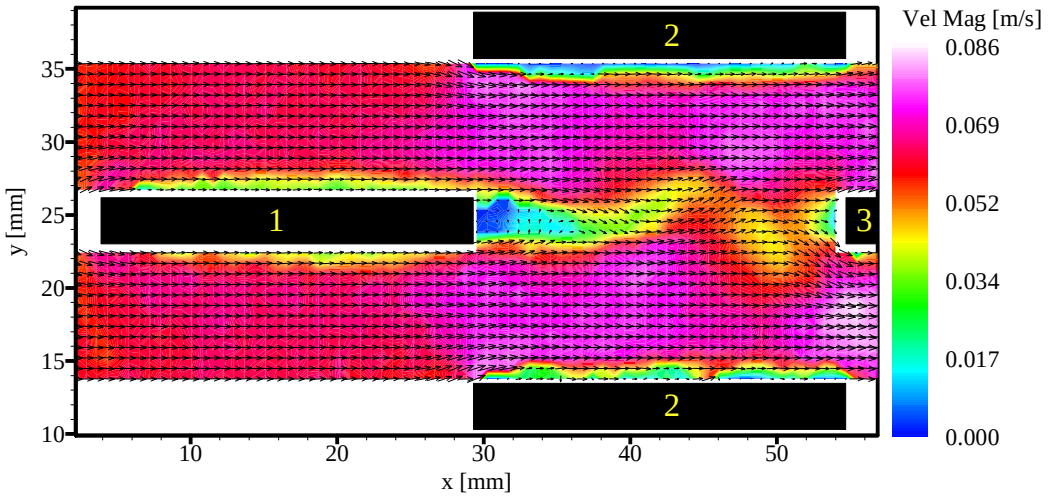

Figure 4.26 – Instantaneous velocity for baseline array at Re = 2450, Rows 1 and 2

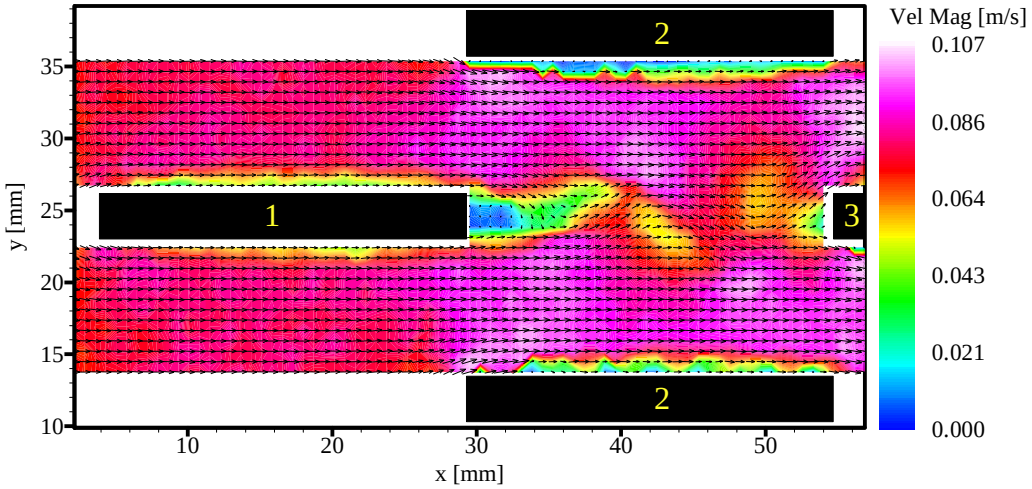

Figure 4.27 – Instantaneous velocity for baseline array at Re = 3120, Rows 1 and 2

The time-averaged velocity field results for row 1 and row 2 are presented in Figure 4.28 to illustrate the time-averaged behavior of the row 1 wake region at Reynolds numbers of 1750, 2450, and 3120. For Re = 1750 (Figure 4.28 (a)), the low-velocity fluid (shown in Figure 4.28 as green and yellow colors) in the row 1 wake region extends all the way to the leading edge of row 3. For Re = 2450 (Figure 4.28 (b)), the low-velocity fluid is limited to only around half of the length of row 2, and high-velocity flow impinges on the leading edge of row 3. The impingement of high-velocity flow on row 3 reduces the negative wake effect of row 1 on downstream fins and contributes to the enhancement of heat transfer performance. For Re = 3120 (Figure 4.28 (c)), the low-velocity fluid is limited to an even smaller area in the wake region of row 1, and higher heat transfer enhancement is expected.

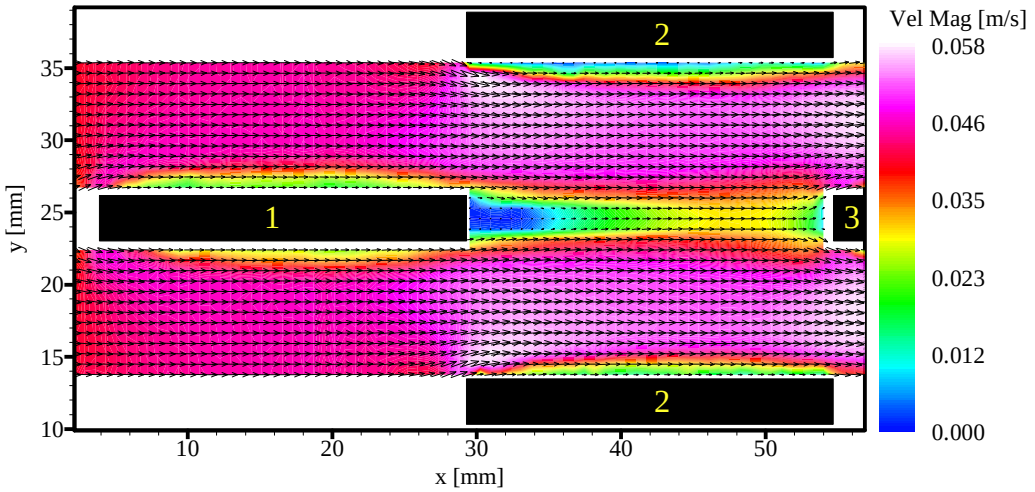

(a)

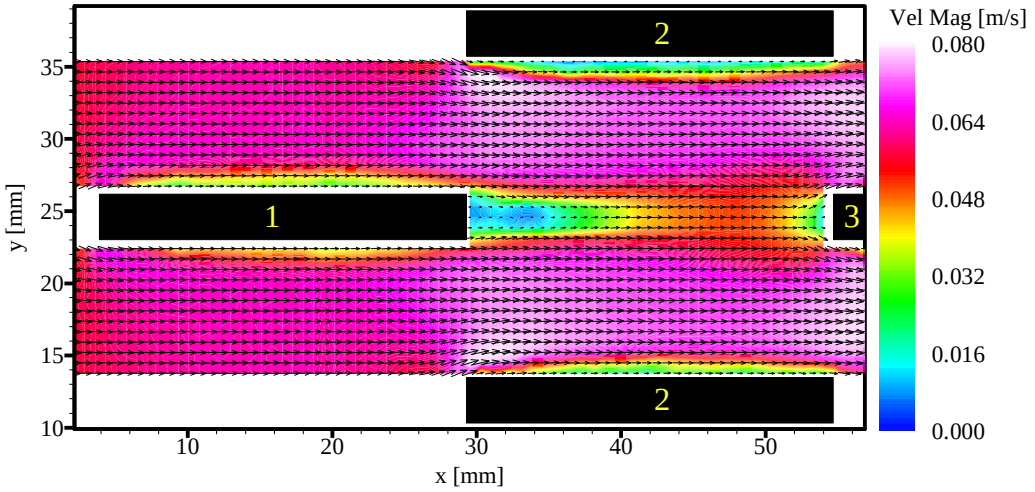

(b)

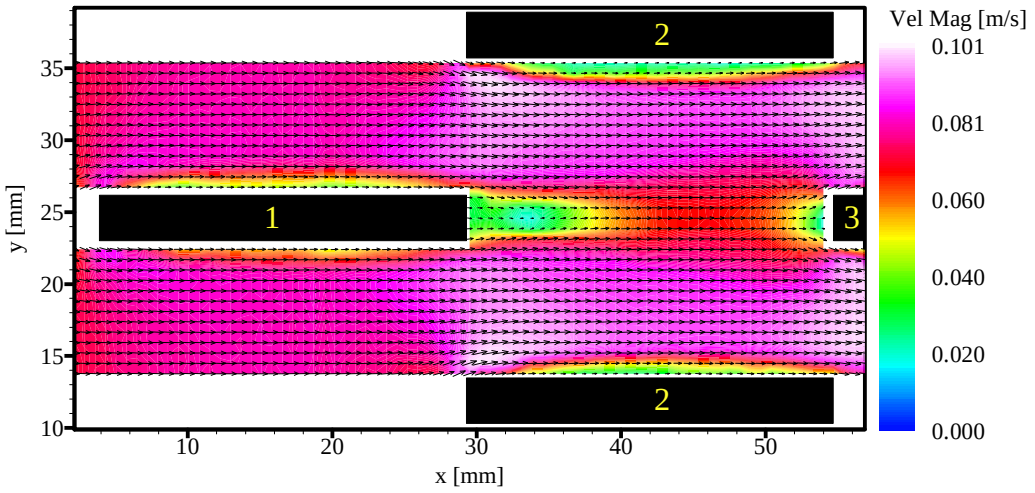

(c)

Figure 4.28 – Time-averaged velocity for baseline array at Rows 1 and 2: (a) Re = 1750; (b) Re = 2450; (c) Re = 3120

Some vorticity field results for the baseline array are presented in Figures 4.29 – 4.34. In these vorticity field plots, the maximum magnitude of the spanwise vorticity is found to increase with increasing Reynolds number. The yellow color indicates low vorticity close to zero in magnitude, while red and green colors indicate high vorticity, but in opposite directions. The high-vorticity region close to the fin surfaces usually correlates well with the shape of the boundary layer. A laminar vorticity field is shown in Figure 4.29 for rows 7 and 8 at Re = 850. Figure 4.30 shows the vorticity field for rows 7 and 8 at Re = 1280. The high-vorticity region near the surfaces of rows 7 and 8 (red and green colors) has a less regular shape than the laminar case at Re = 850. This irregular shape of the boundary layers is an indication of spanwise vortex shedding. The waviness in the wake of row 7 is also reflected in the PIV vorticity field. At Re = 1330, the irregular shape of the boundary layers first occurs at Row 5 (Figure 4.31), indicating the presence of spanwise vortex shedding. As Re is increased to 1750, the boundary layer shape shows irregularities at row 3 (Figure 4.32) and downstream. The vorticity field of row 1 shows a thin boundary layer with smaller scale irregularities than for row 3 (Figure 4.33), indicating the presence of small-scale shear layer instability. Similar results are observed for Re = 2450 and Re = 3120 (Figure 4.34).

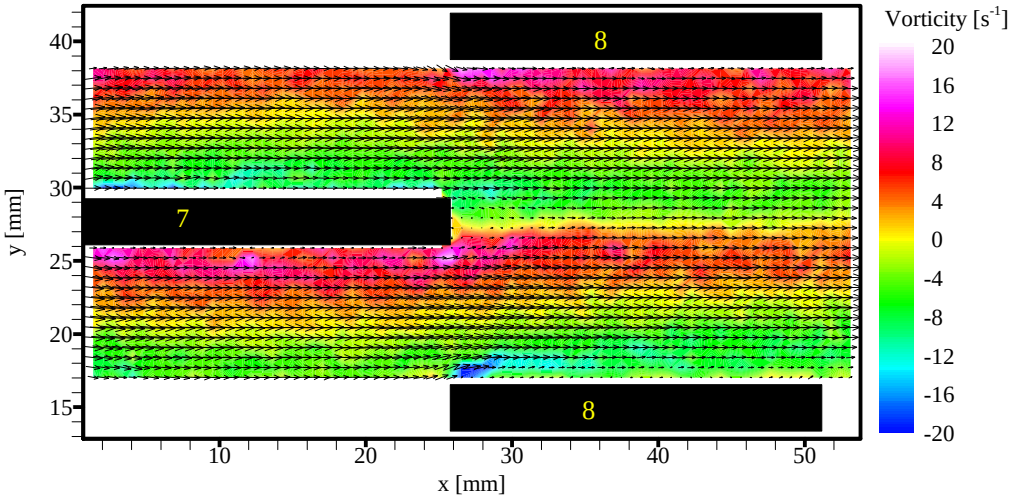

Figure 4.29 – Instantaneous vorticity for baseline array at Re=850, Rows 7 and 8

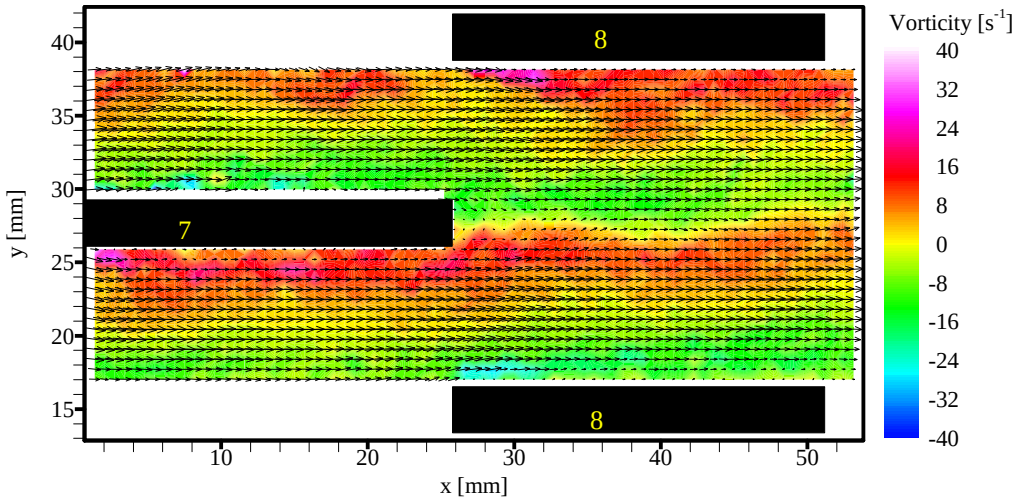

Figure 4.30 – Instantaneous vorticity for baseline array at Re=1280, Rows 7 and 8

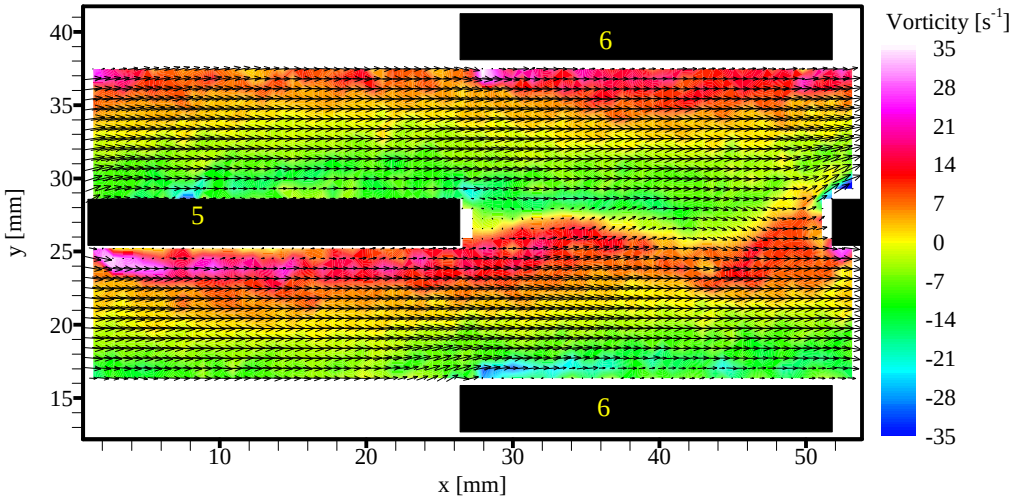

Figure 4.31 – Instantaneous vorticity for baseline array at Re=1330, Rows 5 and 6

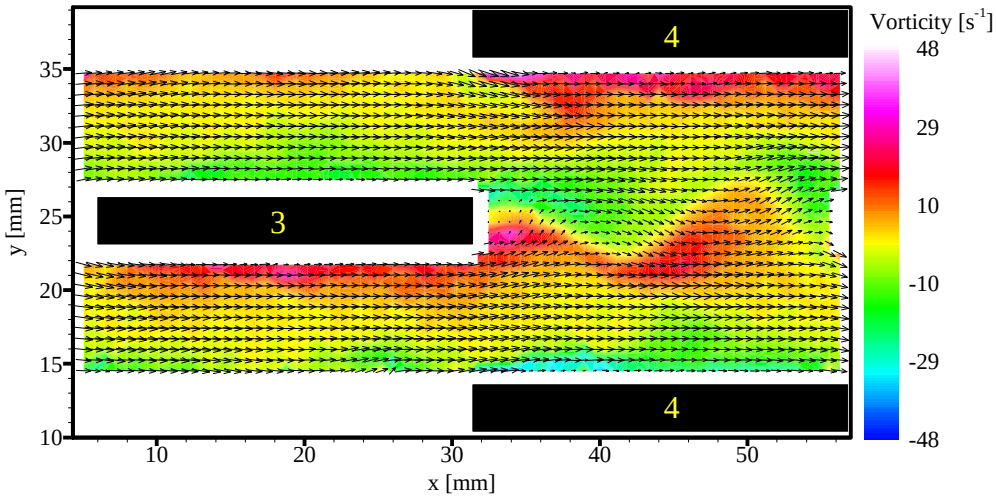

Figure 4.32 – Instantaneous vorticity for baseline array at Re=1750, Rows 3 and 4

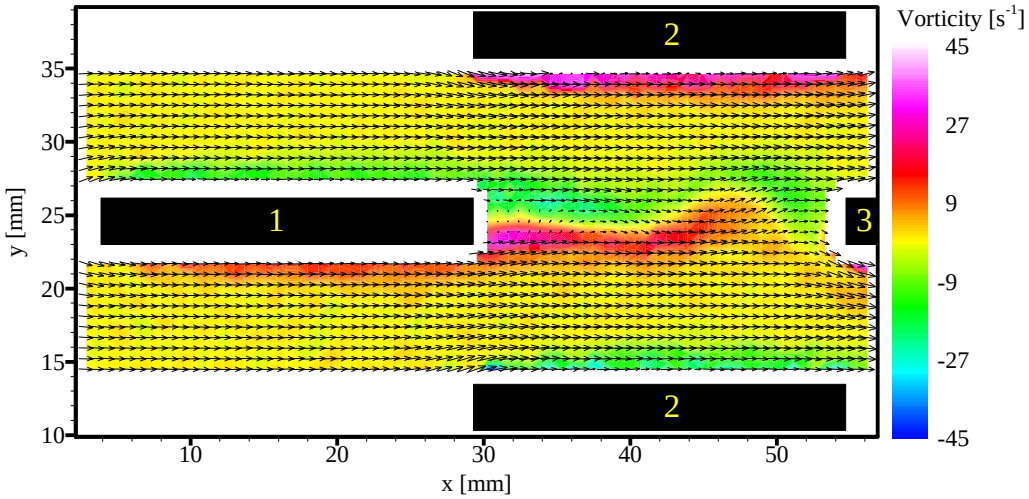

Figure 4.33 – Instantaneous vorticity for baseline array at Re=1750, Rows 1 and 2

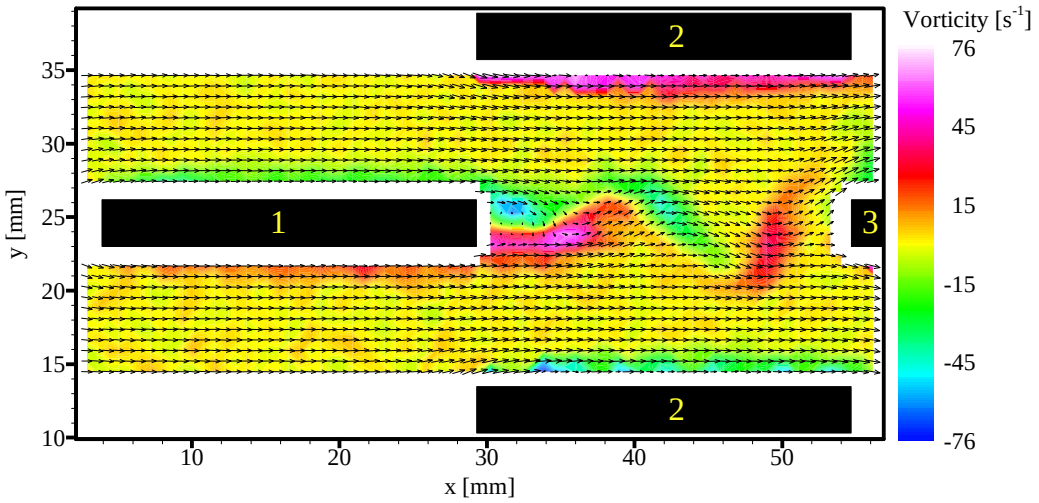

Figure 4.34 – Instantaneous vorticity for baseline array at Re=3120, Rows 1 and 2

Smotrys *et al*. (2001) obtained end-view velocity and vorticity data for the baseline array. The results demonstrate extremely small V-W velocity magnitudes and streamwise vorticity magnitudes for the baseline array, as compared to those for the 2VG-enhanced array. Therefore, no end-view results for the baseline array were obtained in this research.

4.2.2 4VG-Enhanced Array

For the 4VG-enhanced array, the PIV results will be presented in two parts: the side-view results reflecting the spanwise vortex shedding behavior, and the end-view results reflecting the behavior of the streamwise vortices.

4.2.2.1 Side-View Velocity and Vorticity Field Behavior

PIV side-view velocity field results for the 4VG-enhanced array are provided in Figures 4.35 – 4.43.

The side-view velocity field for Re = 850 is shown in Figure 4.35, and the corresponding vorticity field in Figure 4.36. The velocity field results reveal a laminar flow throughout the array, which is similar to the baseline array at Re = 850 (described in Section 4.2.1). However, there are some differences between the 4VG-enhanced array and the baseline array, especially for rows 1 and 2. A low-velocity region (blue color) appears above the top surface and below the bottom surface of row 1. The boundary layer for row 1 is much thicker than that of the baseline array, while the boundary layer for row 2 is thinner than that of the baseline array. This demonstrates the impact of the streamwise vortices generated by the delta wings on the leading edge of row 1. Since the flow field is no longer uniform in the spanwise direction, the spanwise location of the laser sheet that illuminates the flow field plays an important role in the results. In this research, the laser sheet plane is directed to pass one of the inner roots of the delta wings (location 2 as shown in Figure 3.1). The side-view results for rows 1 and 2 indicate that the laser sheet plane is in the upwash region of the streamwise vortices for row 1 and the downwash region for row 2. The upwash movement of the fluid increases the boundary layer thickness of row 1, while the downwash movement of the fluid decreases the boundary layer thickness of row 2. The end-view PIV results and the local mass transfer measurements that will be presented later further confirm this.

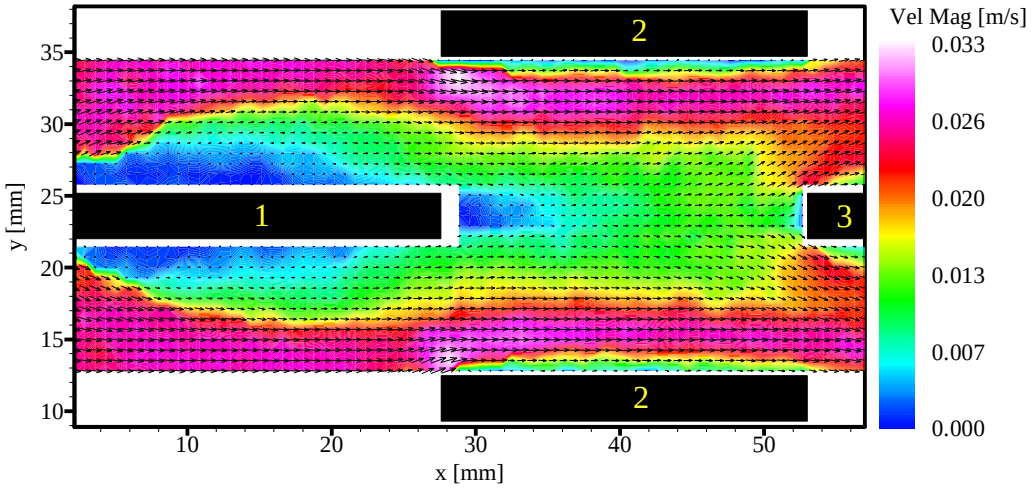
2
1
3
2
y [mm]
x [mm]
Vel Mag [m/s]
0.033
0.026
0.020
0.013
0.007
0.000

(a)

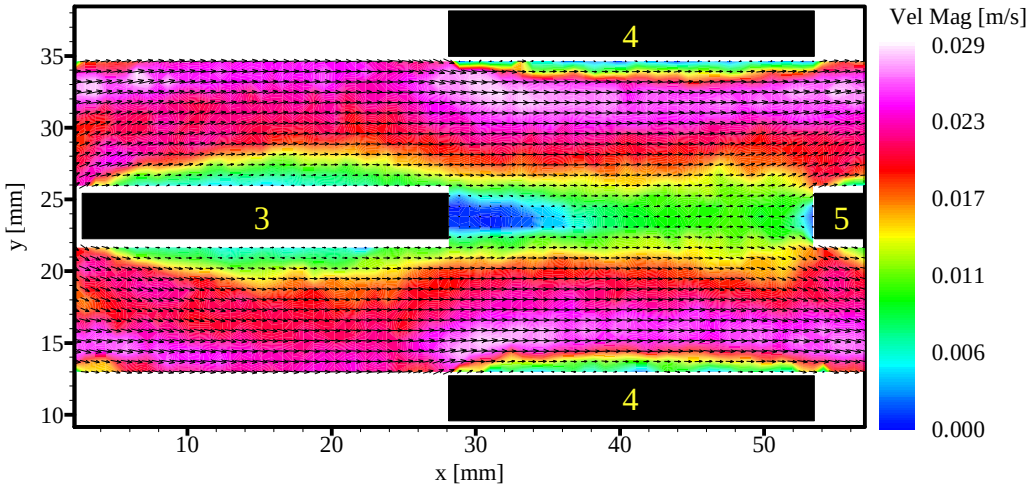
4
3
5
4
y [mm]
x [mm]
Vel Mag [m/s]
0.029
0.023
0.017
0.011
0.006
0.000

(b)

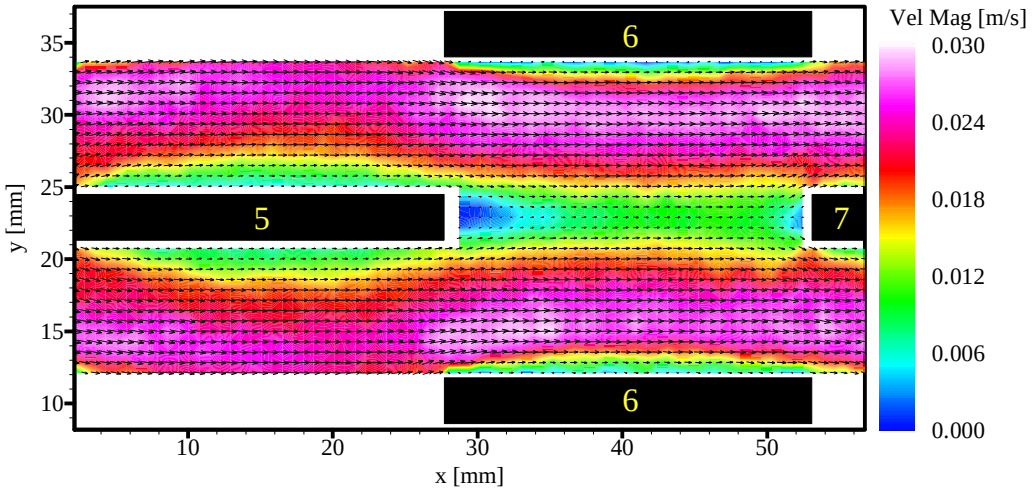
6
5
7
6
y [mm]
x [mm]
Vel Mag [m/s]
0.030
0.024
0.018
0.012
0.006
0.000

(c)

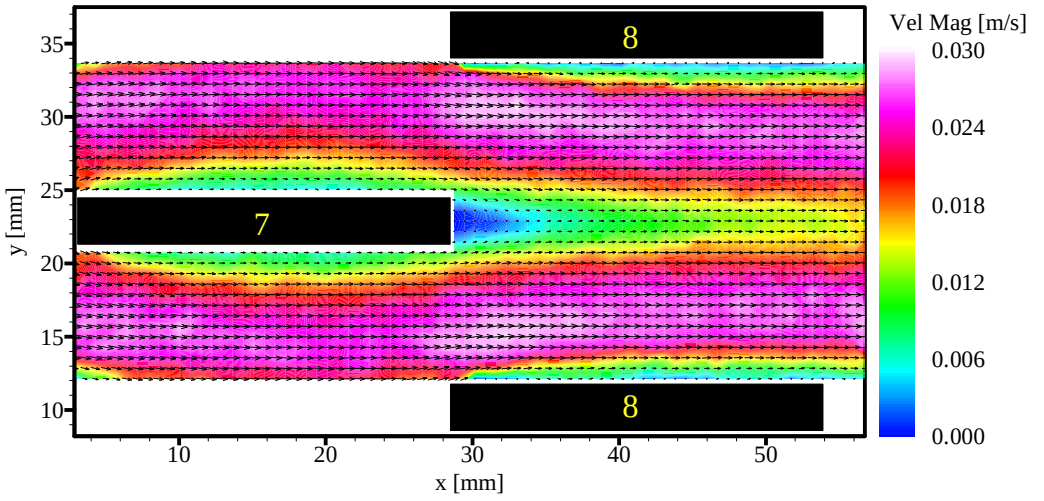

(d)

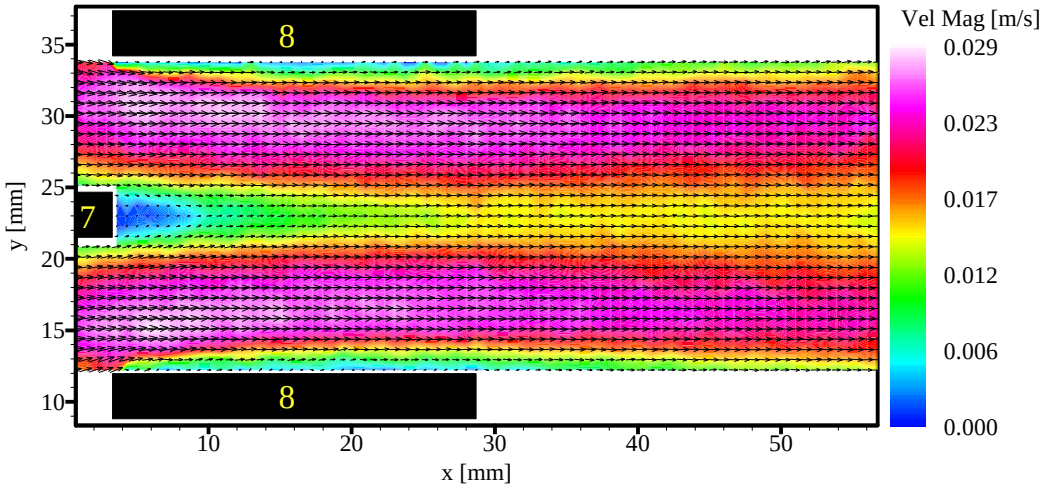

(e)

Figure 4.35 – Instantaneous velocity for 4VG-enhanced array at Re = 850: (a) Rows 1 and 2; (b) Rows 3 and 4; (c) Rows 5 and 6; (d) Rows 7 and 8; (e) Row 8 and downstream

The presence of streamwise vortices is also reflected by the vorticity field results, as shown in Figure 4.36. Two high vorticity streaks (red and green color) originate from the leading edge of row 1 and move away from the top and bottom surfaces (Figure 4.36 (a)), due to the instabilities caused by the streamwise vortices. The high vorticity streaks become weaker and less coherent when moving through the downstream rows (Figures 4.36 (b)-(d)).

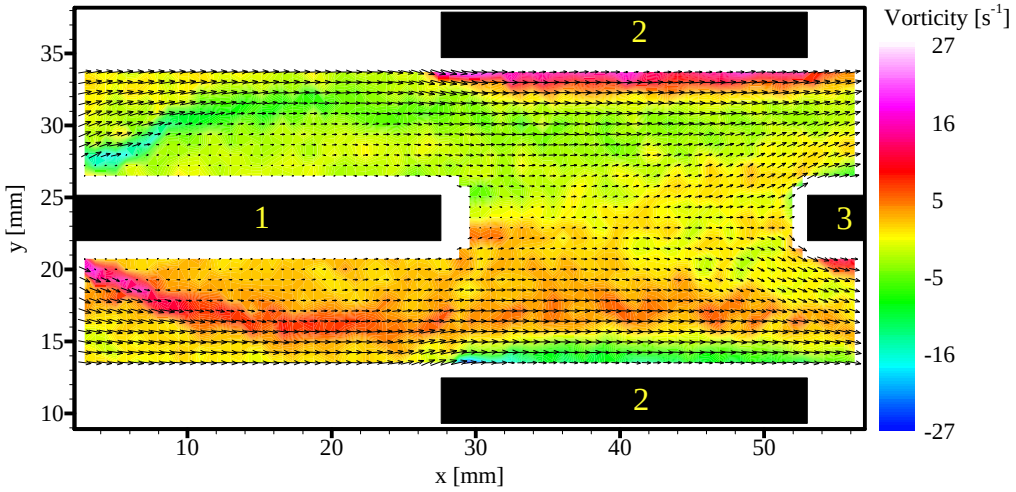
2
1
3
2
y [mm]
x [mm]
Vorticity [s-1]
27
16
5
-5
-16
-27

(a)

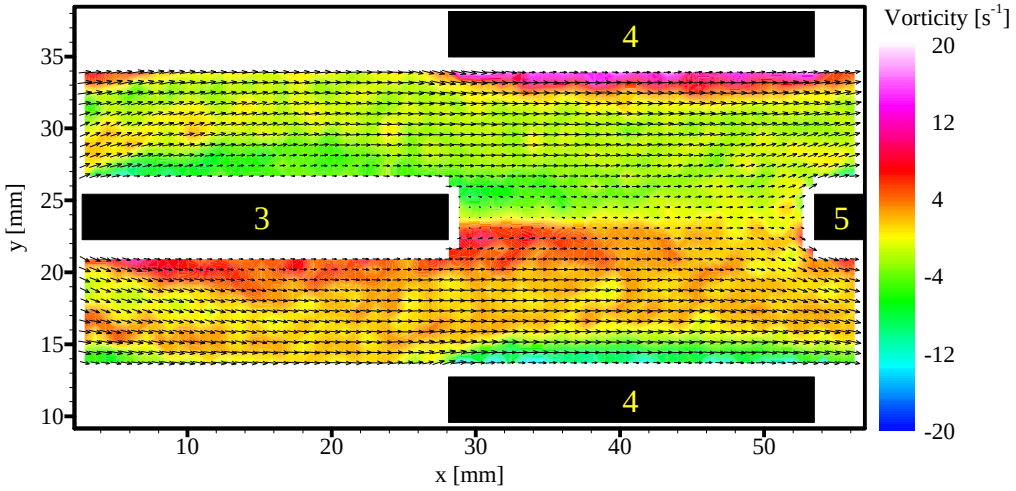
4
3
5
4
y [mm]
x [mm]
Vorticity [s-1]
20
12
4
-4
-12
-20

(b)

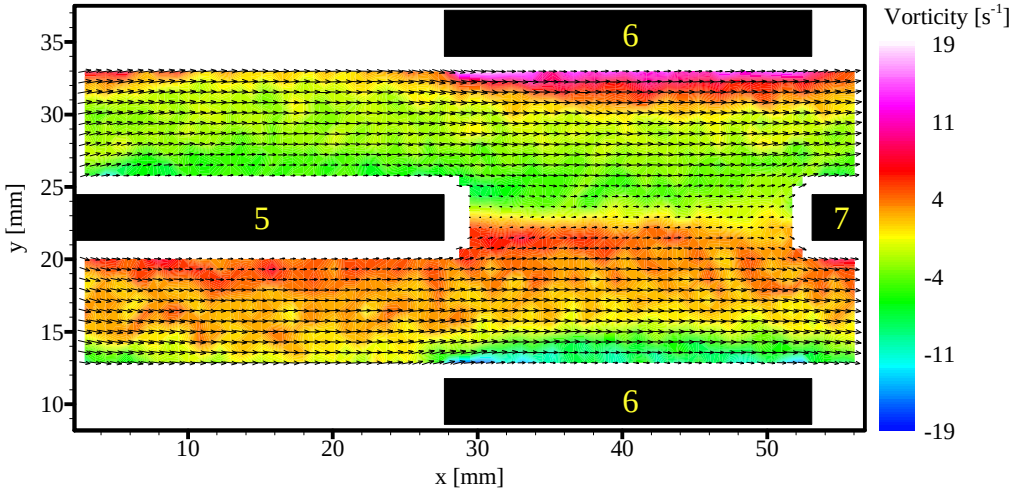
6
5
7
6
y [mm]
x [mm]
Vorticity [s-1]
19
11
4
-4
-11
-19

(c)

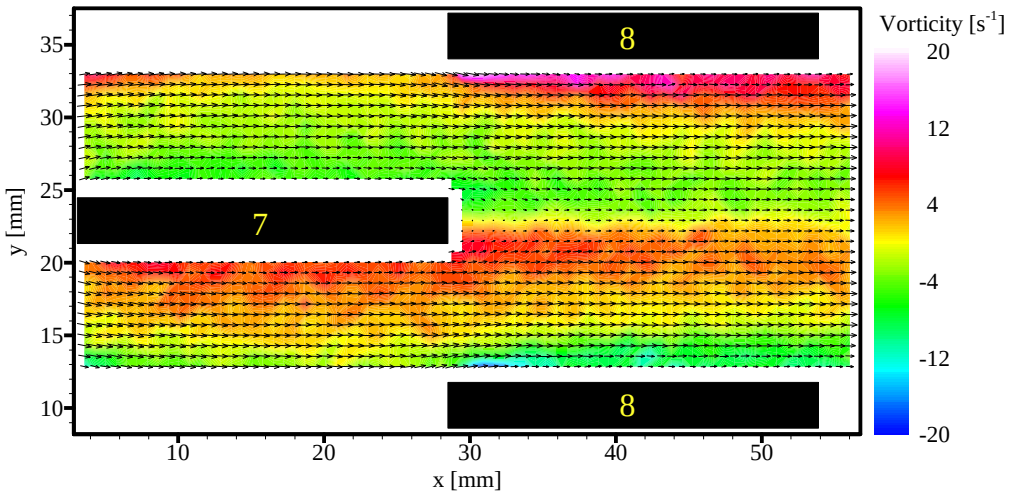

(d)

Figure 4.36 – Instantaneous vorticity for 4VG-enhanced array at Re = 850: (a) Rows 1 and 2; (b) Rows 3 and 4; (c) Rows 5 and 6; (d) Rows 7 and 8

As Re is increased to 1030, the flow instability starts to develop in the wake of the array (Figure 4.37). A similar flow instability is observed at Re = 1520 (Figure 4.38), except that the strength of the instability becomes greater. The flow at the upstream rows is still laminar at Re = 1520. Compared to the baseline array, for which instability is observed in the wake of row 3 and spanwise vortex shedding at row 5 and downstream at Re = 1330, the 4VG-enhanced array inhibits the development of large scale instability (such as spanwise shedding) inside the array. This occurs through the interaction of the streamwise vortices and the spanwise vortices shedding from the fins. It is noted that the PIV results only reflect the flow behavior in the plane where the laser sheet passes. The flow visualization results show weak spanwise vortex shedding for row 5 at Re = 1520 in the spanwise center plane of the array (location B in Figure 3.1), where the influence of streamwise vortices is small. The weak strength of the spanwise vortex shedding in the spanwise center plane also indicates the damping effect of the streamwise vortices on the spanwise vortex shedding in adjacent regions.

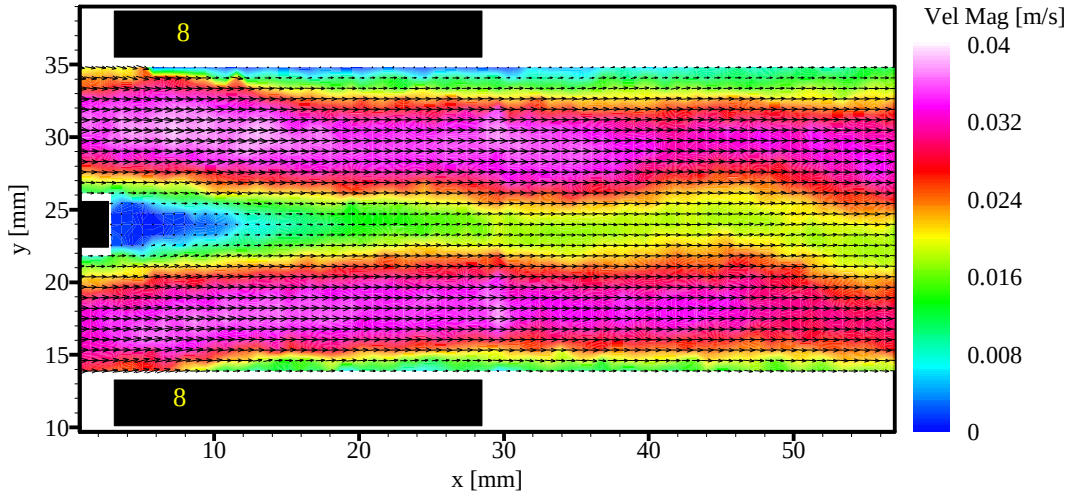

Figure 4.37 – Instantaneous velocity for 4VG-enhanced array at Re = 1030, Row 8 and downstream

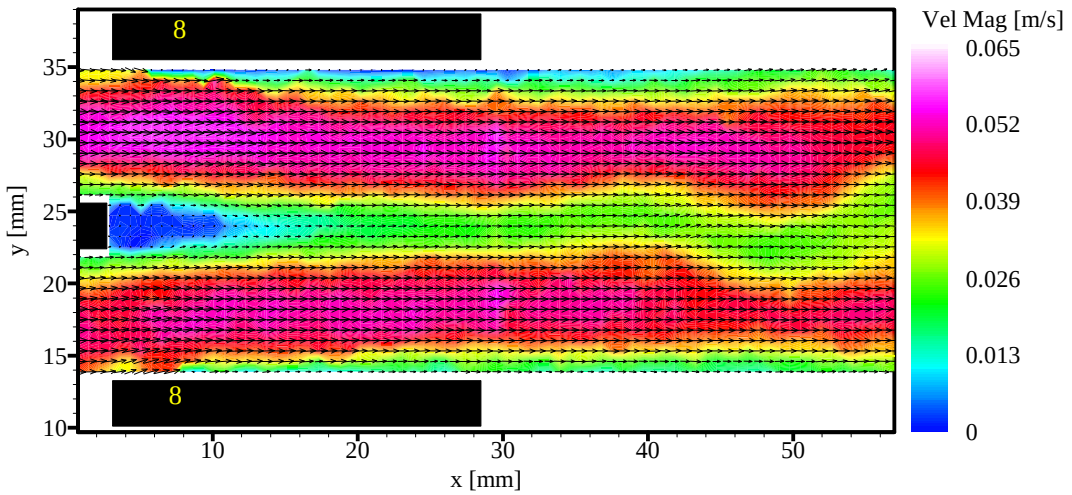

Figure 4.38 – Instantaneous velocity for 4VG-enhanced array at Re = 1520, Row 8 and downstream

The velocity field for Re = 1750 is shown in Figure 4.39. The onset of the instability moves upstream to the wake of row 5, and spanwise vortex shedding is also observed at row 5 and all following rows. Compared to the baseline velocity field, the spanwise vortex shedding is weaker and less coherent for the 4VG-enhanced array at this Reynolds number.

As Re is increased further to 1980 (Figure 4.40), the onset of spanwise vortex shedding moves upstream to row 3. High-velocity fluid pockets are clearly seen in the flow at row 3 and all following rows, as shown in Figures 4.40 (b)-(d). The spanwise vortex shedding is better-defined and more coherent than that at Re = 1750. Compared to Re = 850 (Figure 4.35), rows 1 and 2 (Figure 4.40(a)) show similar behavior, but the upwash fluid movement over row 1 and the downwash fluid movement onto row 2 are much stronger, and the instantaneous velocity field is highly unsteady. The velocity field results at Re = 2450 (Figure 4.41) and Re = 3120 show very similar behavior to that at Re = 1980.

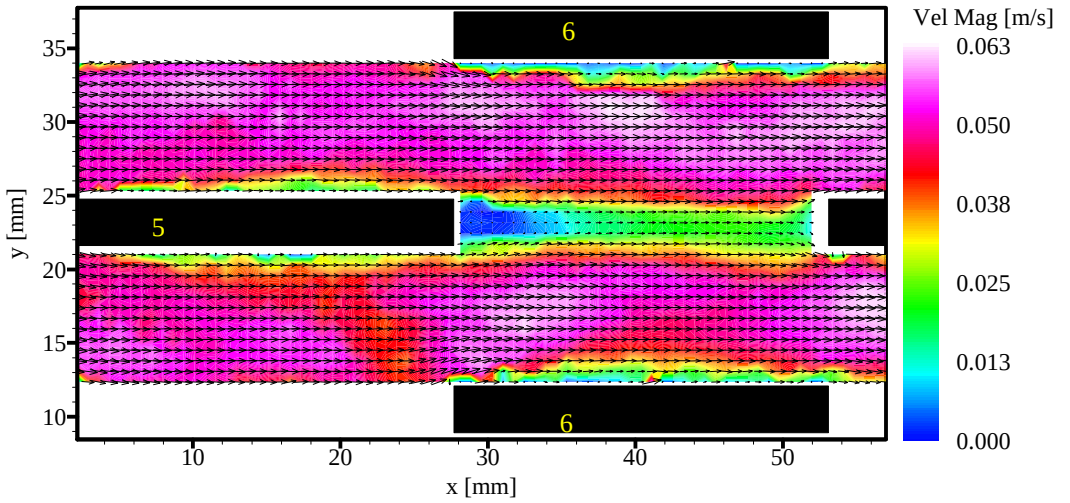

(a)

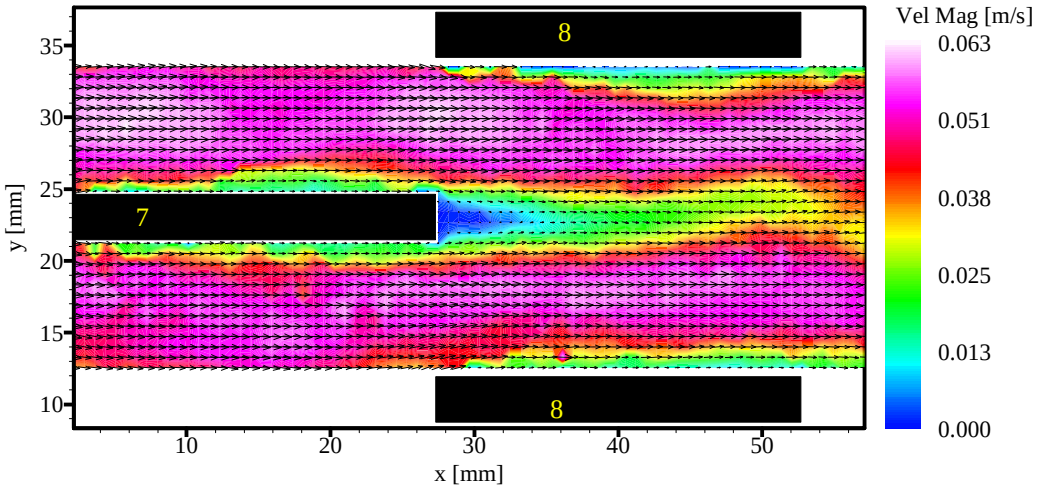

(b)

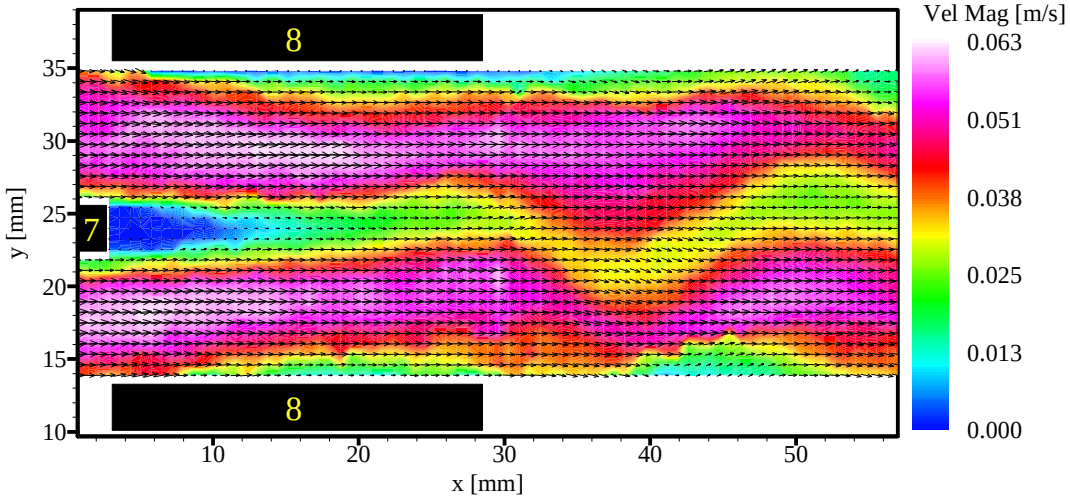

(c)

Figure 4.39 – Instantaneous velocity for 4VG-enhanced array at Re = 1750: (a) Rows 5 and 6; (b) Rows 7 and 8; (c) Row 8 and downstream

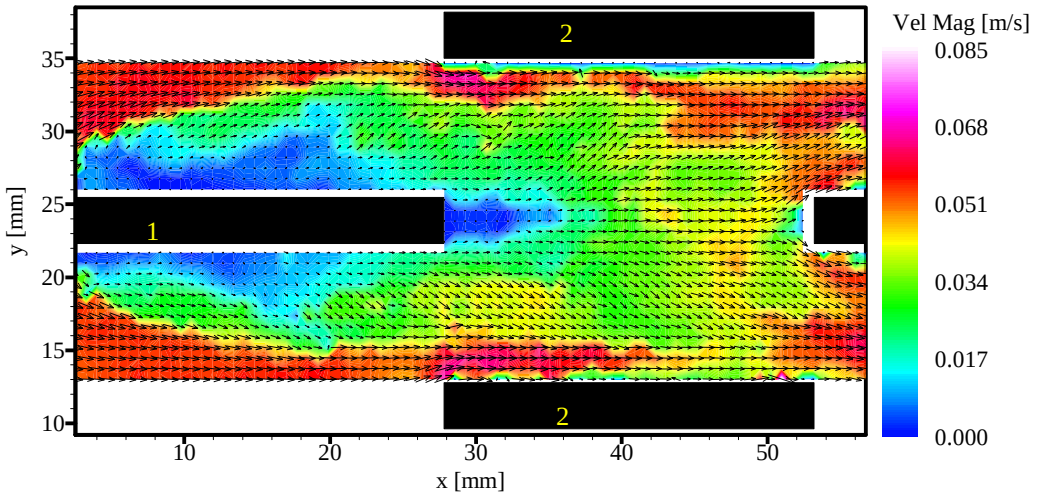
Vel Mag [m/s]
0.085
0.068
0.051
0.034
0.017
0.000
2
1
2
y [mm]
x [mm]
10
15
20
25
30
35
10
20
30
40
50

(a)

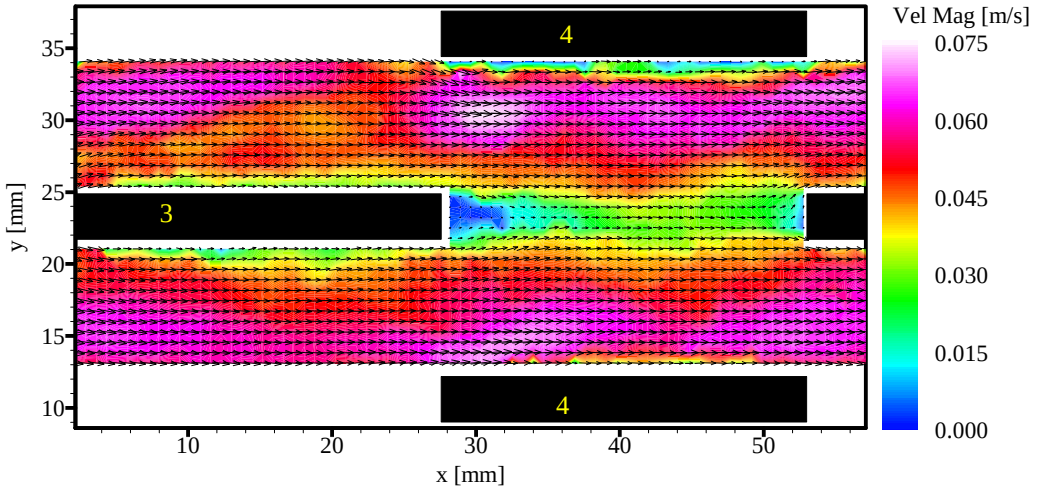
Vel Mag [m/s]
0.075
0.060
0.045
0.030
0.015
0.000
4
3
4
y [mm]
x [mm]
10
15
20
25
30
35
10
20
30
40
50

(b)

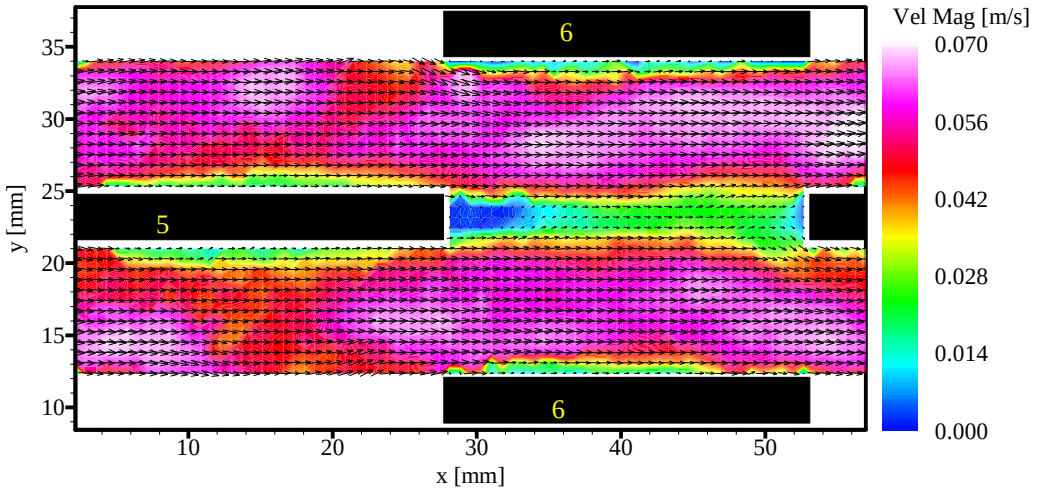
Vel Mag [m/s]
0.070
0.056
0.042
0.028
0.014
0.000
6
5
6
y [mm]
x [mm]
10
15
20
25
30
35
10
20
30
40
50

(c)

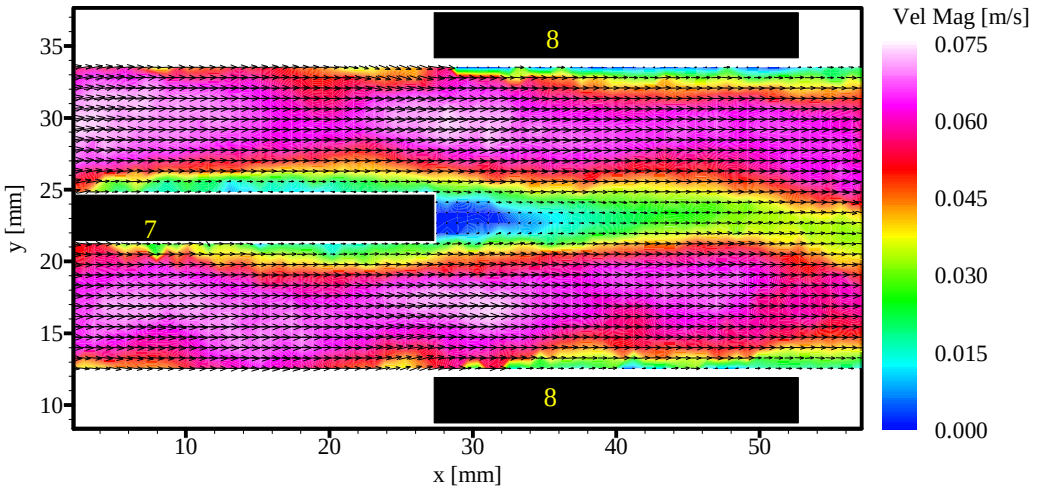

(d)

Figure 4.40 – Instantaneous velocity for 4VG-enhanced array at Re = 1980: (a) Rows 1 and 2; (b) Rows 3 and 4; (c) Rows 5 and 6; (d) Rows 7 and 8

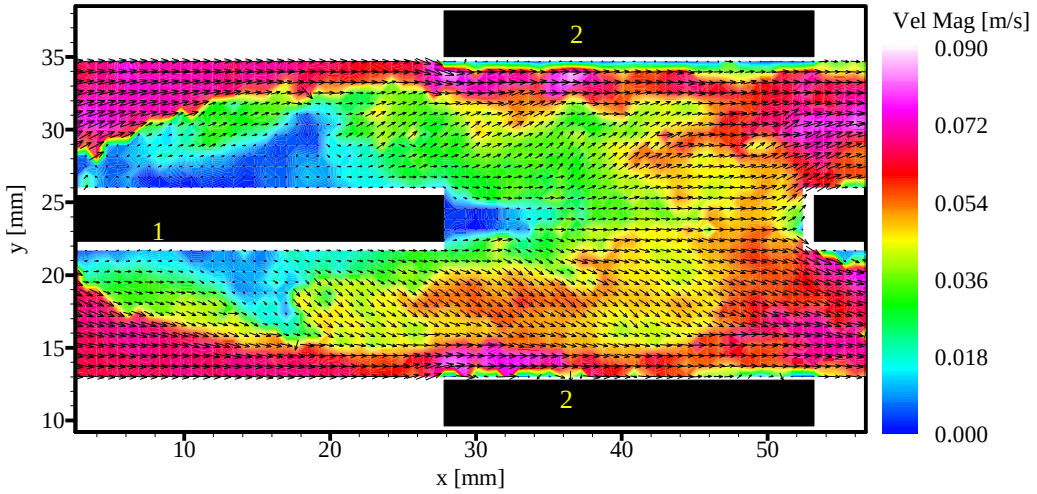

(a)

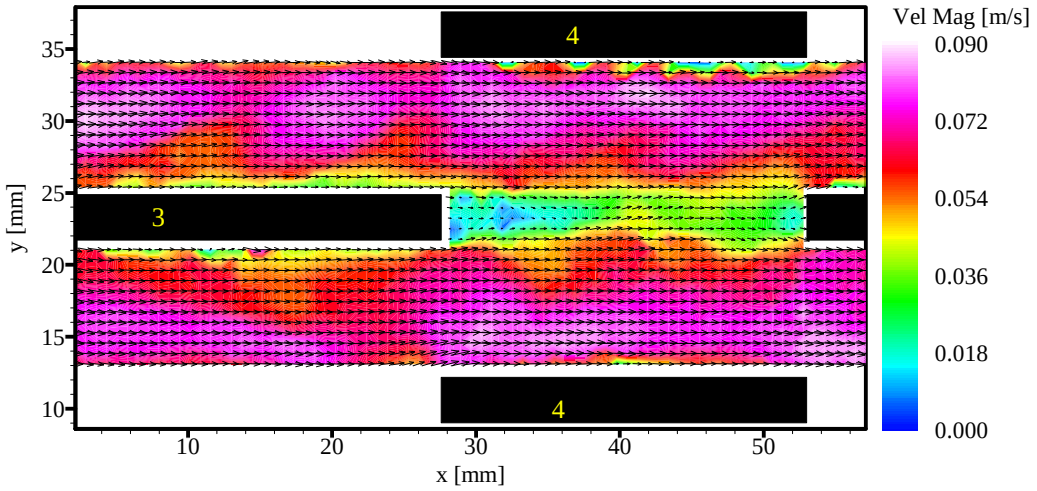

(b)

Figure 4.41 – Instantaneous velocity for 4VG-enhanced array at Re = 2450: (a) Rows 1 and 2; (b) Rows 3 and 4

The time-averaged velocity field for rows 1 and 2 is shown in Figure 4.42 for Re = 2450 and Re = 3120, and the corresponding vorticity field is shown in Figure 4.43. The time-averaged velocity and vorticity fields are similar for both Reynolds numbers. The velocity field results of row 1 show a very thick boundary layer with a low-velocity region (blue color) close to the fin surfaces and an upwash region (green color) caused by the streamwise vortices between the freestream (red color) and the low-velocity region (blue color). Strong vorticity is observed along the borders of the low-velocity region, the upwash region, and the freestream, as shown in Figure 4.43.

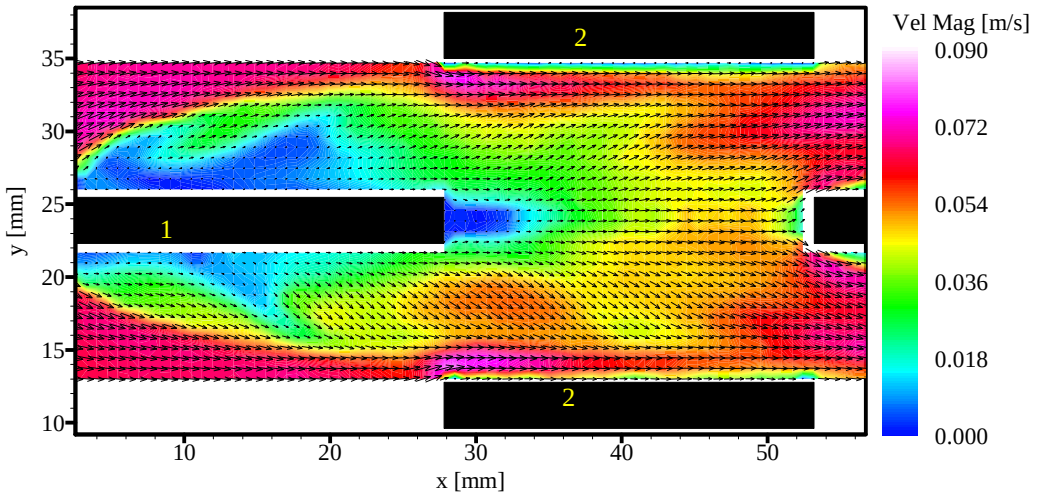

(a)

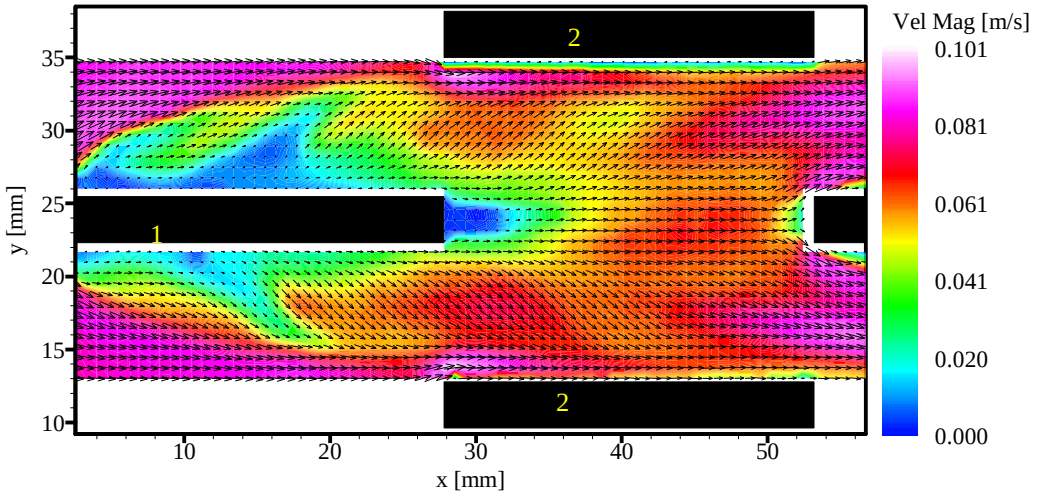

(b)

Figure 4.42 – Time-averaged velocity for 4VG-enhanced array at Rows 1 and 2: (a) Re = 2450; (b) Re = 3120

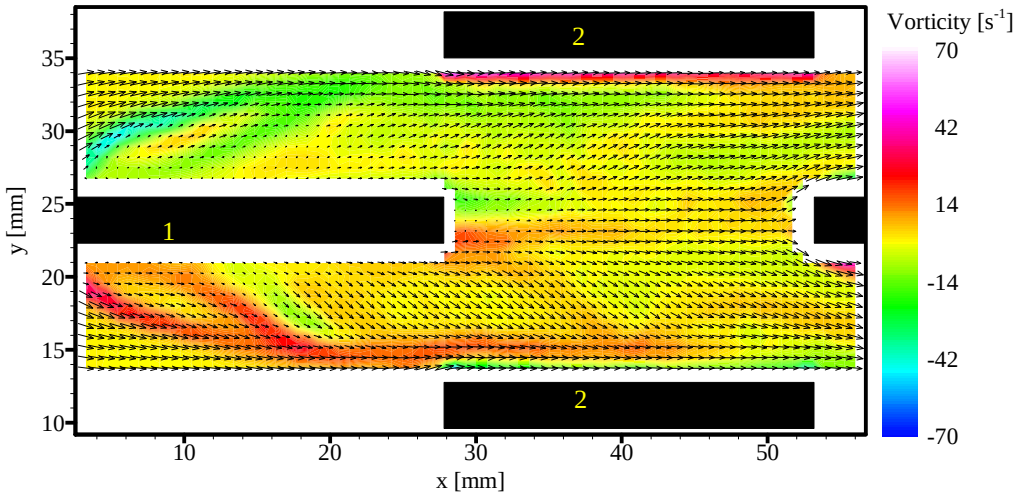

(a)

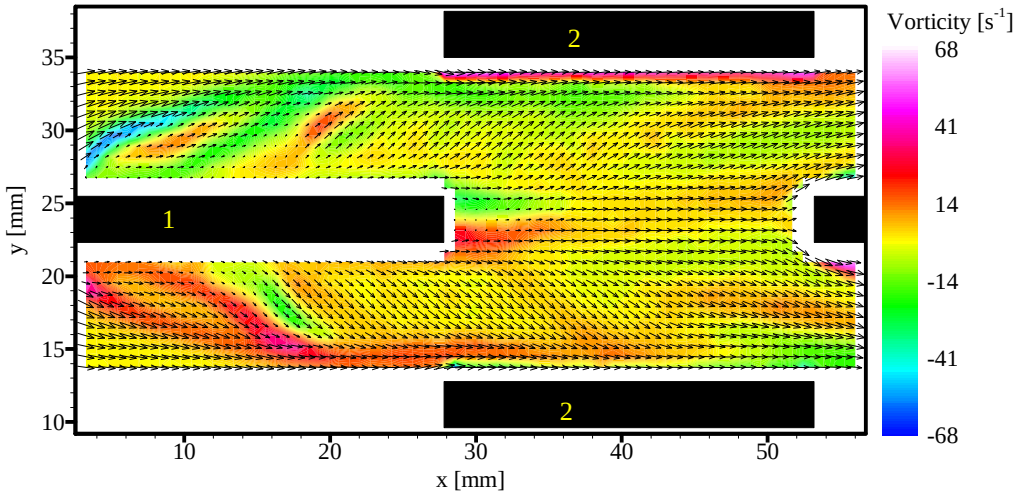

(b)

Figure 4.43 – Time-averaged vorticity for 4VG-enhanced array at Rows 1 and 2: (a) Re = 2450; (b) Re = 3120

4.2.2.2 End-View Velocity and Vorticity Field Behavior

End-view PIV results are necessary to understand the three-dimensional vortical flow field, especially the behavior of the streamwise vortices. These results for the 4VG-enhanced array are discussed in the following.

4.2.2.2.1 Re = 850

The end-view velocity and vorticity results at Re = 850 are shown in Figures 4.44 – 4.51, at different X^* locations. The velocity field for X^*=0.5 (Figure 4.44 (a)) shows counter-rotating vortex pairs behind each delta wing, with clear downwash movement toward the middle fin in the region between the two counter-rotating vortices. For each vortex pair, the vortex cores are close to each other. The vorticity field at X^*=0.5 (Figure 4.44 (b)) clearly reveals the shape, location and strength of the streamwise vortices. The green and red colors outline the shape of the streamwise vortices, while the blue and pink colors indicate the location of the vortex core areas, which possess the maximum vorticity magnitude. Anti-symmetry of the streamwise vorticity is observed across the middle fin (top to bottom) and also across the spanwise center plane between VG tips. Secondary vortices are induced outside the primary vortex pairs, although their size and strength are much smaller than for the primary vortices.

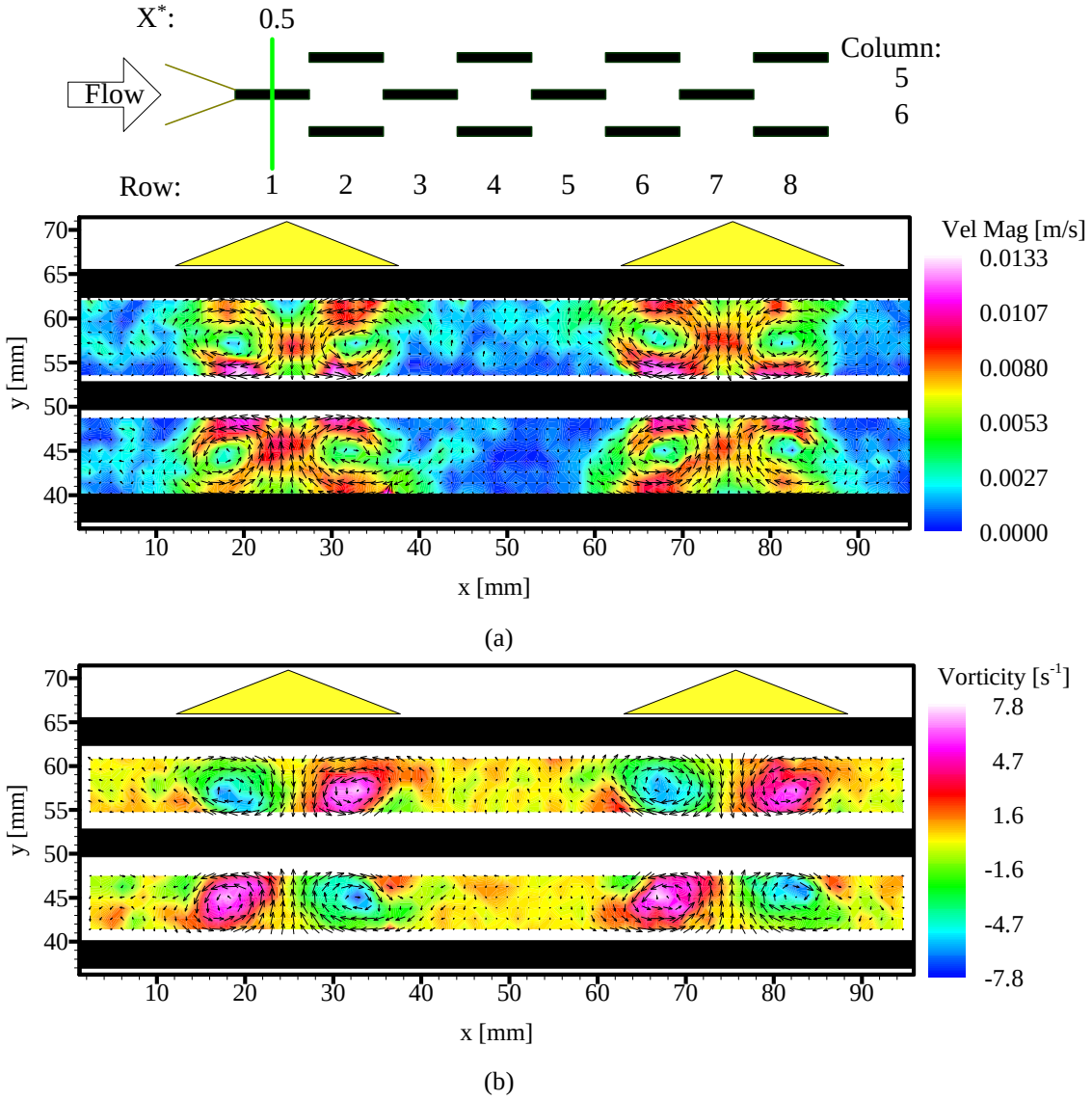

Figure 4.44 – Instantaneous field for 4VG-enhanced array at Re = 850, X^* = 0.5: (a) velocity magnitude; (b) streamwise vorticity

The end-view results for X^*=1.0 (Figure 4.45) also show anti-symmetry across the middle fin and the vertical spanwise center plane between VG tips. However, there are some differences in the velocity field from that at X^*=0.5. The fluid close to the row 2 fin surfaces accelerates in the V-component velocity direction, which changes the vortical shape in the flow field. The acceleration of the V-component velocity is caused by the interaction of the streamwise vortices and the boundary layer restarting at the leading edge of the row 2 fins. The vorticity field results in Figure 4.45 (b) show that the streamwise vortices remain well-defined and quite coherent, while the peak vorticity decreases to about 7.1 s^{-1} from 7.8 s^{-1} at X^*=0.5.

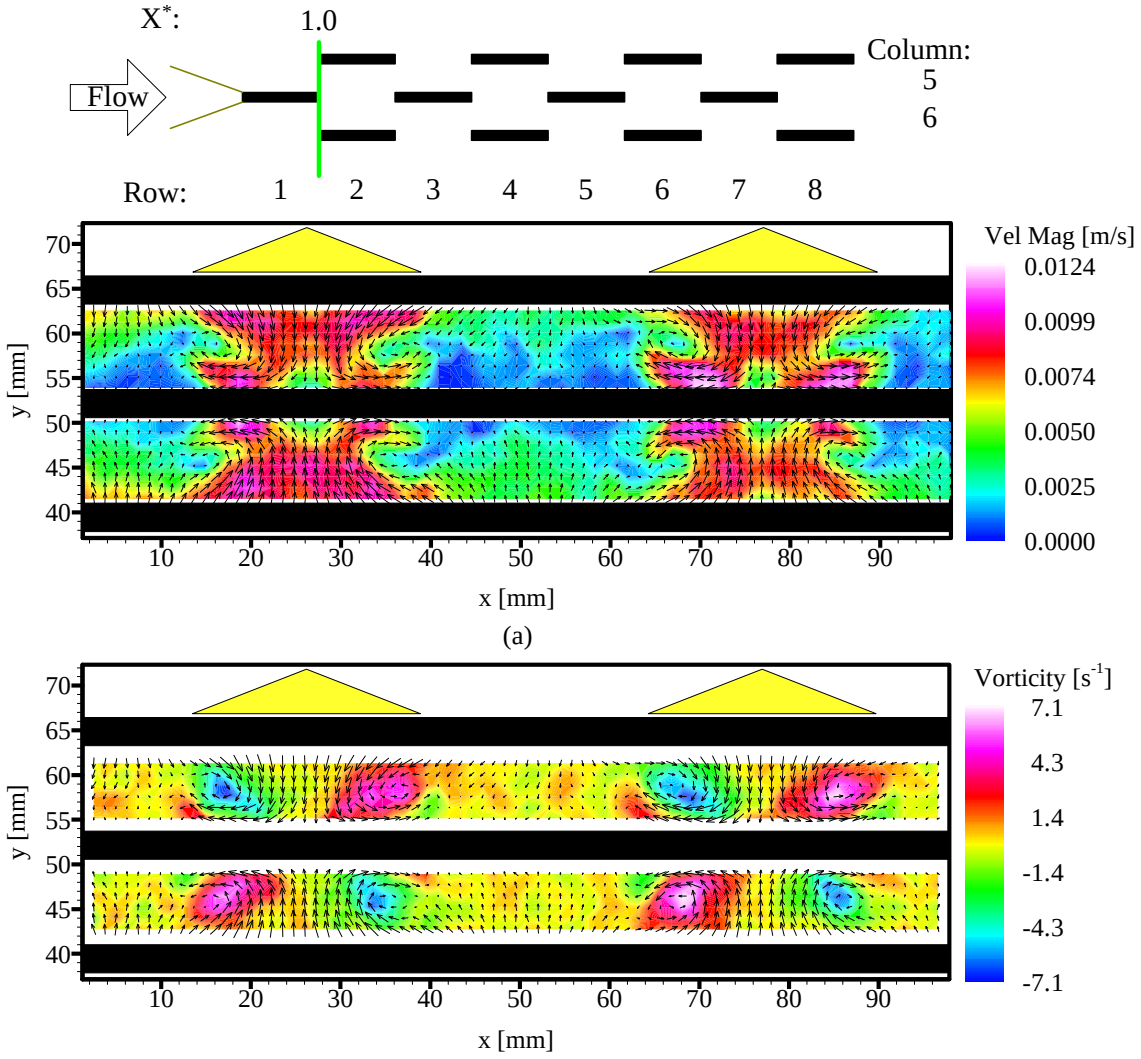

Figure 4.45 – Instantaneous field for 4VG-enhanced array at Re = 850, X^* = 1.0: (a) velocity magnitude; (b) streamwise vorticity

The end-view PIV velocity and vorticity fields at X^*=1.5 (Figure 4.46) show similar streamwise vortex structures as those at X^*=0.5, except that the streamwise vortices in each pair tend to spread away from each other and the maximum vorticity continues to decrease.

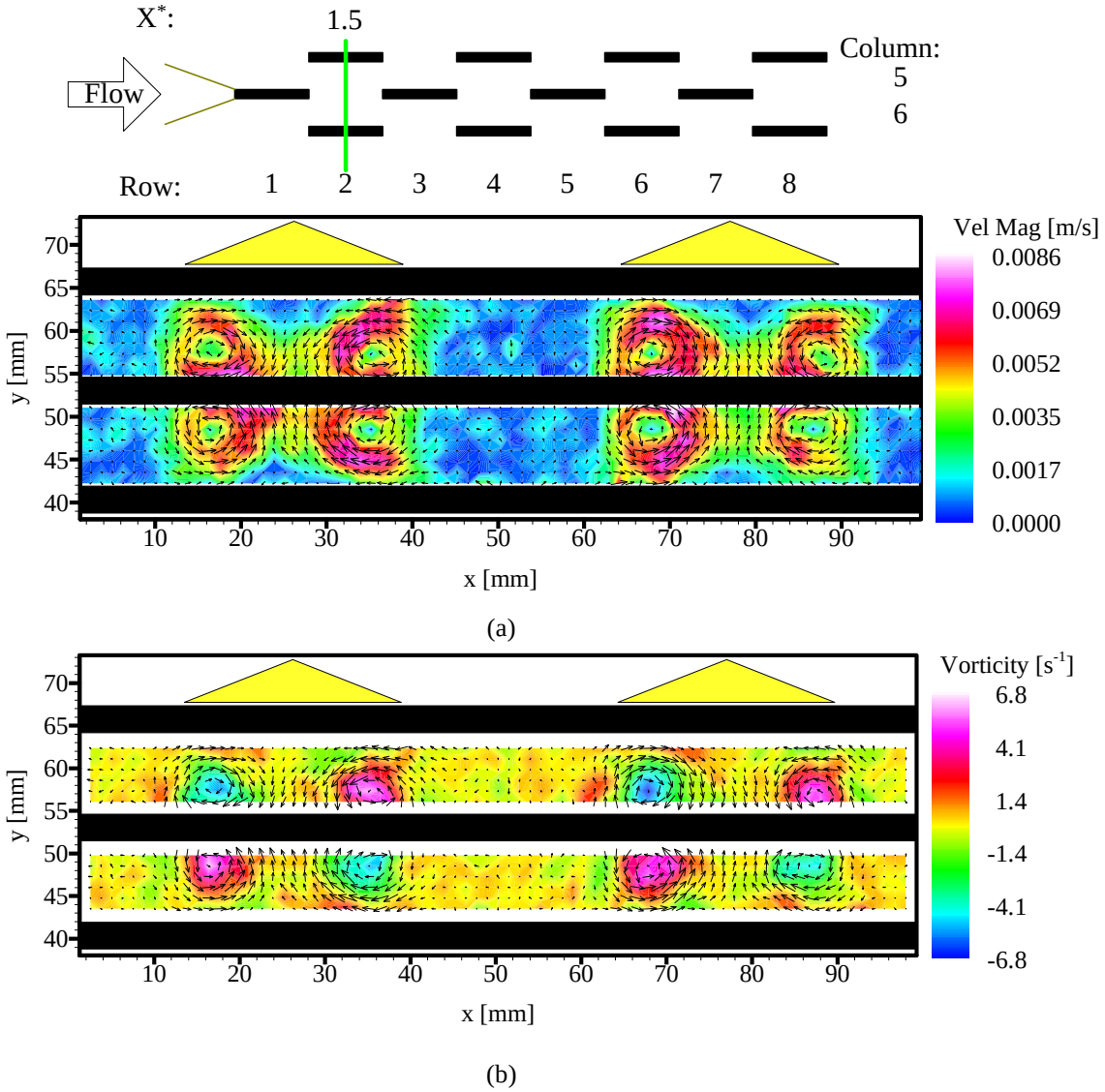

Figure 4.46 – Instantaneous field for 4VG-enhanced array at Re = 850, X^* = 1.5: (a) velocity magnitude; (b) streamwise vorticity

The boundary layer restarts at the leading edge of the middle fin at X^*=2.0 (Figure 4.47). As revealed in the velocity field in Figure 4.47 (a), V-component velocities away from the middle fin are clearly observed. The direction of the V-component velocities is opposite to the downwash velocity component onto the middle fin induced between the two counter-rotating streamwise vortices, which undermines the downwash effect generated by the streamwise vortices.

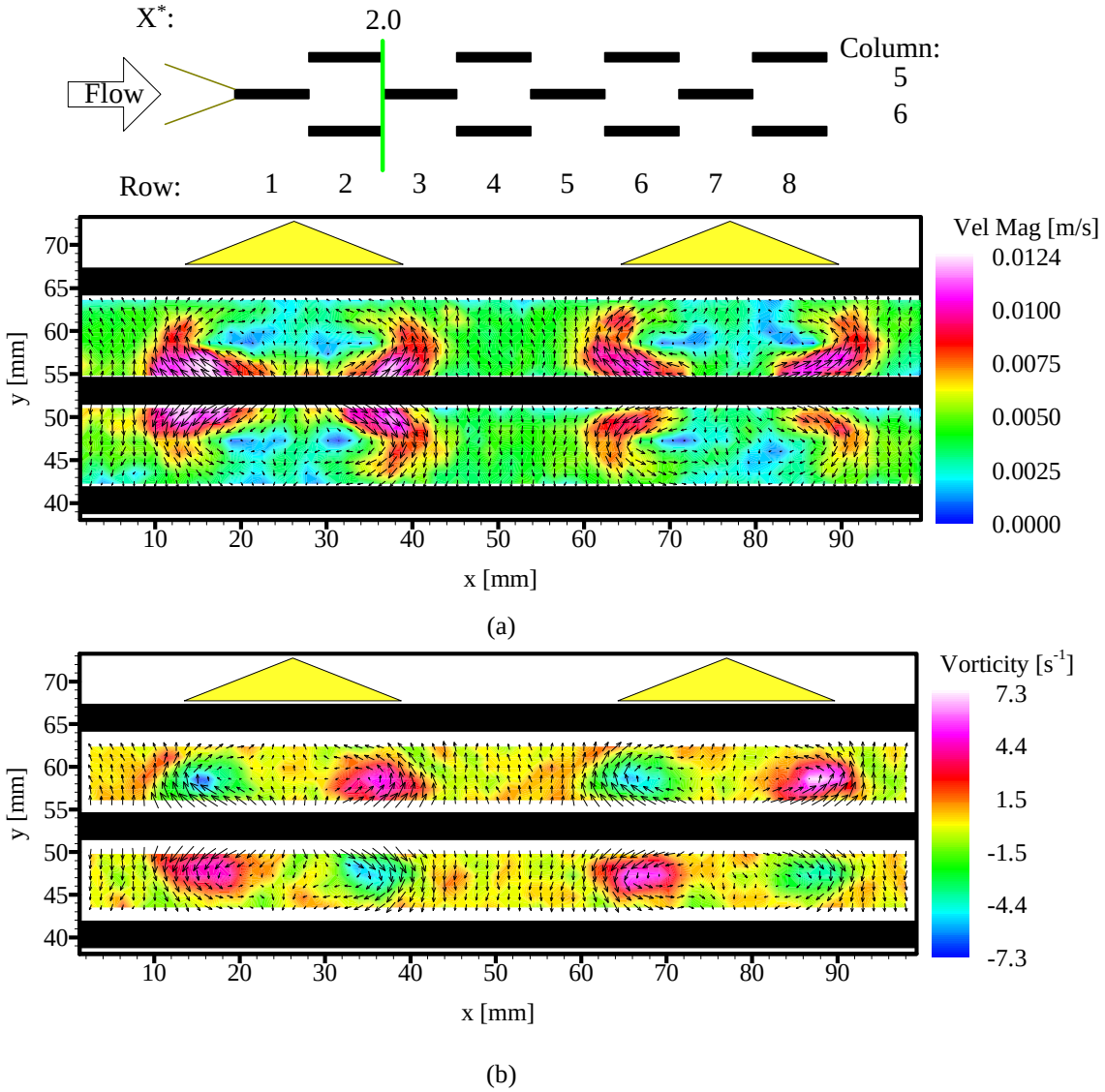

Figure 4.47 – Instantaneous field for 4VG-enhanced array at Re = 850, X^* = 2.0: (a) velocity magnitude; (b) streamwise vorticity

As the streamwise vortices advect downstream further to X^*=2.5 (Figure 4.48), similar streamwise vortex structures as those at X^*=1.5 are observed. The streamwise vortices in each pair are farther away from each other than at X^*=1.5, and the maximum vorticity continues to decrease.

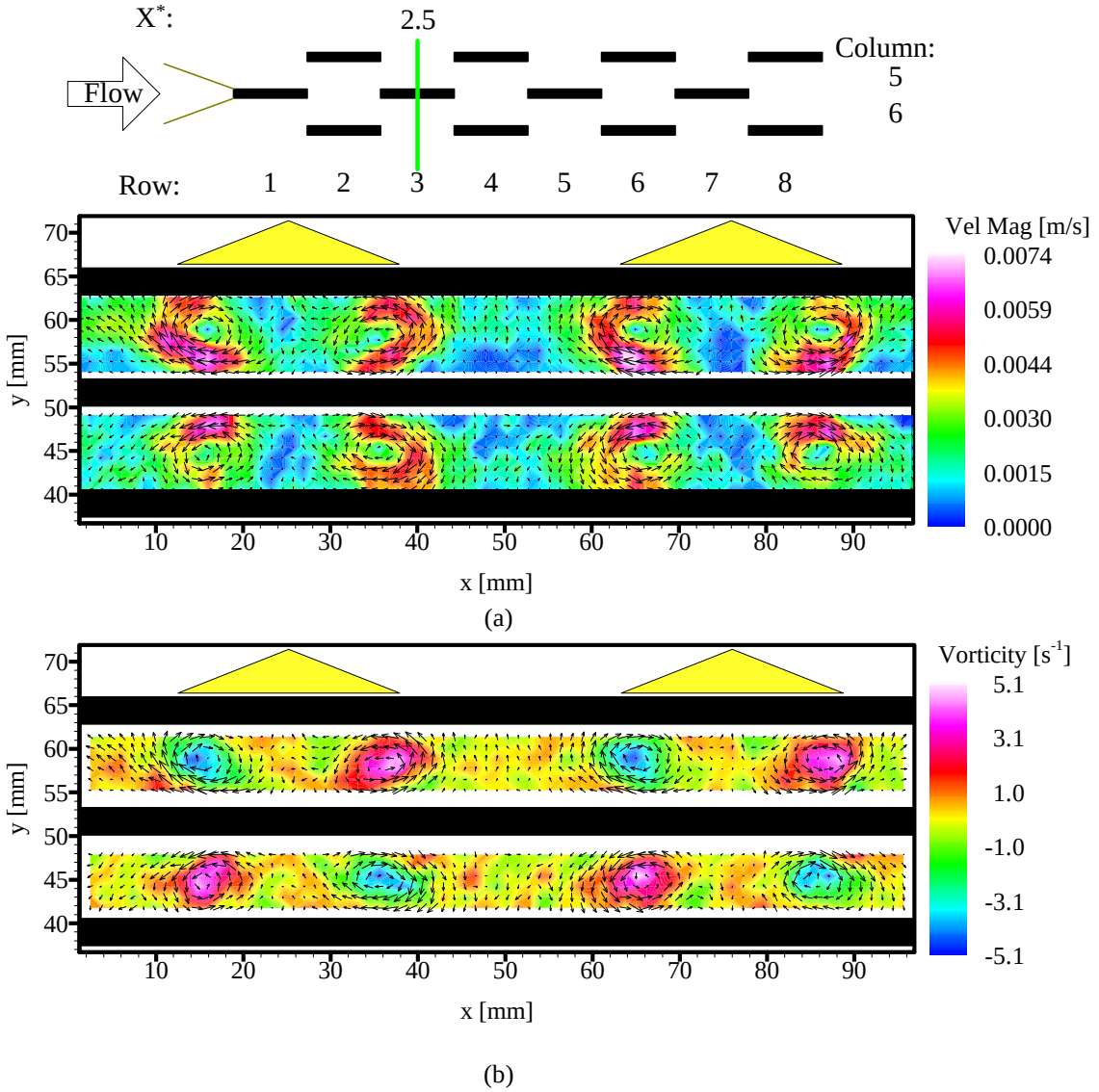

Figure 4.48 – Instantaneous field for 4VG-enhanced array at Re = 850, X^* = 2.5: (a) velocity magnitude; (b) streamwise vorticity

As the flow travels downstream to the second half of the array, the streamwise vortices become weaker, and the streamwise vortices in each pair move farther away from each other. The strong vortical structure generated by the VGs weakens, and more small-scale streamwise vortex structures appear in the end-view vorticity field. The instantaneous end-view velocity and vorticity results at X^*=4.5 (Figures 4.49 (a) and (b)) show similar streamwise vortical behavior as that at X^*=2.5, but with more small-scale structures in the flow field. However, the time-averaged end-view velocity and vorticity results at the same location (Figures 4.49 (c) and (d)) still show well-defined and coherent streamwise vortices.

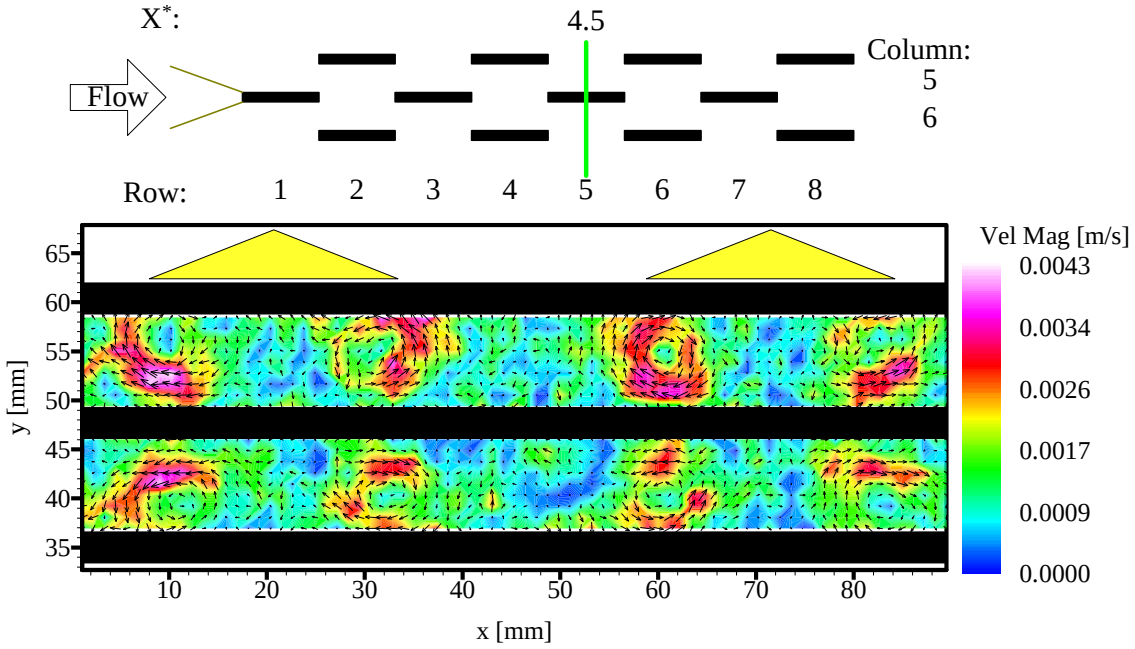
X*:
4.5
Flow
Column:
5
6
Row:
1
2
3
4
5
6
7
8
Vel Mag [m/s]
0.0043
0.0034
0.0026
0.0017
0.0009
0.0000
y [mm]
x [mm]

(a)

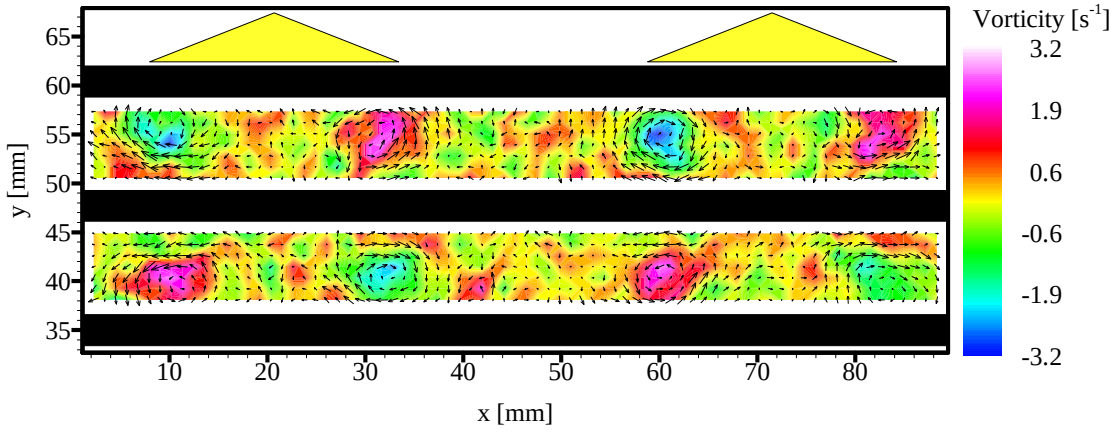
Vorticity [s-1]
3.2
1.9
0.6
-0.6
-1.9
-3.2
y [mm]
x [mm]

(b)

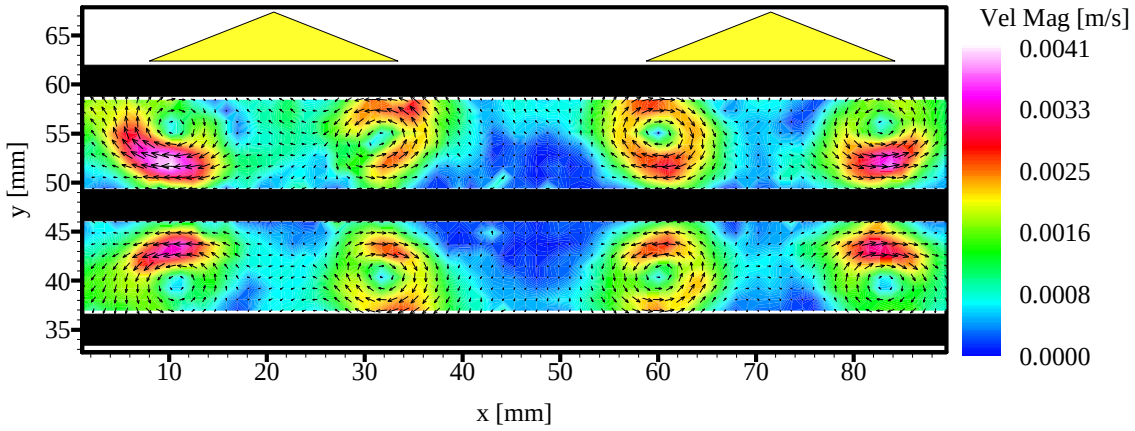
Vel Mag [m/s]
0.0041
0.0033
0.0025
0.0016
0.0008
0.0000
y [mm]
x [mm]

(c)

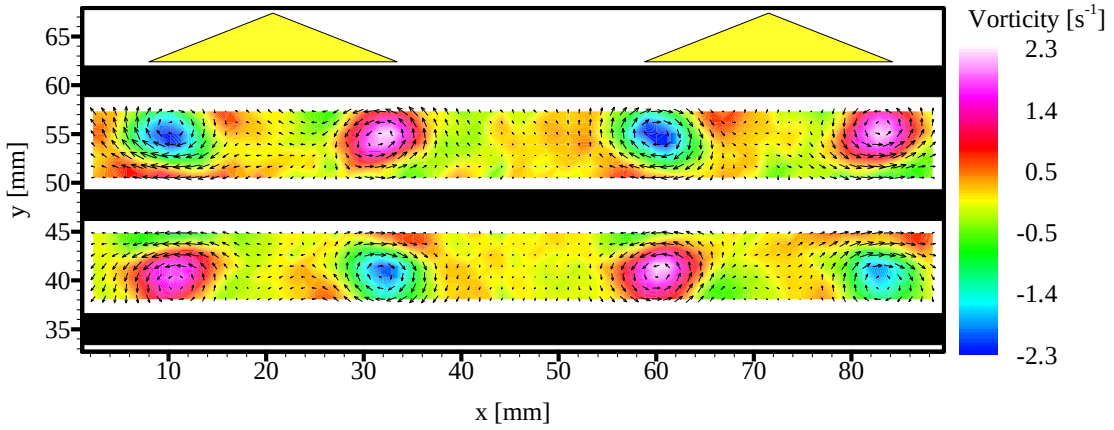

(d)

Figure 4.49 – 4VG-enhanced array at Re = 850, X^* = 4.5: (a) instantaneous velocity magnitude; (b) instantaneous streamwise vorticity; (c) time-averaged velocity magnitude; (d) time-averaged streamwise vorticity

The end-view results at X^*=6.0 are shown in Figure 4.50. The instantaneous velocity field (Figure 4.50 (a)) shows a high-velocity area (red color) across the fin span, which indicates that the V-component velocities caused by boundary-layer restarting are comparable in magnitude to those induced by the streamwise vortices. The time-averaged velocity field (Figure 4.50 (c)) confirms this finding. The instantaneous vorticity field (Figure 4.50 (b)) shows barely identifiable streamwise vortices as well as other small-scale structures, while the time-averaged vorticity field (Figure 4.50 (d)) clearly shows the presence of streamwise vortices.

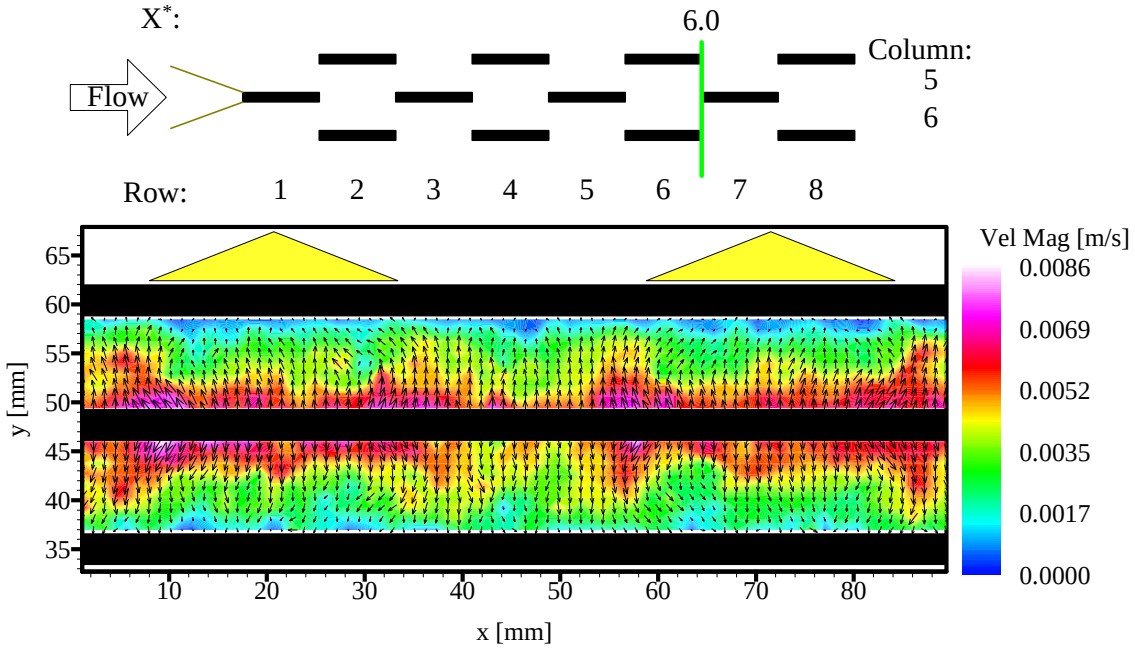
X*:
6.0
Column:
5
6
Flow
Row:
1
2
3
4
5
6
7
8
Vel Mag [m/s]
0.0086
0.0069
0.0052
0.0035
0.0017
0.0000
y [mm]
x [mm]

(a)

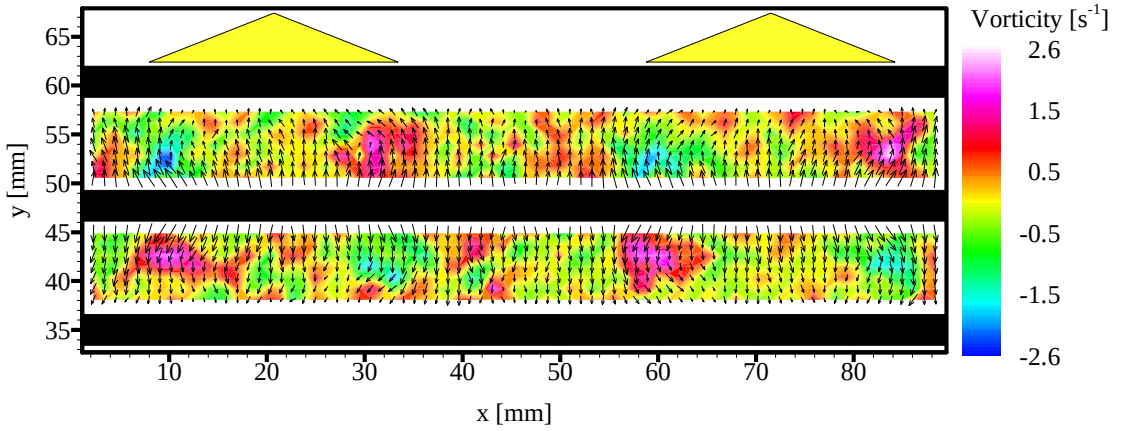
Vorticity [s-1]
2.6
1.5
0.5
-0.5
-1.5
-2.6
y [mm]
x [mm]

(b)

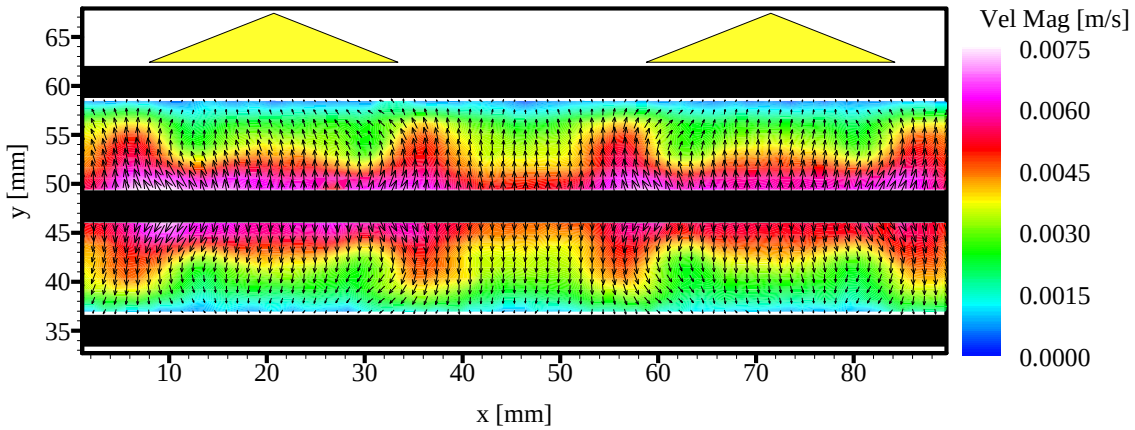
Vel Mag [m/s]
0.0075
0.0060
0.0045
0.0030
0.0015
0.0000
y [mm]
x [mm]

(c)

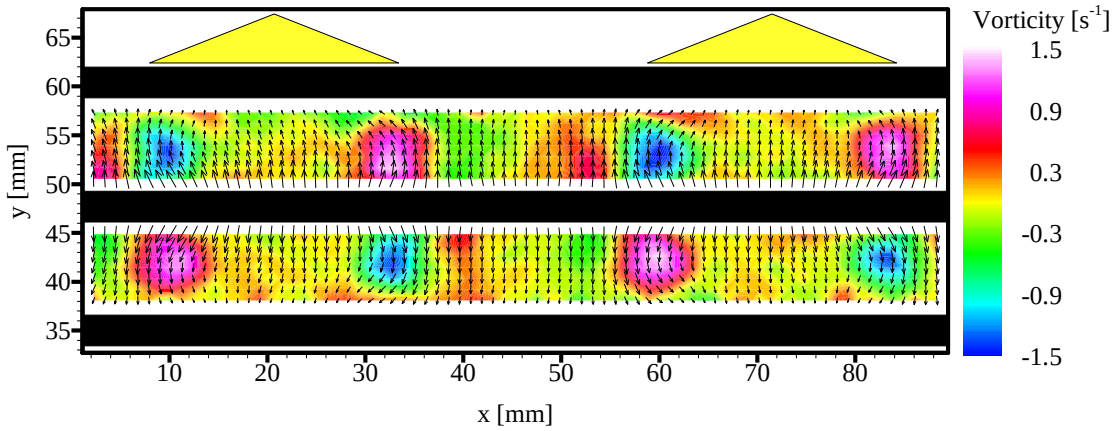

(d)

Figure 4.50 – 4VG-enhanced array at Re = 850, X^* = 6.0: (a) instantaneous velocity magnitude; (b) instantaneous streamwise vorticity; (c) time-averaged velocity magnitude; (d) time-averaged streamwise vorticity

The end-view results at X^*=8.0, which is the trailing edge of the array, are shown in Figure 4.51. The instantaneous velocity and vorticity fields (Figures 4.51 (a) and (b)) show a complex vortical flow with many small-scale structures. The time-averaged velocity field (Figure 4.51 (c)) shows large high-velocity areas on the left and right sides of the flow field, as well as small high-velocity pockets surrounding a very low-velocity region between the delta wings. The time-averaged vorticity field (Figure 4.51(d)) shows that the streamwise vortex structures are still present on average, but with a much reduced strength.

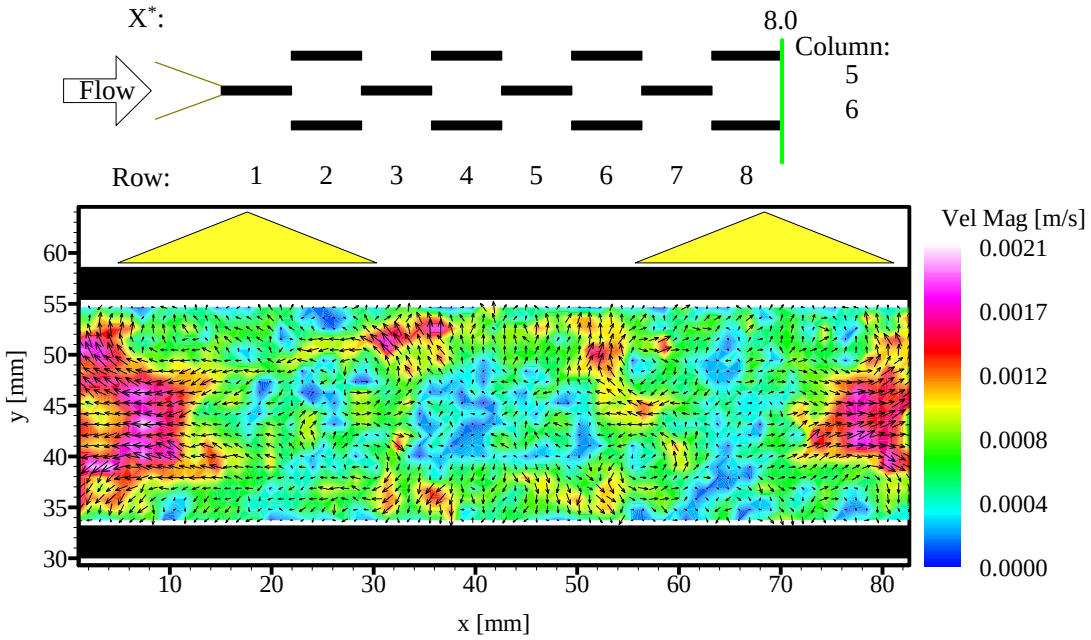
X*:
8.0
Column:
5
6
Flow
Row: 1 2 3 4 5 6 7 8
Vel Mag [m/s]
0.0021
0.0017
0.0012
0.0008
0.0004
0.0000
y [mm]
x [mm]

(a)

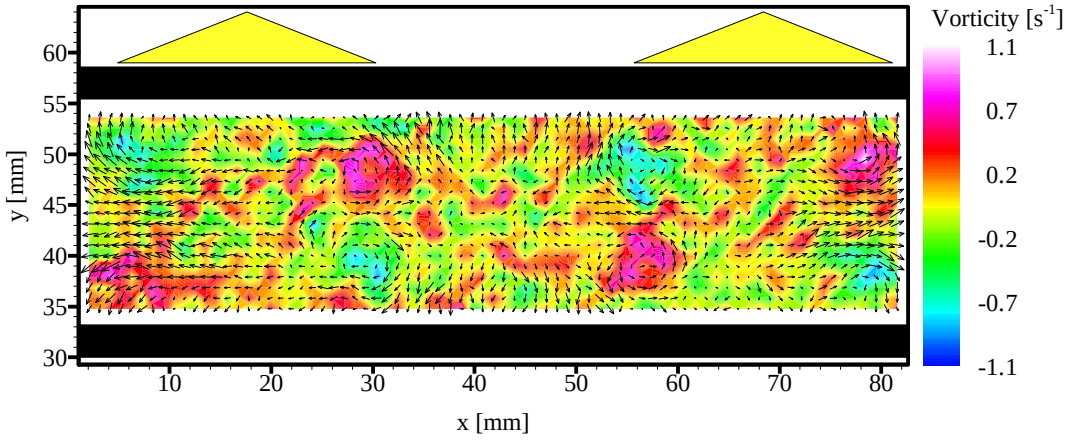
Vorticity [s-1]
1.1
0.7
0.2
-0.2
-0.7
-1.1
y [mm]
x [mm]

(b)

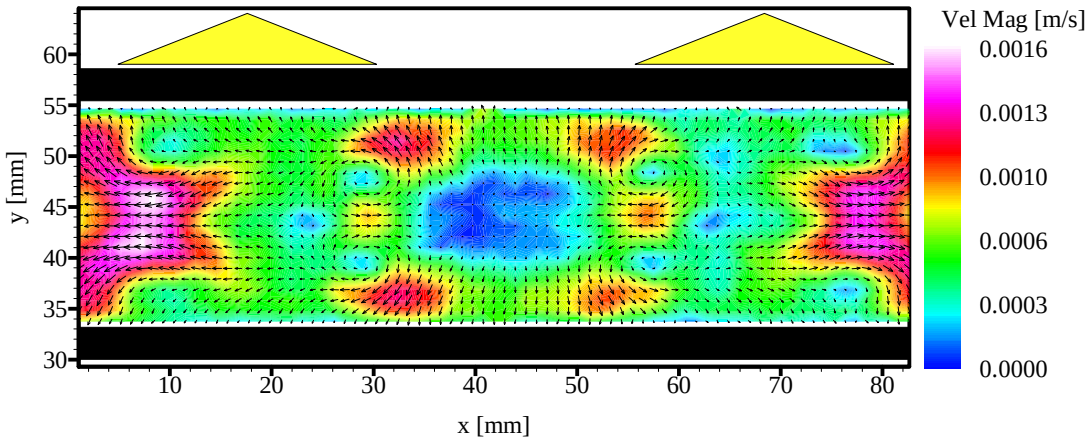
Vel Mag [m/s]
0.0016
0.0013
0.0010
0.0006
0.0003
0.0000
y [mm]
x [mm]

(c)

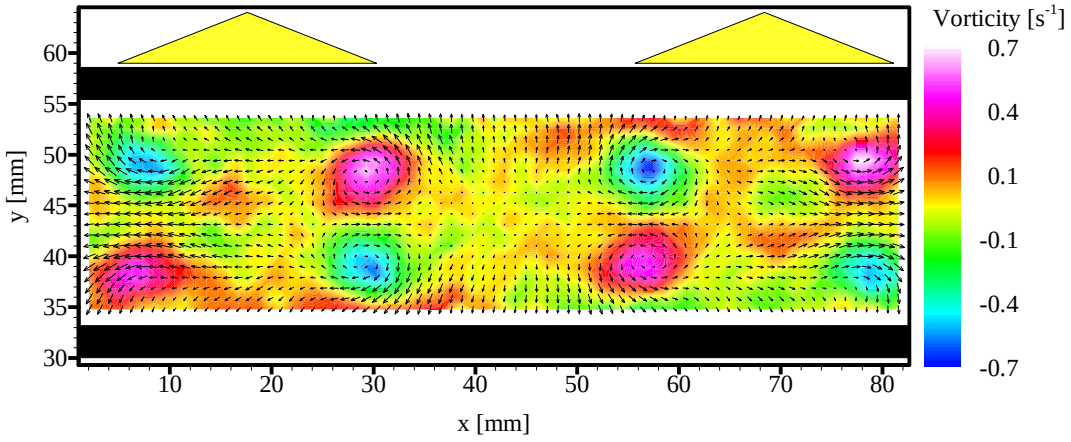

(d)

Figure 4.51 – 4VG-enhanced array at Re = 850, X^* = 8.0: (a) instantaneous velocity magnitude; (b) instantaneous streamwise vorticity; (c) time-averaged velocity magnitude; (d) time-averaged streamwise vorticity

4.2.2.2.2 Re = 1030

The end-view results for Re = 1030 show almost identical behavior as that for Re = 850, except with large magnitude of the velocity components and streamwise vorticity. Thus, this case will not be discussed in detail.

4.2.2.2.3 Re = 1520

The end-view flow field starts to show some differences as the Reynolds number is increased to 1520. The velocity field at X^*=2.0 (Figure 4.52 (a)) shows that four high- velocity pockets occur very close to the middle fin surface near the base of the VGs. This corresponds closely with the flow visualization results shown in Figure 4.8 (a). While higher Re increases the magnitude of streamwise vorticity, it also expands the diameter of the vortex cores in the wake region of the row 1 fins. The edges of streamwise vortices impinge on the leading edge of the row 3 fins and are deflected away from the surfaces, causing a larger end-view velocity magnitude. This is confirmed by the vorticity field (Figure 4.52 (b)) which shows an elongated and flattened shape of the streamwise vortices.

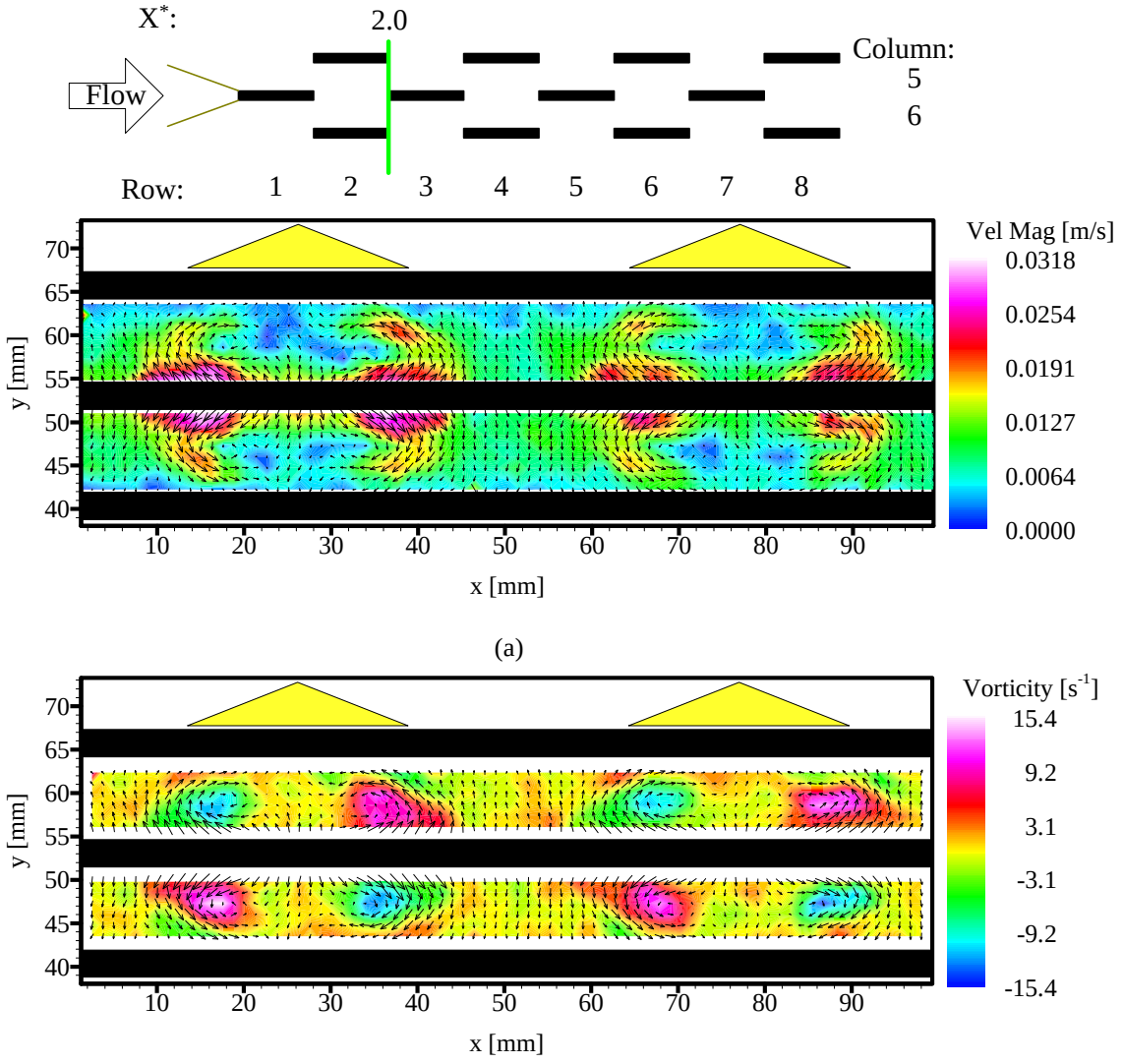

Figure 4.52 – Instantaneous fields for 4VG-enhanced array at Re = 1520, X^* = 2.0: (a) velocity magnitude; (b) streamwise vorticity (similar results at Re = 1750)

The end-view velocity field results at X^*=6.0 (Figure 4.53) show that the end-view flow field at this streamwise location is more vortical than that at Re = 850 (Figure 4.50). The magnitude of the V-component velocity in the upwash region of the streamwise vortices is much larger than that in the downwash region of the streamwise vortices, which indicates increasing influence of the streamwise vortices on the velocity field at this streamwise location.

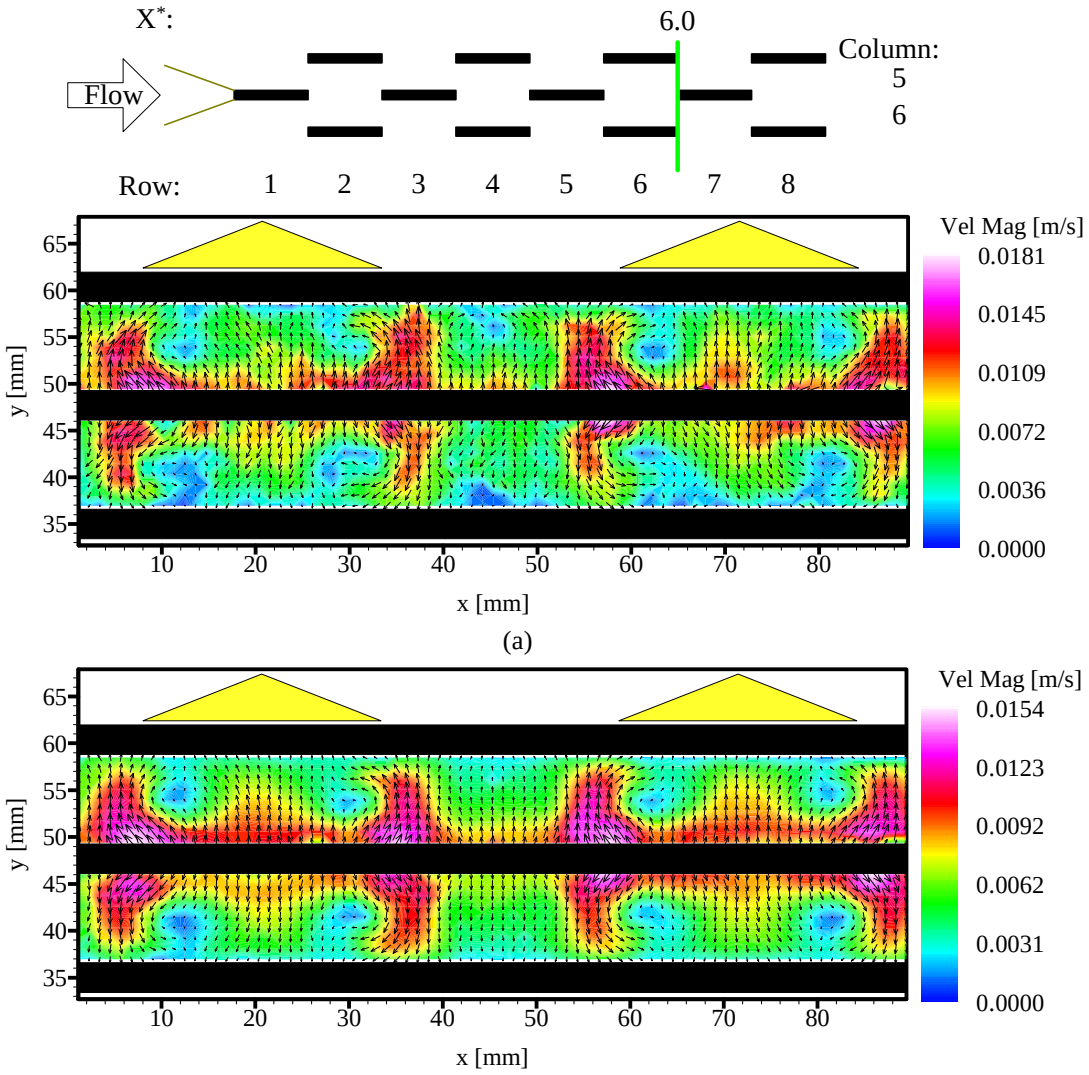

Figure 4.53 – 4VG-enhanced array at Re = 1520, X^* = 6.0: (a) instantaneous velocity magnitude; (b) time-averaged velocity magnitude

As the flow approaches the exit of the array at X^*=8.0 (Figure 4.54), the end-view flow field shows a similar behavior as that for Re = 850 (Figure 4.51), but with better- defined streamwise vortices in the flow field. The instantaneous vorticity field results (Figure 4.54 (b)) show strong primary streamwise vortices and many secondary streamwise vortex structures with irregular shapes. The time-averaged vorticity field (Figure 4.54 (d)) shows four primary streamwise vortex pairs with counter-rotating secondary vortex pairs in between.

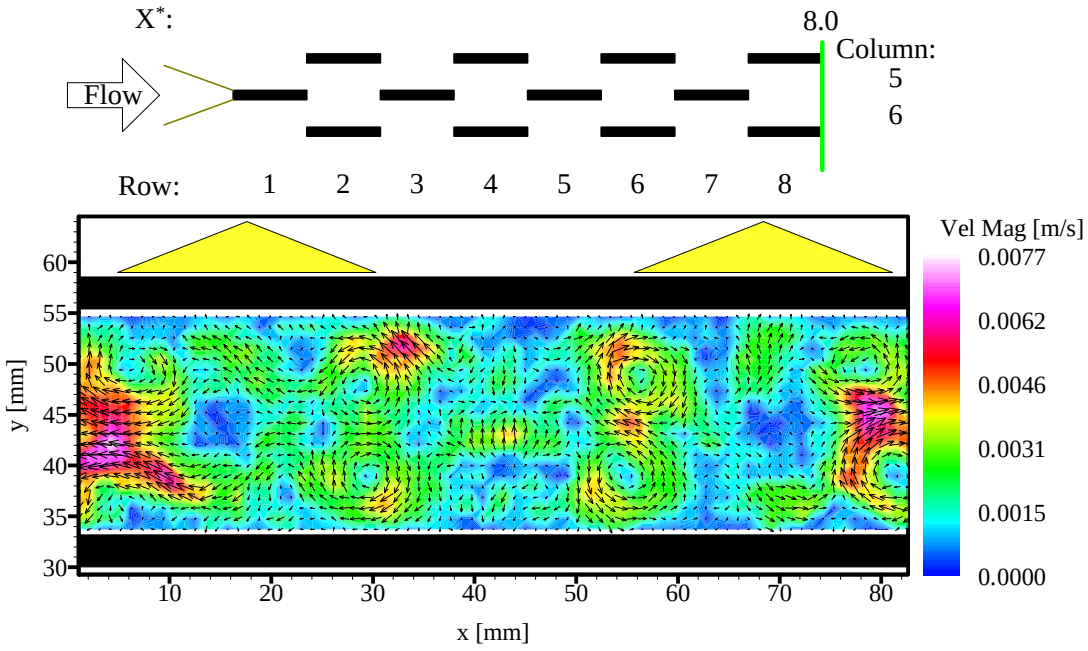
X*:
8.0
Column:
5
6
Flow
Row: 1 2 3 4 5 6 7 8
Vel Mag [m/s]
0.0077
0.0062
0.0046
0.0031
0.0015
0.0000
y [mm]
x [mm]

(a)

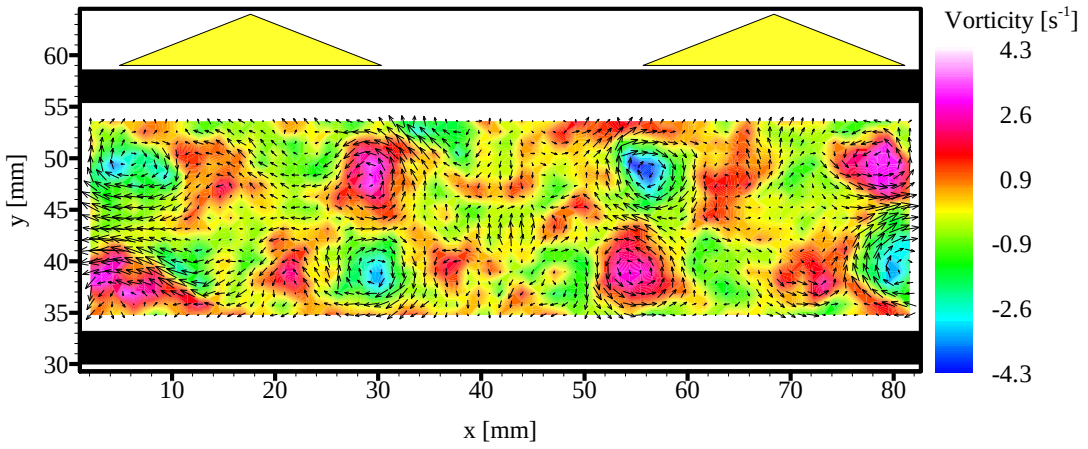
Vorticity [s-1]
4.3
2.6
0.9
-0.9
-2.6
-4.3
y [mm]
x [mm]

(b)

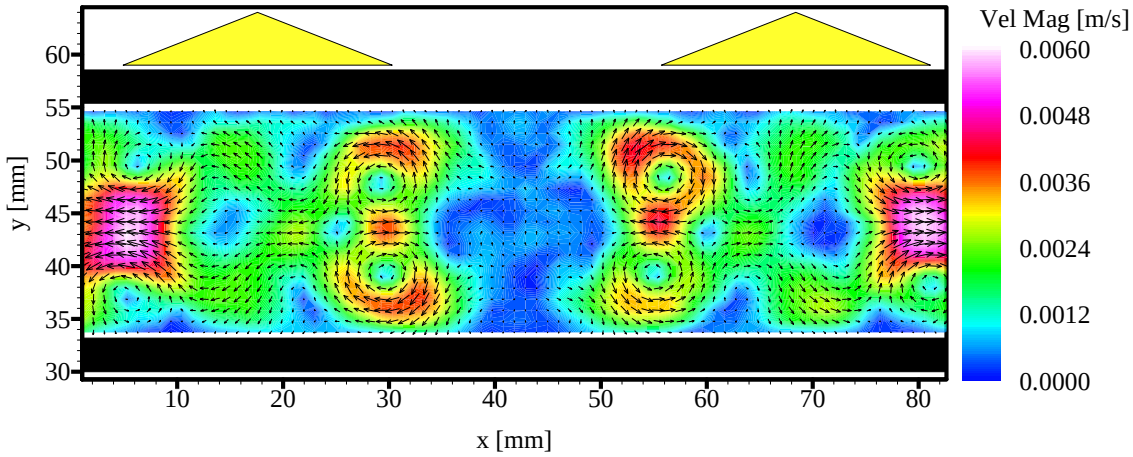
Vel Mag [m/s]
0.0060
0.0048
0.0036
0.0024
0.0012
0.0000
y [mm]
x [mm]

(c)

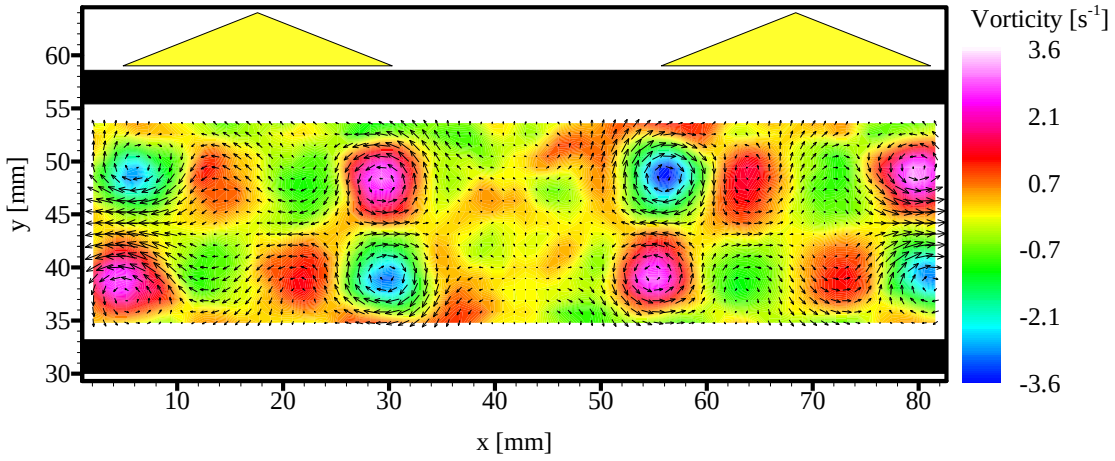

(d)

Figure 4.54 – 4VG-enhanced array at Re = 1520, X^* = 8.0: (a) instantaneous velocity magnitude; (b) instantaneous streamwise vorticity; (c) time-averaged velocity magnitude; (d) time-averaged streamwise vorticity

4.2.2.2.4 Re = 1750

The end-view results for Re = 1750 show similar behavior to that for Re = 1520, except with larger magnitudes of the velocity and streamwise vorticity.

4.2.2.2.5 Re = 2450

The end-view results for Re = 2450 show some flow field differences compared to that at lower Reynolds numbers. At X^*=4.5 (Figure 4.55), the velocity field indicates a highly unsteady flow, with maximum velocity magnitudes of the instantaneous field more than twice those of the time-averaged field. The instantaneous velocity field (Figure 4.55 (a)) shows deformed primary streamwise vortices and irregularly-shaped small-scale streamwise vortex structures in the flow field, which agrees well with the flow visualization result that the unsteady flow at this condition causes the streamwise vortices to become weaker, less well-defined, and less coherent. However, the time-averaged velocity field (Figure 4.55 (b)) still shows well-defined and coherent streamwise vortex pairs, which indicates that the time-averaged effect of the streamwise vortices still exists in the flow field even though the streamwise vortices become unsteady and less coherent.

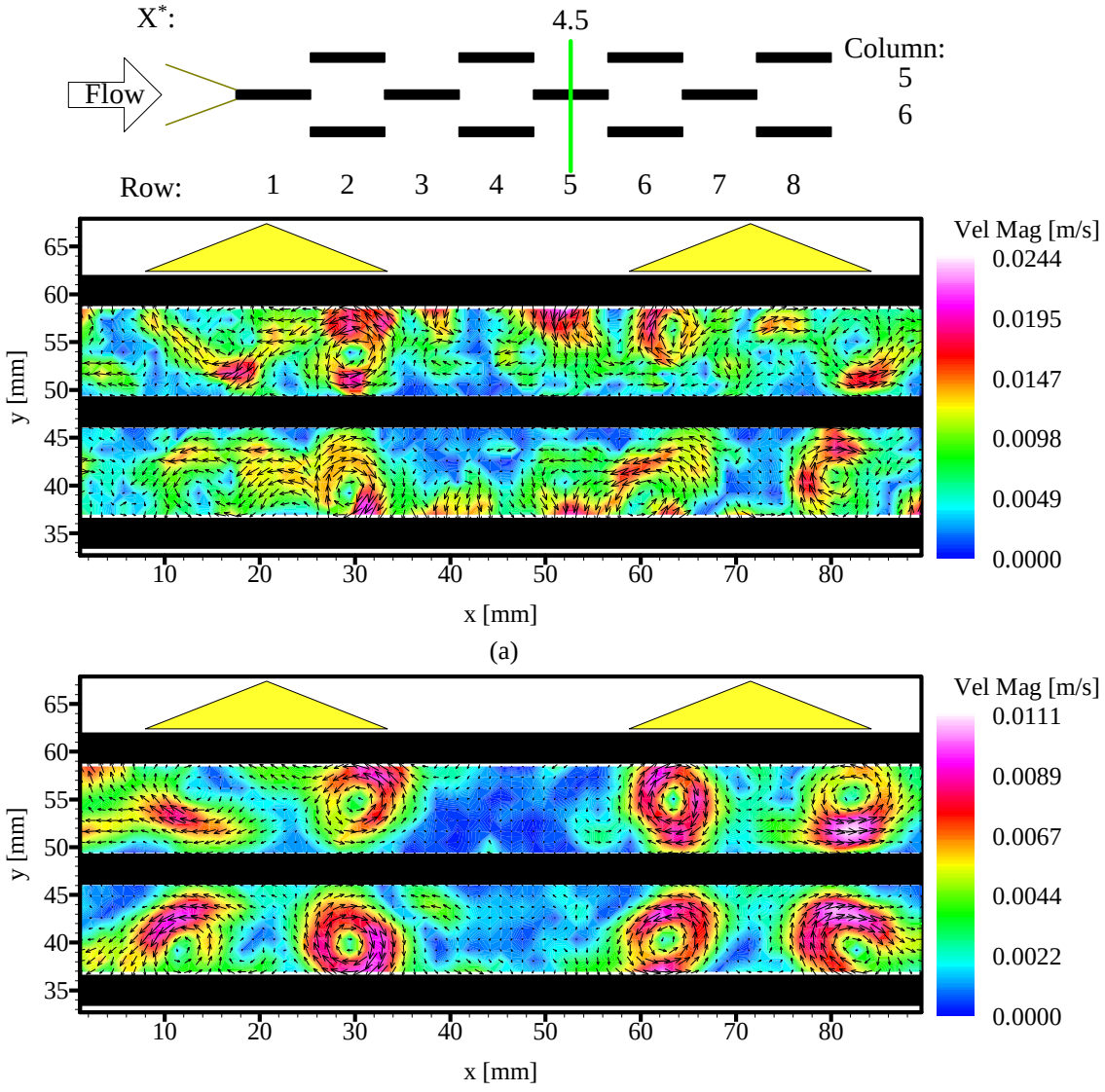

Figure 4.55 – 4VG-enhanced array at Re = 2450, X^* = 4.5: (a) instantaneous velocity magnitude; (b) time-averaged velocity magnitude

The end-view results at X^*=6.0 (Figure 4.56) show even more instability in the flow field. No large streamwise vortex structures are observed in the instantaneous velocity field (Figure 4.56 (a)). Similar to the results at X^*=4.5, the time-averaged velocity field results (Figure 4.56 (b)) show relatively well-organized vortex structures interacting with the boundary layer restarting.

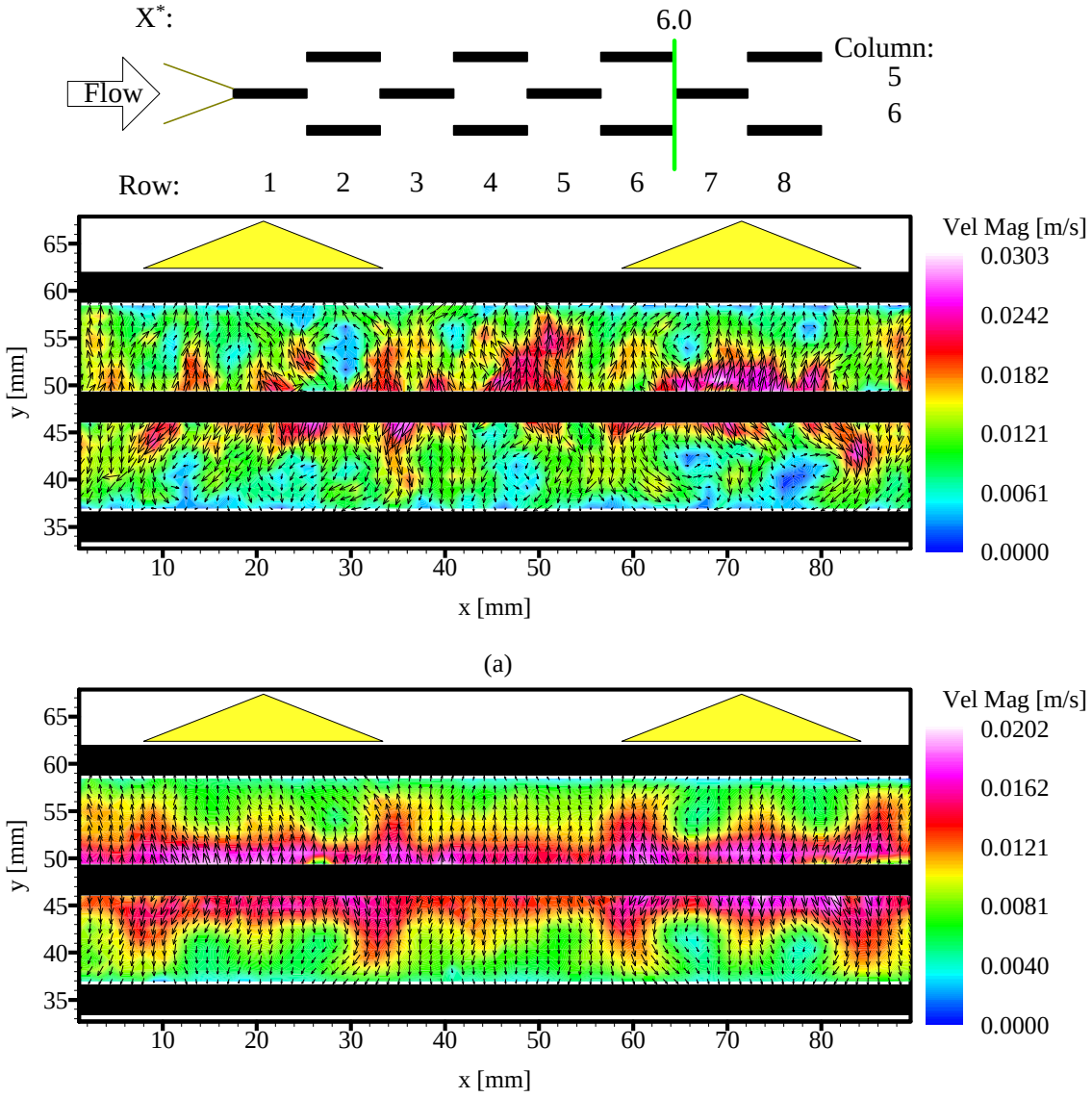

Figure 4.56 – 4VG-enhanced array at Re = 2450, X^* = 6.0: (a) instantaneous velocity magnitude; (b) time-averaged velocity magnitude

As the flow travels to the trailing edge of the array at X^*=8.0 (Figure 4.57), the flow becomes even more unsteady. The instantaneous flow field becomes disorganized and even the time-averaged velocity field (Figure 4.57 (a)) does not show well-organized streamwise vortices. The time-averaged vorticity field, as shown in Figure 4.57 (b), shows poorly-organized and significantly deformed primary vortices, as well as induced secondary streamwise vorticity structures with irregular shape and nearly comparable strengths. These vorticity field results indicate that streamwise vortex breakdown, the disappearance of well-organized and coherent vortex structures, occurs at the trailing edge of the array at this Reynolds number.

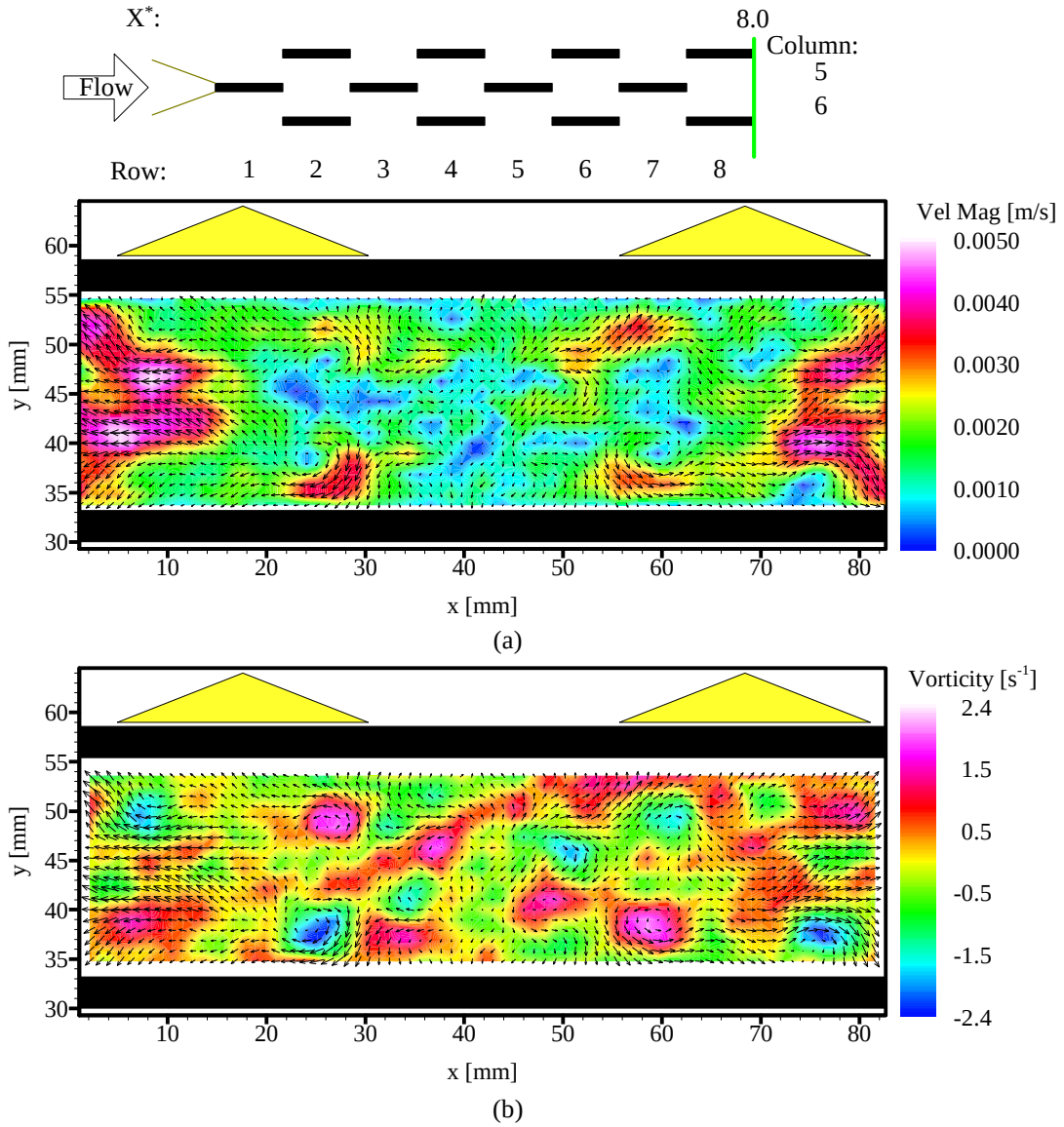

Figure 4.57 – 4VG-enhanced array at Re = 2450, X^* = 8.0: (a) time-averaged velocity magnitude; (b) time-averaged streamwise vorticity

4.2.2.2.6 Re = 3120

The end-view results for Re = 3120 demonstrate that the flow field instability causes the streamwise vortices to deform, weaken, and break down at an earlier location as the Reynolds number increases further. At X^*=6.0, the instantaneous velocity field (Figure 4.58 (a)) shows no organized vortex structures, while the time-averaged velocity field (Figure 4.58 (b)) shows essentially the sole effect of boundary layer restarting. Streamwise vortices generated at the inlet of the array break down before they reach the streamwise location of X^*=6.0, for this Reynolds number.

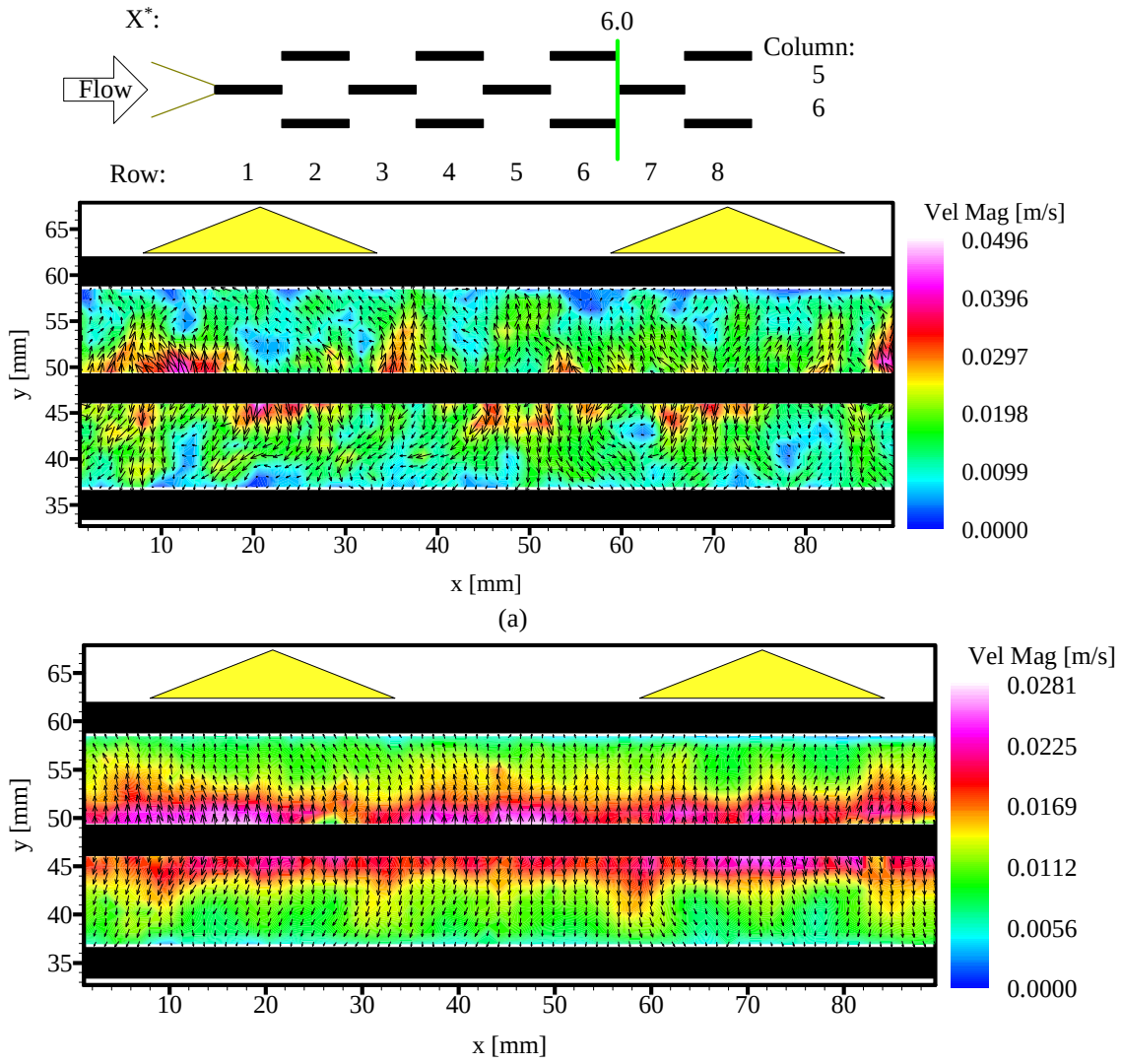

Figure 4.58 – 4VG-enhanced array at Re = 3120, X^* = 6.0: (a) instantaneous velocity magnitude; (b) time-averaged velocity magnitude

The end-view results at X^*=8.0 are shown in Figure 4.59. The time-averaged velocity field (Figure 4.59 (a)) shows more unsteady and chaotic behavior than that for Re = 2450, as does the time-averaged vorticity field (Figure 4.59 (b)). The flow field at this location and Reynolds number shows essentially no evidence of the streamwise vortices generated at the inlet of the array.

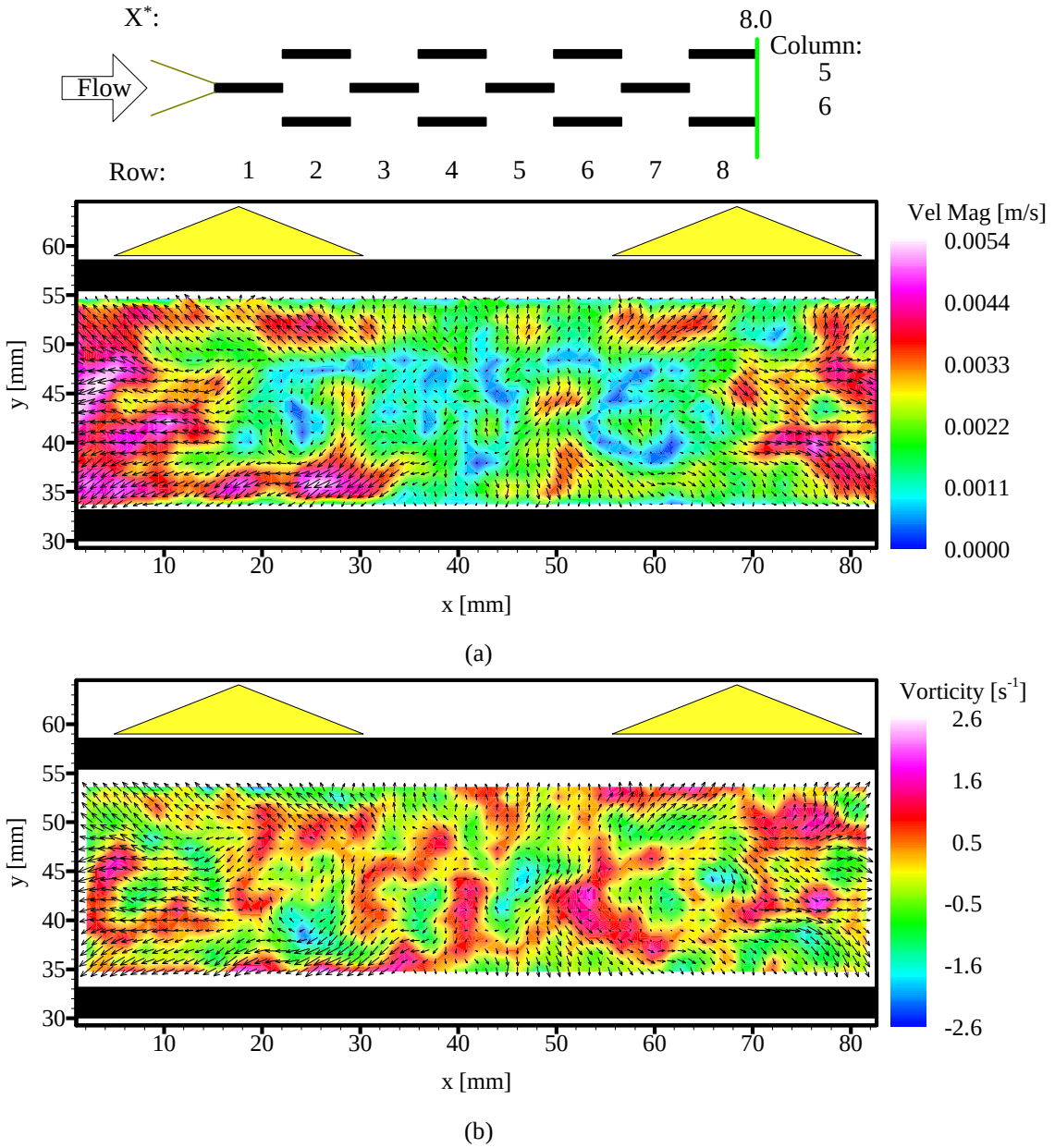

Figure 4.59 – 4VG-enhanced array at Re = 3120, X^* = 8.0: (a) time-averaged velocity magnitude; (b) time-averaged streamwise vorticity

4.2.2.2.7 Summary

Streamwise vortices are generated at the inlet of the array. As the streamwise vortices advect downstream, the counter-rotating vortex pairs interact with the adjacent vortex pairs and the interrupted-fin surfaces. Figure 4.60 shows the maximum time-averaged vorticity magnitude along the flow path for different Reynolds numbers. In general, the maximum vorticity magnitude decreases as the streamwise vortices advect downstream. The maximum vorticity magnitudes at the leading edge of row 2 (X^* = 1) are generally larger than at adjacent streamwise locations, especially at higher Reynolds numbers. The suddenly diverted flow path due to the leading edge of the interrupted fins slightly increases the maximum vorticity magnitude. For Reynolds numbers up to 1750, the vorticity magnitudes decay along the streamwise direction at a roughly similar rate. However, for Re = 2450 and Re = 3120,

the vorticity magnitudes decay very rapidly in the first half of the array, and those magnitudes are even lower than those for Re = 1750 in the second half of the array, at the same streamwise locations. The maximum vorticity magnitudes for the streamwise vortices are found to be about the same order as those for the spanwise vortices.

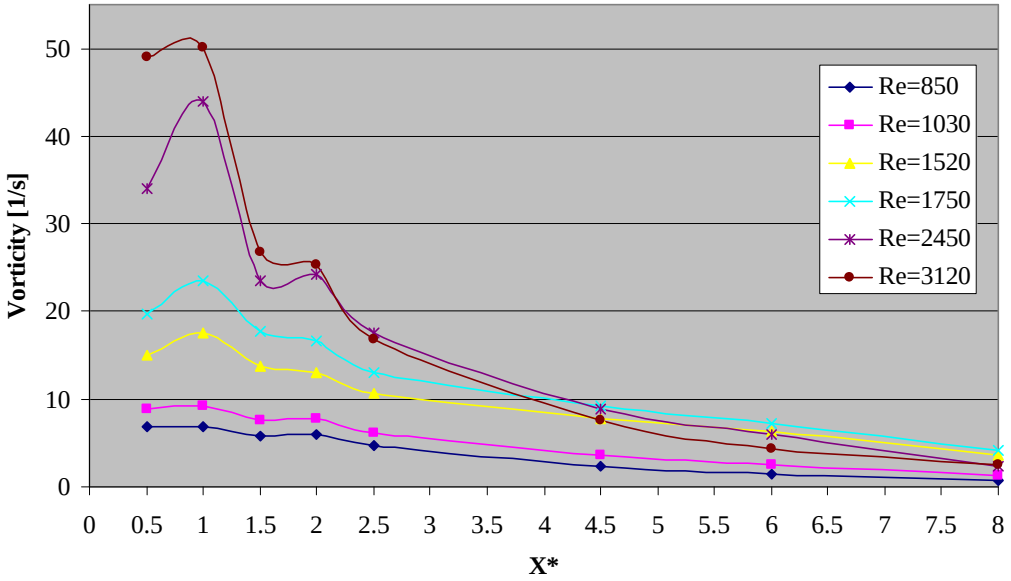

Figure 4.60 – 4VG-enhanced array: maximum vortex strength for time-averaged vorticity fields at different streamwise locations

The relative locations of the streamwise vortices in the flow field have also been evaluated to help understand their development. A schematic defining the vortex core distance, horizontal distance between vortex pairs, and vertical distance from the middle-fin surface, is shown in Figure 4.61. The distances presented here are obtained from the time-averaged vorticity field results.

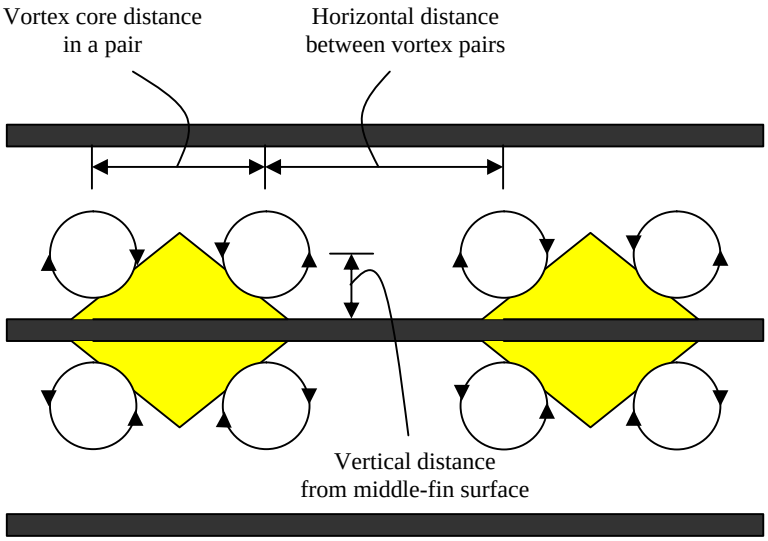

Figure 4.61 – Schematics of vortex core distance in a vortex pair, horizontal distance between vortex pairs and vertical distance from mid-fin surface

The streamwise development of the vortex core distance is shown in Figure 4.62. The vortex core distance is the smallest at X^*= 0.5 for all Reynolds numbers. It then increases substantially at X^*=1.0 and decreases slightly at X^*=1.5. This development of the vortex core distance indicates that the suddenly diverted flow path due to the leading edge of the interrupted fins not only increases the vorticity strength, but also pushes the vortices of the counter-rotating pairs apart. The vortex core distance adjusts to slightly smaller values after the flow pass the leading edges of the fins. All vortex core distances except one data point at Re = 1520 are clearly less than 25.4 mm, which is the base length of the delta wings.

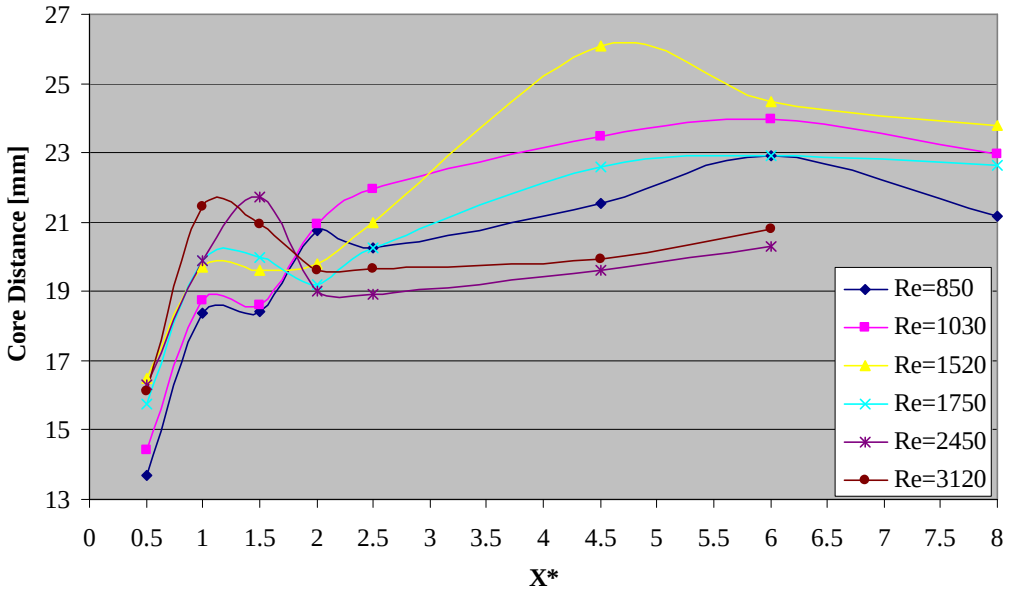

Figure 4.62 –4VG-enhanced array: vortex core distance in a pair for time-averaged vorticity fields at different streamwise locations

The development of the horizontal distance between the vortex pairs, as shown in Figure 4.63, displays an opposite trend to the vortex core distance for Reynolds numbers up to 1750. For Reynolds numbers of 2450 and 3120, the horizontal distances show the opposite trend to the vortex core distances for streamwise locations up to X^*=2.5. However, at X^*=4.5, the horizontal distance increases over that at X^*=2.5, the same as for the vortex core distance. This observation indicates that the leftmost and rightmost streamwise vortices are pushed toward the water tunnel side-wall surfaces.

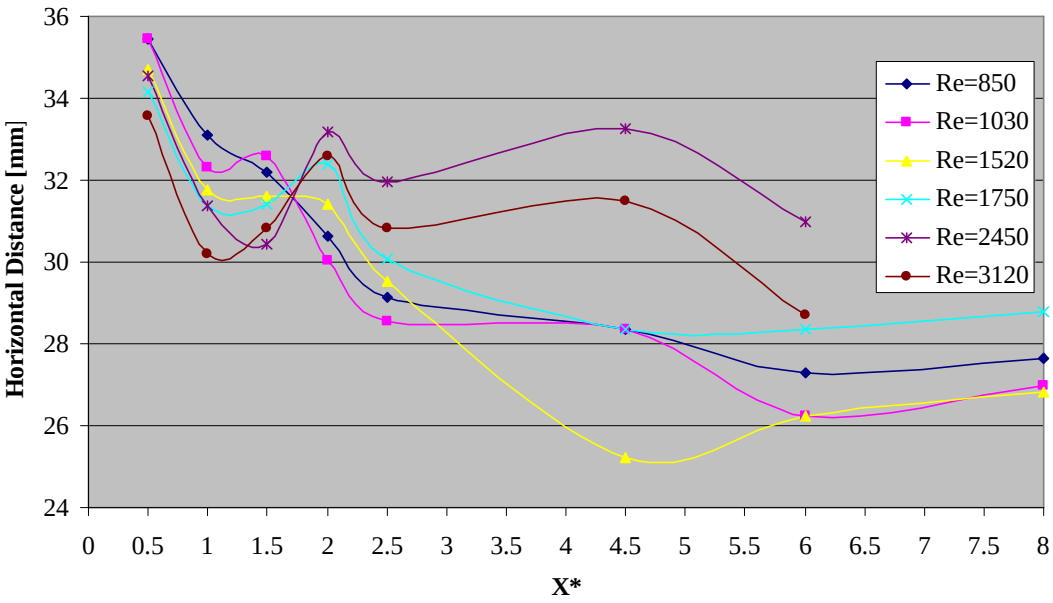

Figure 4.63 – 4VG-enhanced array: horizontal distance between vortex pairs for time-averaged vorticity fields at different streamwise locations

The vertical distance of the streamwise vortices from the middle-fin surface for different streamwise locations and Reynolds numbers is shown in Figure 4.64. A vertical distance of 4.76 mm corresponds to the flow channel centerline. For the 1st row fins, the vortex cores are close to the middle-fin surfaces. The vertical distance of the streamwise vortices decreases rapidly after the vortices enter the 2nd row (from X^*=1 to X^*=1.5), which indicates that the suddenly diverted flow path due to the leading edge of the 2nd row fins tends to push the vortex cores away from the 2nd row fin surfaces. The vertical distance of the streamwise vortices increases rapidly when the streamwise vortices reach the trailing edge of the 2nd row fins and then enter the 3rd row (from X^*=1.5 to X^*=2.5). The flow path at X^*=2 is diverted again after passing the leading edge of the 3rd row fins and the vortex cores tend to move away from the 3rd row fin surfaces. It is believed that a similar pattern of the vortical distance of the streamwise vortices exists for downstream streamwise locations (X^*>2.5), should end-view PIV results be obtained at more streamwise locations between X^*=2.5 and X^*=8.

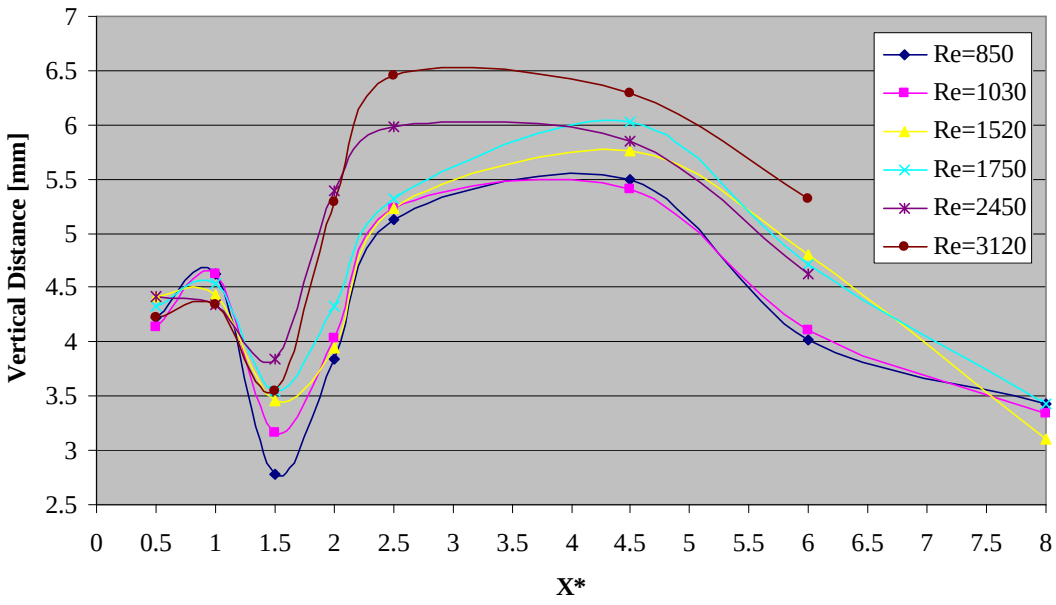

Figure 4.64 – 4VG-enhanced array: vertical distance from mid-fin surface for time-averaged vorticity fields at different streamwise locations

4.2.3 4VG at Rows 1 and 5 - Enhanced Array

The 4VG at Rows 1 and 5 - enhanced array has delta wings at the leading edge of not only the 1st row fins but also the 5th row fins, in order to regenerate the streamwise vortices halfway through the array. The following description will focus on the differences in the quantitative flow field characteristics due to the addition of the second row of delta wings at the leading edge of the 5th row fins.

4.2.3.1 Side-View Velocity and Vorticity Field Behavior

The side-view velocity field results for the 4VG at Rows 1 and 5 - enhanced array are shown in Figures 4.65 – 4.69. The flow field behavior for the first half of the array is observed to be quite similar to that of the 4VG-enhanced array discussed in the previous section, except for areas near the 4th row fins where the tips of the delta wings on the 5th row fins project forward. This observation is confirmed by the following PIV results.

The velocity field results for Re = 850 are shown in Figure 4.65. The velocity field for rows 1 and 2 (Figure 4.65 (a)) show almost identical results to the 4VG-enhanced array (Figure 4.35 (a)), while the velocity field for rows 3 and 4 (Figure 4.65 (b)) show a slight difference ahead of the leading edge of the 5th row fins from the 4VG-enhanced array (Figure 4.35 (b)). The wake region of the 3rd row fins (green color) is wider than that in the 4VG-enhanced array, and the flow immediately upstream of the 5th row fins is accelerated more significantly due to the generation of streamwise vortices by the second row of VGs. The velocity results for rows 5 and 6 (Figure 4.65 (c)) show similar flow behavior as rows 1 and 2, which indicates that the non-uniform incoming flow in front of the 5th row fins does not affect significantly the structure of the regenerated streamwise vortices at this low Reynolds number (Re = 850) when the flow is laminar. The upwash movement of fluid creates a wider wake region (green color) in front of the 7th row fins at this laser sheet location, which affects the velocity field for rows 7 and 8, as shown in Figure 4.65 (d). The velocity field for rows 7 and 8 also shows thicker boundary layers than that of the 4VG-enhanced array, due to the effect of the upwash movement of fluid caused by the re-generated streamwise

vortices. Similarly, thinner boundary layers than those of the 4VG-enhanced array are observed for the 6^{th} row and 8^{th} row fins where downwash movement of fluid occurs. The velocity field downstream of the array (Figure 4.65 (e)) shows laminar flow behavior, with small-scale structures caused by the streamwise vortices in the wake region.

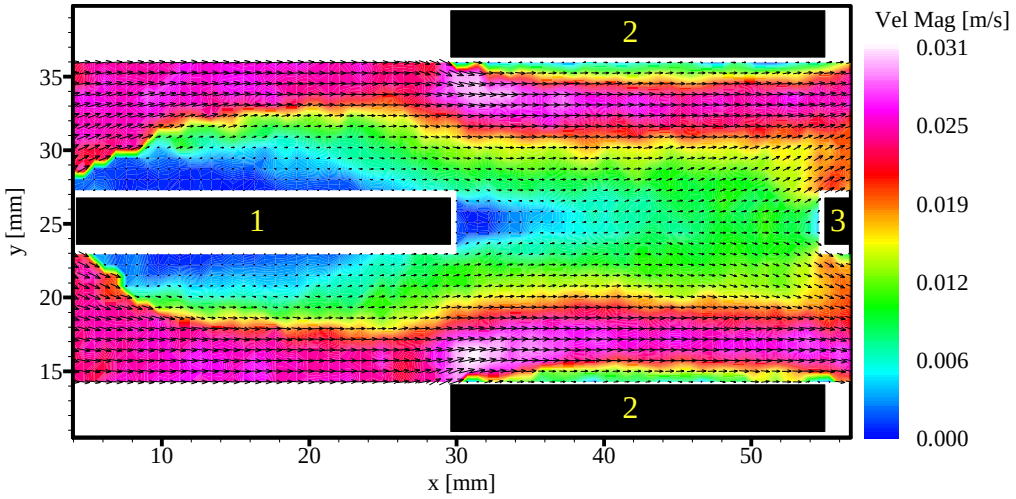
Vel Mag [m/s]
0.031
0.025
0.019
0.012
0.006
0.000
2
1
3
2
y [mm]
x [mm]

(a)

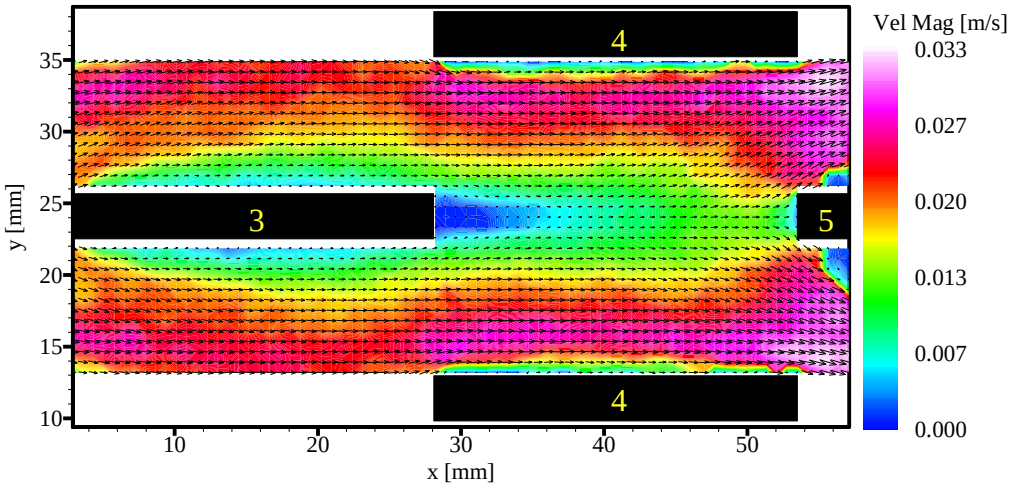
Vel Mag [m/s]
0.033
0.027
0.020
0.013
0.007
0.000
4
3
5
4
y [mm]
x [mm]

(b)

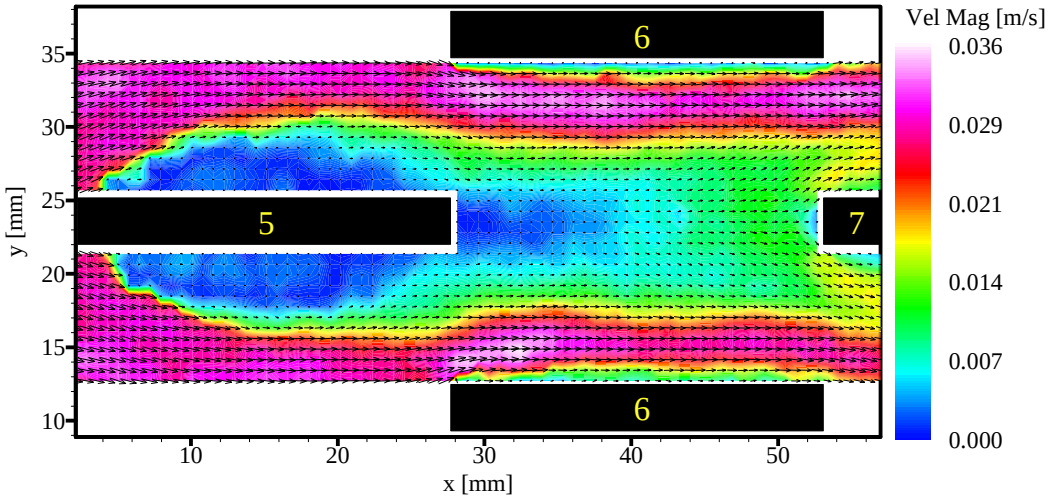
Vel Mag [m/s]
0.036
0.029
0.021
0.014
0.007
0.000
6
5
7
6
y [mm]
x [mm]

(c)

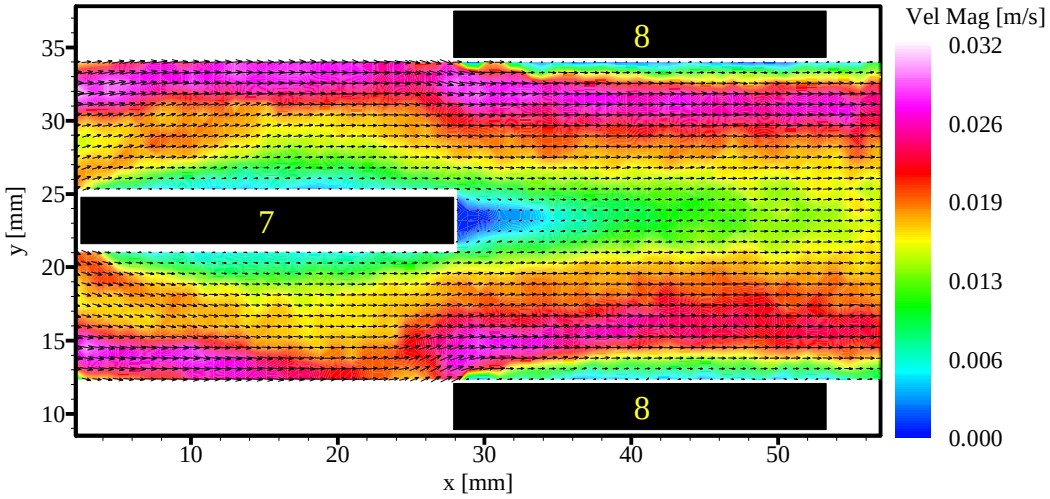

(d)

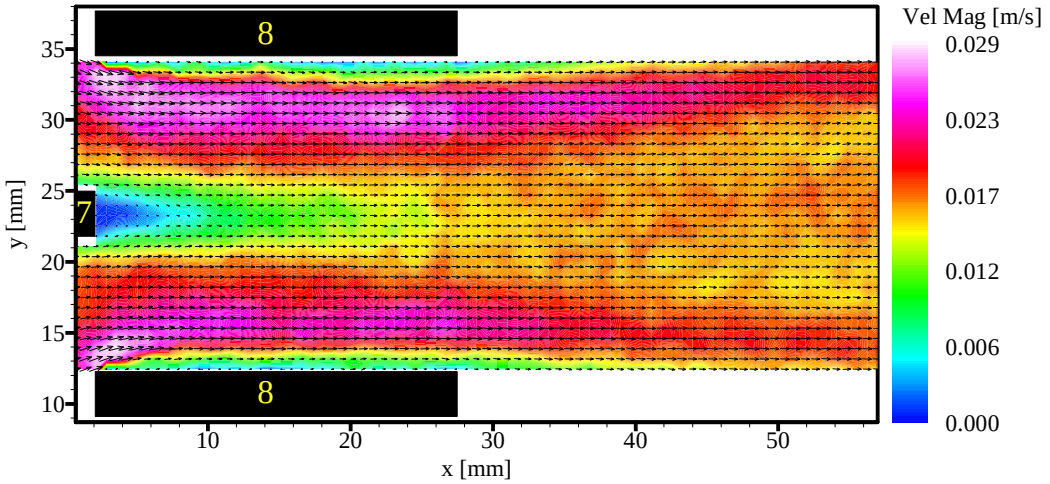

(e)

Figure 4.65 – Instantaneous velocity for 4VG at Rows 1 and 5 - enhanced array at Re = 850: (a) Rows 1 and 2; (b) Rows 3 and 4; (c) Rows 5 and 6; (d) Rows 7 and 8; (e) Row 8 and downstream

As Re is increased to 1030, the front half of the array shows almost the same flow field behavior as that of the 4VG-enhanced array. However, flow instability starts to occur in the second half of the array, which is different from the behavior of the 4VG-enhanced array. As shown in Figure 4.66 (a), the velocity field for rows 5 and 6 shows that instability develops in the row 6 area. The velocity field for rows 7 and 8 (Figure 4.66 (b)) shows that spanwise vortex shedding persists in the row 7 area and starts to diminish when the flow enters the row 8 area. Thus, regenerating streamwise vortices halfway through the offset-strip fin array with a non-uniform vortical incoming flow causes flow instability and spanwise vortex shedding at a lower Reynolds number than for arrays with VGs placed only at the inlet. However, flow instability still exists as the flow travels downstream into the array wake region, which is evidenced by the velocity field results for row 8 and downstream (Figure 4.66 (c)).

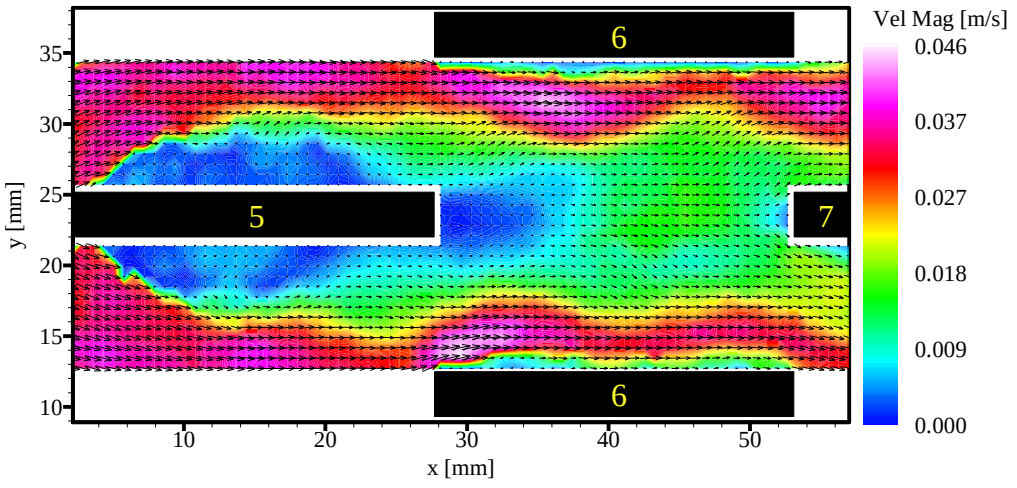

(a)

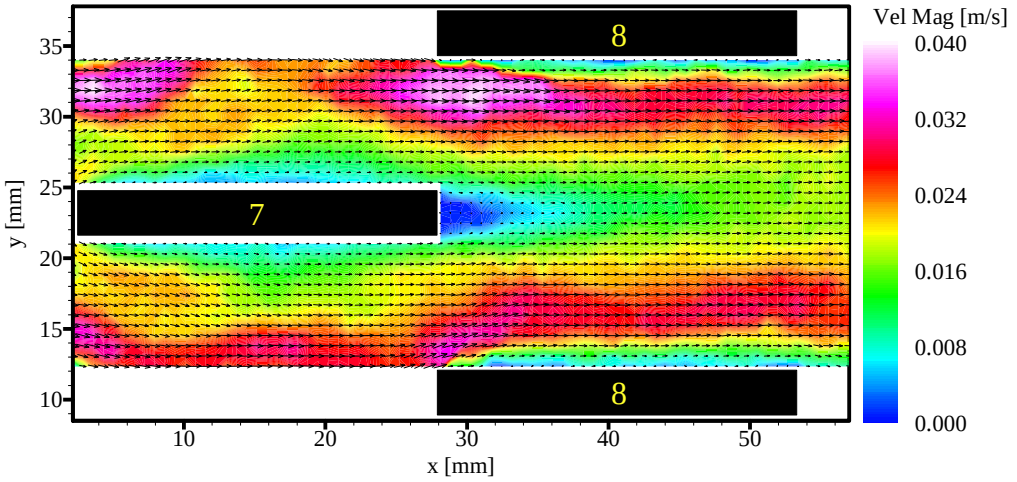

(b)

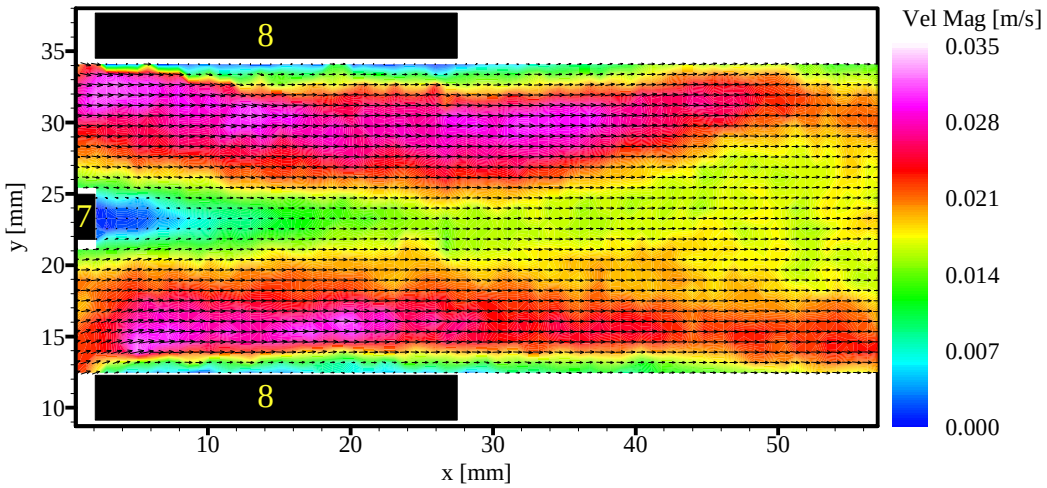

(c)

Figure 4.66 – Instantaneous velocity for 4VG at Rows 1 and 5 - enhanced array at Re = 1030: (a) Rows 5 and 6; (b) Rows 7 and 8; (c) Row 8 and downstream

The side-view velocity field results for Re = 1520 are shown in Figure 4.67. The velocity field for rows 3 and 4 (Figure 4.67 (a)) indicates a laminar flow. The row 3 wake (green color) becomes wider as it approaches row 5, and the fluid is accelerated in the V-velocity direction far before impinging the leading edge of row 5. This observation confirms that the re-generation of streamwise vortices by the row 5 delta wings actually affects the flow in the row 4 area immediately upstream from the leading edge of the 5^{th} row fins. The velocity field in the second half of the array, as shown in Figures 4.67 (b) –(c), reveals similar flow behavior as that for Re = 1030, except that the magnitude of the flow instability is greater. Spanwise vortex shedding occurs at the 7^{th} row and 8^{th} row fins, as well as in the array wake region as shown in Figure 4.67 (d).

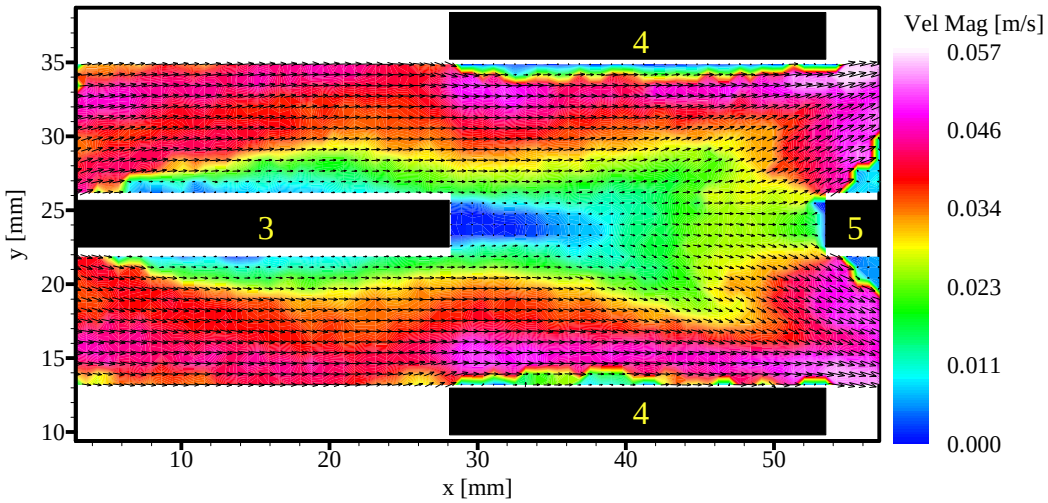
4
3
5
4
y [mm]
x [mm]
Vel Mag [m/s]
0.057
0.046
0.034
0.023
0.011
0.000

(a)

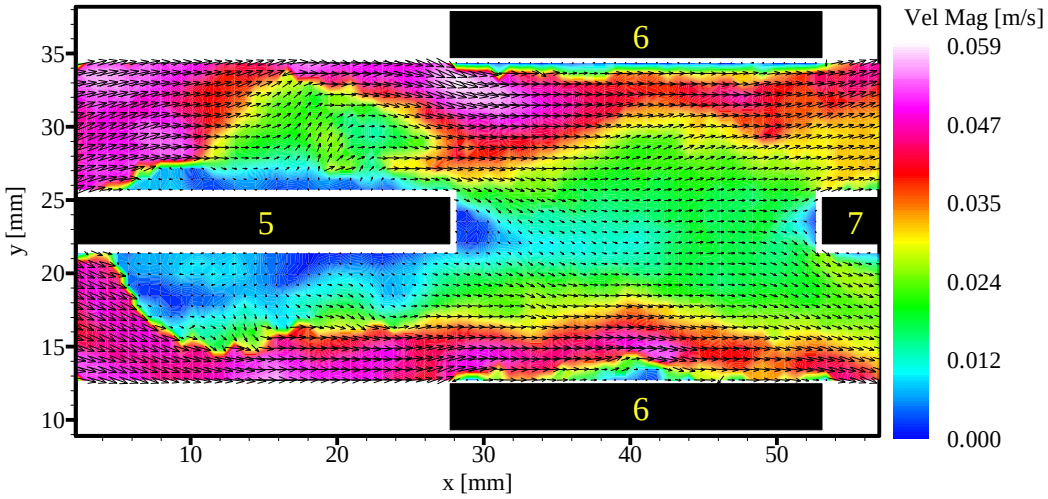
6
5
7
6
y [mm]
x [mm]
Vel Mag [m/s]
0.059
0.047
0.035
0.024
0.012
0.000

(b)

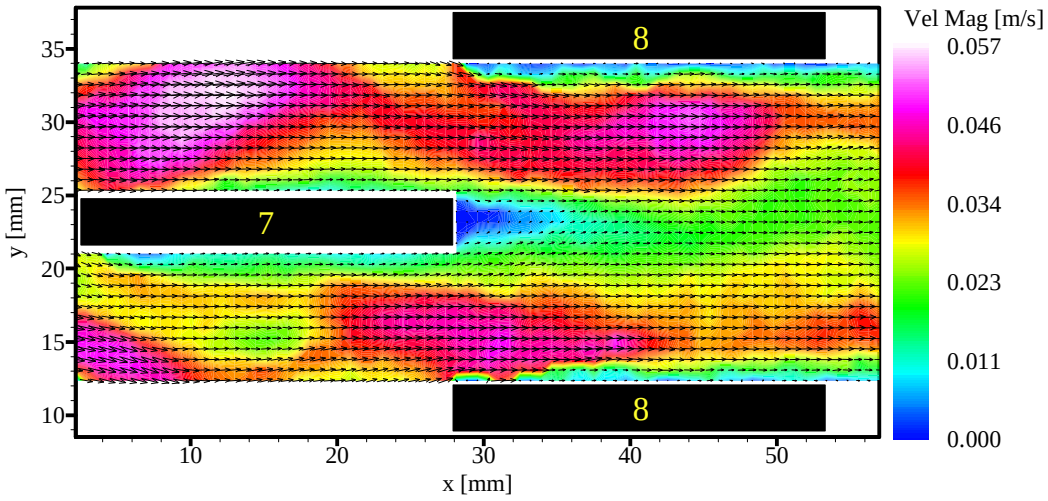
8
7
8
y [mm]
x [mm]
Vel Mag [m/s]
0.057
0.046
0.034
0.023
0.011
0.000

(c)

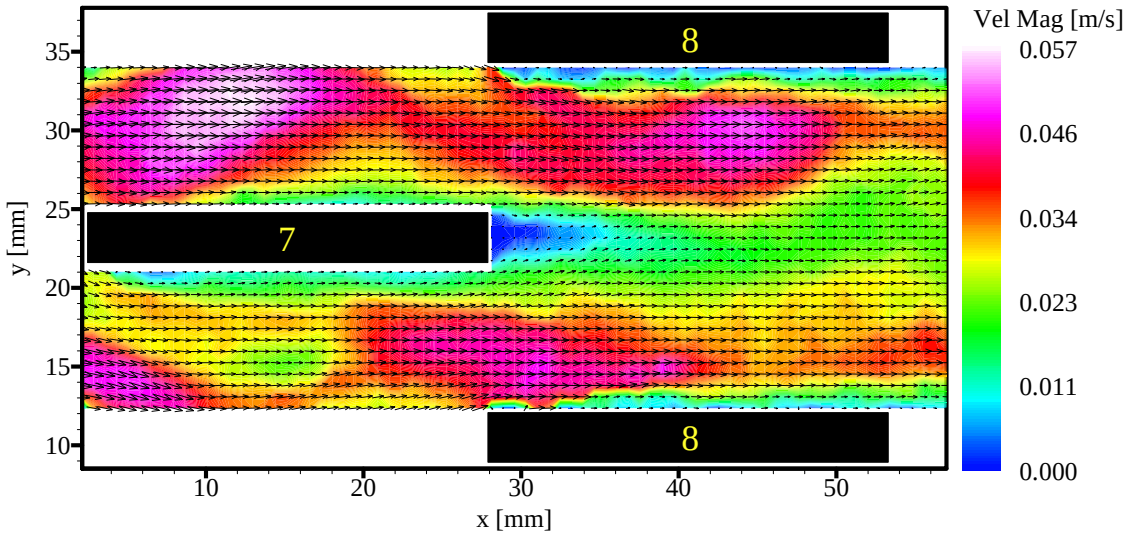

(c)

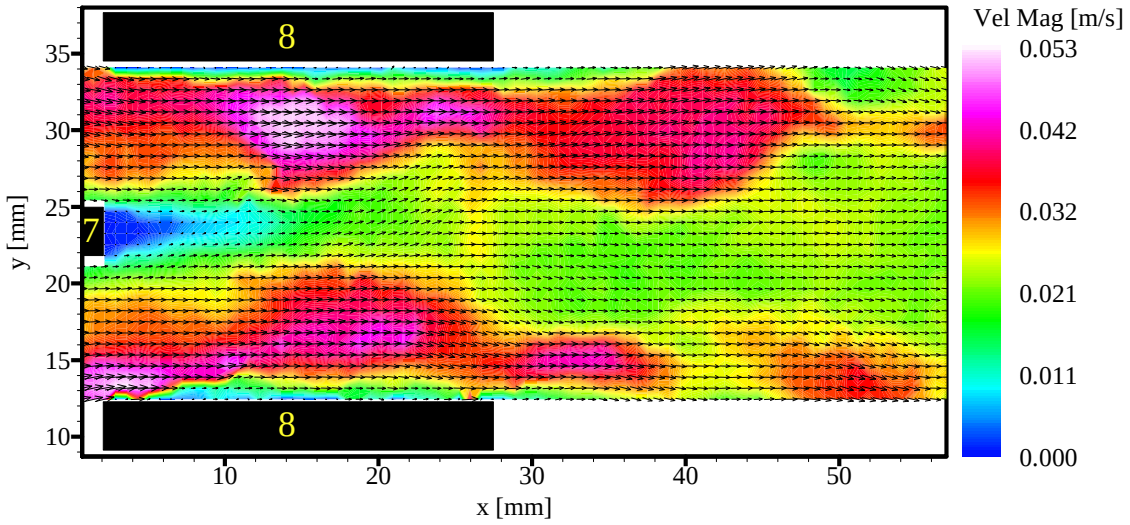

(d)

Figure 4.67 – Instantaneous velocity for 4VG at Rows 1 and 5 - enhanced array at Re = 1520: (a) Rows 3 and 4; (b) Rows 5 and 6; (c) Rows 7 and 8; (d) Row 8 and downstream

Similar flow behavior was observed in the velocity field results for Re = 1750, and will not be discussed in detail.

As Re is increased further, the second half of the array and the array wake region show almost identical flow behavior to that for Re = 1750, but with stronger flow instabilities. At Re = 2450, flow instabilities and spanwise vortex shedding start to occur in the flow field for rows 3 and 4, as shown in Figure 4.68. As compared to the velocity field for the 4VG-enhanced array at the same Reynolds number (Figure 4.41), the velocity field for rows 1 and 2 is almost identical for the 4VG at Rows 1 and 5 – enhanced array, while the velocity field for rows 3 and 4 shows more chaotic characteristics. At Re = 3120, similar flow behavior as that at Re = 2450 is found in the velocity field for rows 3 and 4 (Figure 4.69).

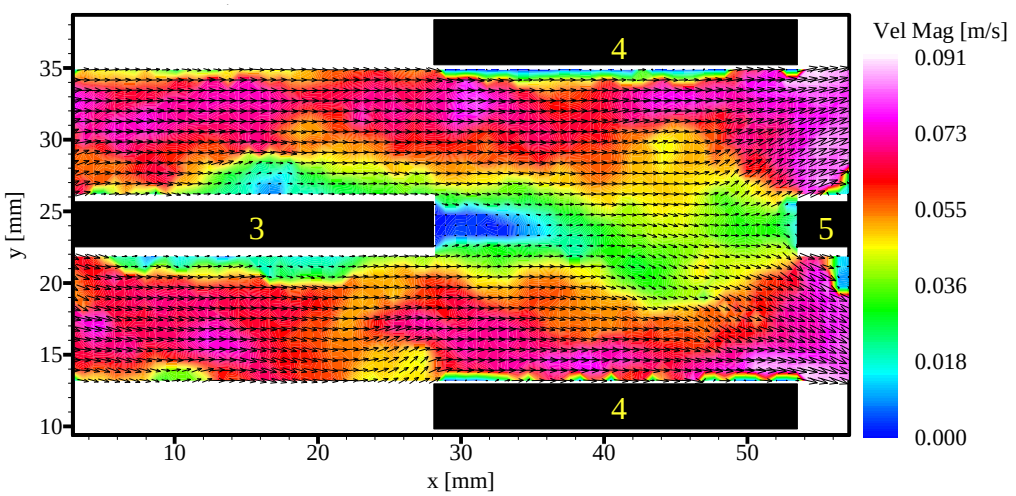

Figure 4.68 – Instantaneous velocity for 4VG at Rows 1 and 5 - enhanced array at Re = 2450: Rows 3 and 4

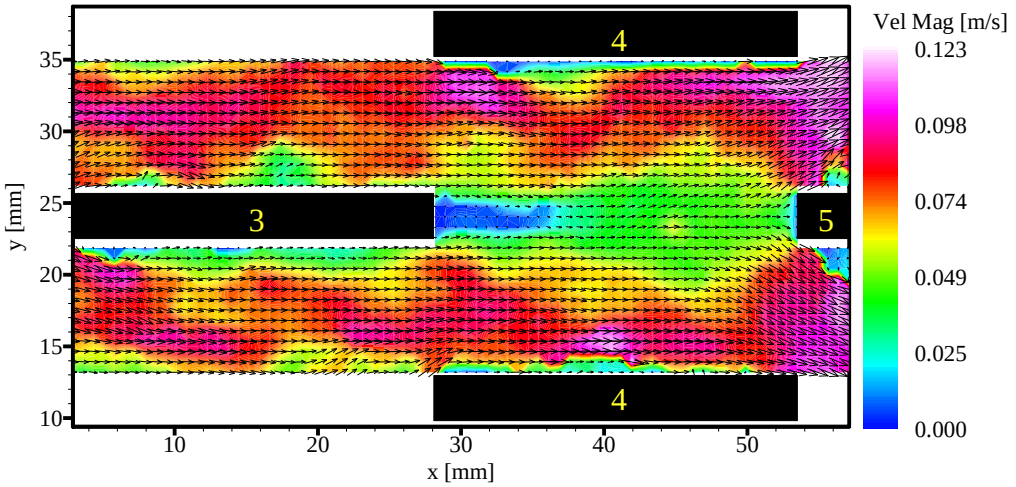

Figure 4.69 – Instantaneous velocity for 4VG at Rows 1 and 5 - enhanced array at Re = 3120: Rows 3 and 4

4.2.3.2 End-View Velocity and Vorticity Field Behavior

The end-view PIV experiments were performed only for three streamwise locations (X^*=4.5, X^*=6.0 and X^*=8.0) in the second half of the array, as the side-view results demonstrate that the flow field for the first three rows in the 4VG at Rows 1 and 5 - enhanced array shows almost identical behavior as that in the 4VG-enhanced array.

The end-view velocity and vorticity field results for Re = 850 are shown in Figures 4.70 – 4.72. At X^*=4.5 (Figure 4.70), the end-view velocity field (Figure 4.70(a)) shows four pairs of well-organized and coherent counter-rotating streamwise vortices. The vorticity field (Figure 4.70(b)) shows a highly anti-symmetrical counter-rotating vortex system. The streamwise vortices in this case show an oval or trapezoidal shape. For each vortex pair, counter-rotating secondary streamwise vortices are induced between the two primary vortices. The vorticity field shows a higher magnitude of peak vorticity and a more stable vortex structure than that of the 4VG-enhanced array (Figure 4.49).

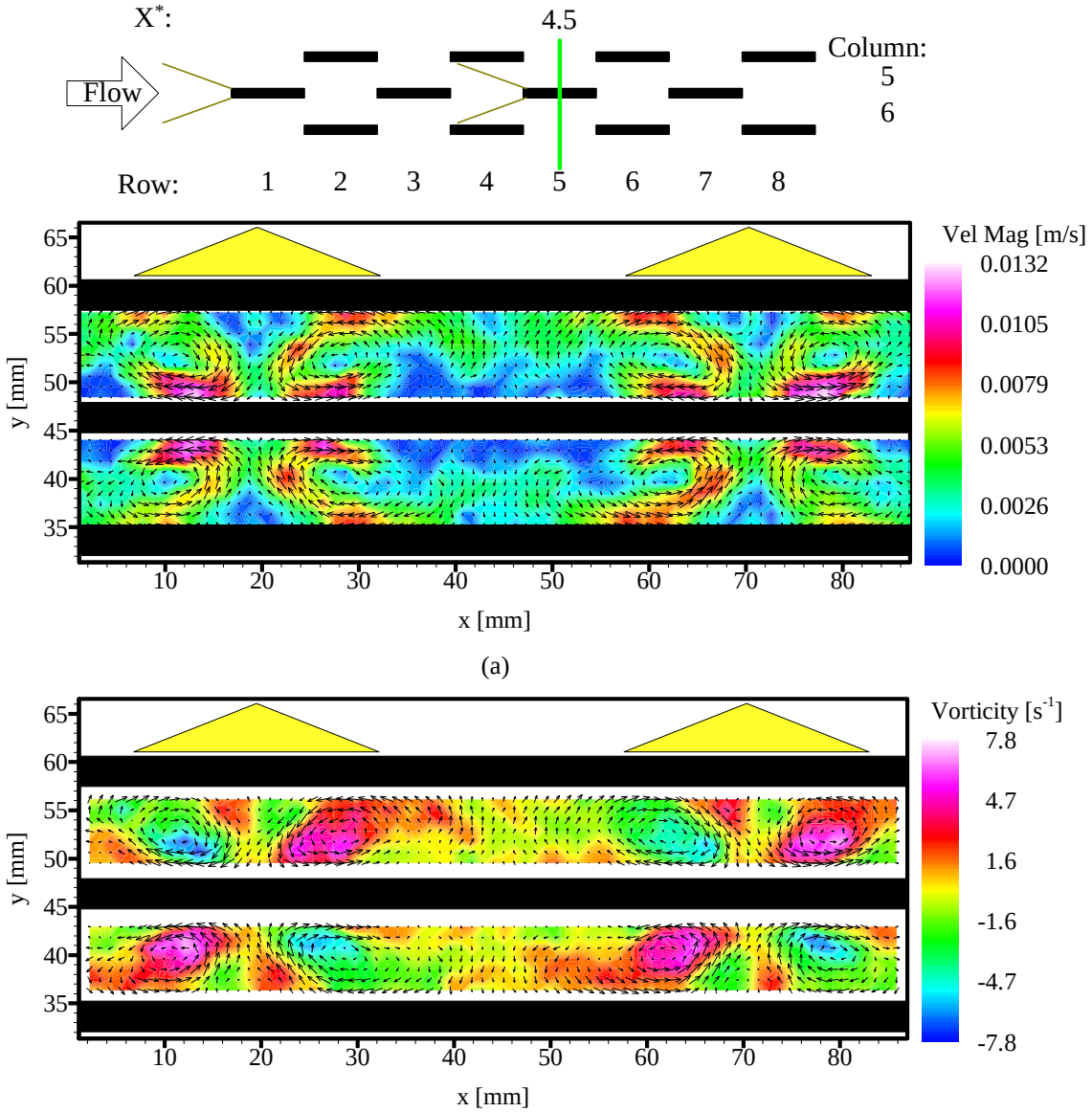

Figure 4.70 – 4VG at Rows 1 and 5 - enhanced array at Re = 850, X^* = 4.5: (a) instantaneous velocity magnitude; (b) instantaneous streamwise vorticity

The end-view velocity and vorticity field results at a downstream location of X^*=6.0 are shown in Figure 4.71. As the flow travels downstream to row 6, the 6th row fins drive the streamwise vortex cores away from their surfaces, which causes a portion of the vortical structures to impinge at the leading edge of the 7th row fins and generates high V-velocity component areas. This is evidenced in the end-view velocity field by four high-velocity pockets observed around the leading edge of the middle fin, as shown in Figure 4.71(a). The vorticity field (Figure 4.71(b)) shows more poorly organized primary streamwise vortices than at X^*=4.5.

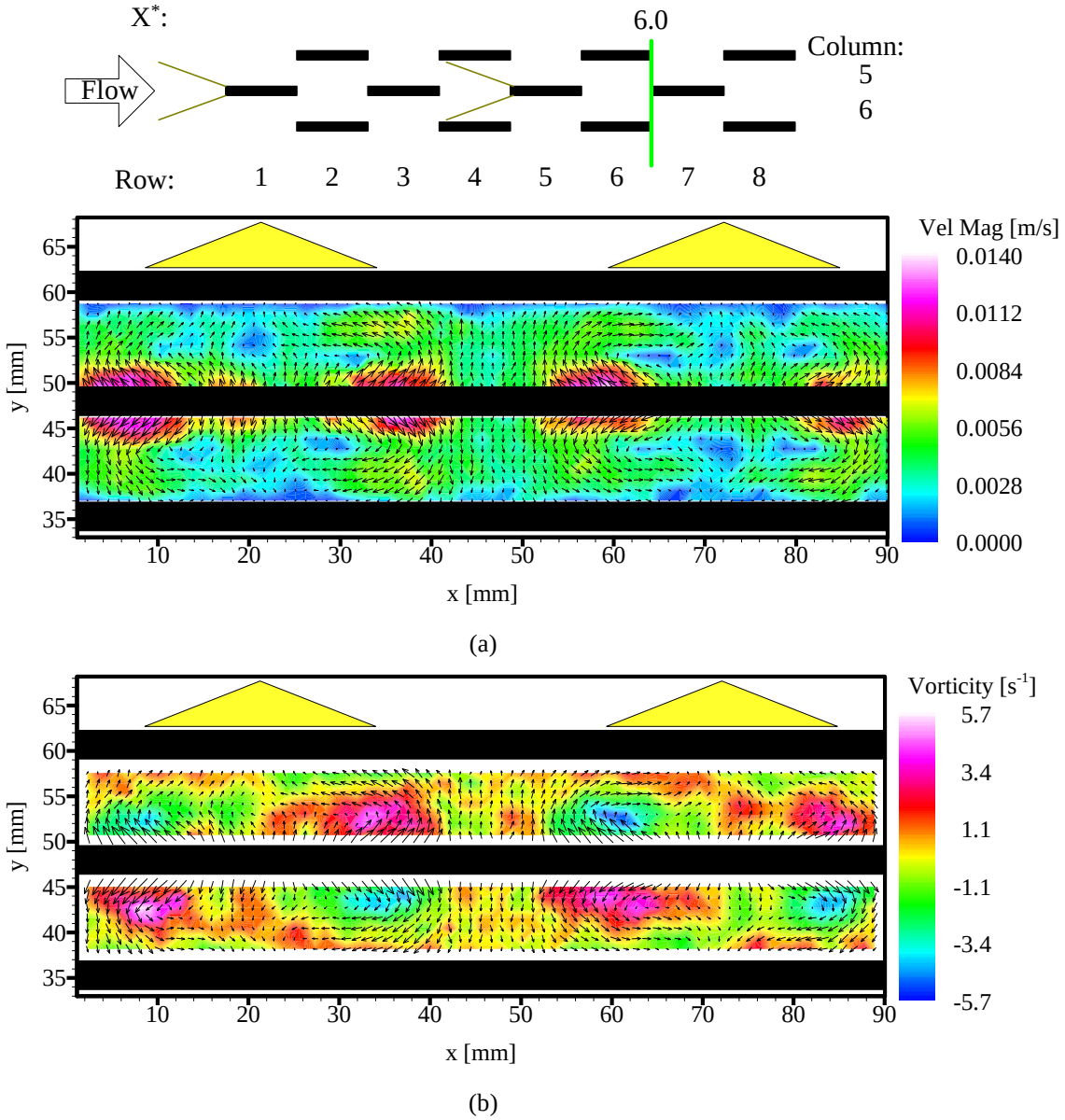

Figure 4.71 – 4VG at Rows 1 and 5 - enhanced array at Re = 850, X^* = 6.0: (a) instantaneous velocity magnitude; (b) instantaneous streamwise vorticity

As the flow approaches the trailing edge of the array (X^*=8.0), the flow becomes unsteady. However, the velocity field, as shown in Figure 4.72(a), still shows four high-velocity pockets in the wake of the 7th row fins, corresponding to the spanwise locations of the upstream primary vortices. The vorticity field results (Figure 4.72(b)) confirm that strong primary vortex pairs exist around the high-velocity pockets, as well as a number of small-scale vortical structures distributed throughout the field. The time-averaged velocity results (Figure 4.72(c)) show a more structured velocity field, with four high-velocity pockets and vortical fluid movement above and below these high-velocity pockets. In the time-averaged vorticity field (Figure 4.72(d)), the streamwise vortices in the center area of the field are stronger and better defined than the counter-rotating vortices at the left and right sides of the field.

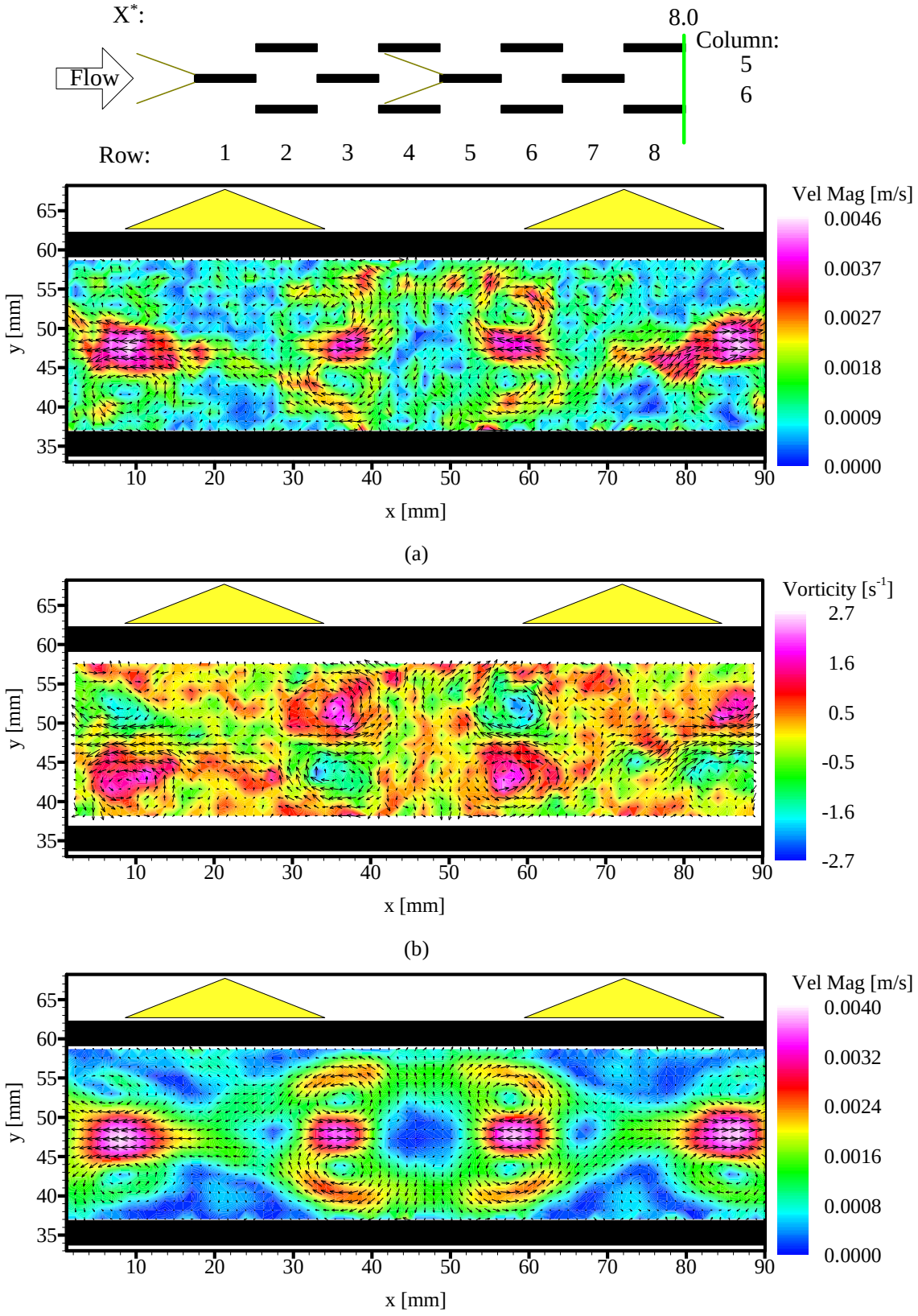
X*:
8.0
Column:
5
6
Flow
Row: 1 2 3 4 5 6 7 8
Vel Mag [m/s]
0.0046
0.0037
0.0027
0.0018
0.0009
0.0000
y [mm]
x [mm]
(a)
Vorticity [s-1]
2.7
1.6
0.5
-0.5
-1.6
-2.7
y [mm]
x [mm]
(b)
Vel Mag [m/s]
0.0040
0.0032
0.0024
0.0016
0.0008
0.0000
y [mm]
x [mm]
(c)

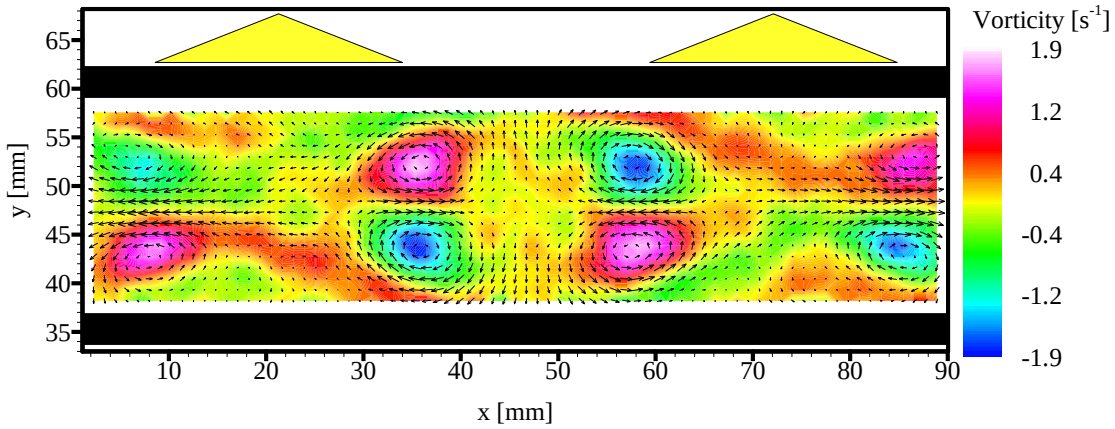

(d)

Figure 4.72 – 4VG at Rows 1 and 5 - enhanced array at Re = 850, X^* = 8.0: (a) instantaneous velocity magnitude; (b) instantaneous streamwise vorticity; (c) time-averaged velocity magnitude; (d) time-averaged streamwise vorticity

As the Reynolds number is increased to 1030, the flow field at X^*=4.5 is similar to that of Re = 850. However, the flow field at X^*=6.0 (Figure 4.73) starts to develop flow instabilities. The velocity field (Figure 4.73(a)) shows that the four high velocity pockets, observed in a regular pattern at Re = 850 (Figure 4.71(a)), become poorly structured and less coherent. Correspondingly, the vorticity field (Figure 4.73(b)) also reveals poorly organized streamwise vortices, with primary vortices breaking down into small-scale structures. The flow field at X^*=8.0 demonstrates similar behavior to that at Re=850, but with increased magnitudes of the velocity and vorticity.

As the Reynolds number is increased further to 1520, the incoming vortical flow in front of the row 5 delta wings becomes strong enough that the interaction between the incoming vortical flow and the re-generated streamwise vortices makes the flow field in the second half of the array more unsteady and less well structured, as confirmed by the end-view flow field results. At X^*=4.5, the velocity field (Figure 4.74 (a)) still shows vortical fluid movement, although the vortex shape is not as well-defined as that at Re = 850 (Figure 4.70(a)). In the vorticity field (Figure 4.74(b)), the primary streamwise vortices show less anti-symmetry of the counter-rotating vortex pairs, as is the case for the induced secondary streamwise vortices.

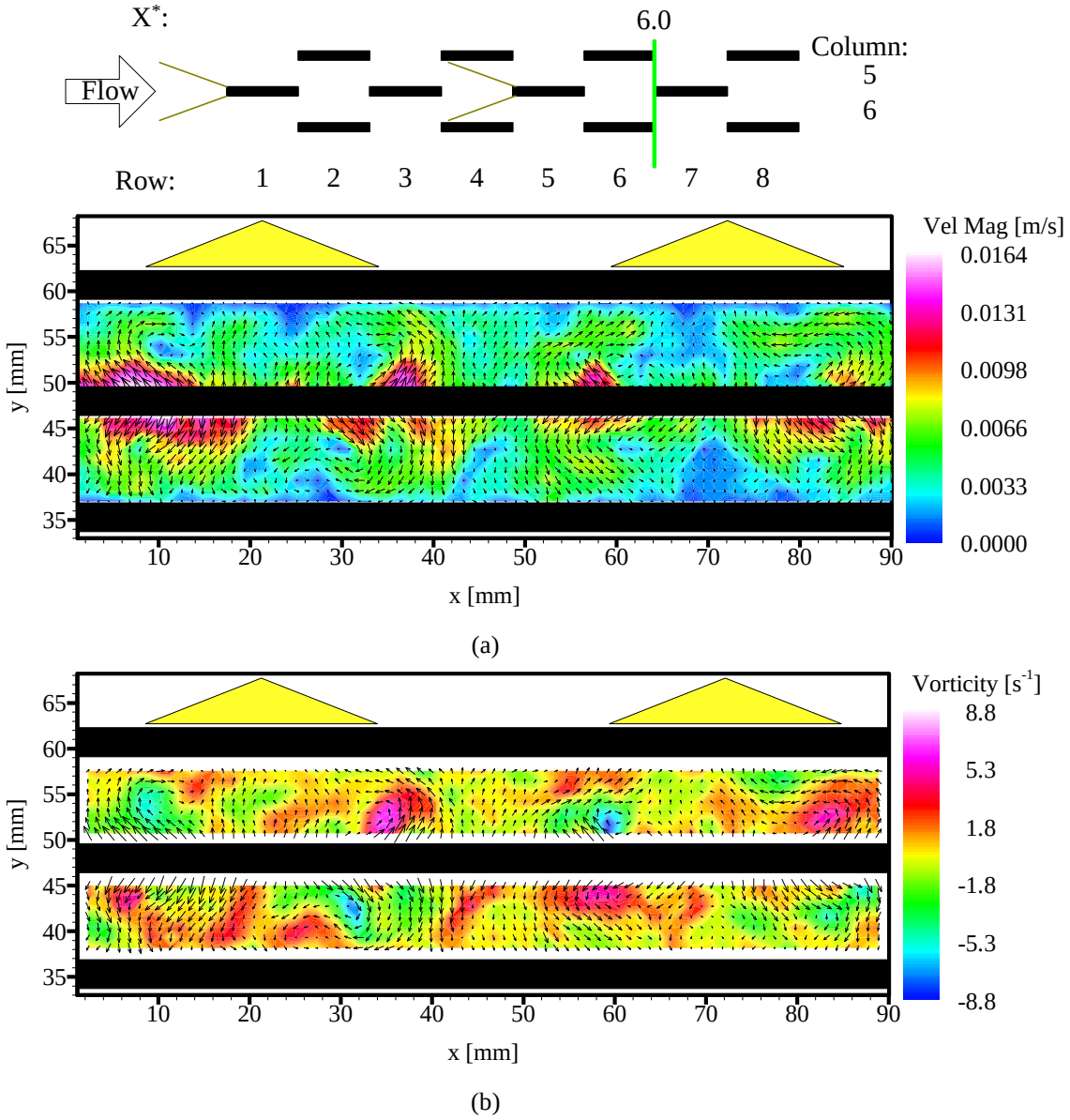

Figure 4.73 – 4VG at Rows 1 and 5 - enhanced array at Re = 1030, X^* = 6.0: (a) instantaneous velocity magnitude; (b) instantaneous streamwise vorticity

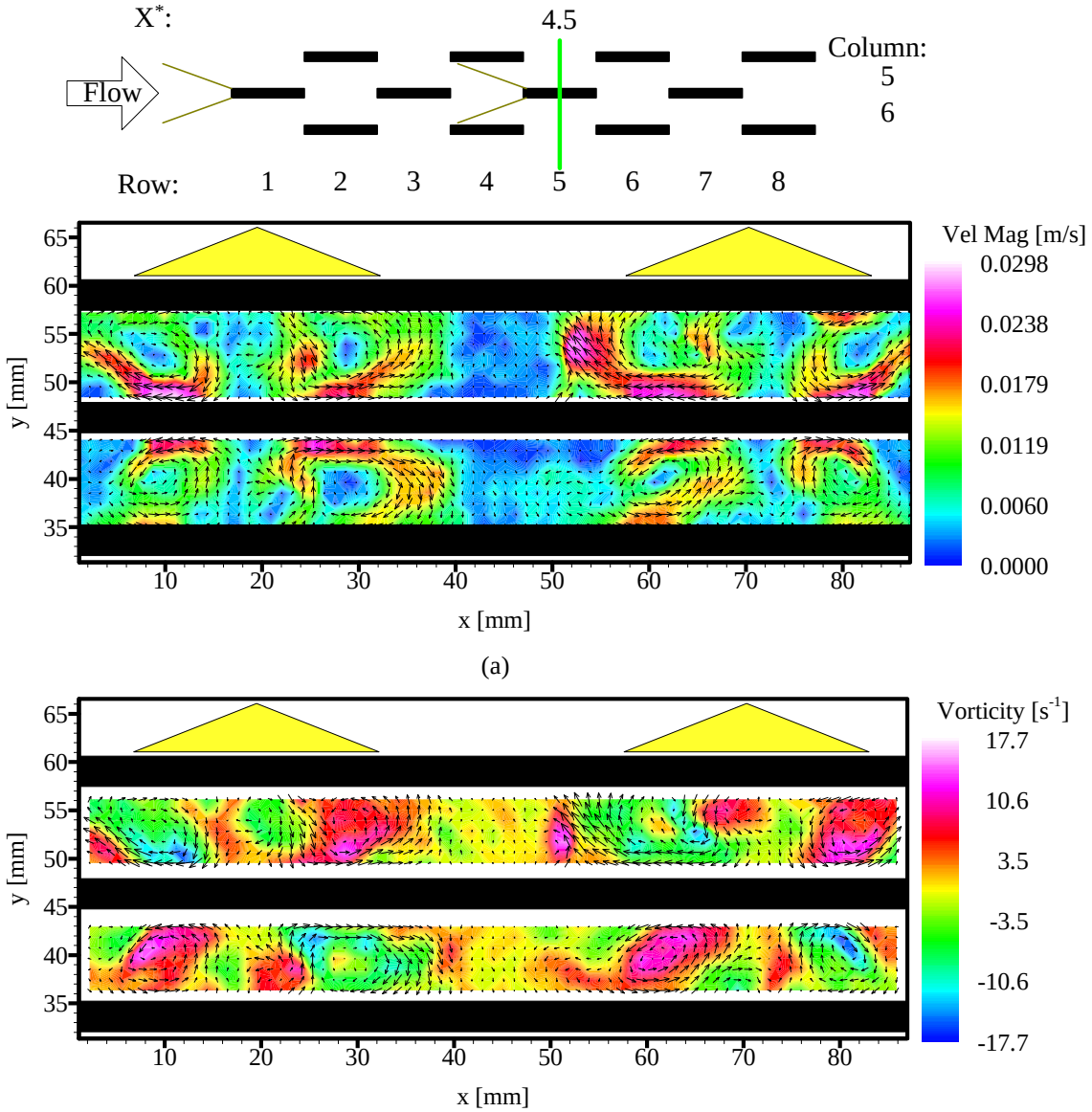

Figure 4.74 – 4VG at Rows 1 and 5 - enhanced array at Re = 1520, X^* = 4.5: (a) instantaneous velocity magnitude; (b) instantaneous streamwise vorticity

At the higher Reynolds number of 2450, the instantaneous flow field at the trailing edge of the array (X^*=8.0) is quite unsteady and chaotic. The time-averaged flow field results are shown in Figure 4.75. Among the four high-velocity pockets that is similar to those at lower Reynolds numbers, the two pockets in the middle become much weaker than the other pockets at the left and right sides. The vorticity field shows similar behavior, with stronger vortices at the left and right sides of the field and weaker vortices in the middle.

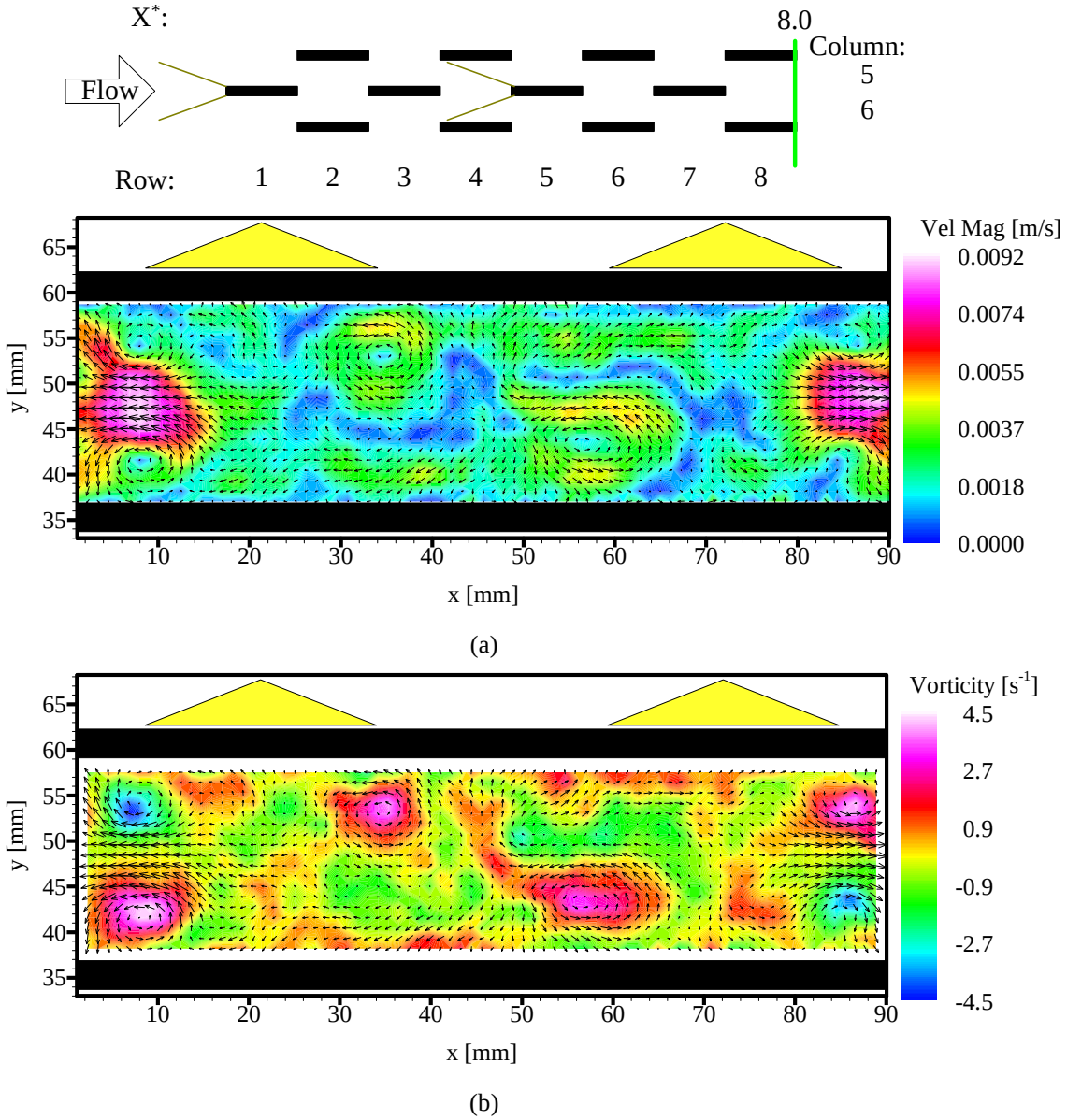

Figure 4.75 – 4VG at Rows 1 and 5 - enhanced array at Re = 2450, X^* = 8.0: (a) time-averaged velocity magnitude; (b) time-averaged streamwise vorticity

The end-view flow field at X^*=4.5 for Re = 3120 is shown in Figure 4.76. Compared to the same location for Re = 1520 (Figure 4.74), the magnitudes of maximum velocity and vorticity are much larger while the flow is more unsteady and chaotic. Smaller streamwise vortex structures with irregular shapes are observed.

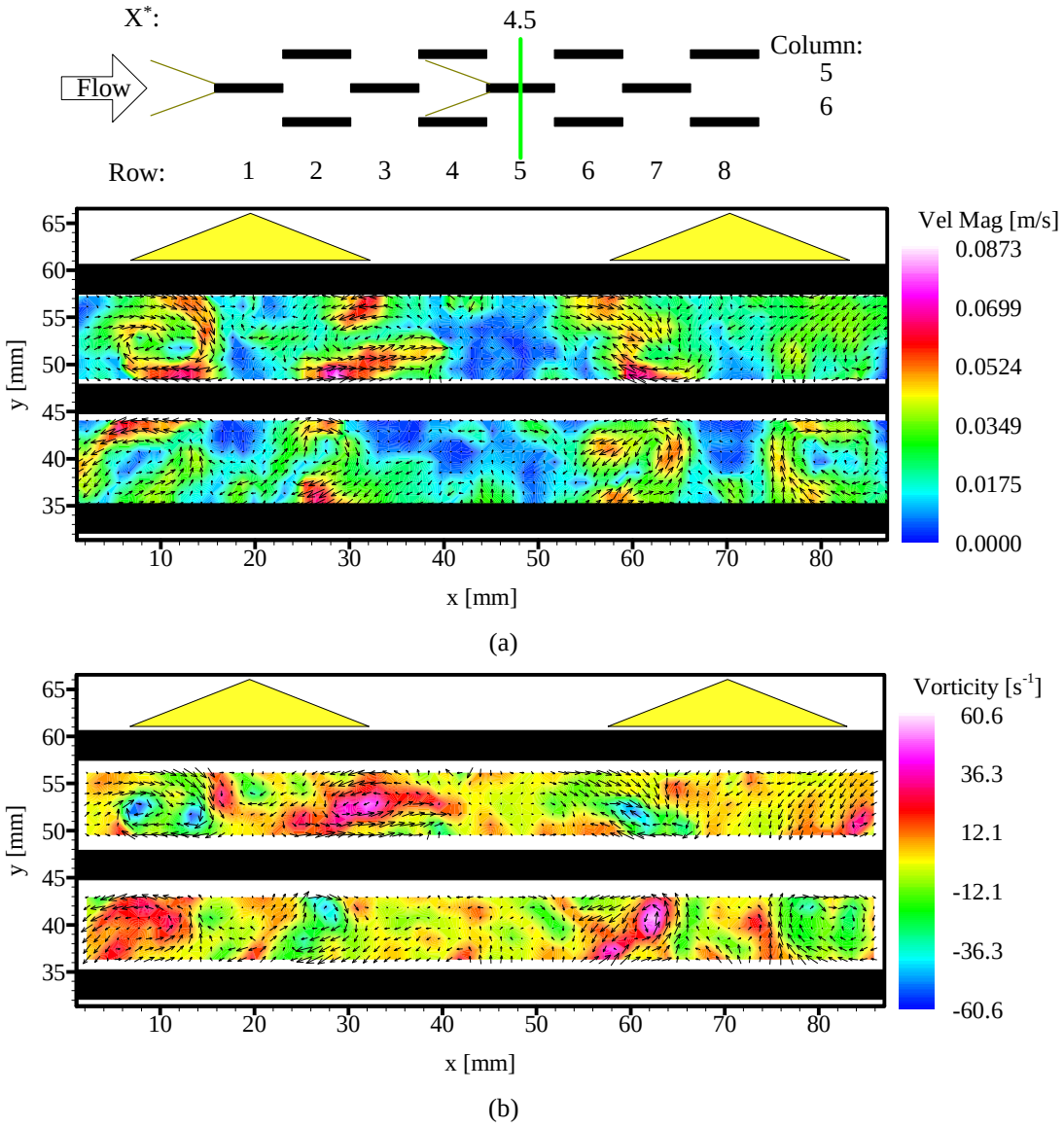

Figure 4.76 – 4VG at Rows 1 and 5 - enhanced array at Re = 3120, X^* = 4.5: (a) instantaneous velocity magnitude; (b) instantaneous streamwise vorticity

The re-generation of streamwise vortices greatly increases the maximum vorticity at X^*=4.5, X^*=6.0, and X^*=8.0. Figure 4.77 (a) shows the maximum vorticity throughout the 4VG at Rows 1 and 5 – enhanced array at various Reynolds numbers. The maximum streamwise vorticity of the 4th, 5th, and 6th rows is greatly enhanced at all Reynolds numbers, and the maximum vorticity magnitude decreases rapidly after the 6th row, where vortex breakdown is observed in the flow field. Figure 4.77 (b) shows the increase of maximum vorticity due to the second row of VGs at these three streamwise locations. The enhancement ratio of maximum vorticity at X^*=4.5 is found to be the largest for all Reynolds numbers, and is followed by that at X^*=6.0 and X^*=8.0. The enhancement of maximum vorticity for all three streamwise locations shows an identical pattern: the enhancement is high at Re = 850 and decreases as the Reynolds number increases. It reaches a minimum at Re = 1520 or Re = 1750, and then increases as the Reynolds number increases, except for Re = 3120 at X^*=8.0.

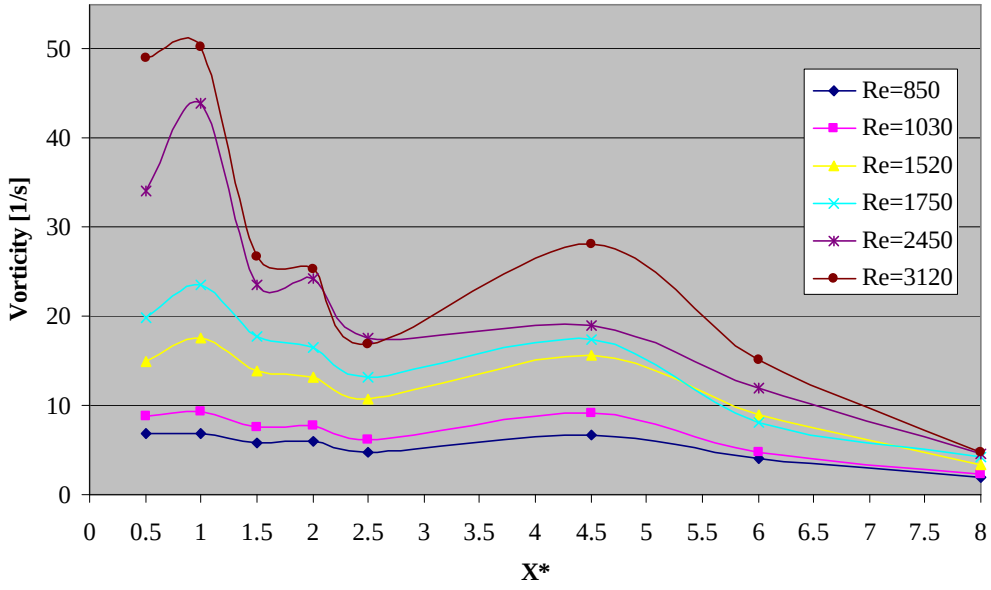

(a)

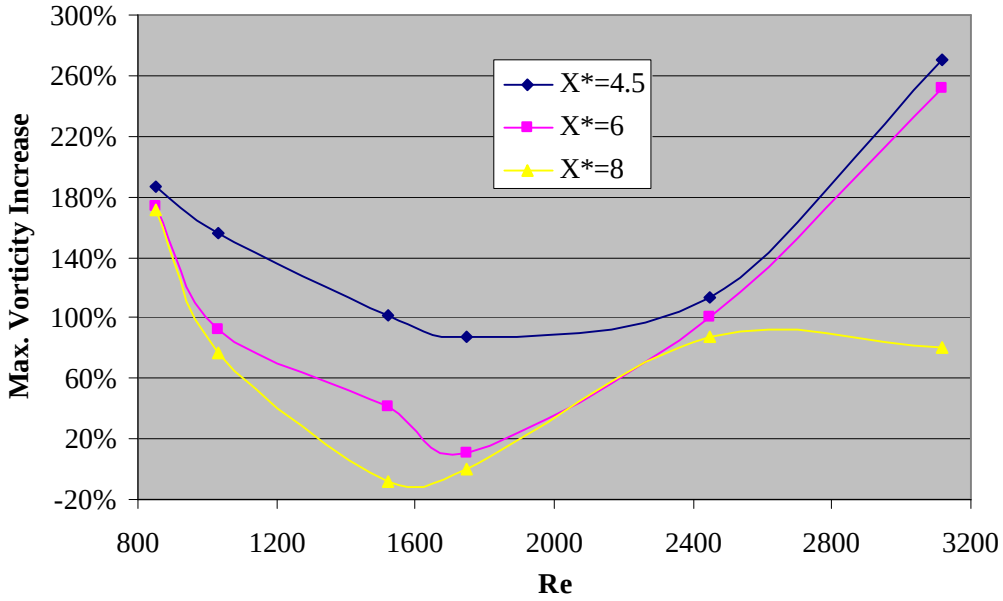

(b)

Figure 4.77 – 4VG at Rows 1 and 5 - enhanced array: (a) maximum vorticity for time-averaged vorticity fields at different streamwise locations; (b) increase of maximum vorticity due to the second row of vortex generators at leading edges of the 5th row fins

The re-generated streamwise vortices in the middle of the array are effective in enhancing the vorticity field in the middle of the array. However, the regenerated streamwise vortices are found to be weaker and decay more quickly in the flow direction than the streamwise vortices generated at the inlet of the array.

Chapter 5. Heat Transfer and Pressure Drop Behavior

In this chapter, the heat transfer and pressure drop behavior will be discussed for the baseline and all VG-enhanced arrays. Fin-averaged and local mass transfer experiments were performed and the results are presented here in the form of the Sherwood number, which is analogous to the Nusselt number for heat transfer performance. Naphthalene sublimation was adopted to obtain both the fin-averaged Sherwood numbers and the local distribution of Sherwood numbers on selected fin surfaces. The pressure drop across the array was measured directly with a differential pressure transducer, and the results are presented in the form of the friction factor *f*, as a function of the Reynolds number.

5.1 Fin-Averaged Mass Transfer Results

Naphthalene sublimation experiments were performed for the baseline array and all the enhanced arrays described in Section 2.3. The row-by-row fin-averaged results were obtained over a Reynolds number range from 400 to 3700. Fin-averaged mass transfer for the 8th row in the array was not measured for all naphthalene sublimation tests; the 8th row is subject to the exit effect, and it is not always desired to measure this effect to understand the performance of deep offset strip fin arrays.

5.1.1 Baseline Array

The fin-averaged row-by-row mass transfer results for the baseline array are shown in Figure 5.1. For Reynolds numbers up to about 1200, the Sherwood number decreases slightly or remains almost constant from the inlet to the exit row of the array. This finding suggests a laminar, steady, developing flow throughout the offset-strip fin array for Re less than or equal to 1200, which agrees with both the flow visualization and PIV results that show no vortex shedding in the array until Re = 1260.

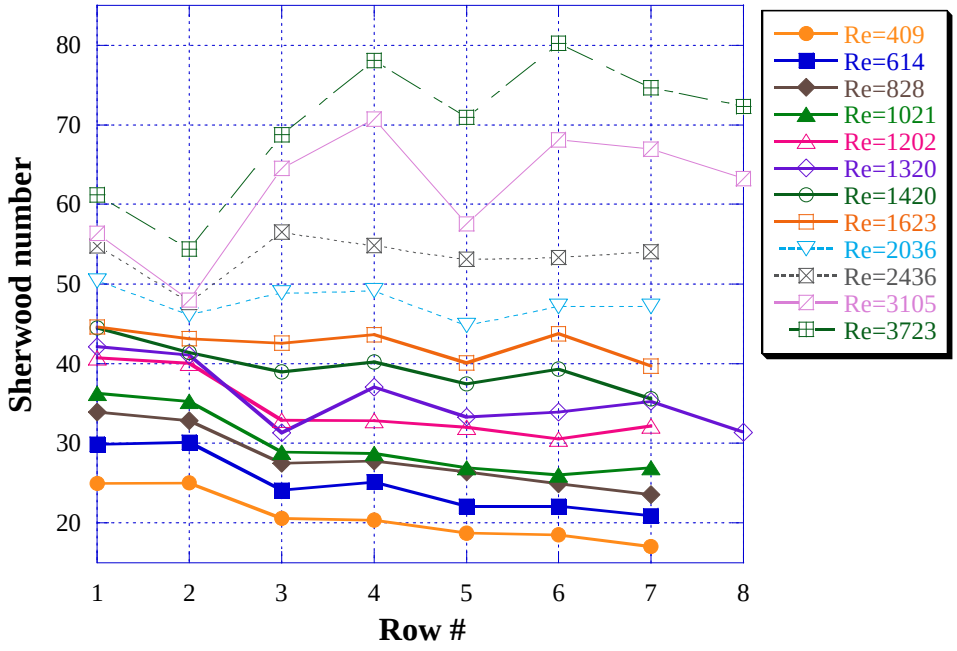

Figure 5.1 – Row-by-row mass transfer results for the baseline array

At Re = 1320, the Sherwood number shows a Sh increase from the 3rd row to the 4th row, as compared to that of Re = 1200. The flow visualization results reveal that spanwise vortex shedding starts at the 7th row in the baseline array for Re = 1260, while the PIV results show that shedding occurs at the 6th row at Re = 1280. Therefore, the Sh increase from the 3rd row to the 4th row suggests that spanwise vortex shedding may occur at the 4th row and all downstream rows for this Reynolds number; shedding improves fluid mixing and increases the heat transfer. The onset location of vortex shedding in the array is generally revealed by a dramatic increase in Sherwood number from one fin to the next. As the Reynolds number is increased to 1420, the onset location of vortex shedding moves to the 3rd row, as suggested by the Sherwood number increase for the 3rd row, as compared to lower Reynolds numbers.

As the Reynolds numbers is increased further, spanwise vortex shedding clearly begins to occur at the 3rd row fins. The mass transfer enhancement associated with vortex shedding is even greater for Reynolds numbers of 3105 to 3723. However, the mass transfer results do not reveal an onset of vortex shedding at the 1st or 2nd rows. The incoming flow for the 1st and 2nd rows (even at high Reynolds numbers) is almost uniform and steady, and spanwise vortex shedding occurs over a narrow Reynolds number range, with both rows showing a similar mass transfer enhancement. The uniform, laminar incoming flow does not create as strong spanwise vortex shedding as is manifest for the 3rd and following rows, which all have a wavy incoming flow. As a result, the mass transfer increases associated with spanwise shedding for the 1st and 2nd rows are smaller than those for the downstream rows at high Reynolds numbers. The flow visualization shows that shedding starts to occur at the 1st row at Re = 1940 and the structure of vortex shedding is much weaker than that for the downstream rows. The PIV results show flow instability at the 1st and 2nd rows for Re > 1750 and stronger vortex shedding at downstream rows. The mass transfer results therefore compare favorably with both the flow visualization data and the PIV data.

5.1.2 2VG-Enhanced Array

The 2VG-enhanced array, as shown in Figure 2.11(a), is asymmetrical in geometry. Streamwise vortices are only generated in the flow channel above the first row fins, not in the channel below the first row fins; therefore, the heat transfer behavior between the top and bottom fin surfaces in this array are quite different. In order to obtain the overall heat transfer of the fins in this array, both the top and bottom surface heat transfer were measured in separate runs to determine the average for each fin.

Figure 5.2 shows the row-by-row averaged Sherwood numbers over a Reynolds number range from 409 to 3723 for this array. The data indicate a laminar flow without vortex shedding for Reynolds numbers of 1230 and smaller. At Re = 1638, there is a small Sherwood number increase for the 6th row, which suggests that spanwise vortex shedding may occur at row 6. As the Reynolds number is increased to 2040, an increase in Sherwood number is clearly observed at the 3rd row, indicating the onset of vortex shedding at the 3rd row. As compared to the baseline array, which sheds vortices at the 4th row when Re = 1320 and the 3rd row when Re = 1420, the onset of vortex shedding in the 2VG-enhanced array is clearly delayed to higher Reynolds numbers.

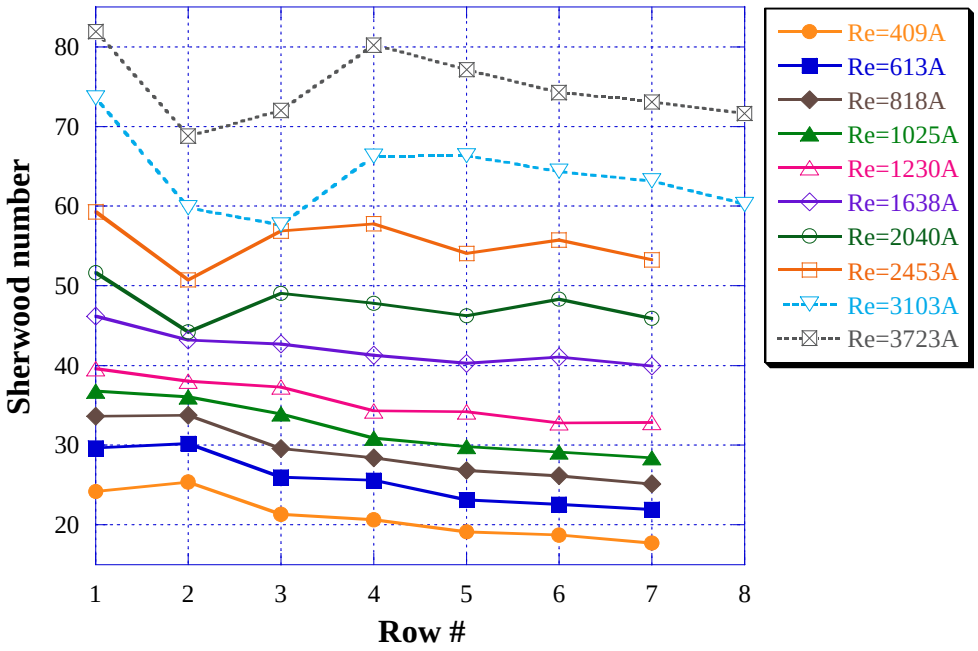

Figure 5.2 – Row-by-row mass transfer results for the 2VG-enhanced array ("A" in the legend means that the Sherwood number is averaged over the top and bottom surfaces)

Flow visualization for the same baseline and 2VG-enhanced arrays was reported by Smotrys *et al.* (2001). Their results show that the 2VG-enhanced array starts to shed spanwise vortices at a higher Reynolds numbers than the baseline array, and the spanwise vortex structure in the 2VG-enhanced array suggests smaller and weaker vortices than that in the baseline array at the same Reynolds number. These earlier findings are corroborated by the row-by-row mass transfer data shown in Figure 5.2.

5.1.3 4VG-Enhanced Array

Figure 5.3 shows the Sherwood number at different Reynolds numbers for the 4VG-enhanced array (Figure 2.11 (b)). On the basis of the flow visualization results, the flow is laminar and no spanwise vortex shedding occurs for Reynolds numbers up to 1438. For these conditions, the streamwise vortices are the only flow mechanism contributing to a heat transfer enhancement. This enhancement is diminished as the streamwise vortices are carried downstream and their strength decreases. As the Reynolds number is increased, vortex shedding first occurs at the downstream fins, as observed in flow visualization and PIV results. Vortex shedding increases fluid mixing and enhances heat transfer. As the Reynolds number increases further, the onset location of vortex shedding moves upstream, and the spanwise vortices become stronger. Meanwhile, the streamwise vortices become less organized at downstream locations, owing to interactions with spanwise vortices. When vortex shedding dominates the secondary flow, a jump in Sherwood number from one row to the next occurs, as reflected in Figure 5.3 for the 3rd row at Re = 1641 and higher. Clearly, spanwise vortex shedding is present at the 3rd row when Re = 1641, which agrees well with the flow visualization results. The streamwise vortex shedding at the 3rd and following rows becomes stronger as the Re is increased to 2089 and 2458. The second row starts to show significant mass transfer enhancement as Re is increased to 3107 and 3723, indicating the occurrence of spanwise vortices at the 2nd row for these Reynolds numbers.

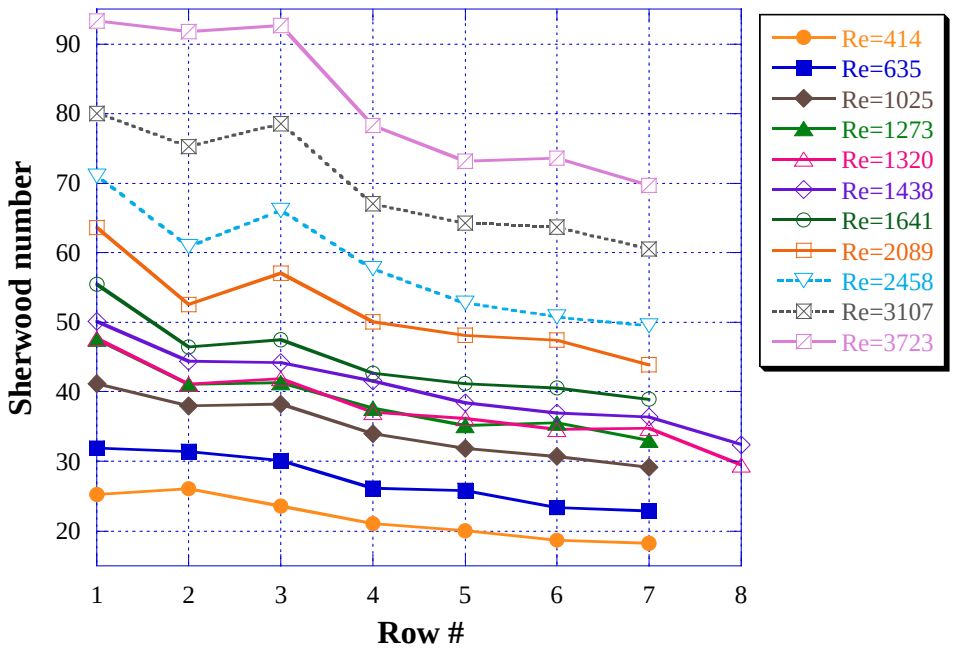

Figure 5.3 – Row-by-row mass transfer results for the 4VG-enhanced array

5.1.4 4VG Staggered-Enhanced Array

The 4VG staggered-enhanced array has 4VGs placed on the top and bottom surfaces of the leading fins in a staggered arrangement, as shown in Figure 2.11 (c). Due to the staggered arrangement, the V-component velocity of the streamwise vortices generated by upward-pointed VGs tends to cancel the V-component velocity of the streamwise vortices generated by downward-pointed VGs. This opposing arrangement of the streamwise vortices causes a diminished heat transfer effect for this arrangement of VGs. The fin-averaged Sherwood numbers for the 4VG staggered-enhanced array is shown in Figure 5.4. Spanwise shedding starts at the 3rd row when Re = 1648. A further increase of the Reynolds number to 2462 and 3081 causes a corresponding increase in Sherwood number, which is more significant for the 4th and downstream rows than for the first 3 rows. However, the magnitude of the Sherwood number for this enhanced array is significantly lower than that of the 4VG-enhanced array at similar Reynolds numbers, due to the vorticity cancellation effect mentioned above.

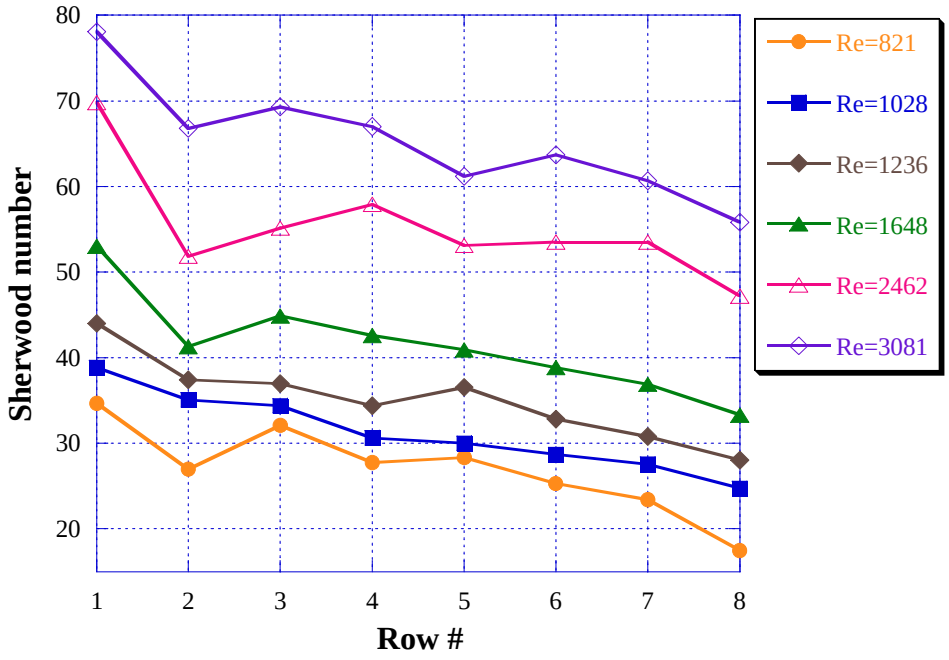

Figure 5.4 – Row-by-row mass transfer results for the 4VG staggered-enhanced array

5.1.5 8VG-Enhanced Array

Since the base length and aspect ratio of the delta wings used in the 8VG-enhanced array are half of those in the 4VG-enhanced array (Figure 2.11 (d)), the total surface area of the delta wings for the 8VG-enhanced array is the same as that of the 4VG-enhanced array. Figure 5.5 shows the fin-averaged Sherwood numbers for the 8VG-enhanced array. Introducing twice the number of streamwise vortices into the flow, results in the Sherwood numbers of the first and third rows being greatly enhanced at all Reynolds numbers, due to the strong downwash effect of the streamwise vortices. The mass transfer results reveal that the flow is laminar and no spanwise vortex shedding occurs for Reynolds numbers up to 1634. The streamwise vortices contribute solely to the heat transfer enhancement. As the Reynolds number is increased to 2028, the 6th row shows signs of spanwise vortex shedding. The onset location of spanwise vortex shedding moves upstream to the 5th row as Re is increased further to 2431, where the effect of the spanwise vortices starts to dominate the streamwise vortices.

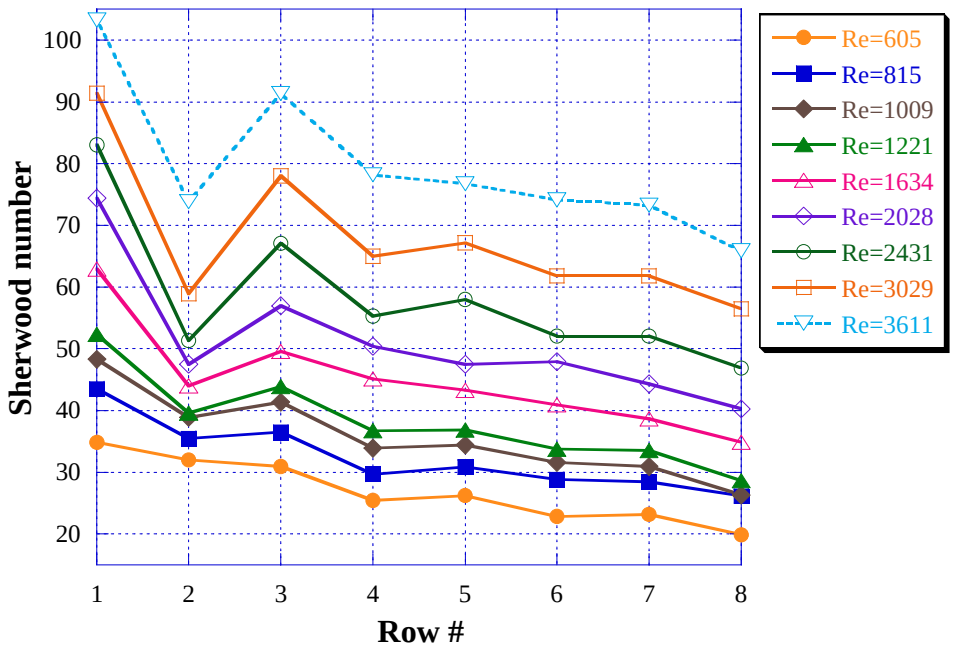

Figure 5.5 – Row-by-row mass transfer results for the 8VG-enhanced array

5.1.6 4VG at Rows 1 and 5 - Enhanced Array

Figure 5.6 shows the Sherwood number at different Reynolds numbers for the 4VG at Rows 1 and 5 - enhanced array. In this array, a second row of delta wings is attached at the leading edge of the fifth row. The tips of the delta wings at the 5th row point forward into the 4th row flow channel and are very close to the fourth row fin surfaces, as shown in Figure 2.12. Therefore, streamwise vortices are re-generated in both the 4th row area and the leading edges of the fifth row. As a result, greater Sherwood number enhancement is experienced at the 4th row and downstream rows throughout the Reynolds number range, as evidenced by the mass transfer results shown in Figure 5.6. The Sherwood number enhancement at the 4th row is larger than that at the 3rd and 5th rows, especially at low Reynolds numbers. As compared to the Sherwood number for the 4VG-enhanced array shown in Figure 5.3, the regeneration of streamwise vortices for this array produces significant heat transfer enhancement for the second half of the array, as well as the 4th row. The Sherwood number results for Re = 1645 show that the Sherwood number decreases dramatically from the sixth row to the eighth row, which indicates that the regenerated streamwise vortices degrade faster in the streamwise direction than the streamwise vortices generated at the inlet of the array. This finding is in excellent agreement with the flow visualization and PIV results presented in Chapter 4.

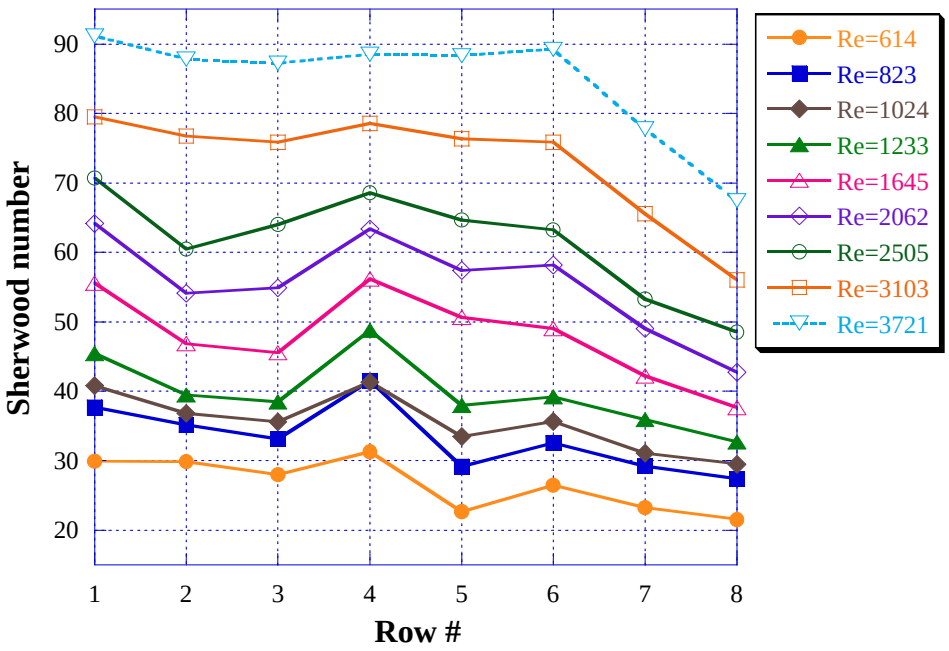

Figure 5.6 – Row-by-row mass transfer results for the 4VG at Rows 1 and 5 - enhanced array

5.1.7 8VG at Rows 1 and 5 - Enhanced Array

The fin-averaged mass transfer results for the 8VG at Rows 1 and 5 – enhanced array are shown in Figure 5.7. The 1st, 2nd, and 3rd rows show very similar magnitude and pattern in Sherwood number as found for the 8VG-enhanced array. The introduction of the second row of delta wings dramatically increases the Sherwood numbers for the 4th and 5th rows. The rest of the array from the 6th to 8th rows also shows some improvement in the Sherwood number, but not as great as for the 4th and 5th rows. This finding further confirms that the non-uniform incoming flow in front of the second row of delta wings causes the re-generated streamwise vortices to become weak and disorganized faster than streamwise vortices introduced at the array inlet.

5.1.8 Array Mass Transfer Performance

In order to evaluate the enhancement potential of the various VG configurations, the array performance averaged over rows 1 to 7 is presented in Figure 5.8. The ratios of averaged Sherwood number for the enhanced arrays over that for the baseline array are shown at different Reynolds numbers.

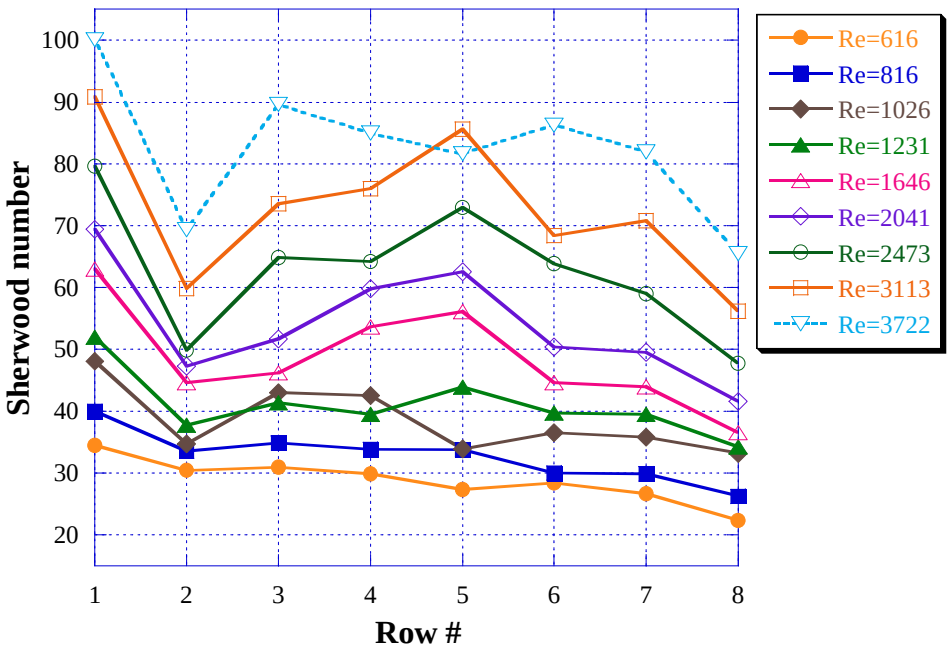

Figure 5.7 – Row-by-row mass transfer results for the 8VG at Rows 1 and 5 - enhanced array

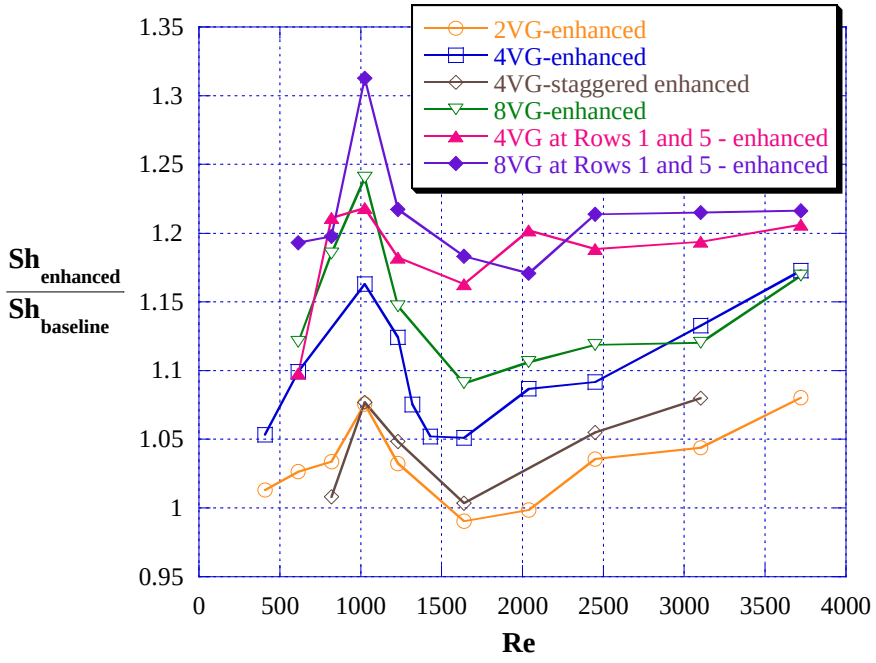

Figure 5.8 – Enhancement of array-wise Sherwood number averaged over the first seven rows for all VG-enhanced arrays at various Reynolds numbers

For the four enhanced arrays with VGs only at the inlet fins, Sherwood number enhancement occurs even for very low Reynolds numbers and the enhancement increases with increasing Reynolds number. The enhancement reaches a maximum at around Re = 1000. Figure 5.9 shows the Sherwood numbers for the baseline, 2VG-enhanced, 4VG-enhanced, and 8VG-enhanced arrays at Re = 1020. The enhanced arrays show Sherwood number enhancement for every row in the array at this Reynolds number. The 8VG-enhanced array has the greatest enhancement for every

row, with the 4VG-enhanced array the second greatest, and the 2VG-enhanced array the least enhancement. In this Reynolds number range of Re = 1020, no vortex shedding occurs in the array for the baseline array, and the heat transfer enhancement for the three enhanced arrays is caused by the streamwise vortices only.

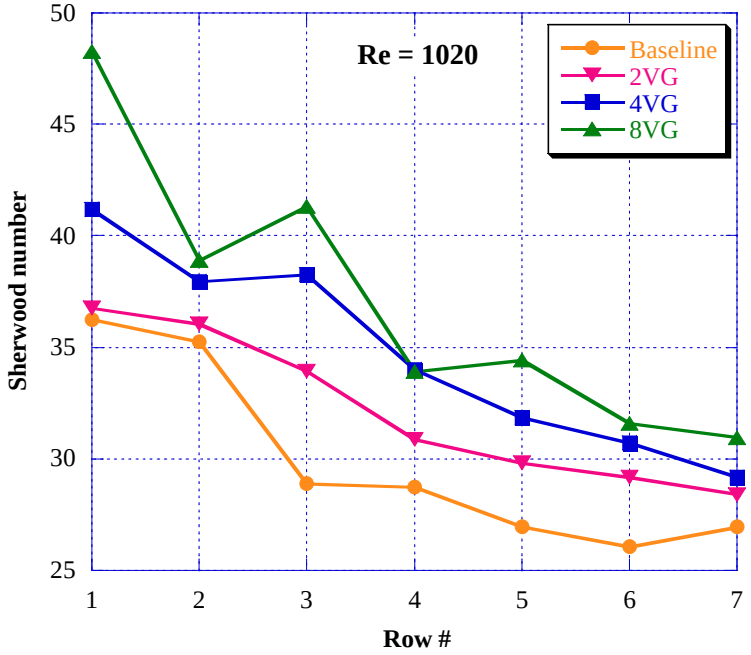

Figure 5.9 – Fin-averaged Sherwood numbers at Re = 1020

As the Reynolds number is increased further, the array-averaged Sherwood number starts to decrease for all VG-enhanced arrays as shown in Figure 5.8. The enhancement effect is at a minimum around Re = 1630 for all enhanced arrays. The Sherwood numbers of the baseline, 2VG-enhanced, 4VG-enhanced, and 8VG-enhanced arrays at Re = 1630 are shown in Figure 5.10. Additional experimental results for the 4VG-enhanced array between Re = 1230 and Re = 1630 show that the array-averaged Sherwood number reaches a minimum at Re = 1440 and remains at that low Sherwood number between Re = 1440 and Re = 1630. At Re = 1440, the flow visualization results for the baseline array show that spanwise vortex shedding occurs from the 3rd row, which contributes to the Sherwood number increase for the downstream rows in that array. However, the Sherwood numbers of the same downstream rows for the three enhanced arrays with the presence of streamwise vortices, as shown in Figure 5.10, are not enhanced at the same level as for the baseline array. The average Sherwood number of those four downstream rows starting from the 4th row for the baseline array is generally higher than for the 2VG-enhanced and 4VG-enhanced arrays, and almost the same as for the 8VG-enhanced array. On the basis of the naphthalene sublimation, flow visualization, and PIV results, it is believed that the streamwise vortices suppress spanwise vortex shedding, and either delay to a higher Reynolds number or weaken spanwise vortex shedding in the regions adjacent to the streamwise vortices, in this Reynolds number range. Therefore, the fluid mixing effect over the array is decreased, especially for downstream rows, which results in the decreasing trend of the Sherwood number enhancement between Re = 1020 and 1630 with a minimum enhancement around Re = 1600 for all enhanced arrays investigated in this research. In this Reynolds number range from 1020 to 1630, the first three rows for all enhanced arrays are

still enhanced by the streamwise vortices (see Figures 5.9 and 5.10). The enhancement generated by the streamwise vortices is greater than the decrease caused by the suppression or weakening of spanwise vortex shedding for the first three rows. For the 2VG-enhanced array, the array performance is decreased due to the weaker streamwise vortices of this case, which could not overcome the heat transfer decrease of the weakened spanwise vortex shedding.

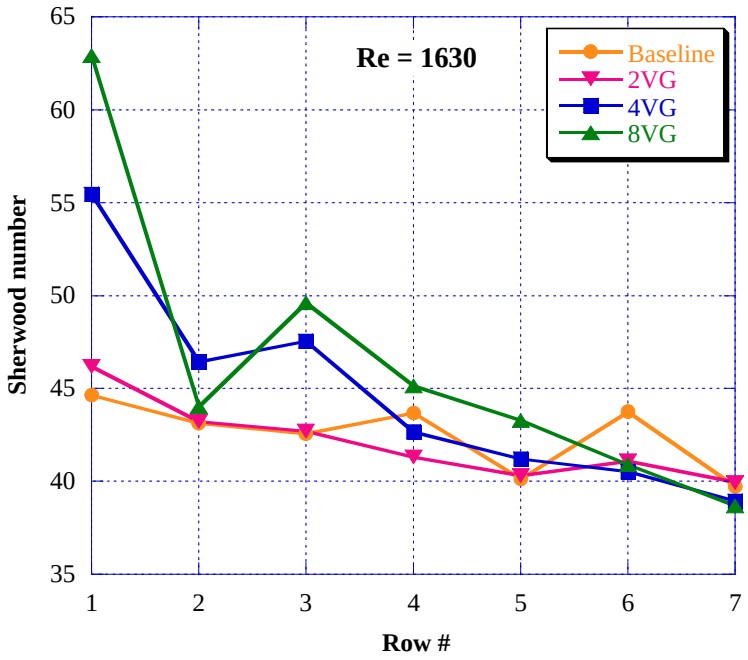

Figure 5.10 – Fin-averaged Sherwood numbers at Re = 1630

As the Reynolds number is increased further to 2040 and higher, the increase of Sherwood number enhancement with increasing Reynolds number returns, as shown in Figure 5.8. In order to understand the enhancement at high Reynolds numbers, Sherwood numbers for the baseline, 2VG-enhanced, 4VG-enhanced, and 8VG-enhanced arrays at Re = 2450 and Re = 3720 are shown in Figure 5.11 and Figure 5.12, respectively. At both Reynolds numbers, the average Sherwood number for the last four rows for all three enhanced arrays is almost the same as for the baseline array, which indicates no difference in the average heat transfer of the last four rows as the flow field becomes chaotic and both spanwise and streamwise vortex structures become disorganized in the last four rows. This finding is in agreement with the flow visualization results presented in Chapter 4. The flow visualization results for the baseline array show that spanwise vortices shed from the 1st row and become disorganized downstream of the 4th row for Re = 1940. For all three VG-enhanced arrays, the flow visualization shows that both the streamwise and spanwise vortices become disorganized downstream of the 4th row for Reynolds numbers higher than 1980. The naphthalene sublimation results reveal that the average heat transfer enhancement is similar once the flow becomes chaotic. Although the three enhanced arrays do not gain a clear heat transfer increase for the last four rows, they show significant heat transfer increase over the baseline array for the first three rows, due to the strong streamwise vortices generated at the inlet of the array. The average enhancement for the first three rows increases with increasing Reynolds numbers due to the stronger streamwise vortices at higher Reynolds numbers.

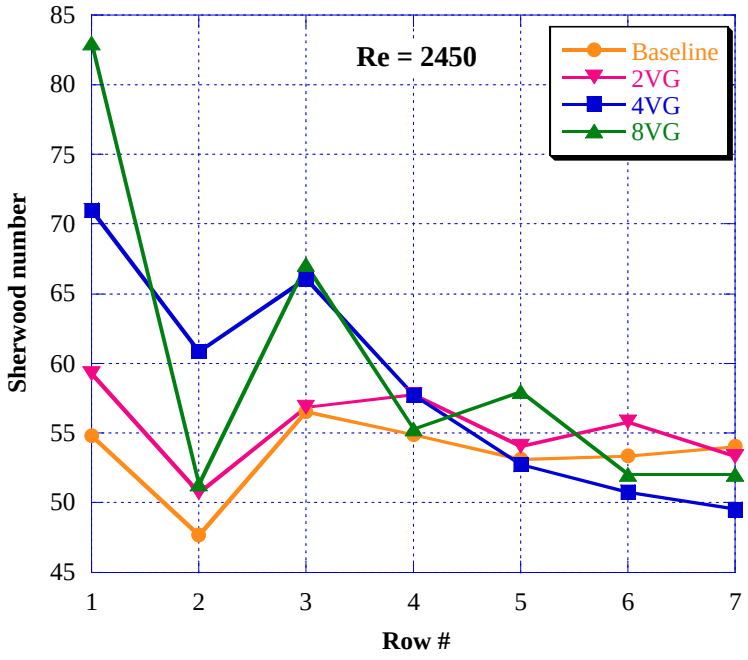

Figure 5.11 – Fin-averaged Sherwood numbers at Re = 2450

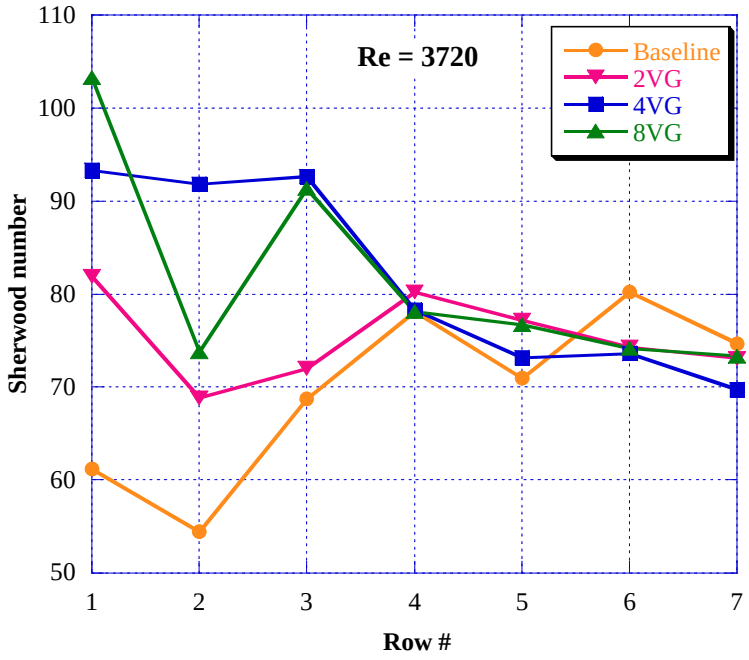

Figure 5.12 – Fin-averaged Sherwood numbers at Re = 3720

The maximum enhancement for all enhanced arrays occurs around Re = 1000, and is about 16% for the 4VG-enhanced array and 24% for the 8VG-enhanced array. The 4VG-staggered enhanced array shows much less enhancement than the 4VG-enhanced array, because the vortices generated by adjacent staggered delta wings tend to weaken each other, decreasing their overall vortex strength.

For the two enhanced arrays with delta wings at both the 1st and 5th rows, even greater array-wise enhancements are observed. Both of these arrays show the same trend with increasing Reynolds number as for the inlet-only vorticity generation approach, except that the enhancement becomes almost constant for all Reynolds numbers exceeding about 2000. Again, the maximum enhancement occurs at Re ≅ 1000, which is about 22% for the 4VG at Rows 1 and 5 - enhanced array and 32% for the 8VG at Rows 1 and 5 - enhanced array.

Thus, a Reynolds number of about 1000 is the preferred Reynolds number for delta-wing enhanced offset-strip fin arrays, with the highest array-wise heat transfer enhancement over a Reynolds number range from 400 to 3700. Most HVAC applications operate in this low Reynolds number range, and could take full advantage of delta-wing enhanced offset-strip fin arrays.

5.2 Fin-Local Mass Transfer Results

Local Sherwood number distributions on the fin surfaces were determined by combining the naphthalene sublimation technique and the laser profilometry technique. Three arrays, including the baseline, 4VG-enhanced, and 4VG at Rows 1 and 5 – enhanced array, were investigated by measuring the fin-local Sherwood number distributions. Each array was measured at three Reynolds numbers Re ≅ 1000, Re ≅ 1600 and Re ≅ 3000. For the 4VG at Rows 1 and 5 – enhanced array, sublimation from only the second half of the array (rows 5, 6, 7 and 8) was measured, because the first half of the array is similar to that of the 4VG-enhanced array.

5.2.1 Baseline Array

The fin-local mass transfer results for the baseline array are given in Figures 5.13 to 5.15. The local Sherwood numbers for 38 streamwise locations from the leading edge to the trailing edge of each fin represent an average of the 80 spanwise points at each corresponding streamwise location. The local Sherwood number for the baseline array is very nearly uniform across the fin span at each streamwise location, as expected.

Figure 5.13 shows the local Sherwood number distribution along the flow direction for all eight rows of the baseline array at Re = 1030. The local Sherwood number distribution for all eight rows shows clear evidence of boundary layer restarting. The Sherwood number is high at the leading edge and decreases rapidly in the flow direction, due to boundary layer growth. When the flow approaches the trailing edge, the Sherwood number increases slightly due to the flow acceleration caused by the reduced flow area as the next fin row is approached.

Figure 5.14 shows the local Sherwood number distribution along the flow direction for all eight rows of the baseline array at Re = 1640. Similar to the Re = 1030 case, all eight rows reveal evidence of boundary layer restarting. The Sherwood number is high at the leading edge, decreases rapidly in the flow direction, and increases as the flow accelerates slightly at the trailing edge. However, for rows 3 to 6, the Sherwood number increase starts at around 60% of the fin length, closer to the leading edge than for the same rows at Re = 1030. The magnitude of the increase near the trailing edge is also larger than that at Re = 1030. These results indicate that spanwise vortex shedding occurs on the fin surfaces of these rows. The spanwise vortices increase the flow mixing, and as a result, the heat transfer enhancement is more evident at streamwise locations closer to the leading edge.

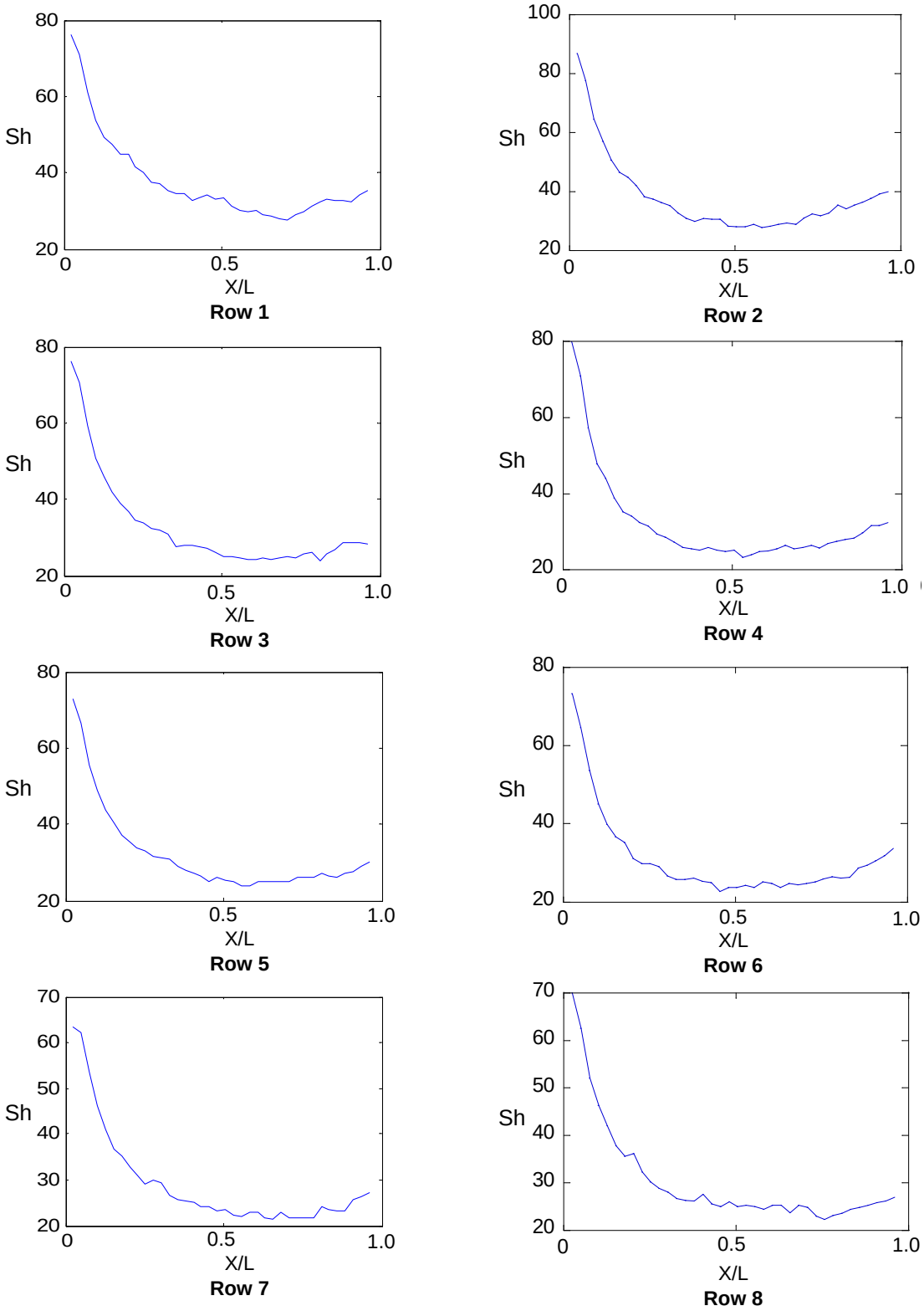

Figure 5.13 – Local Sherwood number distribution for the baseline array at Re = 1030 (X: distance from leading edge; L: fin length)

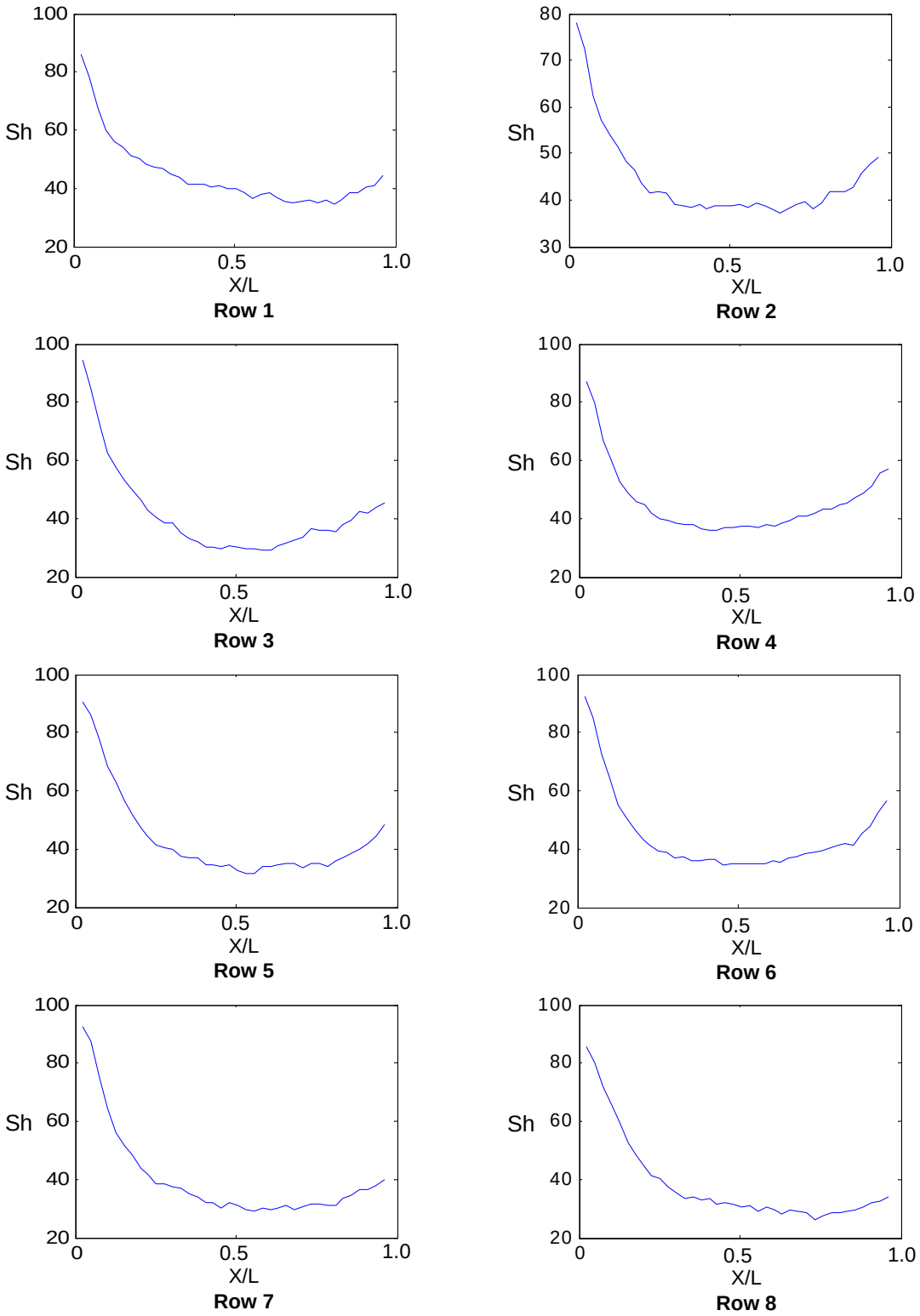

Figure 5.14 – Local Sherwood number distribution for the baseline array at Re = 1640 (X: distance from leading edge; L: fin length)

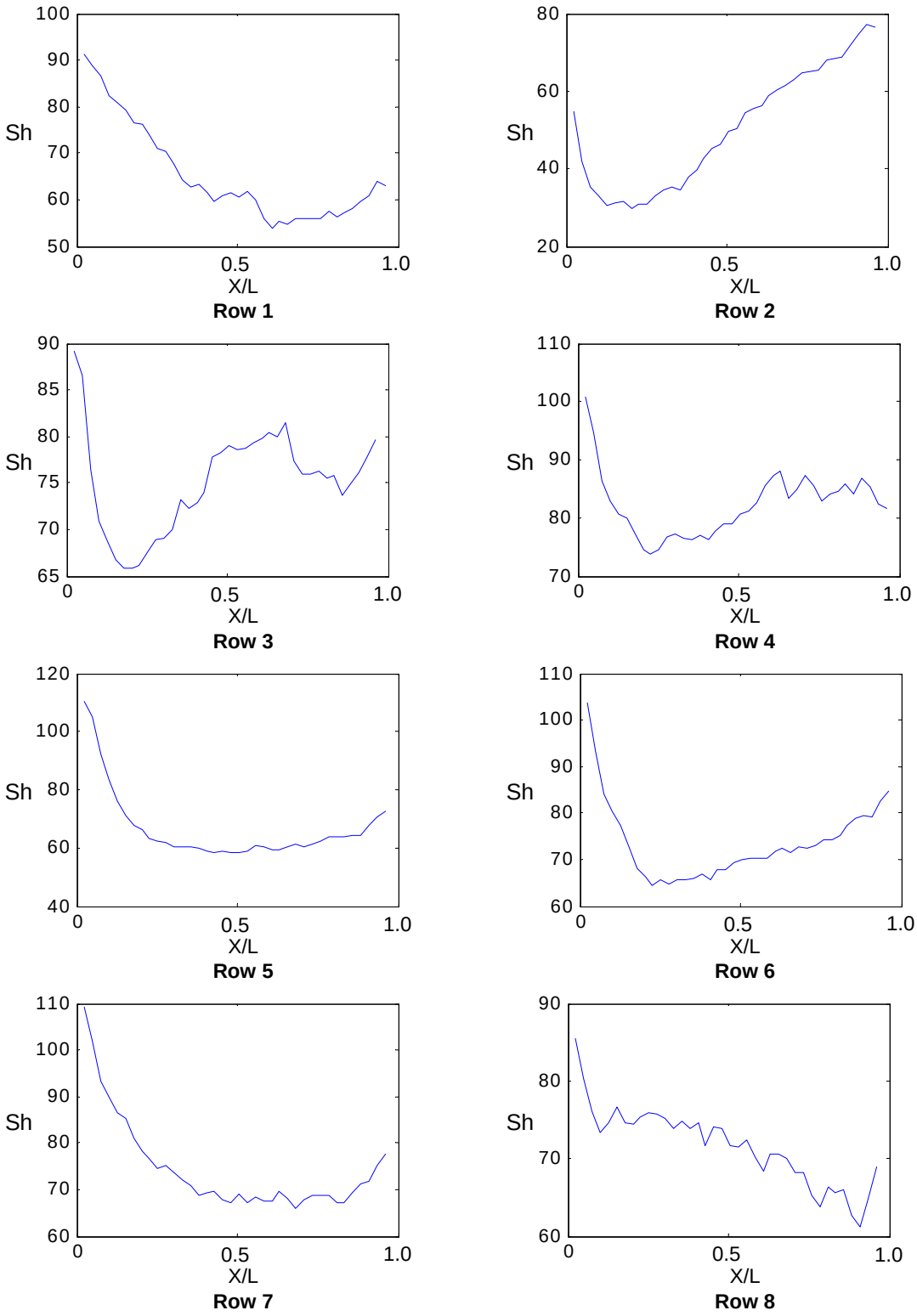

Figure 5.15 – Local Sherwood number distribution for the baseline array at Re = 3090 (X: distance from leading edge; L: fin length)

The local Sherwood number distribution for all eight rows of the baseline array at Re = 3090 is shown in Figure 5.15. The distributions for this Reynolds number are quite different from those at Re = 1030 and Re = 1640. For the 1st row fins, the Sherwood number is high at the leading edge, but decreases less rapidly in the flow direction than for Re = 1030 and Re = 1640. The higher velocity in the freestream (i.e., higher Reynolds number) causes the boundary layer thickness to grow more slowly along the flow direction than at lower Reynolds numbers. Therefore, the Sherwood number decreases less rapidly than at lower Reynolds numbers. For the 2nd row fins, the Sherwood number decreases rapidly from the leading edge, and then increases from about 20% of the fin length. The Sherwood number continues to increase rapidly in the flow direction and exceeds the Sherwood number at the leading edge from around 60% of the fin length. The Sherwood number at the trailing edge is over 40% higher than that at the leading edge. The reason for the significant increase on the second half of the fin length for the 2nd row fins is not clear. It is possible that the streamwise vortices shed from the 1st row fins sweep over the 2nd row fins more on the surface area close to the trailing edge than to the leading edge. For the 3rd and 4th row fins, the Sherwood number is high at the leading edge and decreases rapidly in the flow direction due to the boundary layer growth. Then the local Sherwood number increases from around 20% of the fin length, reaching a maximum that is lower than the local Sherwood number at the leading edge, and then oscillates in a relatively narrow range afterwards. This distribution is believed to be caused by the combined effect of spanwise vortex shedding and the chaotic flow characteristics at this location, as evidenced by the flow visualization and PIV results. For the 5th, 6th, and 7th row fins, the Sherwood number drops quickly in the flow direction and then increases slowly near the trailing edge. For the 8th row fins, the Sherwood number starts high at the leading edge and drops rapidly in the flow direction. From around 10% of the fin length, the Sherwood number oscillates in a relatively narrow range, while maintaining the general decreasing trend.

5.2.2 4VG-Enhanced Array

The surface plots of fin-local mass transfer results of the 4VG-enhanced array at Re = 1040, 1650, and 3120 are given in Figures 5.16 to 5.21.

Figure 5.16 shows the local Sherwood number distribution for the first four rows of the 4VG-enhanced array at Re = 1040. The yellow triangle indicates the spanwise location of two of the four delta wings on each leading fin. For the 1st row fins, strong heat transfer enhancement is found in the surface area right behind the delta wing, due to the downwash region created by the tip vortices. The surface-normal inflow in the downwash region behind the delta wing reduces the average boundary layer thickness in that region, so that the Sherwood number is enhanced greatly. The maximum Sherwood number occurs very close to the fin leading edge, which indicates that the tip vortices are strongest right after they wrap around the delta wing. Outside of the downwash region, there are two neighboring upwash regions. The surface-normal outflow in those upwash regions increases the average thickness of the boundary layer, so that the Sherwood number there is decreased.

For the 2nd row fins, it is found that at the same spanwise location, the enhanced downwash region on the 1st row corresponds with a degraded upwash region on the 2nd row, and vice versa. Therefore, the Sherwood number in the upwash region for the 2nd row is reduced, while the Sherwood number in the neighboring downwash regions is enhanced. The spanwise width of the upwash region decreases from the leading edge to the trailing edge.

The 3rd row fins show similar upwash and downwash behavior as the 1st row fins, although the Sherwood number in the downwash region is not as high as that for the 1st row fins. There is a narrow lower Sherwood number region in the middle of the downwash region, which indicates that the two streamwise vortices in the pair move away from each other while traveling downstream.

The 4th row fins show similar upwash and downwash behavior as the 2nd row fins, except that the Sherwood number in the downwash region is smaller and the area of the upwash region is larger. This behavior also indicates that the streamwise vortices become weaker and spread away from each other as they travel along the flow direction.

Figure 5.17 shows the local Sherwood number distribution for the last four rows of the 4VG-enhanced array at Re = 1040. Here the dashed triangle indicates only the spanwise location of the delta wings on the 1st row fins. The 5th and 7th row fins show the same downwash and upwash behavior as the 1st and 3rd row fins, while the 6th and 8th row fins show similar behavior as the 2nd and 4th row fins. However, as the flow travels downstream, the Sherwood number difference between the downwash and upwash regions becomes smaller and smaller, which indicates that the influence of the streamwise vortices becomes weaker and weaker.

Figure 5.18 shows the local Sherwood number distribution for the first four rows of the 4VG-enhanced array at Re = 1650. The local Sherwood number distribution of the 1st row fins is very similar to that at Re = 1040. However, the surface-normal outflow in the upwash region also creates secondary vortices adjacent to the primary vortices. The secondary vortices create their upwash regions next to the upwash regions of the primary vortices, as well as their downwash regions with the shape of narrow and nearly streamwise-oriented bands of enhanced Sherwood number. The local Sherwood number distribution of the 2nd row fins is similar to that at Re = 1040 except that the spanwise width of the upwash region decreases more rapidly in the flow direction and almost disappears after half of the fin length. The 3rd and 4th row fins show similar downwash and upwash behavior as that at Re=1040, but the border between the upwash and downwash regions becomes less clearly defined.

The upwash and downwash behavior becomes less and less pronounced for the last four rows of the 4VG-enhanced array at Re = 1650, as shown in Figure 5.19. For these downstream rows, the Sherwood number distribution reveals little indication of the existence of downwash and upwash regions, particularly for the 7th and 8th rows. These local Sherwood number results agree with the flow visualization and PIV findings that the streamwise vortices are less organized and that spanwise vortex shedding occurs from the 3rd row at this Reynolds number.

The local Sherwood number distribution at Re = 3120 for the 4VG-enhanced array is shown in Figure 5.20 (Rows 1 to Row 4) and Figure 5.21 (Row 5 to Row 8). The 1st and 2nd row fins show similar downwash and upwash behavior as for those fins at Re=1650. The primary and induced secondary streamwise vortices are more evident in the 1st row fins than at Re=1650. The Sherwood number distribution on the 3rd row fins shows that the two primary vortices in the pair spread away from each other faster at Re=3120 than at lower Reynolds numbers. The Sherwood number distribution from the 4th row fins to the 8th row fins show very little indication of the streamwise vortices. According to the flow visualization and PIV data, the streamwise vortices become highly disorganized and the flow field is chaotic and unsteady after the 3rd row at this Reynolds number. The local Sherwood number distribution from the 4th row to the 8th row further confirms that the influence of the streamwise vortices is very limited for these rows at high Reynolds numbers, such as Re=3120.

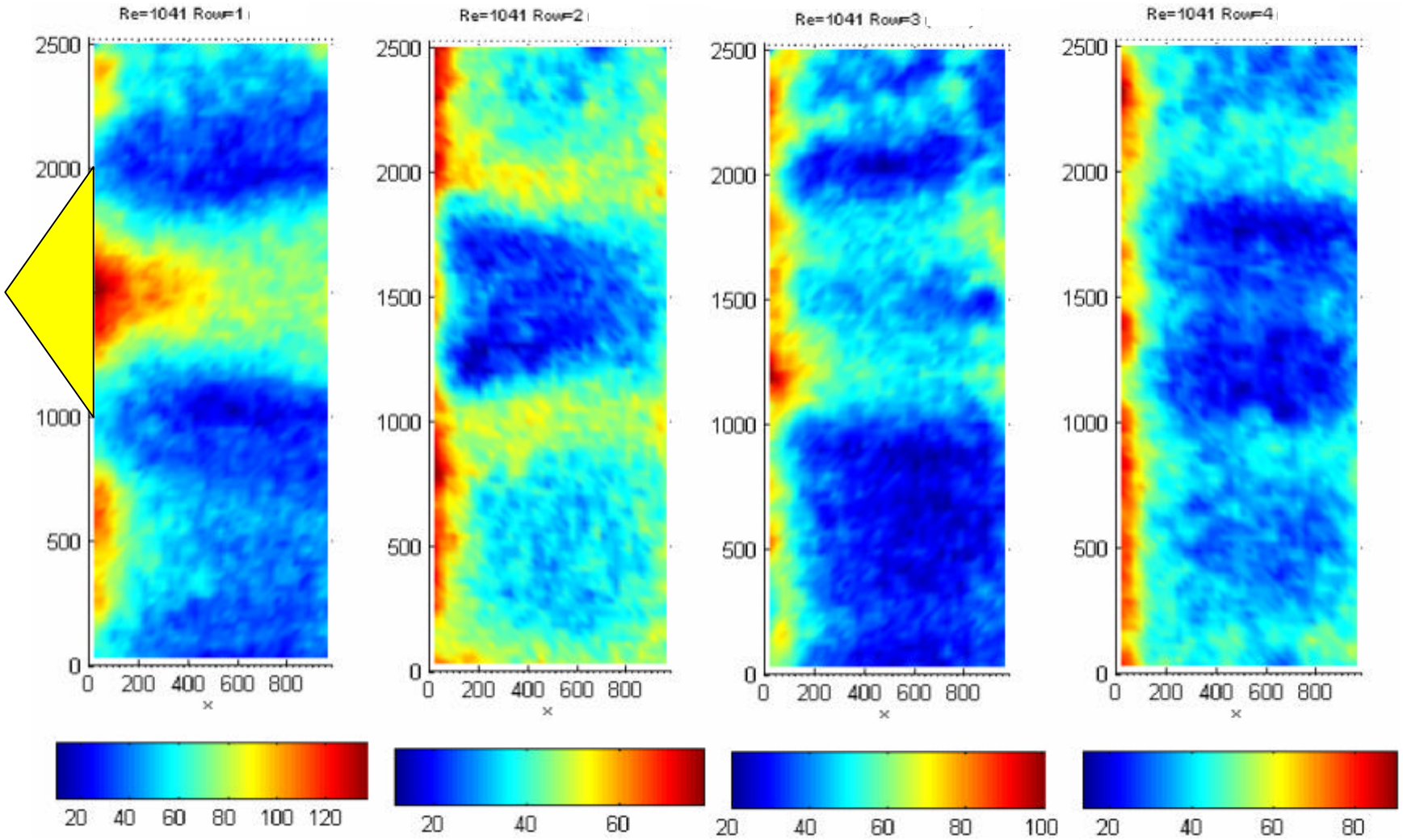

Figure 5.16 – Local Sherwood number distribution for 4VG-enhanced array at Re = 1040: Rows 1, 2, 3, and 4 (x: 0=leading edge)

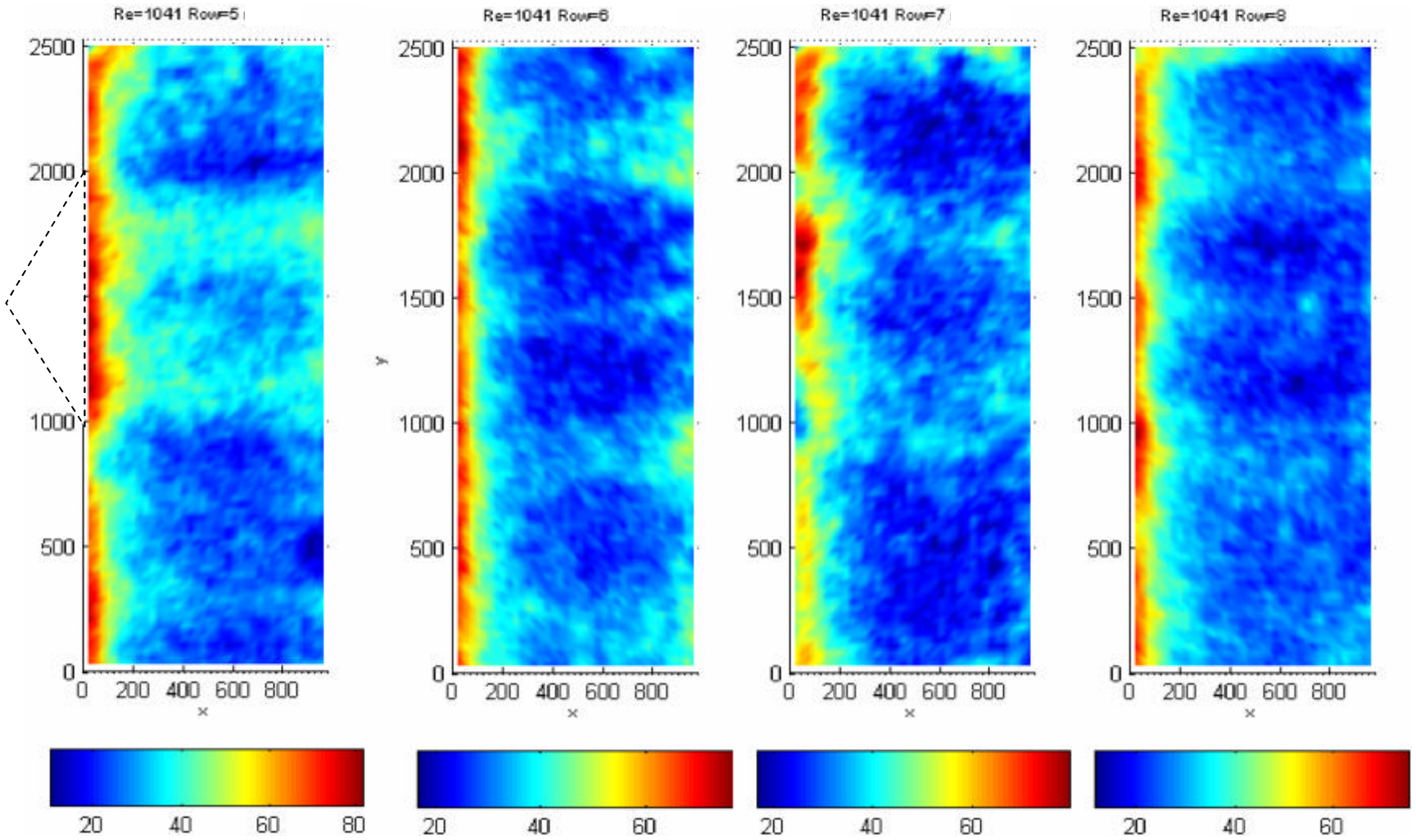

Figure 5.17 – Local Sherwood number distribution for 4VG-enhanced array at Re = 1040: Rows 5, 6, 7, and 8 (x: 0=leading edge)

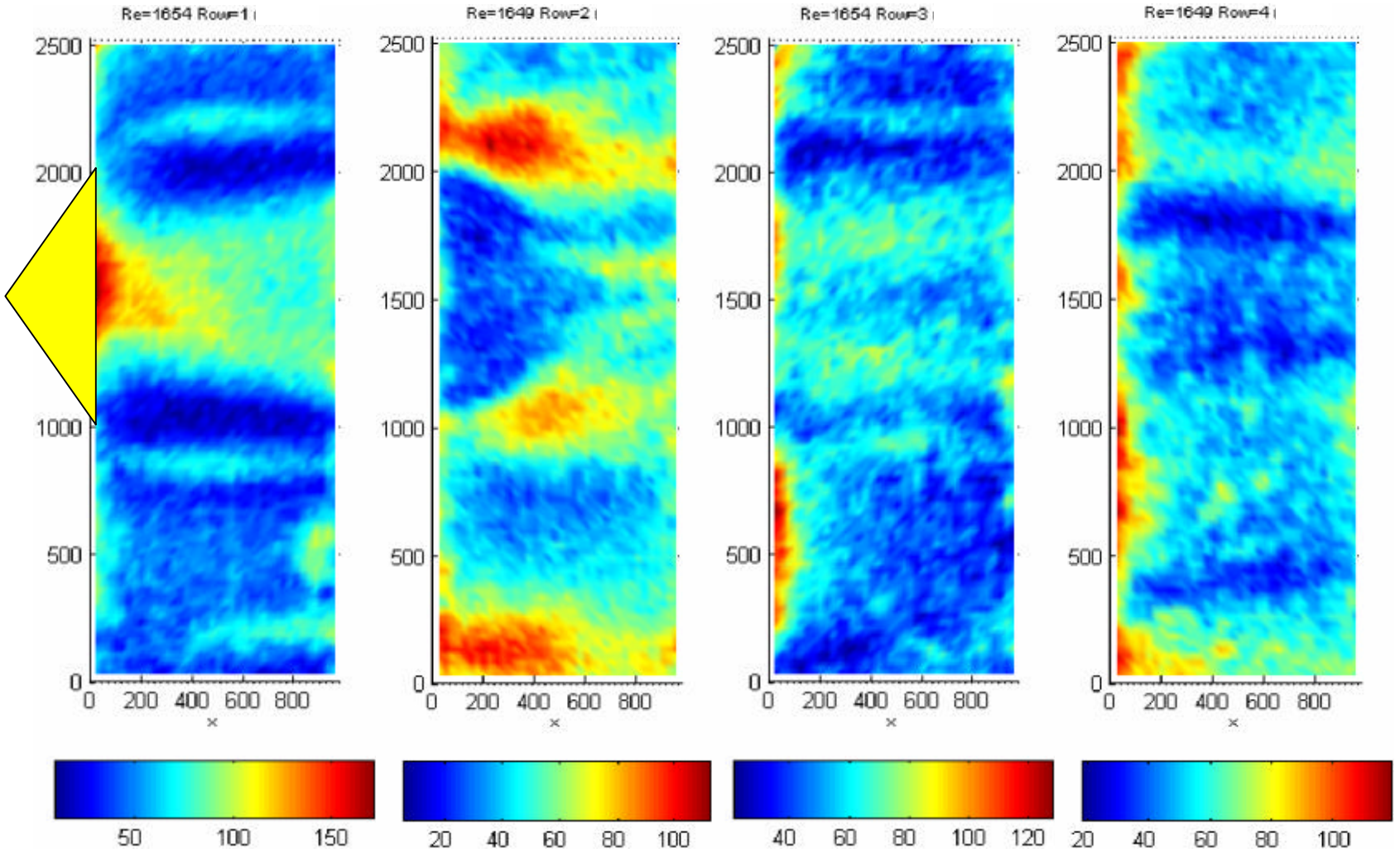

Figure 5.18 – Local Sherwood number distribution for 4VG-enhanced array at Re = 1650: Rows 1, 2, 3, and 4 (x: 0=leading edge)

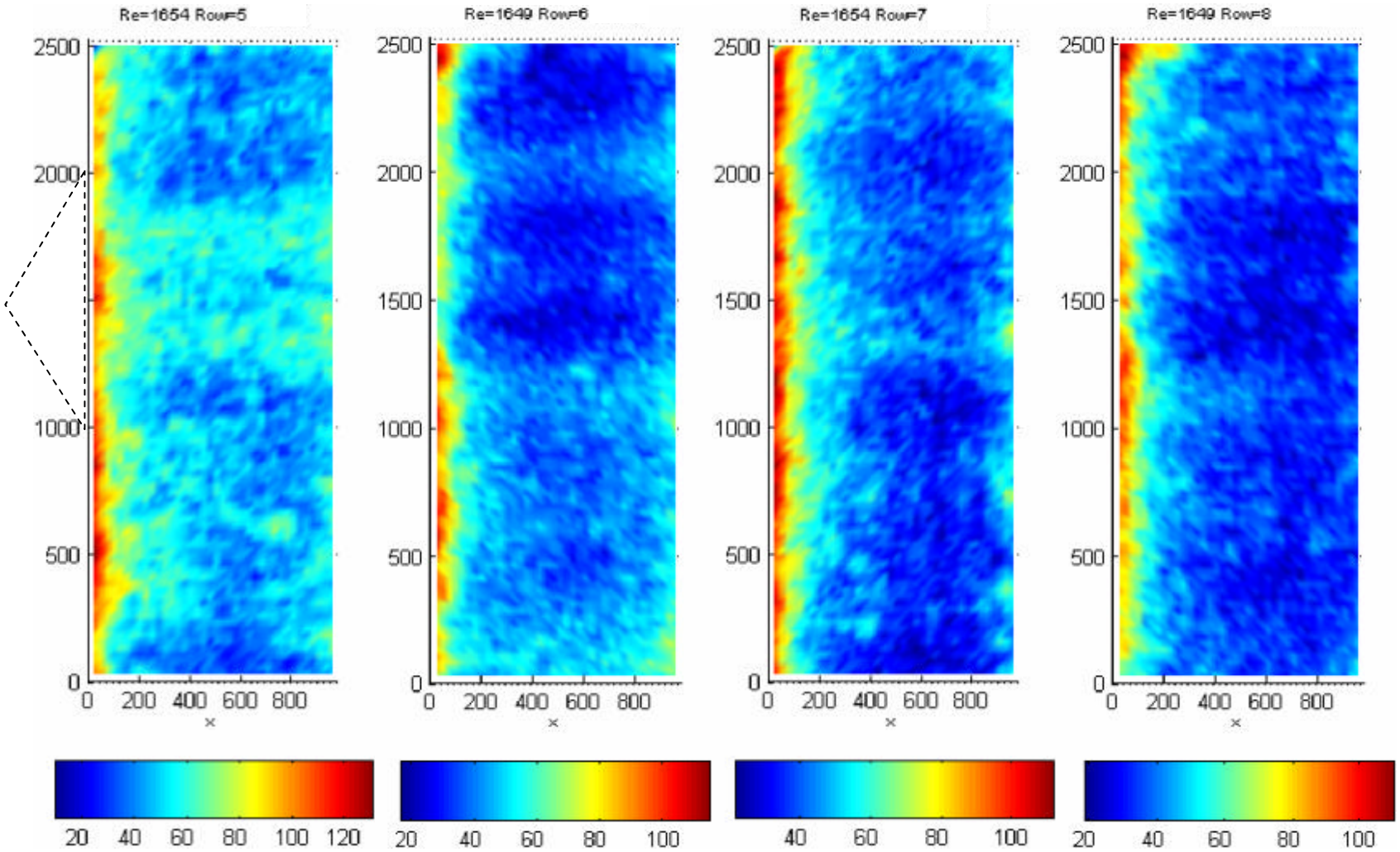

Figure 5.19 – Local Sherwood number distribution for 4VG-enhanced array at Re = 1650: Rows 5, 6, 7, and 8 (x: 0=leading edge)

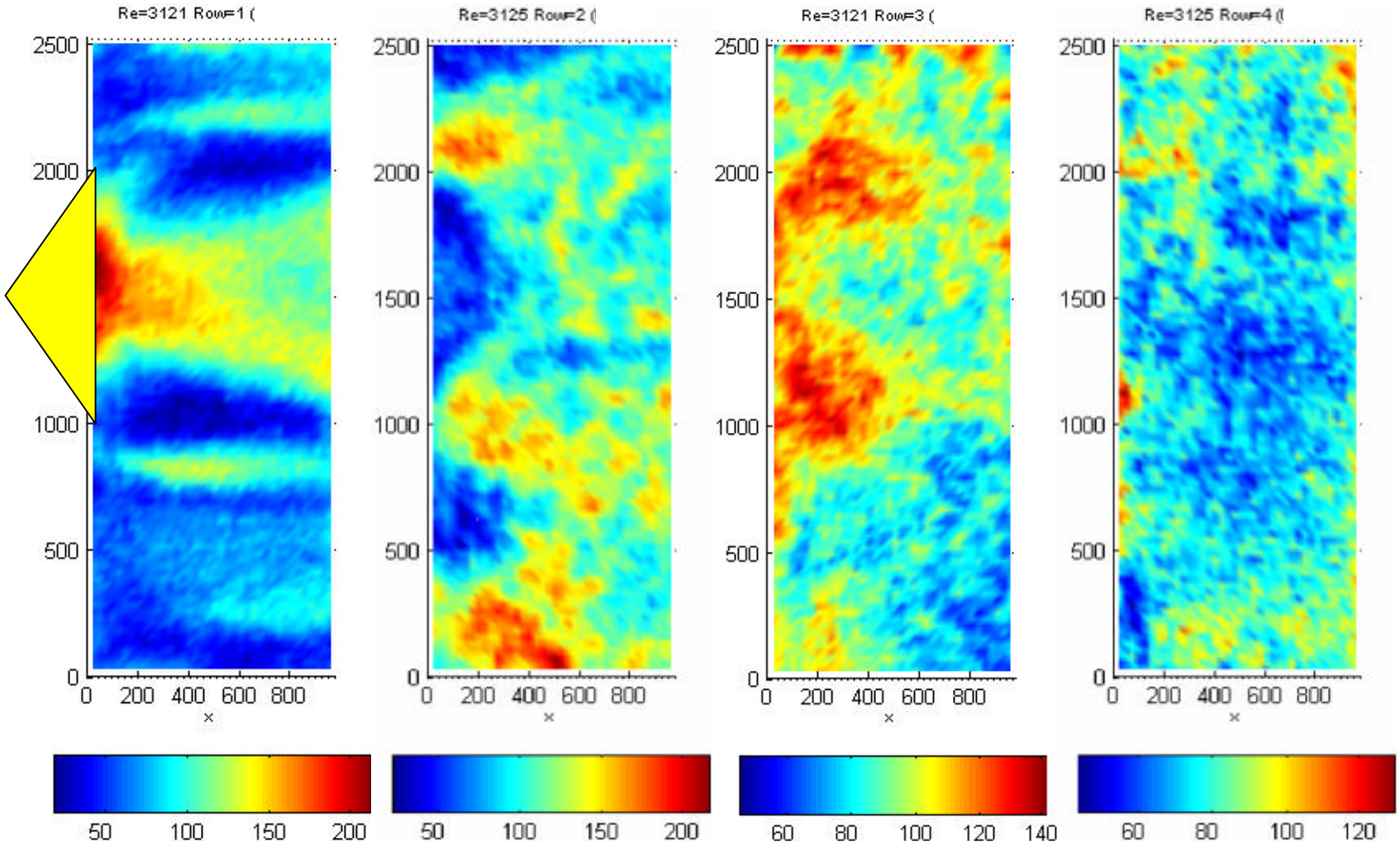

Figure 5.20 – Local Sherwood number distribution for 4VG-enhanced array at Re = 3120: Rows 1, 2, 3, and 4 (x: 0=leading edge)

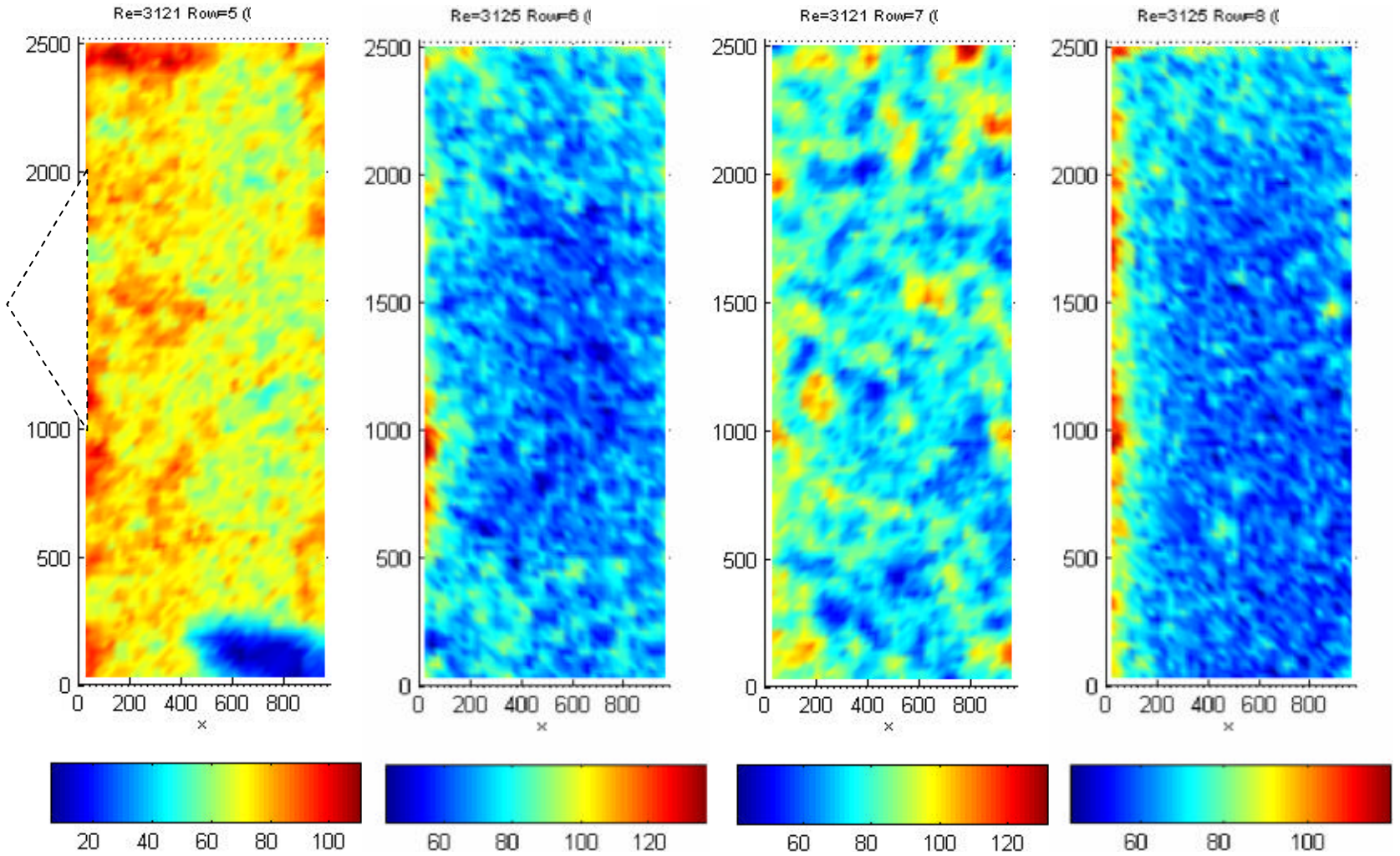

Figure 5.21 – Local Sherwood number distribution for 4VG-enhanced array at Re = 3120: Rows 5, 6, 7, and 8 (x: 0=leading edge)

5.2.3 4VG at Rows 1 and 5 - Enhanced Array

The local mass transfer results for the 4VG at Rows 1 and 5 - enhanced array are given in Figures 5.22 - 5.24. According to the flow visualization and PIV results, the first half of the array shows very similar flow behavior to that of the 4VG-enhanced array. Therefore, the local mass transfer tests were only performed for the second half of the array.

Figure 5.22 shows the local Sherwood number distribution for the last four rows at Re=1020. For the 5th row fins, the re-generated streamwise vortices create a downwash region in the fin surface area right behind the row 5 delta wings, which strongly enhances the local Sherwood numbers for the 5th row fins. Two neighboring upwash regions with decreased Sherwood number are observed outside of the downwash region. All these results are similar to those for the 1st row fins of the 4VG-enhanced array. However, the downwash and upwash regions are of less regular shape than those for the 1st row fins of the 4VG-enhanced array. The 6th row fins show the opposite distribution of the downwash region and the upwash region as compared to the 1st row fins, but the shape of both regions is quite irregular. The 7th and 8th row fins show weak patterns of downwash and upwash regions, which indicates that the influence of the regenerated streamwise vortices fades much faster in the flow direction than for the inlet-generated streamwise vortices. The non-uniform flow in front of the second row of delta wings decreases the organization of the regenerated streamwise vortices, in agreement with the flow visualization and PIV data presented in Chapter 4.

The local Sherwood number distributions from row 5 to row 8 at Re=1630 and Re=3070 are shown in Figures 5.22 and 5.23, respectively. The row 5 and row 6 results show a similar distribution of the downwash and upwash regions as those at Re=1020, except that the streamwise vortices in the pair spread farther away from each other at higher Reynolds numbers. The Sherwood number distributions of the 7th and 8th row fins show little difference across the fin span, indicating little influence of the streamwise vortices in these two rows. This finding is also in good agreement with the flow visualization and PIV findings.

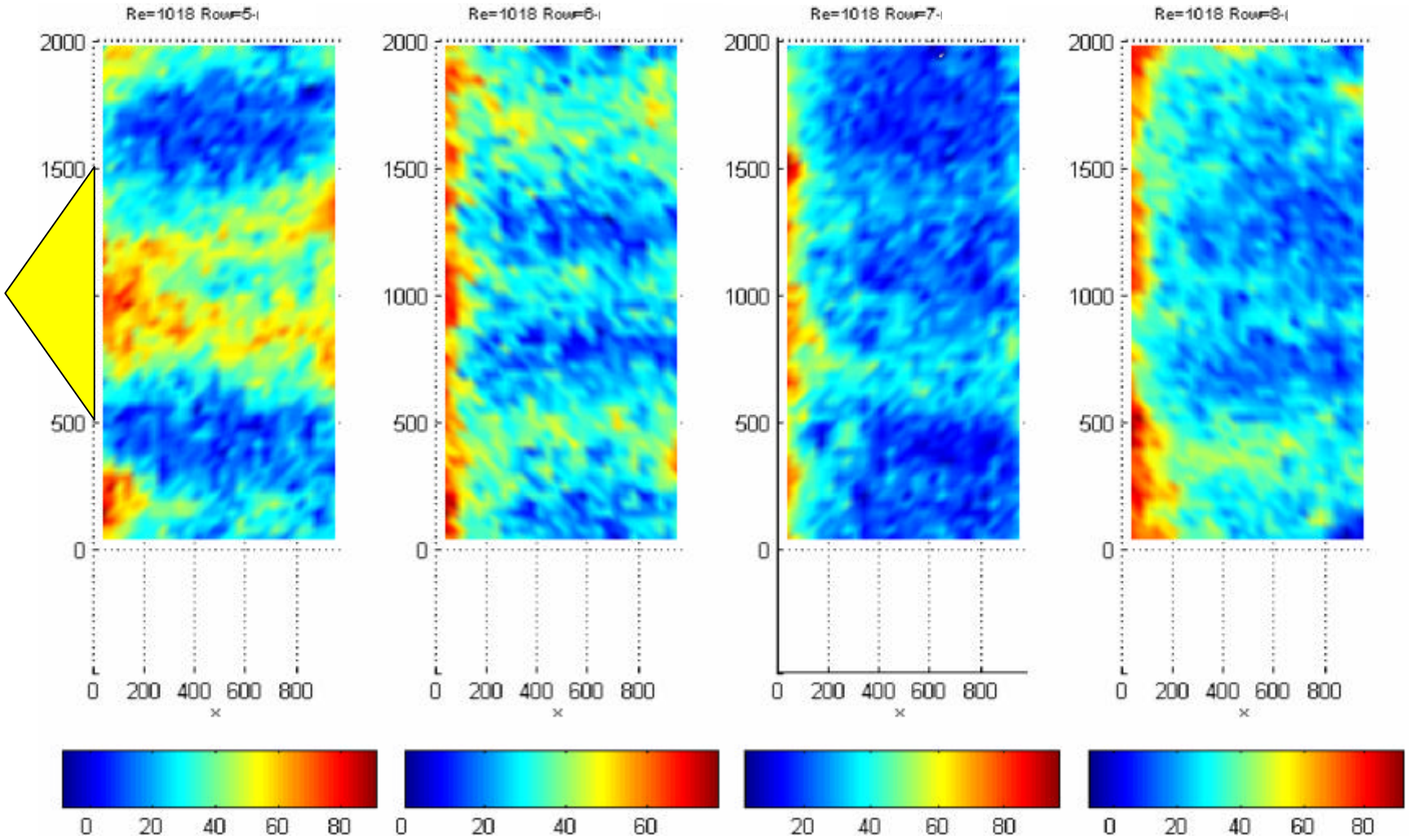

Figure 5.22 – Local Sherwood number distribution for 4VG at Rows 1 and 5 - enhanced array at Re = 1020: Rows 5, 6, 7, and 8 (x: 0=leading edge)

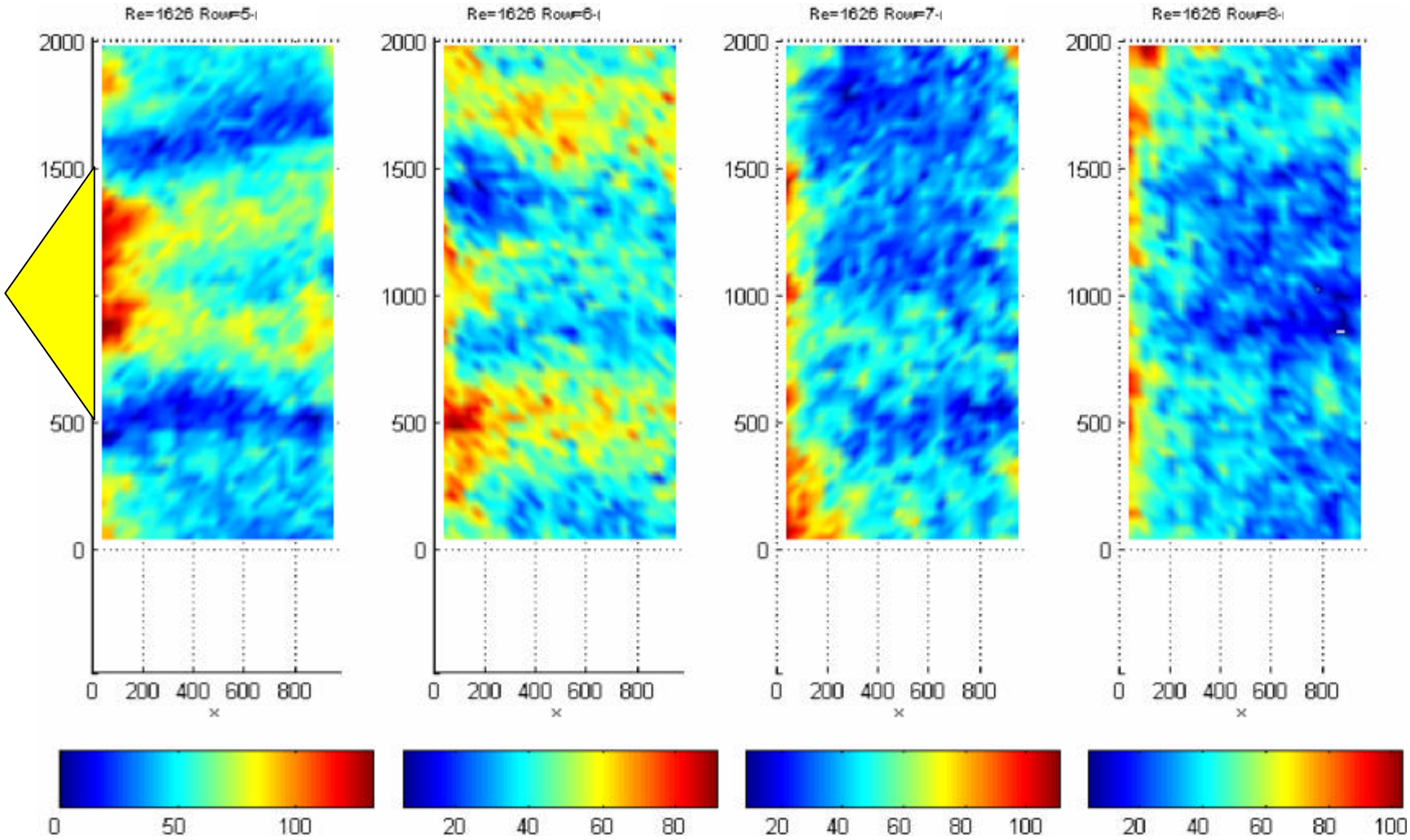

Figure 5.23 – Local Sherwood number distribution for 4VG at Rows 1 and 5 - enhanced array at Re = 1630: Rows 5, 6, 7, and 8 (x: 0=leading edge)

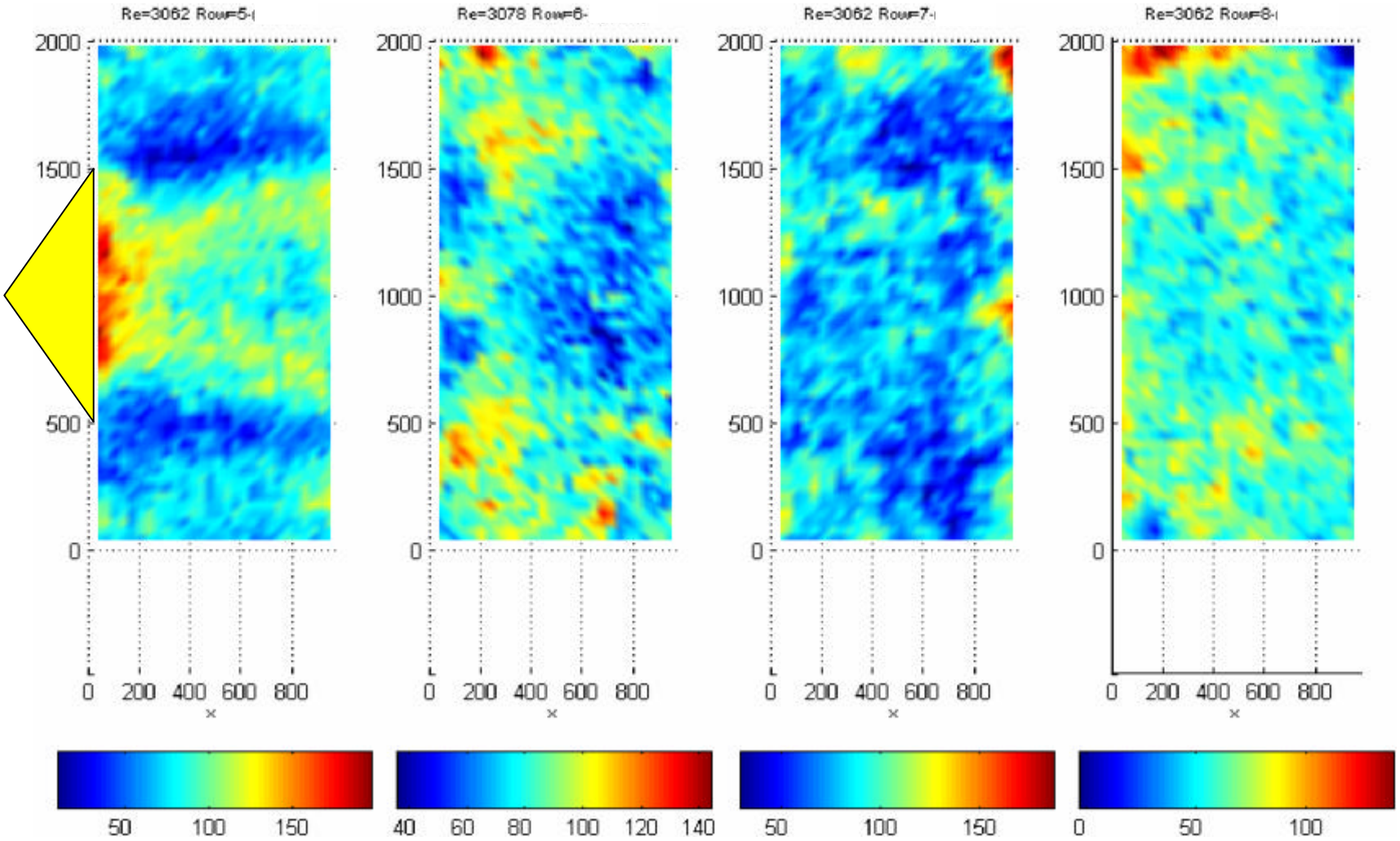

Figure 5.24 – Local Sherwood number distribution for 4VG at Rows 1 and 5 - enhanced array at Re = 3070: Rows 5, 6, 7, and 8 (x: 0=leading edge)

5.3 Array Pressure Drop Results

Pressure drop results are presented and discussed in terms of friction factor *f*. Figure 5.25 shows the pressure drop results across the original baseline and 2VG-enhanced arrays. The array pressure drop at low Reynolds numbers is found to be comparable to the resolution of the transducer (0.1 Pa), which induces a large uncertainty for the *f* factor, as shown in Figure 5.25. A scaled-down array with all length scales equal to half of the original array was built and tested in the same wind tunnel, in order to reduce the uncertainty for the friction factor *f*. The vortex generators for the scaled-down array are of the same aspect ratio and attack angle, and half the base length as those for the original array. The scaled-down array is more compact than the original array; thus, it creates a larger pressure drop over the array at the same Reynolds number, resulting in smaller uncertainty for the *f* factor.

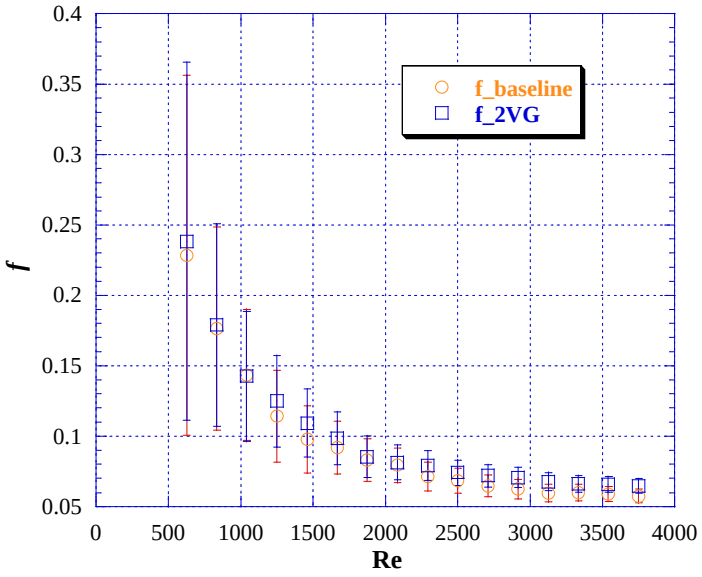

Figure 5.25 – Friction factor *f* for the original L×L baseline and 2VG-enhanced arrays at various Reynolds numbers

Figure 5.26 shows the *f* factors for the baseline, 2VG-enhanced, 4VG-enhanced, and 4VG at Rows1 and 5 - enhanced scaled-down arrays. The *f* factor uncertainties for the scaled-down arrays are much smaller than those for the original arrays at the same Reynolds number. The friction factors for the scaled-down baseline and 2VG-enhanced arrays at high Reynolds numbers were measured to be almost the same as those for the original L×L baseline and 2VG-enhanced arrays, which proves the scalability and similarity between the original arrays and the scaled-down arrays. As shown in Figure 5.26, the 4VG at Rows 1 and 5 – enhanced array has the largest *f* factor, followed by the 4VG-enhanced array, the 2VG-enhanced array, and the baseline array, as expected.

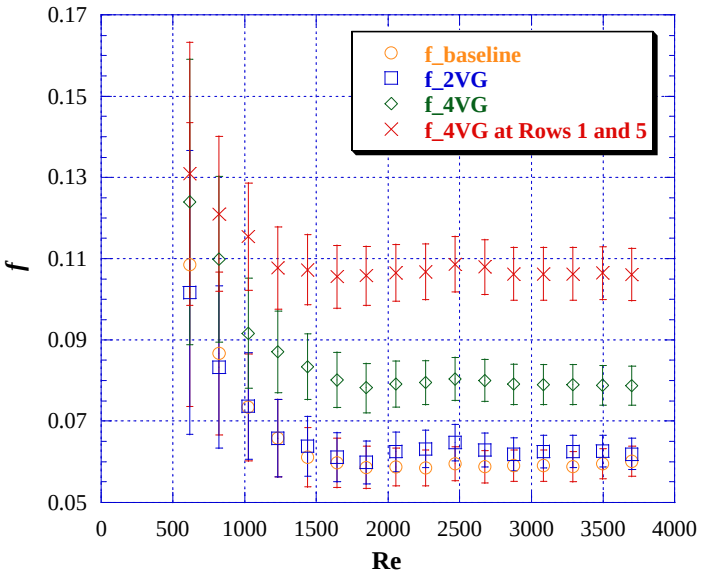

Figure 5.26 – Friction factor *f* for the scaled-down baseline and VG-enhanced arrays at various Reynolds numbers

Figure 5.27 shows the *f* factor ratios for the three scaled-down VG-enhanced arrays over the baseline array - a measure of the pressure drop penalty caused by the vortex generators. At very low Reynolds numbers, the pressure drop penalties are small, with no measurable penalty at all for the 2VG-enhanced array. The pressure drop penalties for all three enhanced arrays increase with increasing Reynolds number and reach a maximum at Re = 2400, where the flow field of the baseline array begins a transition to chaotic and turbulent flow. As the Reynolds number increases further, the pressure drop penalties for all three enhanced arrays decrease slightly. Thus, the maximum pressure drop penalty occurs at Re = 2400, and is 8.8% for the 2VG-enhanced array, 35.1% for the 4VG-enhanced array and 82.5% for the 8VG-enhanced array.

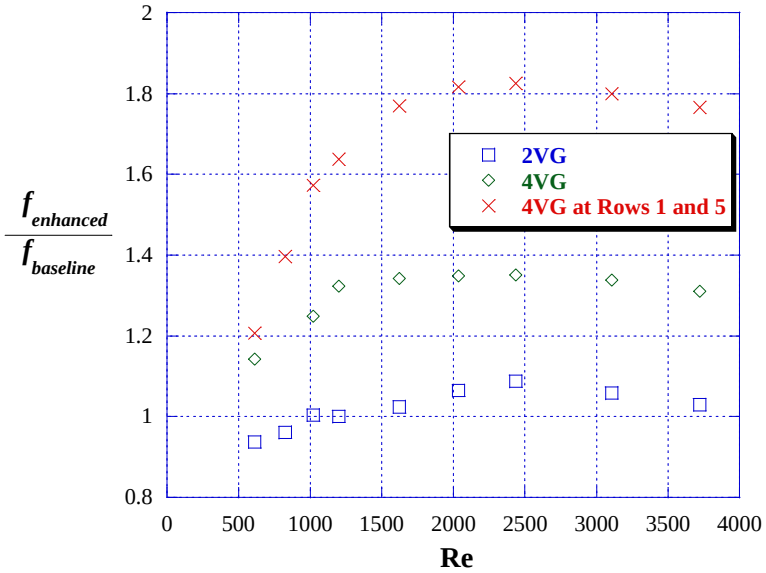

Figure 5.27 – *f* ratio of the scaled-down VG-enhanced arrays over the baseline array at various Reynolds numbers

5.4 Area Goodness Factor j/f for Baseline and Enhanced Arrays

In order to evaluate the overall effect of heat transfer enhancement and pressure drop penalty for the various VG-enhanced arrays, an area goodness factor, defined as the ratio of Colburn *j* factor to the friction factor *f*, is calculated for the baseline and three VG-enhanced arrays. Figure 5.28 shows the *j/f* factors for the baseline, 2VG-enhanced, 4VG-enhanced, and 4VG at Rows 1 and 5 – enhanced arrays. The 2VG-enhanced array displays positive overall effect of *j/f* at Reynolds numbers up to 1200 and for the Reynolds number of 3700, while the overall effect is negative (*j/f* value less than that for the baseline array) at Reynolds numbers between 1600 and 3100. The 4VG-enhanced array and 4VG at Rows 1 and 5 – enhanced array show a negative overall *j/f* effect for all Reynolds numbers between 600 and 3700.

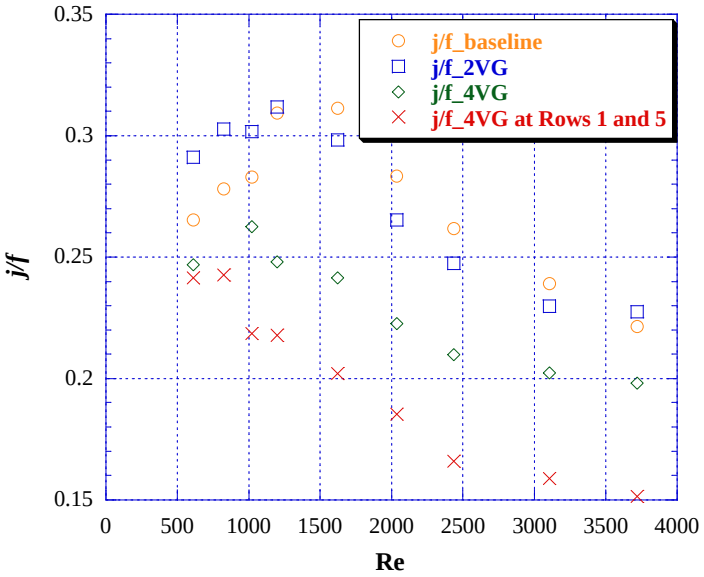

Figure 5.28 – Area goodness factor *j/f* for the scaled-down baseline and VG-enhanced arrays at various Reynolds numbers

Figure 5.29 shows the *j/f* ratios of three scaled-down VG-enhanced arrays over the baseline array, which is a measure of overall heat transfer and pressure drop performance of the VG-enhanced arrays. The maximum *j/f* factor ratios occur at the lowest Reynolds numbers and decrease with increasing Reynolds number. They reach a minimum at Reynolds numbers between 1600 and 2400, and then increase as Reynolds number increases further. For the 2VG-enhanced array, the *j/f* factor is enhanced by 9.7% at Re = 600 compared to the baseline array. The *j/f* factor enhancement occurs for Reynolds numbers up to 1200, and then degradation is found at higher Reynolds numbers. The largest degradation is 6.4% which occurs at Re = 2000. As the Reynolds number increases further, the *j/f* factor degradation become less and less and a *j/f* factor enhancement of 2.8% occurs at Re = 3700. The 4VG-enhanced array and 4VG at Rows 1 and 5 – enhanced array show *j/f* factor degradation for all Reynolds numbers between 600 and 3700. The largest degradation is 22.5% for the 4VG-enhanced array, which occurs at Re = 1600, and is 36.6% for the 4VG at Rows 1 and 5 – enhanced array, which occurs at Re = 2400.

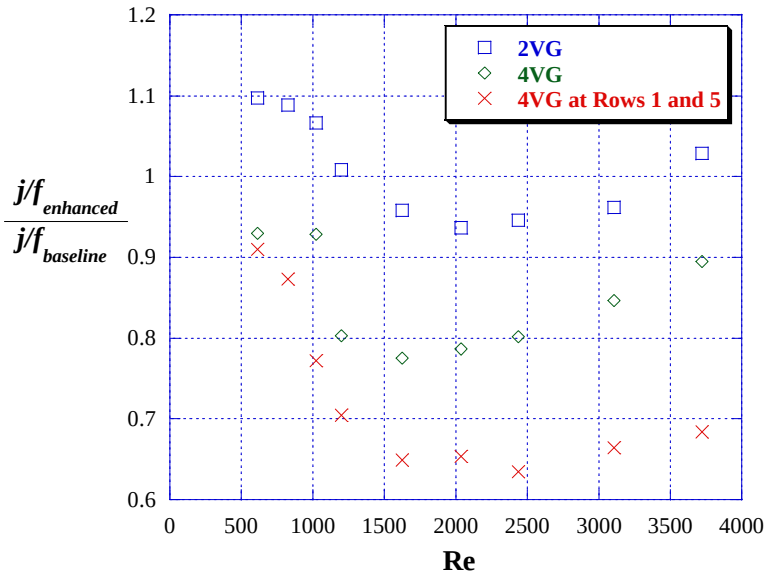

Figure 5.29 – Area goodness factor *j/f* ratio of the scaled-down VG-enhanced arrays over the baseline array at various Reynolds numbers

Chapter 6. Conclusions

6.1 Summary of Results

Through this experimental research, an innovative concept of introducing streamwise vortices into the flow field of offset-strip fin arrays to seek surface heat transfer enhancement was evaluated. Several configurations of delta-wing vortex generators were used to introduce streamwise vortices at the inlet of the array only, as well as at both the inlet and the middle of the array. Flow visualization, PIV, local and average mass transfer, and pressure drop measurements were performed for a baseline offset-strip fin array and six VG-enhanced arrays to investigate the flow field behavior, heat transfer enhancement, and pressure drop penalty associated with this novel concept. Data from the different experimental methods agree well with each other, revealing consistent and complementary flow and heat transfer characteristics. Comprehensive results for heat transfer enhancement and pressure drop penalty, as well as a clear understanding of the associated flow field mechanisms, are provided through this research. A summary of the results will be presented in three sub-sections: the baseline offset-strip fin array, the generation of streamwise vortices at the array inlet only, and the re-generation of streamwise vortices halfway through the array.

6.1.1 Baseline Offset-Strip Fin Array

The flow field for the baseline offset-strip fin array is steady and laminar throughout the array for Reynolds numbers up to about 1030, as observed in both the flow visualization and PIV results. The boundary layer restarts at the leading edge of each fin, and PIV data reveal similar boundary layer development over each fin length. The laminar flow field and boundary layer restarting correlate closely with fin-averaged mass transfer results in the same Reynolds number range. The fin-averaged Sherwood numbers are found to decrease slightly or remain almost the same from inlet to outlet of the array. This behavior is consistent with the behavior anticipated for boundary-layer restarting and flow development in the array.

Flow instability starts to occur in the wake region of the array at Re = 1030. As the Reynolds number increases to 1260, periodic spanwise vortex shedding starts to occur at the 7^{th} fin row. This periodic vortex shedding enhances the heat transfer of corresponding fins, which is suggested in the fin-averaged mass transfer results by a jump in Sherwood number at row 7. The heat transfer enhancement is due to boundary layer restarting and the periodic spanwise vortex shedding. With increasing Reynolds number, the onset location of periodic vortex shedding moves to upstream rows. The onset of vortex shedding is observed at the 3^{rd} row for Re = 1440, and at the 1^{st} row for Re = 1940. The fin-averaged Sherwood number of those fins experiencing shedding is enhanced greater than the upstream fins without periodic shedding.

At higher Reynolds numbers, the structure associated with the spanwise vortices becomes somewhat irregular; for example, for Re=1940 the structure is somewhat irregular after the 5^{th} row. As the Reynolds number increases further to 2040 and higher, the periodic spanwise vortex shedding after the 3^{rd} row begins to show signs of transition to turbulence. Greater heat transfer enhancement is achieved for the downstream fins once the flow becomes chaotic and turbulent, as demonstrated by the fin-averaged mass transfer results at Re = 3105 and 3723. Periodic spanwise vortex shedding occurs at the 1^{st} and 2^{nd} rows at these high Reynolds numbers, due to the uniform incoming flow. The fin-averaged Sherwood number for the 1^{st} and 2^{nd} row fins increases less rapidly with increasing Reynolds number than for the downstream fins.

6.1.2 Generation of Streamwise Vortices at Array Inlet

Streamwise vortices were generated at the inlet of the array by attaching delta wings at the leading edges of the 1st fin row. The flow field becomes three-dimensional after introduction of the streamwise vortices.

Flow visualization and PIV results for the 4VG-enhanced array provide a rich description of the interaction between the streamwise vortices and interrupted-fin flow field. The flow visualizations show a laminar flow with streamwise vortex structures coherent throughout the array for Reynolds numbers up to 1280. Since spanwise vortex shedding occurs at the 7th row for Re = 1260 in the baseline array, the presence of the streamwise vortices clearly delays the occurrence of spanwise vortex shedding. Both PIV data and the local Sherwood number distributions at Re = 1040 indicate the counter-rotating streamwise vortex pair creates spanwise interlaced downwash and upwash regions over the fin surfaces. A downwash region on a given fin always corresponds to an upwash region at the same spanwise location on the fin immediately downstream, and vice versa. Mass transfer enhancement is found in the downwash region and a decrease of mass transfer is found in the upwash region.

As Re is increased to 1520, the tip vortices generated by the VGs become stronger and larger. The vortex structure is well defined and coherent upstream of the 5th fin row, where the streamwise vortices start to manifest a less regular structure. Spanwise vortex shedding is not observed along the path of the streamwise vortices. However, in the center region between two pairs of streamwise vortices, periodic spanwise vortex shedding is observed at the 3rd row. The spanwise vortex shedding becomes weaker at the 5th row and disappears at the 7th row, due to the interaction of the degraded streamwise vortices and the spanwise vortex shedding. This interaction appears to be destructive to spanwise vortex shedding at the downstream rows. The local mass transfer results at Re = 1650 show a spanwise interlacing of the downwash and upwash regions similar to that seen at lower Reynolds numbers. The primary streamwise vortices become strong enough at this Reynolds number to generate counter-rotating secondary vortices in the region next to their upwash regions. However, the border between the upwash and downwash regions becomes less clearly defined after the 5th row, due to the lack of structure and organization in the flow.

As the Reynolds number is increased further to 1750, the streamwise vortices start to become less defined by the 2nd row, and vortex breakdown (disappearance of well-organized and coherent vortex structure) occurs prior to the 3rd row. Well-organized streamwise vortices are essentially impossible to identify at locations downstream of the 3rd row. Spanwise vortex shedding is observed at the 3rd row in the spanwise center region between two streamwise vortex pairs. The shedding becomes weaker at the 5th row and much weaker at the 7th row, and spanwise vortices are impossible to discern in the wake region, apparently due to destructive interactions between the streamwise and spanwise vortices. Spanwise vortex shedding in the center region is observed at the 1st row and becomes very strong at the 3rd row, as Re is increased to 1980. Although vortex shedding becomes weaker along the flow direction, it is present throughout the array and in the wake region.

The PIV side-view results at Re = 2450 and 3120 show that the flow becomes turbulent-like, with large-scale mixing and no clearly-defined streamwise vortex structures after the 3rd row. The streamwise vortices are strong, well-defined, and coherent before streamwise vortex breakdown occurs at the 3rd row.

The PIV end-view data provide the maximum vorticity of the streamwise vortices at various streamwise locations. In general, the maximum vortex strength decreases as the flow advects downstream. The maximum vorticity at the leading edge of Row 2 and Row 3 is higher than at more upstream and downstream locations,

especially at higher Reynolds numbers, due to the reduced flow area and diverted flow path at the leading edge of the interrupted fins. As the flow accelerates around the minimum flow area, the vortex lines are stretched and vortex circulation increases. At Re = 2450 and Re = 3120, the maximum vorticity strength decreases so rapidly in the first half of the array that it is even lower than that at Re = 1750 in the second half of the array. This finding confirms that vortex breakdown occurs in the first half of the array and that the impact of the streamwise vortices is greatly reduced once the flow structure becomes irregular. Another confirmation comes from the fin-averaged mass transfer results of the 4VG-enhanced array, which show much lower Sherwood numbers after the 4^{th} row than for the first 3 rows at Re = 2458.

The Sherwood numbers for the first seven rows of the arrays were averaged to evaluate the overall enhancement for all VG-enhanced arrays. An enhancement is present even for very low Reynolds numbers, and it increases with increasing Reynolds number. The enhancement reaches a maximum around Re = 1000, and is 16% for the 4VG-enhanced array and 24% for the 8VG-enhanced array. The overall enhancement for the 2VG-enhanced, 4VG-enhanced, and 8VG-enhanced arrays is caused by streamwise vortices only; no spanwise vortex shedding is present at these Reynolds numbers. As the Reynolds number is increased further, the array-averaged enhancement starts to decrease and reach a minimum at around Re = 1630 for all enhanced arrays. Additional experimental results for the 4VG-enhanced array between Re = 1230 and Re = 1630 show that the array-averaged Sherwood numbers reach a minimum at Re = 1440 and remain at low values for Reynolds numbers from Re = 1440 to about Re = 1630. The flow field results in the Reynolds number range between 1260 and 1750 show that streamwise vortices suppress spanwise vortex shedding along the paths of their travel; shedding is either delayed to higher Reynolds numbers or weakened in the regions adjacent to the streamwise vortices. Therefore, the overall enhancement decreases in this Reynolds number range. As the Reynolds number is increased further to 2040 and higher, an enhancement returns and increases as Reynolds number increases. The flow field behavior provides an explanation for the enhancement return. At Re > 2000, the flow becomes chaotic and turbulent-like for both the baseline array and the VG-enhanced arrays, except for the first three rows. The impact of the streamwise vortices and spanwise vortex shedding is minimal in the downstream part of the array once the flow becomes highly irregular. The average enhancement for the first three rows increases with increasing Reynolds numbers, because of the stronger streamwise vortices at higher Reynolds numbers, which contributes to the overall enhancement return.

The pressure drop penalty for the 2VG-enhanced array and the 4VG-enhanced array is small at low Reynolds numbers, but increases with increasing Reynolds number. It reaches a maximum at about Re = 2400, with an increase in pressure drop of 8.8% over the baseline case for the 2VG-enhanced array, and an increase of 35.1% for the 4VG-enhanced array. As Reynolds numbers increases further, the pressure drop penalty decreases.

The maximum ratio of area goodness *j/f* factor of the enhanced arrays to that of the baseline array occurs at low Reynolds numbers and decreases with increasing Reynolds number. It reaches a minimum at Reynolds numbers between 1600 and 2000, and then increases as Reynolds number increases further. The *j/f* factor for the 2VG-enhanced array is enhanced by 9.7% at Re = 600, as compared to the baseline array. The *j/f* factor enhancement is positive for Reynolds numbers up to 1200. Then *j/f* degradation occurs between Re = 1600 and Re = 3100, with the largest degradation of 6.4% occurring at Re = 2000. The *j/f* factor enhancement becomes positive again at Re =

3700, for which a 2.8% overall *j/f* enhancement is achieved. The 4VG-enhanced array shows *j/f* factor degradation for all Reynolds numbers between 600 and 3700. The largest degradation for the 4VG-enhanced array is 22.5% and occurs at Re = 1600.

6.1.3 Re-generation of Streamwise Vortices Halfway through the Array

With streamwise vortices generated at the inlet of the array, a second row of vortex generators is attached at the leading edge of the 5th fin row to enhance the streamwise vortices in downstream rows. The first three rows of the 4VG at Rows 1 and 5 – enhanced array show almost the same flow-field behavior as the first three rows of the 4VG-enhanced array, as confirmed by flow visualization and PIV side-view results. Since the physical presence of the second row of delta wings is in the 4th row area, the re-generated streamwise vortices affect the 4th row and all following rows, with very little upstream effect.

The flow field is laminar throughout the array up to Re = 850. The PIV results show the re-generated streamwise vortices are stable and well-defined at Re = 850. As the Reynolds number is increased to 1030 and 1280, the streamwise vortices generated by the second row of delta wings become ill defined downstream of the 5th row; this irregularity is probably due to the non-uniform, unsteady flow approaching the second row of delta wings, as observed in both the flow visualization and PIV results. These irregular streamwise vortices cause flow field waviness in the second half of the array. The flow visualization also shows that these vortices become poorly organized at about the 7th row. As Re is further increased to 1520 and higher, the re-generated streamwise vortices become highly unsteady, and vortex breakdown occurs immediately downstream of the 5th row. A turbulent-like flow develops in the second half of the array at a lower Reynolds number than for the 4VG-enhanced array.

The re-generated streamwise vortices greatly enhance the overall strength of streamwise vorticity for the 4th and following rows; however, the associated convection enhancement is significantly reduced when streamwise vortex breakdown occurs. As shown in the PIV end-view results, the maximum streamwise vorticity at the 4th, 5th, and 6th rows is increased by the second row of vortex generators at all Reynolds numbers, but the magnitude of vorticity enhancement drops rapidly after the 6th row, where vortex breakdown is observed in the flow field. The fin-averaged mass transfer results show that the 4th, 5th, and 6th rows experience significant Sherwood number increases as compared to the same rows in the 4VG-enhanced array, confirming that the enhanced streamwise vorticity due to the second row of delta wings greatly improves the heat transfer of corresponding fins.

Both arrays with two rows of vortex generators show the same trends in Sh as a function of Re as observed for inlet-only streamwise vorticity generation, except that the overall enhancement with two VG rows becomes almost constant for all Reynolds numbers exceeding 2000. The maximum overall enhancement compared to the baseline array occurs at Re ≅ 1000. It is 22% for the 4VG at Rows 1 and 5 - enhanced array and is 32% for the 8VG at Rows 1 and 5 - enhanced array.

Unfortunately, the pressure drop penalty associated with the re-generation of streamwise vortices is much larger than for the inlet-only streamwise vorticity approach. The maximum pressure drop penalty is 82.5% for the 4VG at Rows 1 and 5 - enhanced array at Re ≅ 2400, as compared to 8.8% for the 2VG-enhanced array. The maximum pressure-drop penalty is 35.1% for the 4VG-enhanced array.

The area goodness factor *j/f* for the 4VG at Rows 1 and 5 - enhanced array is lower than for the 2VG-enhanced array and the 4VG-enhanced array. The *j/f* ratio for the 4VG at Rows 1 and 5 - enhanced array (referenced to the baseline array) is highest at low Reynolds numbers and decreases with increasing Reynolds number. It reaches a minimum at Re = 2400, and then increases as Reynolds numbers increases further. The *j/f* performance is degraded for all Reynolds numbers between 600 and 3700, with the largest degradation being 36.6% at Re = 2400.

6.2 Practical Applications

One of the primary objectives of this research was to explore possible heat transfer enhancement of offset-strip fin heat exchangers. Several practical applications are suggested through this research.

1. In most HVAC applications, an offset-strip-fin heat exchanger is operated at low Reynolds numbers (Re<1000). VG enhancement shows the most promise for this operating range, with maximum enhancements consistently measured at Re~1000. In order to effectively exploit this enhancement, an optimal generator geometry should be sought for specific fin arrays, and the heat exchanger should be operated near Re=1000.
2. For offset-strip fin arrays operating at high Reynolds numbers in the turbulent flow regime, the generation of streamwise vortices can significantly enhance the heat transfer performance of the array. However, in this regime careful design trade-offs between the heat transfer enhancement and pressure drop penalty may be required.
3. Higher heat transfer enhancement can be achieved by increasing the number of the vortex generators and arranging the placement of vortex generators symmetrically. Staggered arrangements of vortex generators should be avoided.
4. Streamwise vortices generated at the array inlet decay or break down as they convect downstream. Therefore, re-generation of streamwise vortices within the offset-strip fin array may be needed to achieve similar heat transfer enhancement for deep arrays. The findings of this research suggest re-generation should occur every four or five rows.
5. The pressure drop associated with VG-enhanced arrays is comparable to or higher than the baseline offset-strip fin array. Increasing the number of vortex generators and re-generating streamwise vortices can significantly increase the pressure drop penalty.
6. It is recommended that streamwise vortex generators be used to enhance offset-strip fin heat exchangers for applications in which high heat transfer performance is desired and pressure drop is not critical. If both low fan power and high heat transfer are desired for the application, it is recommended to use a 2VG-enhanced array configuration.

6.3 Future Work

More research is desired to obtain a better understanding of vortex breakdown of streamwise vortices and the destructive interactions between spanwise vortex shedding and streamwise vortices. Other types of vortex generators, such as delta winglets, rectangular winglets, and hemispherical vortex generators, merit investigation, because they might operate with a reduced pressure drop penalty. Some active ways to generate streamwise vortices, such as active fins and virtual jets, might be considered in future investigation. More research on full-scale offset-strip heat exchangers with various vortex generator configurations is desired in the future to further develop this novel heat transfer enhancement technique. A parametric study of VG type, aspect ratio, attack angle, and placement on full-scale offset-strip fin heat exchangers will bring this new technique much closer to real application.

Bibliography

Admiraal, D.M. and Bullard, C.W., 1995, "Experimental Validation of Heat Exchanger Models for Refrigerator/Freezers," ASHRAE Transactions, Vol. 101, Part 1, pp. 34-43.

Adrian, R.J., 1986, "Image Shifting Technique to Resolve Directional Ambiguity in Double-Pulsed Velocimetry," Applied Optics, Vol. 25(21), pp. 3855-3858.

Biswas, G. and Chattopadhyay, H., 1992, "Heat Transfer in a Channel with Built-in Wing-Type Vortex Generators," International Journal of Heat and Mass Transfer, Vol. 35, pp. 803-814.

Biswas, G., Deb, P., and Biswas, S., 1994a, "Generation of Longitudinal Streamwise Vortices – A Device for Improving Heat Exchanger Design," Transactions of ASME - J. Heat Transfer, Vol. 116, pp. 588-597.

Biswas, G., Mitra, N.K., and Fiebig, M., 1989, "Computation of Laminar Mixed Convection Flow in a Channel with Wing-Type Built-in Obstacle," Journal of Thermophysics, Vol. 3, No. 4, pp. 447-453.

Biswas, G., Mitra, N.K., and Fiebig, M., 1994b, "Heat Transfer Enhancement in Fin-Tube Heat Exchangers by Winglet Type Vortex Generators," Int. J. Heat Mass Transfer, Vol. 37, No. 2, pp. 283-291.

Biswas, G., Torii, K., Fujii, D., and Nishino, K., 1996, "Numerical and Experimental Determination of Flow Structure and Heat Transfer Effects of Longitudinal Vortices in a Channel Flow," Int. J. Heat Mass Transfer, Vol. 39, No. 16, pp. 3441-3451.

Chen, Y., Fiebig, M., and Mitra, N.K., 1998a, "Conjugate Heat Transfer of a Finned Oval Tube Part A: Flow Patterns," Numerical Heat Transfer, Part A, Vol. 33, pp. 371-385.

Chen, Y., Fiebig, M., and Mitra, N.K., 1998b, "Conjugate Heat Transfer of a Finned Oval Tube Part B: Heat Transfer Behaviors," Numerical Heat Transfer, Part A, Vol. 33, pp. 387-401.

Chen, Y., Fiebig, M., and Mitra, N.K., 1998c, "Conjugate Heat Transfer of a Finned Oval Tube with a Punched Longitudinal Vortex Generator in Form of a Delta Winglet – Parametric Investigations of the Winglet," Int. J. Heat Mass Transfer, Vol. 41, pp. 3961-3978.

Chen, Y., Fiebig, M., and Mitra, N.K., 1998d, "Heat Transfer Enhancement of a Finned Oval Tube with Punched Longitudinal Vortex Generators In-Line," Int. J. Heat Mass Transfer, Vol. 41, pp. 4151-4166.

Chen, Y., Fiebig, M., and Mitra, N.K., 2000, "Heat Transfer Enhancement of Finned Oval Tubes with Staggered Punched Longitudinal Vortex Generators," Int. J. Heat Mass Transfer, Vol. 43, pp. 417-435.

Deb, P., Biswas, G., and Mitra, N.K., 1995, "Heat Transfer and Flow Structure in Laminar and Turbulent Flows in a Rectangular Channel with Longitudinal Vortices," Int. J. Heat Mass Transfer, Vol. 38, pp. 2427-2444.

DeJong, N.C. and Jacobi, A.M., 1995, "An Experimental Study of Flow and Heat Transfer in Offset Strip and Louvered-Fin Heat Exchangers," ACRC TR-91, Air Conditioning and Refrigeration Center, University of Illinois at Urbana-Champaign, Urbana, Illinois.

DeJong, N.C. and Jacobi, A.M., 1997, "An Experimental Study of Flow and Heat Transfer in Parallel-Plate Arrays: Local, Row-by-Row and Surface Average Behavior," Int. J. Heat Mass Transfer, Vol. 40, pp. 1365-1378.

DeJong, N.C., Zhang, L.W., Jacobi, A.M., Balachandar, S., and Tafti, D.K., 1998, "A Complementary Experimental and Numerical Study of the Flow and Heat Transfer in Offset Strip-Fin Heat Exchangers," Transactions of ASME - J. Heat Transfer, Vol. 120, pp. 690-698.

Edwards, F.J. and Alker, C.J.R., 1974, "The Improvement of Forced Convection Surface Heat Transfer Using Surface Protrusions in the Form of (A) Cubes and (B) Vortex Generators," Proceedings of Fifth International Heat Transfer Conference, Tokyo, Vol. 2, pp. 244-248.

Eibeck, P.A. and Eaton, J.K., 1987, "Heat Transfer Effects of a Longitudinal Vortex Embedded in a Turbulent Boundary Layer," J. Heat Transfer, Vol. 109, pp. 16-24.

Fiebig, M., 1995a, "Embedded Vortices in Internal Flow: Heat Transfer and Pressure Loss Enhancement," Int. J. Heat Fluid Flow, Vol. 16, pp. 376-388.

Fiebig, M., 1995b, “Vortex Generators for Compact Heat Exchangers,” J. Enhanced Heat Transfer, Vol. 2, pp. 43-61.

Fiebig, M., 1996, “Vortices: Tools to Influence Heat Transfer – Recent Developments,” Proc. 2nd European Thermal-Sciences and 14th UIT National Heat Transfer Conference, Vol. 1, pp. 41-56.

Fiebig, M., Brockmeier, U., Mitra, N.K., and Guntermann, T., 1989, “Structure of Velocity and Temperature Fields in Laminar Channel Flows with Longitudinal Vortex Generators,” Numerical Heat Transfer, Part A, Vol. 15, pp. 281-302.

Fiebig, M., Chen, Y., Grosse-Gorgemann, A., and Mitra, N.K., 1995e, “Conjugate Heat Transfer of a Finned Tube Part B: Heat Transfer Augmentation and Avoidance of Heat Transfer Reversal by Longitudinal Vortex Generators,” Numerical Heat Transfer, Part A, Vol. 28, pp. 147-155.

Fiebig, M., Grosse-Gorgemann, A., Chen, Y., and Mitra, N.K., 1995d, “Conjugate Heat Transfer of a Finned Tube Part A: Heat Transfer Behavior and Occurrence of Heat Transfer Reversal,” Numerical Heat Transfer, Part A, Vol. 28, pp. 133-146.

Fiebig, M., Guntermann, T., and Mitra, N.K., 1995c, “Numerical Analysis of Heat Transfer and Flow Loss in a Parallel Plate Heat Exchanger Element With Longitudinal Vortex Generators as Fins,” Trans. of ASME, Vol. 117, pp. 1064-1067.

Fiebig, M., Kallweit, P., and Mitra, N.K., 1986, “Wing Type Vortex Generators for Heat Transfer Enhancement,” Proceedings of Eighth International Heat Transfer Conference, San Francisco, Vol. 5, pp. 2909-2913.

Fiebig, M., Kallweit, P., Mitra, N.K., and Tiggelbeck, S., 1991, “Heat Transfer Enhancement and Drag by Longitudinal Vortex Generators in Channel Flow,” Experimental Thermal and Fluid Science, Vol. 4, pp. 103-114.

Fiebig, M., Mitra, N., and Dong, Y., 1990, “Simultaneous Heat Transfer and Flow Loss Reduction of Fin-Tubes,” Proceedings of Ninth International Heat Transfer Conference, Vol. 4, pp. 51-56.

Fiebig, M., Valencia, A., and Mitra, N., 1993, “Wing-Type Vortex Generators for Fin-and-Tube Heat Exchangers,” Experimental Thermal and Fluid Science, Vol. 7, pp. 287-295.

Fiebig, M., Valencia, A., and Mitra, N., 1994, “Local Heat Transfer and Flow Losses in Fin-and-Tube Heat Exchangers with Vortex Generators: A Comparison of Round and Flat Tubes,” Experimental Thermal and Fluid Science, Vol. 8, pp. 35-45.

Gentry, M.C. and Jacobi, A.M., 1997, “Heat Transfer Enhancement by Delta-Wing Vortex Generators on a Flat Plate: Vortex Interactions with the Boundary Layer,” Experimental Thermal and Fluid Science, Vol. 14, pp. 231-242.

Gentry, M.C. and Jacobi, A.M., 1998, “Heat Transfer Enhancement Using Tip and Junction Vortices,” ACRC TR-137, Air Conditioning and Refrigeration Center, University of Illinois at Urbana-Champaign, Urbana, Illinois.

Goldstein, R.J. and Cho, H.H., 1995, “A Review of Mass Transfer Measurements Using Naphthalene Sublimation,” Experimental Thermal and Fluid Science, Vol. 10, pp. 416-434.

Jacobi, A.M. and Shah, R.K., 1995, “Heat Transfer Surface Enhancement Through the Use of Longitudinal Vortices: A Review of Recent Progress,” Experimental Thermal Fluid Science, Vol. 11, pp. 295-309.

Joshi, H.M. and Webb, R.L., 1987, “Heat Transfer and Friction in the Offset Strip Fin Heat Exchanger,” Int. J. Heat Mass Transfer, Vol. 30, pp. 69-84.

Kays, W.M., and London, A.L., 1984, “Compact Heat Exchangers,” McGraw-Hill, New York.

Keane, R.D. and Adrian, R.J., 1990, “Optimization of Particle Image Velocimeters. Part I: Double Pulsed Systems,” Measurement Science and Technology, Vol. 1, pp. 1202-1215.

Keane, R.D. and Adrian, R.J., 1991a, “Cross-Correlation Analysis of Particle Image Fields for Velocity Measurement,” Experimental and Numerical Flow Visualization, Vol. 128, pp. 1-8.

Keane, R.D. and Adrian, R.J., 1991b, “Optimization of Particle Image Velocimeters. Part II: Multiple Pulsed Systems,” Measurement Science and Technology, Vol. 2, pp. 963-974.

Keane, R.D. and Adrian, R.J., 1992, “Theory of Cross-Correlation Analysis of PIV Images,” Applied Scientific Research, Vol. 49, pp. 191-215.

Kearney, S.P. and Jacobi, A.M., 1995, “Local and Average Heat Transfer and Pressure Drop Characteristics of Annularly Finned Tube Heat Exchangers,” ACRC TR-69, Air Conditioning and Refrigeration Center, University of Illinois at Urbana-Champaign, Urbana, Illinois.

Kline, S.J. and McClintock, F.A., 1953, “Describing Uncertainties in Single Sample Experiments,” Mechanical Engineering, Vol. 75, pp. 3-8.

Liou, T.M., Chen, C.C., and Tsai, T.W., 2000, “Heat Transfer and Fluid Flow in a Square Duct with 12 Different Shaped Vortex Generators,” Journal of Heat Transfer, Vol. 122, pp. 327-335.

Manglik, R.M. and Bergles, A.E., 1995, “Heat Transfer and Pressure Drop Correlations for the Rectangular Offset Strip Fin Compact Heat Exchanger,” Experimental Thermal and Fluid Science, Vol. 10, pp. 171-180.

Mendes, P.R. Souza, 1991, “Review: The Naphthalene Sublimation Technique,” Experimental Thermal and Fluid Science, Vol. 4, pp. 510-523.

Mochizuki, S. and Yagi, Y., 1982, “Characteristics of Vortex Shedding in Plate Arrays,” Flow Visualization II, W. Merzkirch, ed., pp. 99-103, Hemisphere Publishing, Washington, D.C.

Mochizuki, S., Yagi, Y., and Yang, W., 1987, “Transport Phenomena in Stacks of Interrupted Parallel-Plate Surfaces,” Experimental Heat Transfer, Vol. 1, pp. 127-140.

Mullisen, R.S. and Loehrke, R.I., 1986, “A Study of the Flow Mechanisms Responsible for Heat Transfer Enhancement in Interrupted-Plate Heat Exchangers,” J. Heat Transfer, Vol. 108, pp. 377-385.

Pauley, W.R. and Eaton, J.K., 1988, “Experimental Study of the Development of Longitudinal Vortex Pairs Embedded in a Turbulent Boundary Layer,” AIAA Journal, Vol. 26(7), pp. 816-823.

Prasad, A.K., Adrian, R.J., Landreth, C.C., and Offutt, P.W., 1992, “Effect of Resolution on the Speed and Accuracy of Particle Image Velocimetry Interrogations,” Experiments in Fluids, Vol. 13, pp. 105-116.

Raffel, M., Willert, C., and Kompenhans, J., 1998, “Particle Image Velocimetry: A Practical Guide,” Springer, Berlin, Germany.

Russell, C.M.B., Jones, T.V., and Lee, G.H., 1982, “Heat Transfer Enhancement Using Vortex Generators,” Proceedings of Seventh International Heat Transfer Conference, New York, Vol. 2, pp. 283-288.

Smotrys, M. L., Dutton, J.C., and Jacobi, A.M., 2001, “A Particle Image Velocimetry Study of Flow Structure in an Offset-Strip Array with Delta-Wing Vortex Generators,” ACRC TR-182, Air Conditioning and Refrigeration Center, University of Illinois at Urbana-Champaign, Urbana, Illinois.

Sparrow, E.M. and Hajiloo, A., 1980, “Measurements of Heat Transfer and Pressure Drop for an Array of Staggered Plates Aligned Parallel to an Air Flow,” J. Heat Transfer, Vol. 102, pp. 426-432.

Tiggelbeck, S., Mitra, N., and Fiebig, M., 1992, “Flow Structure and Heat Transfer in a Channel With Multiple Longitudinal Vortex Generators,” Experimental Thermal and Fluid Science, Vol. 5, pp. 425-436.

Tiggelbeck, S., Mitra, N., and Fiebig, M., 1993, “Experimental Investigation of Heat Transfer Enhancement and Flow Losses in a Channel with Double Rows of Longitudinal Vortex Generators,” Int. J. Heat Mass Transfer, Vol. 36, No. 9, pp. 2327-2337.

Torii, K., Yanagihara, J.I., and Nagai, Y., 1991, “Heat Transfer Enhancement by Vortex Generators,” ASME/JSME Thermal Engineering Proceedings, Vol. 3, pp. 77-83.

Torii, K., Nishino, K., and Nakayama, K., 1994, “Mechanism of Heat Transfer Augmentation by Longitudinal Vortices in a Flat Plate Boundary Layer,” Proceedings of Tenth International Heat Transfer Conference, Vol. 6, pp. 123-128.

Turk, A.Y. and Junkhan, G.H., 1986, “Heat Transfer Enhancement Downstream of Vortex Generators on a Flat Plate,” Proceedings of Eighth International Heat Transfer Conference, San Francisco, Vol. 6, pp. 2903-2908.

Valencia, A., Fiebig, M., and Mitra, N.K., 1996, “Heat Transfer Enhancement by Longitudinal Vortices in a Fin-Tube Heat Exchanger Element with Flat Tubes,” Journal of Heat Transfer, Vol. 118, pp. 209-211.

Westerweel, J., 1993, “Digital Particle Image Velocimetry - Theory and Application,” Delft University, Delft, Netherlands.

Wieting, A.R., 1975, “Empirical Correlations for Heat Transfer and Flow Friction Characteristics of Rectangular Offset-Fin Plate-Fin Heat Exchangers,” J. Heat Transfer, Vol. 97, pp. 488-490.

Xi, G., Futagami, S., Hagiwara, Y., and Suzuki, K., 1991, “Flow and Heat Transfer Characteristics of Offset-Fin Array in the Middle Reynolds Number Range,” ASME/JSME Thermal Engineering Proceedings, Vol. 3, pp. 151-156.

Yanagihara, J.I. and Torii, K., 1990, “Heat Transfer Characteristics of Laminar Boundary Layers in the Presence of Vortex Generations,” Proceedings of Ninth International Heat Transfer Conference, Vol. 6, pp. 323-328.

Zhang, L.W., Balachandar, S., Tafti, D.K., and Najjar, F.M., 1997, “Heat Transfer Enhancement Mechanisms in Inline and Staggered Parallel-Plate Fin Heat Exchangers,” Int. J. Heat Mass Transfer, Vol. 40, pp. 2307-2325.